California AHMCT Program
University of California at Davis
California Department of Transportation

# SIMULATION OF CRANES USING A BOOM SUPPORT VEHICLE

George W. Burkett
John T. McDonald
Steven A. Velinsky

AHMCT Research Report
UCD-ARR-02-06-30-03

Final Report of Contract
65A0091

June 30, 2002

This report has been prepared in cooperation with the State of California, Business Transportation and Housing Agency, Department of Transportation and is based on work supported by Contract Number RTA 65A0091 through the Advanced Highway Maintenance and Construction Technology Research Center at the University of California at Davis.

**Technical Documentation Page**

| | | |
|---|---|---|
| 1. Report No.<br>FHWA/CA/TO-2002/16 | 2. Government Accession No. | 3. Recipient's Catalog No. |
| 4. Title and Subtitle<br>SIMULATION OF CRANES<br>**USING A BOOM SUPPORTVEHICLE**<br>(FORMERLY CRANE DOLLY SUSPENSION STUDY FOR DYNAMIC WEIGHT DISTRIBUTION) | | 5. Report Date<br>June 30, 2002<br>6. Performing Organization Code |
| 7. Author(s):<br>George W. Burkett, John T. McDonald, Steven A. Velinsky | | 8. Performing Organization Report No.<br>UCD-ARR-02-06-30-03 |
| 9. Performing Organization Name and Address<br>AHMCT Center<br>UCD Dept of Mechanical & Aeronautical Engineering<br>Davis, California 95616-5294 | | 10. Work Unit No. (TRAIS)<br>11. Contract or Grant<br>RTA 65A0091 |
| 12. Sponsoring Agency Name and Address<br>California Department of Transportation<br>P.O. Box 942873, MS#83<br>Sacramento, CA 94273-0001 | | 13. Type of Report and Period Covered<br>Final Report<br>July 2000 - June 2002<br>14. Sponsoring Agency Code |
| 15. Supplementary Notes | | |

16. Abstract

The Advanced Highway Maintenance and Construction Technology (AHMCT) Research Center is a cooperative venture between the University of California at Davis and the California Department of Transportation (Caltrans). The research and development projects have the goal of increasing safety and efficiency of roadwork operations. Mobile cranes are common heavy vehicles that are transported on roadways. Quantifying the loads generated by cranes will develop an understanding of the damage they cause allowing a more efficient regulation of axle load limits. This report describes the simulation of cranes using a boom support vehicle, with emphasis on dynamic road loads.

In developing a computer simulation, a pitch plane model of the crane was developed. The final computer simulation is a tool to help develop an understanding of dynamic road loads A finite element model is used to characterize the motion of the boom. Other components of the system are treated as rigid bodies. The simulation can characterize both the traditional and modern styles of mobile cranes. The traditional style uses a walking beam suspension on the carrier and a leaf spring suspension on the dolly. The modern cranes implement a hydro-pneumatic carrier suspension and an air ride suspension on the dolly.

The model presented here is purely theoretical. However, the fundamental dynamics of the system are captured through the implementation of commonly used modeling techniques. This model provides insight to the dynamic road loads generated by mobile cranes. The simulation results show that modern cranes generate significantly lower dynamic loads then traditional cranes. This indicates that there is a need to regulate axle load limits in a manner that compensates for different suspension systems.

| | | | |
|---|---|---|---|
| 17. Key Words<br>Crane Dynamics, Dynamic Modeling, Heavy Vehicle Dynamics, Pitch Plane, Quarter Car, Air Ride, Hydro-pneumatic, Finite Element Beam, Modal Reduction Random Road Generation, Road Loads | | 18. Distribution Statement<br>No restrictions. This document is available to the public through the National Technical Information Service, Springfield, Virginia 22161. | |
| 20. Security Classif. (of this report)<br>Unclassified | 20. Security Classif. (of this page)<br>Unclassified | 21. No. of Pages<br>203 | 22. Price |

Form DOT F 1700.7 (8-72) Reproduction of completed page authorized
(PF V2.1, 6/30/92)

# ABSTRACT

The Advanced Highway Maintenance and Construction Technology (AHMCT) Research Center is a cooperative venture between the University of California at Davis and the California Department of Transportation (Caltrans). The research and development projects have the goal of increasing safety and efficiency of roadwork operations. Mobile cranes are common heavy vehicles that are transported on roadways. Quantifying the loads generated by cranes will develop an understanding of the damage they cause allowing a more efficient regulation of axle load limits. This report describes the simulation of cranes using a boom support vehicle, with emphasis on dynamic road loads.

In developing a computer simulation, a pitch plane model of the crane was developed. The final computer simulation is a tool to help develop an understanding of dynamic road loads A finite element model is used to characterize the motion of the boom. Other components of the system are treated as rigid bodies. The simulation can characterize both the traditional and modern styles of mobile cranes. The traditional style uses a walking beam suspension on the carrier and a leaf spring suspension on the dolly. The modern cranes implement a hydro-pneumatic carrier suspension and an air ride suspension on the dolly.

The model presented here is purely theoretical. However, the fundamental dynamics of the system are captured through the implementation of commonly used modeling techniques. This model provides insight to the dynamic road loads generated by mobile cranes. The simulation results show that modern cranes generate significantly lower dynamic loads then traditional cranes. This indicates that there is a need to regulate axle load limits in a manner that compensates for different suspension systems.

# EXECUTIVE SUMMARY

The California budget allotted $8.3 billion dollars to the California State Department of Transportation for its various responsibilities including maintaining California roadways [5]. Highway maintenance includes many tasks such as removal of debris, maintaining lane delineations, etc. On a per mile basis, the most costly procedures involve the remediation of highway damage due to repeated traffic loads. Of this damage, the biggest contributors are heavy vehicles due to the large loads they impose on the road. In an effort to reduce the damage generated by heavy vehicles, regulatory agencies such as Caltrans impose weight restrictions on these vehicles.

The Advance Highway Maintenance and Construction Technology (AHMCT) Research Center at the University of California at Davis has developed a tool to help build an understanding of the dynamic road loads generated by mobile cranes implementing a boom support dolly, which are classified as heavy vehicles. Vehicle models can be developed in order to gain a better understanding of the dynamics associated with the system. In order to develop a model, it is important to completely define which aspect of the system to focus on. In the model developed here, the focal point is the dynamic road loads generated by the vehicle, which is the main cause of pavement damage. A pitch plane model of the vehicle can be used to capture this aspect of the system.

The crane model utilizes many different modeling techniques to develop a set of equations to represent the system. In developing the mathematical representation of the crane, the system is broken into carrier, dolly and boom subsystems. Both the carrier and dolly subsystems are further subdivided into it's sprung portion and an associated suspension system. Some subsystem- equations are derived from the bond graph approach, while others use the Newton-Euler approach to develop the equations. The model uses a distributed parameter system to capture the motion of the boom. The stiffness and mass matrices associated with the boom are developed in terms of node displacements and rotations. Once these two matrices are determined, the set of equations used to describe the boom motion in terms of displacements and rotations is reduced using a modal transformation to capture the motion of the boom that lies within the frequency range of interest. The motivation of using this approach for the boom is because it is believed that boom flexibility plays a significant role in the system dynamics.

After developing an understanding of the general structure of the equations involved in the crane model, a software package was developed. The software is written to facilitate the user's ability to look at many different crane configurations. The software utilizes a graphical interface to facilitate the user's ability to interactively change various vehicle parameters. MATLAB was selected as the platform on which the final simulation software was developed due to the commonality and the large function library of this particular program.

A significant reduction in dynamic loads associated with hydro-pneumatic suspension carriers over walking beam suspension carriers is demonstrated through the simulation. Many of the effects due to differences in suspension are supported through a simplified quarter car model. The difference in simulation results demonstrated by the two different suspension configurations present a reasonable basis for establishing weight regulations on a more suspension specific basis.

The simulation has helped to develop an understanding of the dynamic loads generated by mobile cranes. The computer model reasonably captures the fundamental dynamic loads generated by mobile cranes. However, steps should be taken to verify the model before any major changes in crane regulations are made based on simulation results.

TABLE OF CONTENTS

Abstract ..... v
Executive Summary ..... vii
Table of Contents ..... ix
List of Figures ..... xiii
List of Tables ..... xvii
Disclaimer/Disclosure ..... xix
Chapter 1 Introduction ..... 1
1.1 Motivation for Investigation of Dynamic Forces ..... 1
1.2 Literature Review ..... 2
1.3 Modeling Approach of the Crane Study ..... 3
Chapter 2 Derivation of equations ..... 9
2.1 Overview ..... 9
2.2 Boom Configurations ..... 10
2.2.1 Lattice Boom Configurations ..... 10
2.2.2 Telescoping Boom Configurations ..... 11
2.3 Connecting the Boom with the Carrier and Dolly ..... 12
2.4 Derivation of Boom Equations ..... 13
2.4.1 Beam Element Formulation ..... 13
2.4.2 Assembling Global Matrices ..... 16
2.4.3 Modal Equations ..... 16
2.4.4 Boom Gravitational Force ..... 18
2.5 Assembling Boom Equations in the State Space System ..... 20
2.5.1 General Carrier and Dolly Equations of Motion ..... 20
2.5.2 Coupling State Space Equations ..... 23
2.6 Summary ..... 27
Chapter 3 Suspension Sub-models ..... 29
3.1 Overview ..... 29
3.2 Derivation of the Suspension Input Velocity From the Sprung Mass ..... 29
3.3 Tire Model ..... 31
3.4 Leaf Spring Suspension ..... 32
3.5 Walking Beam Suspension ..... 34
3.6 Hydro-Pneumatic Suspension Configurations ..... 36
3.6.1 Conventional Axle Suspension ..... 36
3.6.2 Independent Axle Suspension ..... 36
3.6.3 Hydraulic System Configurations ..... 37
3.7 Hydro-Pneumatic Suspension Sub-model ..... 38
3.7.1 Two Axle Hydro-Pneumatic Configuration ..... 38
3.7.2 Hydro-Pneumatic State Equations ..... 39
3.8 Air Ride Suspension Sub-model ..... 43
3.8.1 Air Ride Configuration and Assumptions ..... 43
3.8.2 Air Ride State Equations ..... 45
3.9 Additional Considerations for Air Ride and Hydro-Pneumatic Suspensions ..... 46
3.10 Summary ..... 47
Chapter 4 Road Input Generation ..... 49
4.1 Overview ..... 49

4.2 Tying the Road Input to the Model ..... 49
4.3 Mathematical Road Generation Using a Random White Noise Process ..... 50
4.4 Road Profile From Data File ..... 55
4.5 Summary ..... 62
Chapter 5 Program Structure ..... 63
5.1 Overview ..... 63
5.2 Platform ..... 63
5.3 Directory Structure ..... 64
5.4 Crane Simulation Program Architecture ..... 66
5.4.1 Pre-Processing ..... 68
5.4.2 Processing ..... 72
5.4.3 Post-Processing ..... 76
5.5 Summary ..... 82
Chapter 6 Quarter Truck Model ..... 83
6.1 Overview ..... 83
6.2 Quarter Truck Formulation ..... 83
6.2.1 Leaf Spring Quarter Truck ..... 84
6.2.2 Walking Beam Quarter Truck ..... 85
6.2.3 Hydro-Pneumatic Quarter Truck ..... 85
6.2.4 Air Ride Quarter Truck ..... 86
6.3 Comparison of Quarter Truck Characteristics ..... 87
6.3.1 General Quarter Truck Comparison ..... 87
6.3.2 Comparison of Wide Based Single and Conventional Dual Tires ..... 88
6.3.3 Comparison of Unsprung Masses ..... 89
6.3.4 Comparison of Sprung Masses ..... 90
6.4 Hydro-pneumatic Suspension Comparison ..... 92
6.4.1 Variation of Hydraulic Line Diameter ..... 92
6.4.2 Variation of Hydraulic Line Length ..... 93
6.4.3 Variation of Hydraulic System Operating Pressure ..... 94
6.5 Summary ..... 94
Chapter 7 Simulation of Mobile Cranes ..... 97
7.1 Overview ..... 97
7.2 Dynamics of Traditional Lattice Boom Cranes ..... 98
7.2.1 System Mode Shapes and Power Spectral Density ..... 98
7.2.2 Configuration Case Variation ..... 101
7.2.3 Load Block Mass Variation ..... 104
7.2.4 Dolly Connection Variation ..... 105
7.3 Dynamics of Traditional Telescoping Boom Cranes ..... 106
7.3.1 System Mode Shapes and Power Spectral Density ..... 106
7.3.2 Configuration Case Variation ..... 109
7.3.3 Load Block Mass Variation ..... 112
7.3.4 Dolly Connection Variation ..... 113
7.4 Dynamics of Telescoping Boom Cranes with Hydro-pneumatic Carriers ..... 114
7.4.1 Four Axle Hydro-pneumatic Carrier ..... 114
7.4.2 Six Axle Hydro-pneumatic Carrier ..... 119
7.5 Truck and Semi-trailer Model ..... 124

7.5.1 System Mode Shapes and Power Spectral Density ..... 124
7.6 Truck and Semi-Trailer Comparison ..... 127
7.7 Summary ..... 129
Chapter 8 Conslusion ..... 131
Appendix A Derivation of Finite Element Matrices ..... 133
Appendix B Derivation of Suspension Sub-Models ..... 137
Appendix C Derivation of Initial Suspension Forces ..... 151
Appendix D Load Characterization ..... 157
Appendix E Quarter Truck Properties ..... 163
Appendix F Crane Parameters ..... 167
References ..... 181

LIST OF FIGURES

Figure 1.1 Four Axle Carrier with Three Axle Boom Dolly and a Telescoping Boom..... 1
Figure 2.1 Simulation Schematic ..... 10
Figure 2.2 Lattice Boom Schematic ..... 11
Figure 2.3 Finite Element Representation of the Lattice Boom ..... 11
Figure 2.4 Telescoping Boom Schematic ..... 11
Figure 2.5 Finite Element Representation of the Telescoping Boom ..... 12
Figure 2.6 Boom/Rigid Body Connection ..... 12
Figure 2.7 Beam Element ..... 13
Figure 2.8 Beam Segment in Bending ..... 15
Figure 2.9 Boom Gravitational Force ..... 19
Figure 2.10 General Carrier Free Body Diagram ..... 21
Figure 2.11 General Dolly Free Body Diagram ..... 22
Figure 3.1 Model/Sub-model Interaction ..... 30
Figure 3.2 Tire Model Schematic ..... 31
Figure 3.3 Physical Representation of Leaf Spring Model ..... 32
Figure 3.4 Mathematical Leaf Spring Model Characterization ..... 33
Figure 3.5 Physical Characterization of Walking Beam Suspension ..... 34
Figure 3.6 Mathematical Walking Beam Suspension Characterization..... 34
Figure 3.7 Conventional Axle Suspension ..... 36
Figure 3.8 Megatrak Suspension ..... 37
Figure 3.9 Hydraulic System Schematic ..... 38
Figure 3.10 Two Axle Hydro-pneumatic Sub-model ..... 39
Figure 3.11 Bond Graph of Two Axle Hydro-pneumatic Sub-model ..... 40
Figure 3.12 Hydraulic Ram with Stiff Spring in Plunger ..... 41
Figure 3.13 Trailing Arm Velocity Diagram ..... 43
Figure 3.14 Air Ride Sub-model ..... 44
Figure 3.15 Bond Graph of Air Ride Sub-model ..... 45
Figure 3.16 Additional Suspension Considerations ..... 47
Figure 4.1 Autocorrelation Function of Road Elevation ..... 51
Figure 4.2 Random Probability Distribution Used for Artificial Road Profile Generation ..... 52
Figure 4.3 Rescaled Random Number Distribution Used for Input Road Velocity ..... 53
Figure 4.4 Artificial Road Generated by Using Random Process Sampled at 150Hz..... 54
Figure 4.5 Artificial Road Generated Using Random Process Sampled at 5Hz. ..... 55
Figure 4.6 Comparison of Analytical Signal to Spline Fit Using 2 Data Points Per Cycle. ..... 57
Figure 4.7 Comparison of Analytical Signal to Spline Fit Using 3 Data Points Per Cycle ..... 57
Figure 4.8 Higher Frequency Regenerated Signal ..... 58
Figure 4.9 Analytical Derivative vs. Forward Difference ..... 59
Figure 4.10 Analytical Derivative vs. Forward Difference Using Correction Terms..... 60
Figure 4.11 Integrated Forward Difference vs. Initial Analytical Signal..... 61
Figure 4.12 Road Data and Regenerated Input Signal Using the Process Discussed Above..... 62
Figure 5.1 Directory Structure ..... 65
Figure 5.2 Program Structure ..... 67
Figure 5.3 Simplified Program Structure ..... 67
Figure 5.4 General Program Flow of Pre-processing Section ..... 68

Figure 5.5 Main Program Screen ..... 69
Figure 5.6 Dolly and Carrier Pre-processing Loop ..... 70
Figure 5.7 Typical Input Screen ..... 70
Figure 5.8 The Road Pre-processing Loop ..... 71
Figure 5.9 The Boom Pre-processing Loop ..... 72
Figure 5.10 Processing Section ..... 73
Figure 5.11 SIMULINK Template File ..... 74
Figure 5.12 SIMULINK Template File Editing Sequence ..... 74
Figure 5.13 Edited SIMULINK File ..... 75
Figure 5.14 Post-processing ..... 76
Figure 5.15 Summary Window ..... 78
Figure 5.16 Sample Movie Frame ..... 80
Figure 5.17 Data Manager ..... 81
Figure 6.1 Quarter Truck Connection Diagram ..... 84
Figure 6.2 Quarter Truck Leaf Spring Tandem ..... 84
Figure 6.3Quarter Truck Walking Beam Tandem ..... 85
Figure 6.4 Quarter Truck Hydro-pneumatic Tandem ..... 86
Figure 6.5 Quarter Truck Air Ride Tandem ..... 86
Figure 6.6 Quarter Truck Comparison ..... 88
Figure 6.7 Wide Based Single vs. Conventional Dual Tire ..... 89
Figure 6.8 Comparison of Unsprung Mass ..... 90
Figure 6.9 Sprung Mass Variation ..... 91
Figure 6.10 Variation of Hydraulic Line Diameter ..... 92
Figure 6.11 Variation of Hydraulic Line Length ..... 93
Figure 6.12 Variation of Hydraulic System Operating Pressure ..... 94
Figure 7.1 Traditional Lattice Boom Crane (American 8470) ..... 98
Figure 7.2 Traditional Lattice Boom Crane ~ Mode Shapes ..... 99
Figure 7.3 Traditional Lattice Boom Crane ~ PSD ..... 100
Figure 7.4 Traditional Lattice Boom Crane ~ Axle Loads ..... 102
Figure 7.5 Traditional Lattice Boom Crane ~ Boom Connection Forces ..... 102
Figure 7.6 Traditional Lattice Boom Crane ~ Boom Vibration Variation ..... 104
Figure 7.7 Traditional Lattice Boom Crane ~ Load Block Variation ..... 105
Figure 7.8 Traditional Lattice Boom Crane ~ Dolly Connection Variation ..... 106
Figure 7.9 Traditional Telescoping Boom Crane (Grove TM9120) ..... 106
Figure 7.10 Traditional Telescoping Boom Crane ~ Mode Shapes ..... 107
Figure 7.11 Traditional Telescoping Boom Crane ~ PSD ..... 108
Figure 7.12 Traditional Telescoping Boom Crane ~ Axle Loads ..... 110
Figure 7.13 Traditional Telescoping Boom Crane ~ Boom Connection Forces ..... 111
Figure 7.14 Traditional Telescoping Boom Crane ~ Boom Vibration Variation ..... 112
Figure 7.15 Traditional Telescoping Boom Crane ~ Load Block Variation ..... 113
Figure 7.16 Traditional Telescoping Boom Crane ~ Connection Variation ..... 114
Figure 7.17 Four Axle Hydro-pneumatic Carrier ~ Mode Shapes ..... 115
Figure 7.18 Four Axle Hydro-pneumatic Carrier ~ PSD ..... 116
Figure 7.19 Four Axle Hydro-pneumatic Carrier ~ Axle Loads ..... 118
Figure 7.20 Four Axle Hydro-pneumatic Carrier ~ Boom Connection Forces ..... 118
Figure 7.21 Six Axle Hydro-pneumatic Carrier (Grove GMK6250) ..... 119

Figure 7.22 Four Axle Hydro-pneumatic Carrier ~ Mode Shapes ..... 120
Figure 7.23 Four Axle Hydro-pneumatic Carrier ~ PSD ..... 121
Figure 7.24 Four Axle Hydro-pneumatic Crane ~ Axle Loads ..... 123
Figure 7.25 Four Axle Hydro-pneumatic Crane ~ Boom Connection Forces..... 123
Figure 7.26 Five Axle Truck and Semi-trailer Configuration ..... 124
Figure 7.27 Five Axle Truck and Semi-trailer ~ Mode Shapes..... 125
Figure 7.28 Five Axle Truck and Semi-trailer ~ PSD ..... 126
Figure 7.29 Truck Load Plot..... 127
Figure 7.30 Dynamics Associated with Rear Carrier Axles..... 128

# LIST OF TABLES

Table 1.1 Models Available in the Program ..... 6
Table 1.2 Road Input Routines ..... 6
Table 3.1 Typical Linear Tire Values ..... 32
Table 4.1 Typical Values for the Road Roughness Parameter ..... 50
Table 5.1 Output Routines ..... 82
Table 7.1 Traditional Lattice Boom Crane ~ Power Percentage ..... 100
Table 7.2 Traditional Telescoping Boom Crane ~ Power Percentage ..... 108
Table 7.3 Four Axle Hydro-pneumatic Carrier ~ Power Percentage ..... 116
Table 7.4 Four Axle Hydro-pneumatic Crane ~ Power Percentage ..... 122
Table 7.5 Five Axle Truck and Semi-trailer Configuration ~ Power Percentage ..... 126
Table 7.6 Summary of Models ..... 128

## DISCLAIMER/DISCLOSURE

The research reported herein was performed as part of the Advanced Highway Maintenance and Construction Technology (AHMCT) Research Center, within the Department of Mechanical and Aeronautical Engineering at the University of California, Davis and the Division of New Technology and Materials Research at the California Department of Transportation. It is evolutionary and voluntary. It is a cooperative venture of local, state and federal governments and universities.

The contents of this report reflect the views of the authors who are responsible for the facts and the accuracy of the data presented herein. The contents do not necessarily reflect the official views or policies of the STATE OF CALIFORNIA or the FEDERAL HIGHWAY ADMINISTRATION and the UNIVERSITY OF CALIFORNIA. This report does not constitute a standard specification, or regulation.

# CHAPTER 1
# INTRODUCTION

## 1.1 Motivation for Investigation of Dynamic Forces

In 2001, the California budget allotted $8.3 billion dollars to the California State Department of Transportation (Caltrans) for its various responsibilities including maintaining California roadways [5]. Highway maintenance includes many tasks such as debris removal, pavement repair, etc. On a per mile basis, the most costly procedures involve the remediation of highway damage due to repeated traffic loads.

Heavy vehicles such as legal trucks and extralegal weight permit vehicles are a contributor to pavement damage. Extralegal weight permit vehicles are 1-3% of the total truck population on the highways. Extralegal weight cranes are a small percentage of these vehicles. The damage caused by the cyclic loads of these vehicles is commonly quantified through a power law relationship. Pavement damage is commonly characterized as basically the tire force magnitude raised to a scaling power. The commonly accepted range for these powers is between 2 and 6 [8]. This relationship reaffirms that heavy vehicles cause a substantial portion of the roadway damage.

The goal of this study is to determine the dynamic road loads generated by mobile cranes. One way to analyze these loads is by collecting experimental results for a wide range of cases; this can be very costly approach. A more cost effective method of determining dynamic loads is through a mathematical model. This study will generate a model and simulate several representative crane configurations to determine resulting dynamic loads.

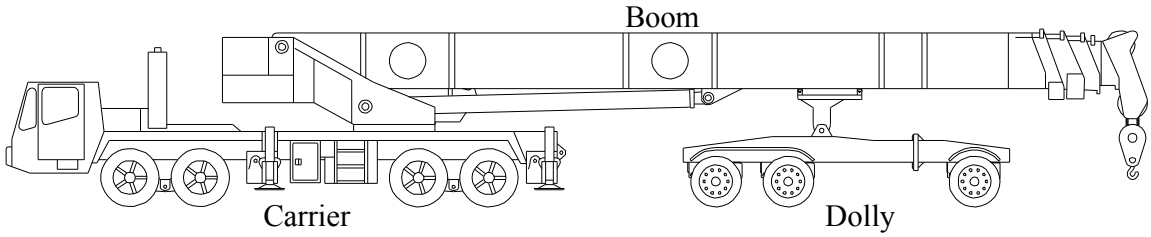


*Figure 1.1 Four Axle Carrier with Three Axle Boom Dolly and a Telescoping Boom*

Figure 1.1 introduces the general configuration of a mobile crane. The boom is supported by a dolly, which removes a substantial portion of the boom's mass from the carrier during transportation. One typical boom structure for mobile cranes is a lattice boom. This is a tube steel framework with removable sections for transportation. A second structure is the telescoping boom. It consists of inner-stacked box tube sleeves that are retracted during transportation. A load block is typically supported at the end of the boom tip, reducing weight on the carrier and increasing the load on the boom support dolly. To facilitate the owners needs, extra axles may be added to the dolly and additional components such as a counter weight may be transported on the dolly.

Regulatory agencies, such as Caltrans, impose weight limitations on heavy vehicles based on static axle weights and axle configurations. The goal of these limitations is to assure that

extralegal weight vehicles do not exceed bridge capacity and also to minimize the road damage generated by heavy vehicles on roadways. Acceptable levels have been determined in order to safe guard bridges and make it practical for larger vehicles to operate on roadways. The axle loads of these heavy vehicles are governed by Caltrans permit policy and acceptable routes are determined by bridge capacity.

The allowable static axle loading of cranes dollies is a long debated subject. Crane carriers are granted maximum axle load (Purple Weight) allowed by Caltrans permit policy. However, dollies are restricted to 80.1kN (18,000 pounds) for a single axle and 142.3kN (32,000 pounds) for a tandem pair. This restriction was limited to the legal axle weight at the time permit policy was enacted and was placed due to dynamic impact load concerns. Caltrans engineers reasoned that forces created from the whipping motion of the boom are transferred directly through the dolly to the roadway below.

Crane industry members have requested for many years that dolly axle loads be increased. They contend that the above inequities do not exist and in fact a crane transported on a trailer is dynamically no different than a self-propelled crane with a boom supported on a dolly. Since the heavy haul tractor semi-trailer combination receives purple weight, the crane dolly should be increased.

To honor crane industry's claim, a recent weigh in motion field test was conducted on the Grove GMK 6250, a modern six-axle carrier with hydro-pneumatic suspension. The test crane supported the boom on a three axle dolly with air ride suspension. In this test, the carrier preformed very well while the dolly still exceeded the allowable impact load limits. As a result of this test, this crane model with hydro-pneumatic suspension on the carrier and air ride on the dolly was approved for green permit weight on the dolly.

The biggest ramification the weight limitations have on the crane industry is that various components of the crane may need to be removed for transport. Additional time is required to remove these pieces for transport and then re-install them for the crane to operate. In addition to the time lost disassembling and reassembling the crane, the removed pieces must also be separately transported to the new location. This requires the use of additional vehicles to transport the various components. Basically put, the weight limitations established by regulatory agencies impose additional operating costs on the crane industry.

## 1.2 Literature Review

Various studies have been conducted to provide insight to the dynamic road loads generated by vehicles. Many people have established these loads through both simulation and experimentation. The dynamic loads generated by cranes are not a common focus in literature, hence a need to develop an understanding of mobile crane dynamics becomes apparent. Many people have looked at the dynamic loads of tractor semi-trailer models, which provide a starting point to begin developing a crane model.

In 1987, J. Felez and C. Vera simulated the roll dynamics of large cranes with hydro-pneumatic suspension [12]. Though the only carrier dynamics during cornering were considered, the study did aid in establishing hydro-pneumatic response characteristics.

In 1994-90, Ken Kirschke conducted a Caltrans funded study on crane dynamics [6]. Kirschke developed a simulation to compare the Grove TM9120 to a standard 5-axle truck. Simulation results indicated carrier rear axles loads over 50% higher than the static and dolly axles 25% over the static load. A truck simulation indicated the truck produced negligible dynamic loads.

Kirschke's work was important for establishing the dynamic loads of the carrier axles. Caltrans originally believed the boom mainly affected dolly dynamics, but Kirschke's work brought into question the role of boom dynamics on the carrier.

In Kirschke's model, the equations of motion were developed using a bond graph representation of the system. The model was based on a lumped parameter system using linear force generating elements. Unfortunately, Kirschke passed away before he was able to complete his work. However, Kirschke had documentation of the vehicle parameters used in his simulation. These parameters provided representative numbers for the model that was developed in this work.

### 1.3 Modeling Approach of the Crane Study

The focus of this study is on the dynamic road loads generated by steady-state transportation of cranes. On the highway, cranes typically do not undergo heavy braking or acceleration. Lane change and cornering maneuvers often occur slowly. Assuming that the dynamic road loads generated by left and right wheel tracks is commonly accepted and exercised in the model [23]. Considering these facts, the model assumes that he crane travels at a constant velocity with a constant vehicle heading. Vehicle yaw and roll motion are also neglected. These assumptions reduce the model to the formulation of a pitch plane model.

The boom model must capture the boom interactions with other components of the system. The boom-carrier connection is modeled as a free pin connection. The same pin connection is used to represent the interaction for three axle dollies. In the cases where one and two axle dollies are used, the interaction is modeled as a rigid interaction.

The pin assumption physically reduces the degrees of freedom in the system by creating a geometric motion constraint. The motion constraint is generated because the displacement, velocity, and acceleration of a point relative to the Newtonian reference frame in two of the bodies must be equal at all times. One way is to deal with a constraint is to enforce the algebraic relationship in the equations of motion. Another way to deal with the constraint mathematically is using the Karnopp-Margolis method [16]. A motion constraint generated by a pin connection can be modeled by using a stiff linear spring. This idea is used to eliminate the algebraic constraints in order to simplify the mathematical representation of the system.

There are fundamentally two downfalls to this method. The algebraic constraint could be used to reduce the number of degrees of freedom in the system, making the simulation computationally faster. By using the Karnopp-Margolis [16] method, the degree of freedom that the algebraic constraint would eliminate is still included in the system equations. In addition to preventing the ability to eliminate an additional degree of freedom, the large stiffness value

affects the numerical integration step-size. The integration step-size is typically associated with the natural frequencies in the system. The natural frequencies of a system are generally given by

$$w = \sqrt{\frac{k}{m}}. \tag{1.1}$$

A large frequency is introduced into the system of equations due to the stiff spring. These frequencies do not significantly affect the dynamic response of the system in comparison to the response obtained by implementing the algebraic constraint equations. However, the high frequencies force the integration routine to take smaller time steps. The stiffness value used to alleviate the motion constraint must be large enough to capture the desired dynamics. However a smaller value is desired to allow the program to run at an optimum speed.

In order to reduce the computational time required by the simulation, a stiff solver is used [17]. A stiff solver is helpful when numerically integrating equations with a large span of natural frequencies. A stiff solver allows the integration routine to take larger time-steps, allowing the simulation to numerically integrate the set of equations faster.

The mathematical treatment of one and two axle boom dollies is considerably different then the three axle cases. In these cases, the sprung mass associated with the dolly is rigidly attached to the boom. In the case of a two axle dolly, rotational inertia of the dolly is directly incorporated into the finite element model as an additional parameter. However, the simulation does not internally correct for the fact that the dolly's center of gravity is below the boom in a vertical sense. No relative rotation between the boom and the sprung dolly mass can occur. This allows the sprung dolly mass to be lumped into the equations used to model the boom.

The fundamental equations used in the model are the Newton-Euler equations, given by

$$\sum F = ma \tag{1.2}$$

and

$$\sum M = I\alpha. \tag{1.3}$$

By applying these equations to each rigid body in the system, a set of equations to represent the system are developed.

The mobile crane's dynamic response due to surface irregularities in the road should not be large enough to cause the vehicle to undergo large rotations (greater then $5^0$). Therefore, the small angle approximation is reasonable in this case and is given as

$$\sin(\theta) \approx \theta \tag{1.4}$$

and

$$\cos(\theta) \approx 1. \tag{1.5}$$

With the small angle approximation, the equations of motion become linear in terms of the vehicle pitch. This simplification allows many of the equations of motion to be expressed in matrix form, allowing the equations to be written in a more compact and concise form.

In this project, a computer simulation package that allows the mathematical representation of various crane models is developed. In order to fully understand the details of the model it is useful to have some general understanding of the bigger picture. The system is broken down into various sub-systems to aid in looking at different configurations, without having to derive a complete set of equations for each particular case. This facilitates looking at a larger system because the response of each subsystem can be looked at for stability characteristics. This feature is particularly useful in the development of different suspension sub-models.

The three main subsystems in the model are the carrier, dolly and boom. Both the carrier and the dolly are represented as rigid bodies. The mathematical representation of the boom is based on a finite element model. In order to reduce the number of integration variables in the simulations, the equations used to describe the boom in displacement coordinates are transformed into modal coordinates, capturing the lower frequency range of the boom. The high frequencies associated with the boom flex are neglected since the associated high frequency does not significantly affect dynamic road loads.

The carrier and dolly subsystems are further separated into sprung mass motion and suspension motion. This allows the equations of motion for the sprung masses to be easily expressed and facilitates the implementation of complex suspension sub-models. The suspension sub-models, are derived to accept velocity inputs from the sprung mass and the road. Each suspension sub-models determines the suspension force generated on the pavement and on the sprung mass. This idea allowed the suspension sub-models to be developed before implementing them in a full-scale model.

A list of the models available in the program is provided in Table 1.1 and Table 1.2. The models are presented in this manner because each sub-system is treated independently. This allows each combination to be a viable option for the simulation program. The only combination of subsystems that is not allowed by the program is a combination of truck model components with mobile crane components. This was felt to be an unrealistic model so no effort was made in the program to allow this.

In this report, a presentation of the general equations used in the simulation will be provided. These equations are a framework, for the overall system. Each of the matrices presented contains a larger amount of detail pertaining to the overall system. By representing each subset of equations in this way, different matrices can be used for the various configurations provided that they are derived in a manner that is consistent with the general framework. This allows additional models to be easily implemented.

| | |
|---|---|
| **Carrier** | The carrier is treated as a rigid structure |
| 4-AC-WB--- | 4 axle carrier with a walking beam suspension |
| 5-AC-WB-IF | 5 axle carrier with a leaf spring front and 2 walking beam groups |
| 6-AC-WB--- | 6 axle walking beam carrier |
| 4-AC-HG--- | 4 axle hydro pneumatic carrier |
| 6-AC-HG--- | 6 axle hydro pneumatic carrier |
| 4-AC-WB--M | 4 axle carrier with a sprung mount walking beam suspension. |
| Truck----- | 3 axle semi with a leaf spring front and spring mount walking beam rear |
| **Dolly** | The dolly is treated as a rigid structure |
| 1-AD-IF--- | 1 axle leaf spring dolly |
| 2-AD-WB--- | 2 axle walking beam dolly |
| 3-AD-WB-IR | 3 axle dolly with a walking beam pair and a leaf spring rear axle |
| 3-AD-AR--- | 3 axle air ride dolly |
| 3-AD-HG--- | 3 axle hydro pneumatic dolly |
| 3-AD-LS—I | 3 axle independent leaf spring dolly |
| TRAILER--- | 2 axle trailer (essentially a pure spring mount walking beam group) |
| **Boom** | The boom is treated as a flexible structure implementing a FEM |
| Lattice | Lattice boom structure |
| Telescoping | Telescoping boom structure |
| Trailer | The sprung mass portion of the Semi-trailer |

*Table 1.1 Models Available in the Program*

| | |
|---|---|
| **Road** | Road input velocity models |
| Random road | Implements an artificial road generation routine |
| Road data file | Implements a road elevation data file |
| Sine wave | Allows a pure sine wave velocity to be implemented to the tires |

*Table 1.2 Road Input Routines*

Once the fundamental framework of the system is understood, a more detailed look will be taken at some of the key subsystems. In the simulation, leaf spring, walking beam, hydro-pneumatic, and air ride suspension sub-models are implemented. Details on the various suspension sub-models will be presented in Chapter 3.

The road is very important aspect that needs to be modeled to provide an accurate representation of the inputs to the system. A reasonable input must be used in order to result in a reasonable system response. Chapter 4 presents the method for generating an artificial road. Additionally, the program has the ability to implement a road displacement data file. The method behind the implementation of this file is also discussed in Chapter 4.

In order to exercise the model, a computer simulation program was developed. The program dynamically couples the various sub-systems that are presented here. Through the program execution, a single set of differential equations to represent a configuration specified by the user is derived. This set of equations can then be numerically integrated to represent the motion of the system. Chapter 5 will explain the platform that was chosen and the basic flow of

the program. The discussion of the program flow will be more of an overview of the program structure without going into direct details of code.

Finally, after the program has been described, a look at some of the system results will be taken in Appendix D. Here, an understanding of the vehicle response will be built by looking at various configurations and looking at the dynamic load coefficient, which is a quantity used to represent the dynamic loads generated by a vehicle [8]. It is anticipated that by understanding the dynamics associated with mobile cranes, regulatory agencies will have a way to establish a basis for the weight limitations imposed on mobile cranes.

# CHAPTER 2
# DERIVATION OF EQUATIONS

## 2.1 Overview

When simulating a dynamic system, it is important to accurately account for all components that significantly contribute to the motion of the system. In a road vehicle model, suspension and tire dynamics are evaluated while frame flexibility is often ignored. The vehicle frame vibration frequencies are typically much higher than the suspension and tire frequencies therefore contributing very little to the overall dynamics of the system.

During transportation, the boom is supported on a dolly and towed behind the carrier. Due to the mass and slender nature of the typical crane boom, it has vibration frequencies on the same order of magnitude as the suspension frequencies. The low vibration frequencies and substantial mass make modeling the boom an important exercise.

The finite element method will be used to formulate mass, stiffness and gravitational force matrices. These matrices will be used to generate a subset of modal equations that include only the frequencies and corresponding mode shapes that significantly contribute to the dynamics of the boom. Finally, modal boom equations of motion will be combined with general carrier and dolly equations to create a linear state space representation.

To aid in modeling different configurations within the program, the system is broken into three main sub-models: the carrier, the dolly, and the boom. Every carrier and dolly subsystem is further separated into the suspended rigid body and the associated suspension system. A general illustration of the model breakdown is shown Figure 2.1.

By breaking the model up into subsystems and replacing the appropriate blocks from Figure 2.1, the computer can dynamically derive the set of equations required to represent a particular configuration. A suspension sub-model then provides the rigid bodies with suspension support forces. Each suspension sub-model receives a velocity corresponding to the movement of the suspended masses' connection points and input velocities from a road model. The same road input velocity signal is propagated to sequential tires based on the wheel spacing and the vehicle's forward velocity. The flexible boom communicates with the rigid bodies through a common force and displacement relationship. This chapter discusses the mathematical breakdown of the sprung portion model and how the equations are coupled together into a single set to represent this portion of the vehicle.

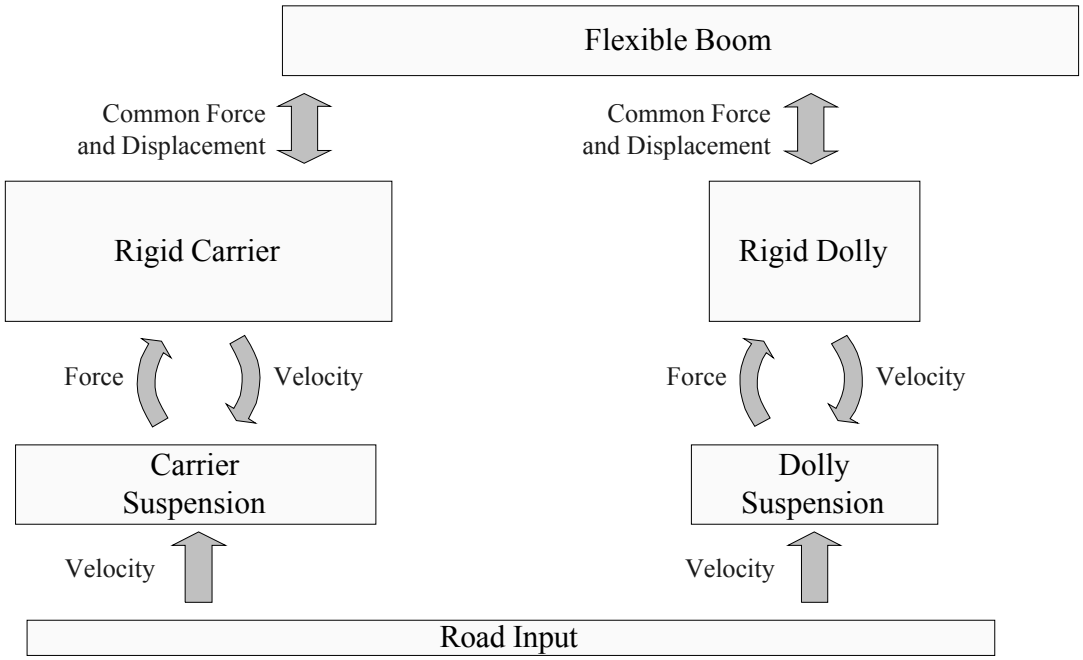


*Figure 2.1 Simulation Schematic*

## 2.2 Boom Configurations

Two general boom structures are found on cranes: the lattice boom and the telescoping boom. Though structurally quite different, the modeling approach allows for a single formulation method.

One-dimensional beam finite elements are used to generate element matrices. The element matrices are then assembled in sections that separate changes in cross-section and rigid body connection points. This formulation approach results in a node at each connection point, eliminating the need for interpolation between nodes.

The load block is always connected to the last node of the final section. This massive load block is suspended by cable, and it is assumed that the cable always remains in tension with negligible stretch relative to the rest of the boom. As a result, the mass of the block is lumped into the end node. The rotational inertia is ignored since the block hangs from cable and does not rotationally interact with the boom.

### 2.2.1 Lattice Boom Configurations

A lattice boom, shown in Figure 2.2, is a tube steel framework. Cord tube extends the length of the boom providing its strength while rigidity is achieved by a latticework of smaller tubes steel and cables.

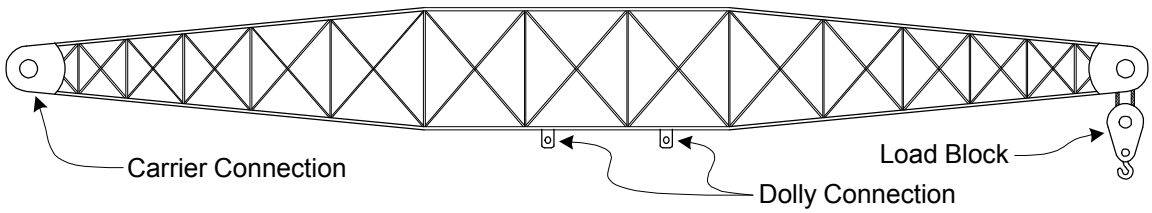


*Figure 2.2 Lattice Boom Schematic*

During transportation, boom center sections are removed, leaving a much shorter structure that can be supported on a dolly. Front and rear tapered sections remain and in some cases, a single constant sized center section used. The load block is suspended from the end of the boom during transportation.

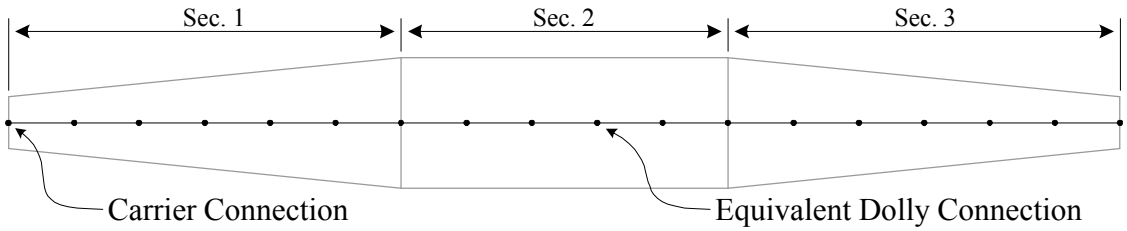


*Figure 2.3 Finite Element Representation of the Lattice Boom*

Figure 2.3 shows the finite element representation of the lattice boom. The front and rear tapered sections (sections 1 and 3, respectively) have linearly varying cross sectional area and inertia, while section 2 has constant cross section. The carrier connects to the first node of section 1 and the load block is accounted for in the last node of section 3. The dolly can connect anywhere along the boom by spacing the elements such that a boom node coincides with the dolly connection. For a boom transported with front and rear sections only, section 2 is omitted.

### 2.2.2 Telescoping Boom Configurations

Telescoping booms are composed of several rectangular cross-section sleeves (see Figure 2.4). Each sleeve is slightly smaller than the previous so the sections can be slid inside each other to create a transportable structure.

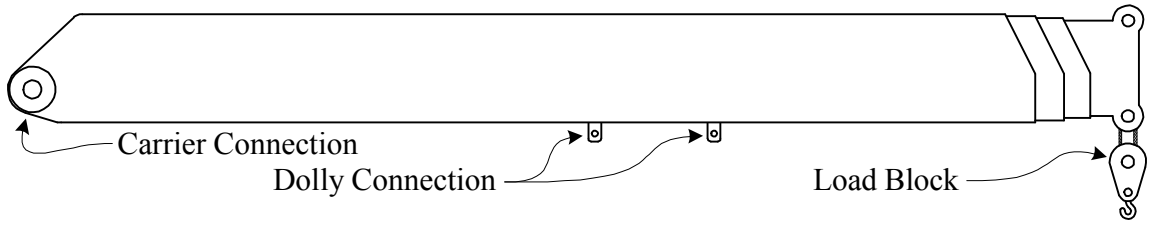


*Figure 2.4 Telescoping Boom Schematic*

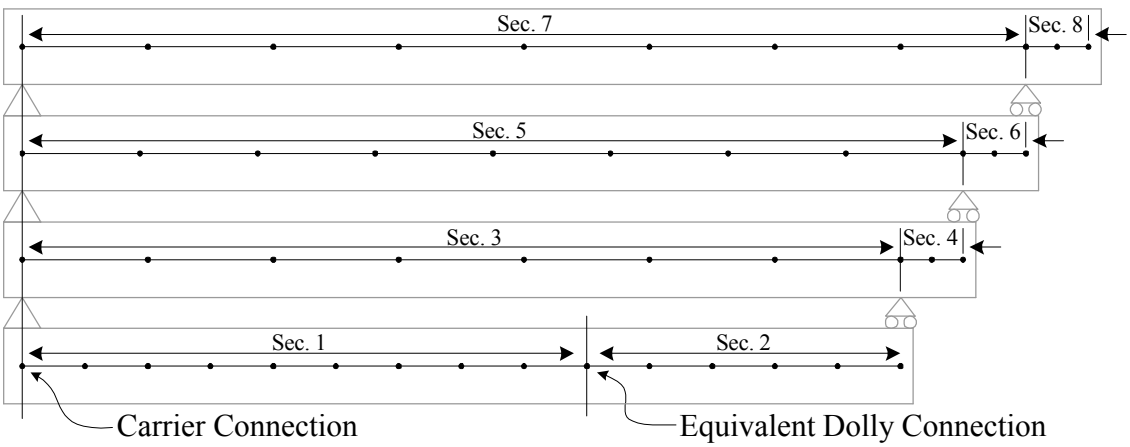


*Figure 2.5 Finite Element Representation of the Telescoping Boom*

Figure 2.5 illustrates the telescoping boom model. It should be noted that boom sleeves are drawn as stacked on top of each other for clarity and the actual boom sleeves rest inside one another. Each inner boom sleeve rests on rollers inside the outer section and these rollers are modeled as pin connections.

Sections 1 and 2 are the outer boom sleeve and they connect to the carrier and dolly. Sections 3, 5 and 7 are the inner boom sleeves that remain inside the boom shell while sections 4, 6 and 8 are the sleeve portions that extend beyond the outer shell. The load block is lumped into the last node of section 8. Figure 2.5 is a representative model of a four sleeve boom and a five sleeve boom would have additional sections 9 and 10 that would attach in a similar manner.

## 2.3 Connecting the Boom with the Carrier and Dolly

The carrier and dolly are modeled as individual rigid bodies. These rigid bodies connect to the boom model at the connection nodes. Attempting to constrain the boom and rigid bodies through a configuration constraint results in a causal conflict. All three of these models receive force as the causal input and specify velocities and displacements as outputs. This conflict results because both the boom and rigid bodies are attempting to set the state of the system.

Hookes law is used to relate the relative displacement of the bodies to a pair of equal and opposite forces. These forces are used as causal inputs to the boom and rigid bodies. The spring connection is shown in Figure 2.6.

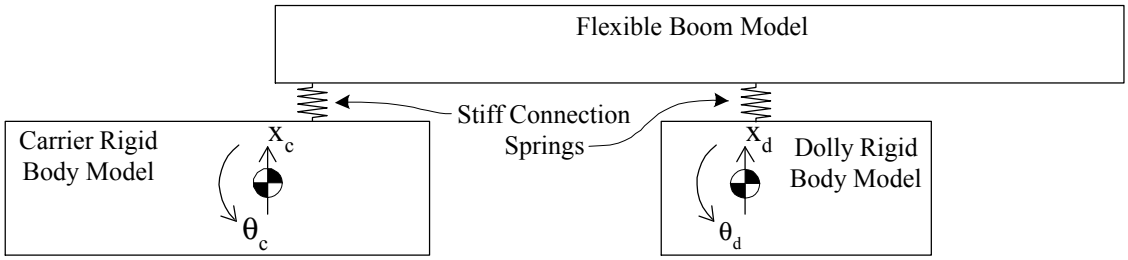


*Figure 2.6 Boom/Rigid Body Connection*

Choosing a high relative spring constant approximates the pin connection by maintaining small relative displacement. A high spring constant also has associated frequencies that are much higher than the system frequencies and therefore make no significant contribution to the overall system dynamics [16].

The dolly rigid body connects to the boom at a single node. One and two axle boom dollies are typically connected rigidly to the boom. Due to this connection, the dolly mass and inertia are lumped into the dolly connection node. The dolly suspension is then connected directly to this node. Three-axle boom dollies have a pivot between the boom cradle and dolly chassis. Therefore, the dolly is modeled as an independent rigid body.

## 2.4 Derivation of Boom Equations

The general time dependent equation of motion for a system of beam finite elements is

$$[M]\frac{d^2\{d\}}{dt^2}+[K]\{d\}=\{F\}. \tag{2.1}$$

In this familiar equation, [M] is the consistent mass matrix and [K] is the material stiffness matrix. Nodal displacements and rotations are contained in vector {d} and {F} describes external forces acting at each node.

### 2.4.1 Beam Element Formulation

The boom is modeled using Bernoulli-Euler beam assumptions considering only axial linear-elastic strain. Finite element matrices are generated from the beam element illustrated in Figure 2.7. The beam element spans a length L with nodes at $x_1$ and $x_2$. Each node has displacement, d and rotation, φ, degrees of freedom that define its configuration. The next two sections derive the shape functions and formulate element mass, stiffness and external force matrices.

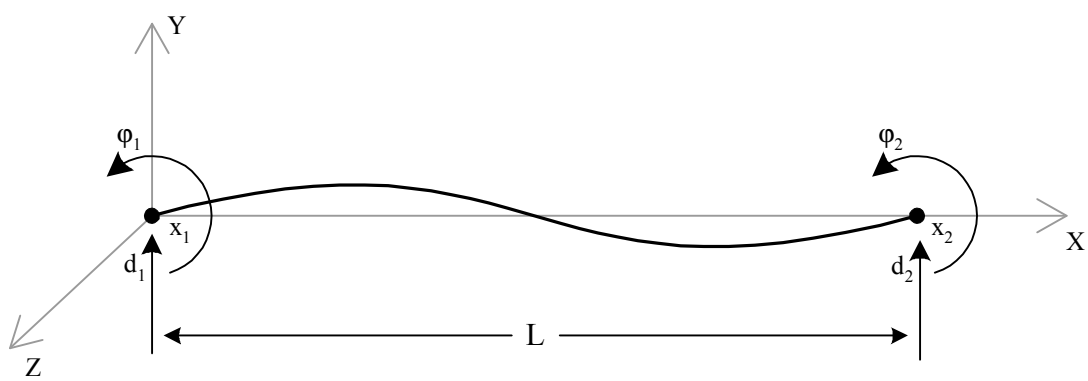


*Figure 2.7 Beam Element*

#### 2.4.1.1 Shape Functions

Derivation of the beam element shape function begins with a third order polynomial

$$d = a_1 + a_2 x + a_3 x^2 + a_4 x^3 . \tag{2.2}$$

Equation (2.2) describes the displacement of any point along the beam and differentiation with respect to x yields the rotation at any point. From Figure 2.7, the nodal coordinate locations are $x_1 = 0$ and $x_2 = L$. Rewriting Equation (2.2) in terms of each nodal degree of freedom yields

$$\begin{aligned} d_1 &= a_1 \\ \frac{d(d_1)}{dx} &= \mathrm{j}_1 = a_2 \\ d_2 &= a_1 + +a_2 L + a_3 L^2 + a_4 L^3 \\ \frac{d(d_2)}{dx} &= \mathrm{j}_2 = a_2 + 2a_3 L + 3a_4 L^2 \end{aligned} . \tag{2.3}$$

Equation (2.3) is used to solve for the $a_i$ values and then they are substituted back into Equation (2.2). This result is rearranged to produce

$$d = N_1 \cdot v_1 + N_2 \cdot \mathrm{j}_1 + N_3 \cdot v_2 + N_4 \cdot \mathrm{j}_2 \tag{2.4}$$

where the shape function values are

$$\begin{aligned} N_1 &= 1 - \frac{3}{L^2} x^2 + \frac{2}{L^3} x^3 \qquad & N_2 &= x - \frac{2}{L} x^2 + \frac{1}{L^2} x^3 \\ N_3 &= \frac{3}{L^2} x^2 - \frac{2}{L^3} x^3 \qquad & N_4 &= \frac{-1}{L} x^2 + \frac{1}{L^2} x^3 \end{aligned} \tag{2.5}$$

[18].

2.4.1.2 <u>Mass, Stiffness and Gravitational Force Matrices</u>

Element matrices are generated from the shape functions presented above. The following indicated integrals are carried out using every shape function combination to generate these matrices.

The consistent mass matrix, for a beam element, is calculated from

$$[M] = \int \mathrm{r} A \lfloor N \rfloor^T \lfloor N \rfloor dx \tag{2.6}$$

where material density is ρ and area is A [18]. A variable cross section element linearly varies the area over the element by

$$A(x) = A_1 + \frac{x}{L} A_2 . \tag{2.7}$$

The left end of the element is area $A_1$ and the right end is $A_1$+$A_2$ with an element length L. Appendix B contains a complete derivation of the mass matrix.

Derivation of the stiffness matrix requires additional steps, which have been included for completeness. The stiffness matrix must satisfy the following

$$\{\varepsilon\} = \lfloor B \rfloor \{v\}. \tag{2.8}$$

where ε denotes axial strain, B is a vector of stress-strain relationships, and v denotes vertical displacement.

To analyze a one dimensional beam element, the axial strain displacement will be assumed to be small so that

$$\varepsilon_x(X,Y) = \frac{du}{dx} \tag{2.9}$$

where u is the axial displacement.

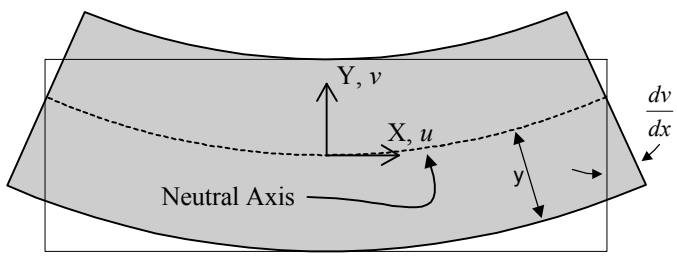


*Figure 2.8 Beam Segment in Bending*

The distance to the neutral axis (shown in Figure 2.8) is represented by y. Using the Bernoulli-Euler beam theory assumption that plane cross-sections remain plane during deformation, transverse displacement is assumed to be

$$u = -y\frac{dv}{dx}. \tag{2.10}$$

Combining Equations (2.9) and (2.10) yields

$$\varepsilon_x(X,Y) = -y\frac{\partial^2 v}{dx^2}. \tag{2.11}$$

Equation (2.11) is identical to Equation (2.8), therefore the resulting [B] vector is

$$\lfloor B \rfloor = -y\frac{d^2\lfloor N \rfloor}{dx^2}.$$

This $\lfloor B \rfloor$ vector is used in the stiffness matrix formulation [18].

The stiffness matrix is finally calculated from

$$[K] = \int \rho A \lfloor B \rfloor^T [D] \lfloor B \rfloor dx \tag{2.12}$$

[18]. A, from Equation (2.7), represents a linearly varying element area. The complete derivation of the stiffness matrix in Appendix B shows each stiffness matrix term has a first moment of area term

$$I = \int y^2 dA = A \cdot y^2 .$$

Making this substitution results in a linearly varying inertia term for variable cross section elements.

The final beam matrix captures the external force vector. In this model the force vector will be used to determine the gravitational force at each boom connection point. This matrix is given by

$$\{F_g\} = \int \rho A \lfloor N \rfloor dx \tag{2.13}$$

[18]. Again, Equation (2.7) linearly varies the area for variable cross section elements, and a complete derivation is provided in Appendix 1.

### 2.4.2 Assembling Global Matrices

The elements are combined into global matrices using the direct stiffness method. By superimposing element matrices, nodal compatibility is enforced. Since the boom is modeled as a one-dimensional structure, no coordinate transformation matrices are needed. Section 2.2 discussed finite element representations of the booms; therefore this section briefly covers superposition details.

Element matrices that share common nodal degrees of freedom are superimposed. When assembling a boom section, common nodal displacement and rotation degrees of freedom are combined. Only displacement terms are superimposed when assembling the pinned configuration in the telescoping booms. In this configuration the two beams can rotate independently but are forced to share a common displacement.

When combining variable cross section elements, the area must be added. The area at the end of the previous section is used as the area of the next section. As a result, the area at the end of the last element is the beginning area of the first plus the sum of the change in area of all the elements.

Recall that the load block is suspended from the end of the boom by steel cable. It is assumed that the cable transmits vertical but not the rotational forces between the bodies. To model the load block, its mass added to the displacement term of final boom node.

### 2.4.3 Modal Equations

The general boom equation of motion, presented in Equation (2.1), is transformed to modal coordinates. Once in the modal domain, only a subset of modal equations will be used in the simulation. These equations only include the modes that make significant contribution to the dynamics of the boom. Such modal reduction methods are commonly employed for large systems [25].

Mode shapes and natural frequencies of the boom are found by solving the Eigenvalue problem

$$[K]\{\phi\} = \{\omega^2\}[M]\{\phi\} \tag{2.14}$$

where ω is the natural frequency and ϕ is the corresponding mode shape vector. Recall, the mass matrix, [M], is from Equation (2.6) and the stiffness matrix, [K], is from Equation (2.12).

The mode shape column vectors generated from Equation (2.14 are assembled in the mode matrix

$$\Phi = \begin{bmatrix} \phi_1(d_1) & \phi_2(d_1) & \phi_3(d_1) & \cdots \\ \phi_1(d_2) & \phi_2(d_2) & \phi_3(d_2) & \\ \vdots & & & \end{bmatrix}. \tag{2.15}$$

Equation (2.15) includes the two rigid body modes and the low frequency bending modes. Rigid body modes result from the free boundary conditions used to model the boom structure. These two modes correspond to boom rigid body displacement and rotation and have two zero associated frequencies. The mode matrix is a linear transformation between displacement coordinates {d} and modal amplitude factors {q}. This transformation is defined by

$$\{d\} = [\Phi]\{q\}. \tag{2.16}$$

The general boom Equation (2.1) is transformed to modal coordinates by

$$[\Phi]^T[M][\Phi]\{\ddot{q}\} + [\Phi]^T[K][\Phi]\{q\} = [\Phi]^T\{F\}. \tag{2.17}$$

Carrying out the mode matrix multiplications results in diagonalized modal mass and stiffness matrices. Multiplying by the inverse of the modal mass matrix yields

$$\{\ddot{q}\} + [m_b]^{-1}[k_b]\{q\} = [m_b]^{-1}[\Phi]\{F\} \tag{2.18}$$

where $[m_b]$ is the modal mass matrix and $[k_b]$ is the modal stiffness matrix.

Structural damping will be included via the damping ratio matrix, [ζ]. This is a diagonal matrix with lightly damped terms corresponding to bending modes only. As a result, the final modal boom equation used in the simulation is

$$\{\ddot{q}\} = -2[\zeta][\omega]\{\dot{q}\} - [\omega]^2\{q\} + [m_b]^{-1}[\Phi]^T\{F_c\}. \tag{2.19}$$

The force vector, $\{F_c\}$ contains the time dependent boom connection forces joining the boom and rigid body models (carrier and dolly). Assuming the dolly connection is at the $n^{th}$ boom node, this vector is more clearly written as

$$\{F_c\} = \begin{Bmatrix} F_{cc} \\ 0 \\ \vdots \\ 0 \\ F_{cd} \\ 0 \\ \vdots \end{Bmatrix} = \begin{Bmatrix} \kappa\left(x_c + L_c q_c - \lfloor f(d_1) \rfloor \{q\}\right) \\ 0 \\ \vdots \\ 0 \\ \kappa\left(x_d - L_d q_d - \lfloor f(d_{2n-1}) \rfloor \{q\}\right) \\ 0 \\ \vdots \end{Bmatrix} \tag{2.20}$$

where $\{F_{cc}\}$ and $\{F_{cd}\}$ are the respective carrier and dolly connection forces. These terms, introduced in Section 2.3 as stiff spring connection equations, have a spring constant κ followed by a relative displacement term. The first portion of the relative displacement terms,

$$\begin{matrix} x_c + L_c q_c \\ x_d + L_d q_d \end{matrix},$$

define carrier and dolly position and are discussed in Section 2.5.1. The second terms,

$$\begin{matrix} \lfloor f(d_1) \rfloor \{q\} \\ \lfloor f(d_{2n-1}) \rfloor \{q\} \end{matrix},$$

are the displacement of the boom connection node after the modal transformation of Equation (2.16). The final term of Equation (2.19) is the modal displacement term most concisely written

$$\begin{aligned} [m_b]^{-1}[\Phi]^T\{F_c\} = {} & [m_b]^{-1}\lfloor \Phi(d_1) \rfloor^T \kappa x_c + [m_b]^{-1}\lfloor \Phi(d_1) \rfloor^T \kappa L_c q_c \\ & + [m_b]^{-1}\lfloor \Phi(d_{2n-1}) \rfloor^T \kappa x_d - [m_b]^{-1}\lfloor \Phi(d_{2n-1}) \rfloor^T \kappa L_d q_d \\ & - [m_b]^{-1}\begin{bmatrix} \Phi(d_1) \\ \Phi(d_{2n-1}) \end{bmatrix}^T \kappa \begin{bmatrix} \Phi(d_1) \\ \Phi(d_{2n-1}) \end{bmatrix}\{q\} \end{aligned} \tag{2.21}$$

The terms of this equation can be found expanded into matrix form in the final state space matrix Equations (2.37) and (2.39).

### 2.4.4 Boom Gravitational Force

Gravitational force is applied to the boom through the external force vector of Equation (2.13). This vector acts at each node of the finite element boom. To simplify simulation equations, boom gravitational force will be formulated as two equivalent forces acting at the boom connection points. Recall that the dolly is connected to the boom at the $n^{th}$ node.

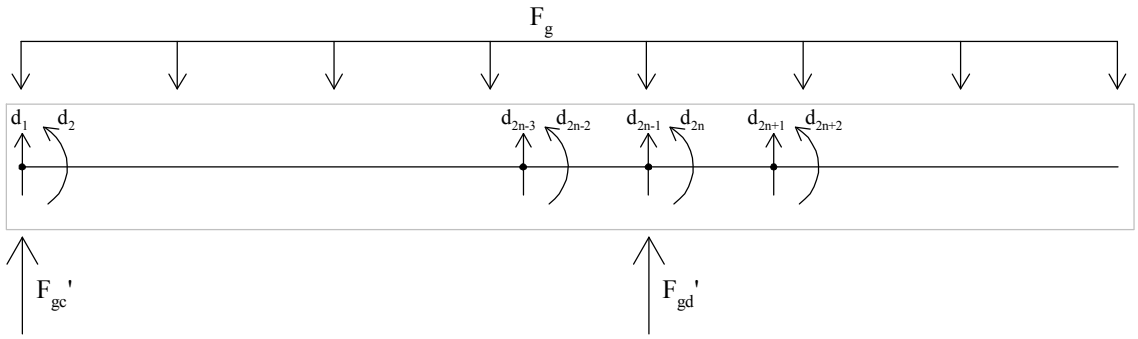


*Figure 2.9 Boom Gravitational Force*

Figure 2.9 illustrates the boom subjected to the gravitational force $F_g$ and supported by static forces $F_{gc}$' and $F_{gd}$'. This problem is mathematically stated

$$[K]\begin{Bmatrix} 0 \\ d_2 \\ \vdots \\ d_{2n-2} \\ 0 \\ d_{2n} \\ \vdots \end{Bmatrix} = -\{F_g\} - \begin{Bmatrix} F_{gc} \\ 0 \\ \vdots \\ 0 \\ F_{gd} \\ 0 \\ \vdots \end{Bmatrix} \tag{2.22}$$

where the support nodes are assumed to have zero vertical displacement. In Equation (2.22), the support forces and all but the two connection node displacements are unknown. The known displacement and their corresponding terms in the stiffness matrix are reordered and replaced by the unknown support forces. This reordering results in

$$\begin{bmatrix} k_{1,1} & k_{1,2n-1} \\ k_{2,1} & k_{2,2n-1} \\ \vdots & \vdots \\ & \\ & \\ & \\ & \end{bmatrix}\begin{Bmatrix} 0 \\ 0 \end{Bmatrix} + \begin{bmatrix} -1 & k_{1,2} & \cdots & k_{1,2n-2} & 0 & k_{1,2n} & \cdots \\ 0 & k_{2,2} & & k_{2,2n-2} & 0 & k_{2,2n} & \\ \vdots & & & & & & \\ 0 & k_{2n-2,2} & & k_{2n-2,2n-2} & 0 & k_{2n-2,2n} & \\ 0 & k_{2n-1,2} & & k_{2n-1,2n-2} & -1 & k_{2n-1,2n} & \\ 0 & k_{2n,2} & & k_{2n,2n-2} & 0 & k_{2n,2n} & \\ \vdots & & & & & & \end{bmatrix}\begin{Bmatrix} F_{gc}' \\ d_2 \\ \vdots \\ d_{2n-2} \\ F_{gd}' \\ d_{2n} \\ \vdots \end{Bmatrix} = -\{F_g\} \tag{2.23}$$

where terms removed from the stiffness matrix are multiplied by the zero displacements. Multiplying through by the inverse of the modified stiffness matrix yields

$$\begin{Bmatrix} F_{gc}' \\ d_2 \\ \vdots \\ d_{2n-2} \\ F_{gd}' \\ d_{2n} \\ \vdots \end{Bmatrix} = -\begin{bmatrix} 1 & k_{1,2} & \cdots & k_{1,2n-2} & 0 & k_{1,2n} & \cdots \\ 0 & k_{2,2} & & k_{2,2n-2} & 0 & k_{2,2n} & \\ \vdots & & & & & & \\ 0 & k_{2n-2,2} & & k_{2n-2,2n-2} & 0 & k_{2n-2,2n} & \\ 0 & k_{2n-1,2} & & k_{2n-1,2n-2} & 1 & k_{2n-1,2n} & \\ 0 & k_{2n,2} & & k_{2n,2n-2} & 0 & k_{2n,2n} & \\ \vdots & & & & & & \end{bmatrix}^{-1} \{F_g\}. \tag{2.24}$$

$F_{gc}$' and $F_{gd}$' act on the boom while the forces on the carrier are

$$\begin{aligned} F_{gc} &= -F_{gc}' \\ F_{gd} &= -F_{gd}' \end{aligned}. \tag{2.25}$$

The constant boom gravitational forces are applied to the carrier and dolly at the boom connection points.

## 2.5 Assembling Boom Equations in the State Space System

The carrier, dolly and boom are written in linear state space equations. This section briefly introduces general carrier and dolly equations of motion and covers the combination with boom equations. State space equations will take the standard form

$$\begin{aligned} \{\dot{x}\} &= [A]\{x\} + [B]\{u\} \\ \{y\} &= [C]\{x\} \end{aligned} \tag{2.26}$$

where {x} is the state vector, {y} is the output vector and {u} is the input vector. The A, B and C matrices are the system dynamics, input and output matrices respectively.

### 2.5.1 General Carrier and Dolly Equations of Motion

The carrier and dolly are both modeled as rigid bodies. Each rigid body receives gravitational force input resulting from the rigid body mass and equivalent boom gravitational force. The boom dynamic force is applied to the rigid body as well.

In the crane model, the rigid bodies and suspension sub-models are connected through a common force/velocity relationship. The rigid bodies receive connection forces from the suspension and specify the velocity of the connection points. In turn, the suspension sub-models receive velocity input and specify force to the rigid body models. Details and an illustration of this connection is provided in Chapter 4.

The following carrier and dolly equations are formulated in the most general form with m suspension forces acting on the carrier and p suspension forces on the dolly. Rigid body formulation is presented in this manner because many different suspension configurations are used and this will result in a general set of state equations that will be valid for all models.

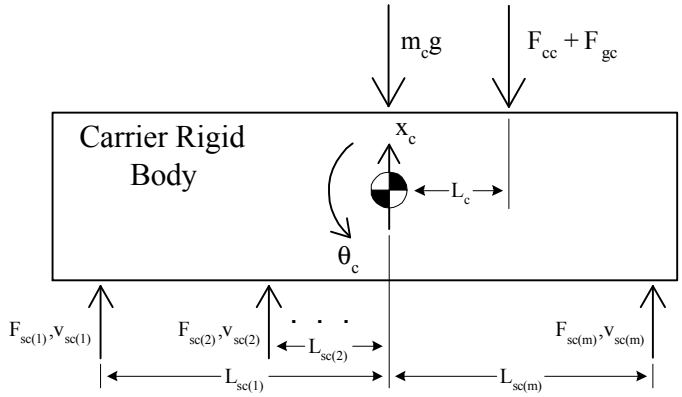


*Figure 2.10 General Carrier Free Body Diagram*

The carrier rigid body is shown in Figure 2.10. Boom connection and gravitational forces are shown acting on the top of the rigid bodies while representative suspension forces act below. The carrier model is assumed to have a total of m suspension forces acting on the rigid body.

Summing the forces and moments about the center of gravity generates equations of motion. From the free body diagram shown in Figure 2.10, the result is

$$\begin{aligned} m_c \ddot{x}_c &= -F_{cc} - F_{gc} + \sum_{i=1}^{m} F_{sc(i)} - m_a g \\ I_c \ddot{\mathsf{q}}_c &= -L_c \left( F_{cc} + F_{gc} \right) + \sum_{i=1}^{m} L_{sc(i)} F_{sc(i)} \end{aligned} \quad . \tag{2.27}$$

The boom/carrier connection force is

$$F_{cc} = \mathsf{k}\left( x_c + L_c \mathsf{q}_c - \lfloor \mathsf{f}(d_1) \rfloor \{q\} \right) \tag{2.28}$$

where the term in parentheses is the relative displacement across the stiff spring connecting the boom and carrier. The first two terms relate the carrier connection displacement while the final term results in the boom connection node displacement.

Equation (2.27) is rewritten in acceleration terms and the suspension forces are represented in vector format to facilitate state matrix formulation. The result is

$$\begin{aligned} \ddot{x}_c &= -\frac{x_c}{m_c} - \frac{L_c \mathsf{q}_c}{m_c} + \frac{\lfloor \mathsf{f}(d_1) \rfloor \{q\}}{m_c} + \frac{\lfloor 1 \rfloor}{m_c} \{F_{sc(i)}\} - \left( \frac{F_{gc}}{m_c g} + 1 \right) g \\ \ddot{\mathsf{q}}_c &= -\frac{L_c x_c}{I_c} - \frac{L_c^2 \mathsf{q}_c}{I_c} + \frac{L_c \lfloor \mathsf{f}(d_1) \rfloor \{q\}}{I_c} + \frac{\lfloor L_{sc(i)} \rfloor}{I_c} \{F_{sc(i)}\} - \left( \frac{F_{gc}}{m_c g} \right) g \end{aligned} \tag{2.29}$$

The velocity of each suspension connection point is determined by

$$\{v_{sc(i)}\} = \{1\} x_c + \{L_{sc(i)}\} \mathsf{q}_c \, . \tag{2.30}$$

where the connection point velocity is a function of the carrier displacement and rotation. In the general case, there are a total of m suspension forces that will specify connection velocities to the sub-models.

The dolly rigid body is shown in Figure 2.11. Boom connection and gravitational forces are shown acting on the top of the rigid bodies while representative suspension forces act below. The dolly model is assumed to have a total of p suspension forces acting on the rigid body.

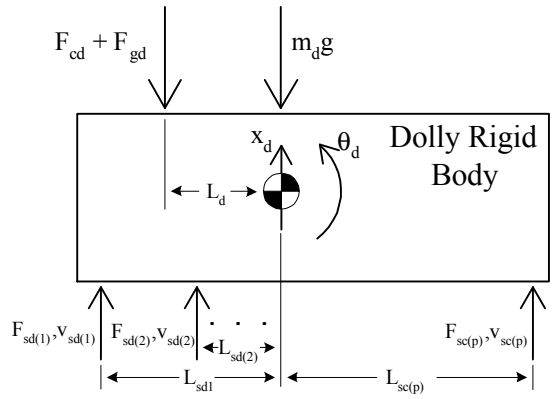


*Figure 2.11 General Dolly Free Body Diagram*

Summing the forces and moments acting about the center of gravity generates the equations of motion. From the free body diagram shown in Figure 2.11, the resulting equations are

$$\begin{aligned} m_d \ddot{x}_d &= -F_{cd} - F_{gd} + \sum_{i=1}^{p} F_{sd(i)} - m_a g \\ I_d \ddot{q}_d &= -L_c\left(F_{cd} - F_{gd}\right) + \sum_{i=1}^{p} L_{sd(i)} F_{sd(i)} \end{aligned} \tag{2.31}$$

The boom connection force is

$$F_{cd} = k\left(x_d - L_d - \lfloor f\left(d_{2n-1}\right)\rfloor\{q\}\right) \tag{2.32}$$

where the term in parentheses is the relative displacement across the stiff spring connecting the boom and dolly. The first two terms relate the dolly connection displacement while the final term results in the connection node displacement.

In order to determine the sign of the moment generated by the suspension support forces, a sign convention for the $L_{sc(i)}$ and $L_{sd(i)}$ variables was established. The values of the $L_{sc(i)}$ and $L_{sd(i)}$ are defined in words as the positive distance the suspension point is behind the center of gravity. With this convention, suspension points in front of the center of gravity have a negative value. The sign of the moment generated by the suspension forces on the rigid body is automatically determined by the associated $L_{sc(i)}$ or $L_{sd(i)}$ value. This convention is handled internally by the simulation, and the user will solely need to enter positive distances.

Equation (2.31) is rewritten in acceleration terms and the suspension forces are represented in vector format to facilitate state matrix formulation. The result is

$$\begin{aligned} \ddot{x}_d &= -\frac{x_d}{m_d} + \frac{L_d \theta_c}{m_d} + \frac{\lfloor f(d_{2n-1}) \rfloor \{q\}}{m_d} + \frac{\lfloor 1 \rfloor}{m_d}\{F_{sd(i)}\} - \left(\frac{F_{gd}}{m_c g} + 1\right) g \\ \ddot{\theta}_d &= -\frac{L_d x_d}{I_d} + \frac{L_d^2 \theta_d}{I_d} + \frac{L_d \lfloor f(d_{2n-1}) \rfloor \{q\}}{I_d} + \frac{\lfloor L_{sd(i)} \rfloor}{I_d}\{F_{sd(i)}\} - \left(\frac{L_c F_{gc}}{m_c g}\right) g \end{aligned} \quad . \tag{2.33}$$

The velocity of each suspension connection point is determined by

$$\{v_{sd(i)}\} = \{1\} x_d - \{L_{sd(i)}\} \theta_d \tag{2.34}$$

where the connection point velocity is a function of the carrier displacement and rotation. In the general case, there are a total of m suspension forces that will specify connection velocities to the sub-models.

### 2.5.2 Coupling State Space Equations

The final goal is to generate state space matrices that contain carrier, dolly and boom equations. This is accomplished by combining Equation (2.29) (carrier), Equation (2.33) (dolly) and Equation (2.19) (boom). The state vector is ordered as:

| | | |
|---|---|---|
| $x_c$ | $\equiv$ | Carrier vertical displacement |
| $\dot{x}_c$ | $\equiv$ | Carrier vertical velocity |
| $\theta_c$ | $\equiv$ | Carrier angular displacement |
| $\dot{\theta}_c$ | $\equiv$ | Carrier angular velocity |
| $x_d$ | $\equiv$ | Dolly vertical displacement |
| $\dot{x}_d$ | $\equiv$ | Dolly vertical velocity |
| $\theta_d$ | $\equiv$ | Dolly angular displacement |
| $\dot{\theta}_d$ | $\equiv$ | Dolly angular velocity |
| $\{q\}$ | $\equiv$ | Modal boom displacement amplitude factors |
| $\{\dot{q}\}$ | $\equiv$ | Modal boom velocity amplitude factors |

Equation (2.37) presents the general case state equation for a carrier, dolly and boom. Carrier equations are contained in the first four rows followed by the dolly equations in rows 5 through 8. Notice the input vector contain the suspension connection forces. Boom equations are in the last two rows of Equation (2.37). The terms of the boom connection force Equation (2.21) can be found in the final row of the A matrix.

The output equation has been included in Equation (2.38). It is a result of assembling Equations (2.31) and (2.34). Again, these suspension connection velocities will serve as input to suspension sub-models.

Cranes modeled with one and two axle dollies are considered a special case. The dolly is rigidly connected to the boom and to simplify simulation equations, the dolly mass and inertia is lumped into the dolly connection node of the boom. In this case, the suspension force/velocity relationship is shared directly with the dolly connection node of the boom.

The boom connection force equation (2.20) is modified to

$$\{F_c\} = \begin{Bmatrix} \mathsf{k}\left(x_c + L_c \mathsf{q}_c - \lfloor \mathsf{f}(d_1) \rfloor \{q\}\right) \\ 0 \\ \vdots \\ 0 \\ F_{sd} \\ 0 \\ \vdots \end{Bmatrix}. \tag{2.35}$$

where the boom receives the force, $F_{sd}$, from the suspension sub-model. As before, multiplication of the last term in Equation (2.19) with the new force vector results in

$$\begin{aligned} [m_b]^{-1}[\Phi]^T\{F_c\} = {} & [m_b]^{-1}\lfloor \Phi(d_1) \rfloor^T \mathsf{k} x_c + [m_b]^{-1}\lfloor \Phi(d_1) \rfloor^T \mathsf{k} L_c \mathsf{q}_c \\ & - [m_b]^{-1}\lfloor \Phi(d_1) \rfloor^T \mathsf{k} \lfloor \Phi(d_1) \rfloor \{q\} + [m_b]^{-1}\lfloor \Phi(d_1) \rfloor^T F_{sd} \end{aligned}. \tag{2.36}$$

The state equation for the one and two axle dollies is presented in Equation (2.39). Notice the state vector is reduced to carrier and boom states only. The state equations are very similar to the general case except the suspension connects directly to the suspension receiving a single force at the dolly connection node.

The output equation is presented in Equation (2.40). It is a combination of Equation (2.31) and the velocity of the dolly connection boom node determined by

$$v_{sd} = \lfloor \mathsf{f}(d_{2n-1}) \rfloor \{\dot{q}\}.$$

These suspension connection velocities are used as input to the suspension sub-models.

$$
\begin{Bmatrix} \dot{x}_c \\ \ddot{x}_c \\ \dot{\mathsf{q}}_c \\ \ddot{\mathsf{q}}_c \\ \dot{x}_d \\ \ddot{x}_d \\ \dot{\mathsf{q}}_d \\ \ddot{\mathsf{q}}_d \\ \dot{q} \\ \ddot{q} \end{Bmatrix}
=
\begin{bmatrix}
0 & 1 & 0 & 0 & 0 & 0 & 0 & 0 & \lfloor 0 \rfloor & \lfloor 0 \rfloor \\
\frac{\mathsf{k}}{m_c} & 0 & 0 & 0 & 0 & 0 & 0 & 0 & -\frac{\mathsf{k}}{m_c}\lfloor \mathsf{f}(d_1) \rfloor & \lfloor 0 \rfloor \\
0 & 0 & 0 & 1 & 0 & 0 & 0 & 0 & \lfloor 0 \rfloor & \lfloor 0 \rfloor \\
0 & 0 & \frac{L_c\mathsf{k}}{m_c} & 0 & 0 & 0 & 0 & 0 & -\frac{L_c\mathsf{k}}{m_c}\lfloor \mathsf{f}(d_1) \rfloor & \lfloor 0 \rfloor \\
0 & 0 & 0 & 0 & 0 & 1 & 0 & 0 & \lfloor 0 \rfloor & \lfloor 0 \rfloor \\
0 & 0 & 0 & 0 & \frac{\mathsf{k}}{m_d} & 0 & 0 & 0 & -\frac{\mathsf{k}}{m_d}\lfloor \mathsf{f}(d_{2n-1}) \rfloor & \lfloor 0 \rfloor \\
0 & 0 & 0 & 0 & 0 & 0 & 0 & 1 & \lfloor 0 \rfloor & \lfloor 0 \rfloor \\
0 & 0 & 0 & 0 & 0 & 0 & \frac{L_d\mathsf{k}}{m_d} & 0 & -\frac{L_d\mathsf{k}}{m_d}\lfloor \mathsf{f}(d_{2n-1}) \rfloor & \lfloor 0 \rfloor \\
\{0\} & \{0\} & \{0\} & \{0\} & \{0\} & \{0\} & \{0\} & \{0\} & [0] & [I] \\
\mathsf{k}[m_b]^{-1}\lfloor \mathsf{f}(d_1) \rfloor^T & 0 & \mathsf{k}[m_b]^{-1}\lfloor \mathsf{f}(d_1) \rfloor^T L_c & 0 & \mathsf{k}[m_b]^{-1}\lfloor \mathsf{f}(d_{2n-1}) \rfloor^T & 0 & -\mathsf{k}[m_b]^{-1}\lfloor \mathsf{f}(d_{2n-1}) \rfloor^T L_d & 0 & -[\mathsf{w}]^2 - \mathsf{k}[m_b]^{-1}\begin{bmatrix} \mathsf{f}(d_1) \\ \mathsf{f}(d_{2n-1}) \end{bmatrix}^T \begin{bmatrix} \mathsf{f}(d_1) \\ \mathsf{f}(d_{2n-1}) \end{bmatrix} & -2\mathsf{z}[\mathsf{w}]
\end{bmatrix}
\begin{Bmatrix} x_c \\ \dot{x}_c \\ \mathsf{q}_c \\ \dot{\mathsf{q}}_c \\ x_d \\ \dot{x}_d \\ \mathsf{q}_d \\ \dot{\mathsf{q}}_d \\ \{q\} \\ \{\dot{q}\} \end{Bmatrix}
\tag{2.37}
$$

$$
+
\begin{bmatrix}
\lfloor 0 \rfloor & \lfloor 0 \rfloor & 0 \\
\frac{\lfloor 1 \rfloor}{m_c} & \lfloor 0 \rfloor & -\left(\frac{Fgc}{m_c g}+1\right) \\
\lfloor 0 \rfloor & \lfloor 0 \rfloor & 0 \\
\frac{\lfloor L_{sc(i)} \rfloor}{I_c} & \lfloor 0 \rfloor & -\frac{L_c Fgc}{m_c g} \\
\lfloor 0 \rfloor & \lfloor 0 \rfloor & 0 \\
\lfloor 0 \rfloor & \frac{\lfloor 1 \rfloor}{m_d} & \left(\frac{Fgd}{m_c g}+1\right) \\
\lfloor 0 \rfloor & \lfloor 0 \rfloor & \lfloor 0 \rfloor \\
\lfloor 0 \rfloor & \frac{\lfloor L_{sc(i)} \rfloor}{I_c} & -\frac{L_d Fgd}{m_d g} \\
[0] & [0] & \{0\} \\
[0] & [0] & \{0\}
\end{bmatrix}
\begin{Bmatrix} \{F_{sc(i)}\} \\ \{F_{sd(i)}\} \\ g \end{Bmatrix}
$$

$$\begin{Bmatrix} \{v_{sc(i)}\} \\ \{v_{sd(i)}\} \end{Bmatrix} = \begin{bmatrix} \{0\} & \{1\} & \{0\} & \{L_{sc(i)}\} & \{0\} & \{0\} & \{0\} & \{0\} & [0] & [0] \\ \{0\} & \{0\} & \{0\} & \{0\} & \{0\} & \{1\} & \{0\} & \{L_{sd(i)}\} & [0] & [0] \end{bmatrix} \begin{Bmatrix} x_c \\ \dot{x}_c \\ \mathsf{q}_c \\ \dot{\mathsf{q}}_c \\ x_d \\ \dot{x}_d \\ \mathsf{q}_d \\ \dot{\mathsf{q}}_d \\ \{q\} \\ \{\dot{q}\} \end{Bmatrix} \tag{2.38}$$

$$\begin{Bmatrix} \dot{x}_c \\ \ddot{x}_c \\ \dot{\mathsf{q}}_c \\ \ddot{\mathsf{q}}_c \\ \dot{q} \\ \ddot{q} \end{Bmatrix} = \begin{bmatrix} 0 & 1 & 0 & 0 & \lfloor 0 \rfloor & \lfloor 0 \rfloor \\ \dfrac{\mathsf{k}}{m_c} & 0 & 0 & 0 & -\dfrac{L_c \mathsf{k}}{m_c} \lfloor \mathsf{f}(d_1) \rfloor & \lfloor 0 \rfloor \\ 0 & 0 & 0 & 1 & \lfloor 0 \rfloor & \lfloor 0 \rfloor \\ 0 & 0 & \dfrac{L_c \mathsf{k}}{I_c} & 0 & -\dfrac{L_c \mathsf{k}}{I_c} \lfloor \mathsf{f}(d_1) \rfloor & \lfloor 0 \rfloor \\ \{0\} & \{0\} & \{0\} & \{0\} & [0] & [I] \\ \mathsf{k}[m_b]^{-1} \lfloor \mathsf{f}(d_1) \rfloor^T & \{0\} & \mathsf{k}[m_b]^{-1} \lfloor \mathsf{f}(d_1) \rfloor^T L_c & \{0\} & -[\mathsf{w}]^2 - \mathsf{k} \lfloor \mathsf{f}(d_1) \rfloor^T \lfloor \mathsf{f}(d_1) \rfloor & -2[\mathsf{z}][\mathsf{w}] \end{bmatrix} \begin{Bmatrix} x_c \\ \dot{x}_c \\ \mathsf{q}_c \\ \dot{\mathsf{q}}_c \\ q \\ \dot{q} \end{Bmatrix} + \begin{bmatrix} \lfloor 0 \rfloor & 0 & 0 \\ \dfrac{\lfloor 1 \rfloor}{m_c} & 0 & -\left( \dfrac{F_{gc}}{m_c g} + 1 \right) \\ \lfloor 0 \rfloor & 0 & 0 \\ \dfrac{\lfloor L_{sc(i)} \rfloor}{I_c} & 0 & -\dfrac{L_c F_{gc}}{m_c g} \\ [0] & \{0\} & \{0\} \\ [0] & [m_b]^{-1} \lfloor \mathsf{f}(d_{2n-1}) \rfloor^T & \{0\} \end{bmatrix} \begin{Bmatrix} \{F_{sc(i)}\} \\ F_{sd} \\ g \end{Bmatrix} \tag{2.39}$$

$$\begin{Bmatrix} \{v_{sc(i)}\} \\ v_{sd} \end{Bmatrix} = \begin{bmatrix} \{0\} & \{1\} & \{0\} & \{L_{sc(i)}\} & [0] & [0] \\ 0 & 0 & 0 & 0 & \lfloor 0 \rfloor & \lfloor \mathsf{f}(d_{n2-1}) \rfloor \end{bmatrix} \begin{Bmatrix} x_c \\ \dot{x}_c \\ \mathsf{q}_c \\ \dot{\mathsf{q}}_c \\ \{q\} \\ \{\dot{q}\} \end{Bmatrix} \tag{2.40}$$

## 2.6 Summary

This chapter provided the mathematical breakdown of the equations used to describe the motion of the sprung mass. The equations of motion for the carrier and dolly were determined using the Newton-Euler approach. Boom motion is captured through a finite element model. Shape functions are used to represent the motion of the boom in terms of displacement coordinates. The displacement coordinates are then transformed to modal coordinates to reduce the number of equations required to represent the system. The velocities of the various suspension connections points were also defined because they are required as an input to the suspension sub-models. Both equations (2.37) and (2.39) can be treated as a state space representation of the system. In this representation, the suspension support forces are treated as system inputs which are dependent on the state vector. Now that the motion of the sprung mass is represented, the sub-models that describe the motion of the various suspension systems must be developed.

(This page is left intentionally blank)

# CHAPTER 3
# SUSPENSION SUB-MODELS

## 3.1 Overview

In vehicle dynamics, one of the key aspects of the vehicle that must be captured by a model is the suspension. This is the most significant aspect to look at in order to understand the motion of the system. The crane industry implements a wide array of suspension configurations. In the simulation, the individual suspension systems were reduced to separate sub-models that interact with the sprung masses. By developing individual suspension sub-models, an understanding of individual suspension systems could be developed from a quarter truck standpoint before being implemented on a complete crane model and is presented in Chapter 6. The model implements many different suspension configurations, but two configurations are felt to be more common in industry can be labeled as the older suspension configuration vs. the modern configuration.

Older cranes are commonly equipped with a walking beam suspension on the carrier and leaf spring suspension on the dolly. This suspension style was the industry standard for large cranes. Many cranes that are still used in industry today implement this suspension configuration. However, this suspension style is slowly being phased out over the more modern suspension configuration.

Modern cranes are commonly equipped with hydro-pneumatic suspension on the carrier and air ride suspension on the dolly. These suspensions have become the industry standard on large hydraulic cranes. The dynamic behaviors of these newer suspensions are notably different than the conventional walking beam and leaf spring configurations. Thus, characterizing their response is the motivation for this investigation.

The focus of this Chapter is to determine the leaf spring, walking beam, hydro-pneumatic and air ride suspension state equations. These suspension configurations are introduced, reduced to representative models, and from each model, the equations of motion are formulated. The Newton-Euler approach is used to determine the mathematical representation of the leaf spring and walking beam suspension models. Bond graphs are used to formulate both the state equations and the output equations required for simulation for the hydro-pneumatic and air ride models. The bond graph approach is an energy-based method relating multi-port elements through power bonds.

## 3.2 Derivation of the Suspension Input Velocity From the Sprung Mass

In actuality, cranes have a variety of different suspension types and configurations. In this formulation, the carrier and dolly are modeled as individual rigid bodies. The suspension sub-models are combined with these rigid bodies to create the vehicle configuration of interest. Sub-models include the vehicle suspension components and the tires connected to these components. This model formulation approach allows for a single crane model with several suspension subsystem options.

Each independent portion of the vehicle's suspension is represented in a sub-model. Suspension sub-models are combined with the rigid bodies (carrier and dolly) through a common

force/velocity relationship. In general, the rigid body specifies the necessary velocities to the sub-model and, in turn, the sub-model specifies the forces to the rigid body. This process is illustrated in Figure 3.1.

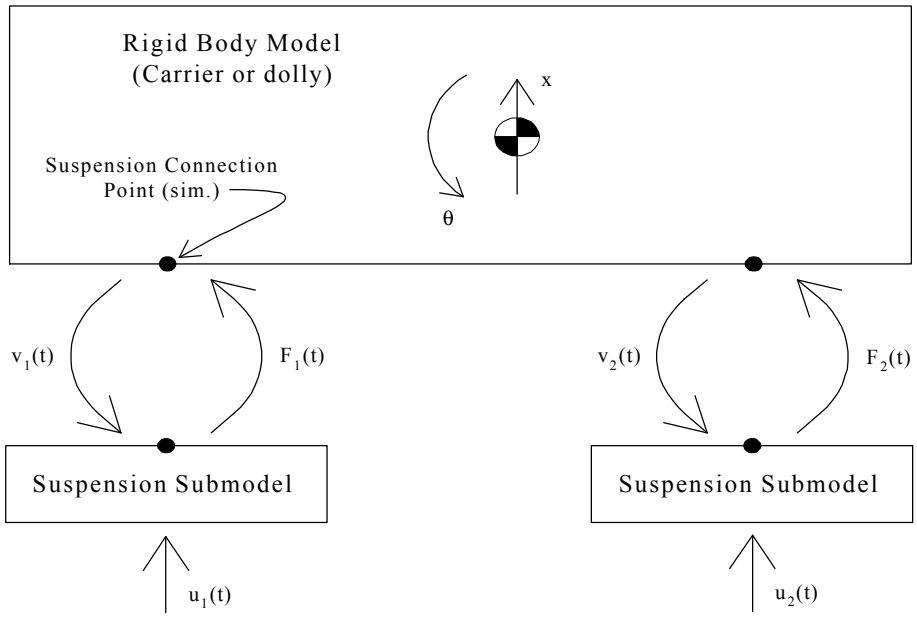


*Figure 3.1 Model/Sub-model Interaction*

The modeling assumptions greatly simplify the force/velocity relationship. Recall that the crane has been investigated as a pitch plane model with constant forward velocity and a small angle approximation is employed relating to the vehicle pitch. As a result of these modeling assumptions, the rigid bodies only require a vertical force input at each suspension connection point. Conversely, the sub-models only require vertical velocity inputs from the rigid bodies above.

The desired outputs of the model are the suspension forces that are fed into the input vector in equations (2.38) and (2.40), and the tire forces. In general, these forces can be expressed as

$$\{F_S\} = f(\{v_{sc}\},\{v_{sd}\},\{v_i\}) \tag{3.1}$$

and

$$\{F_t\} = f(\{v_{sc}\},\{v_{sd}\},\{v_i\}) \tag{3.2}$$

where $\{v_{sc}\}$ denotes the carrier suspension point velocities, $\{v_{sd}\}$ denotes the dolly suspension velocities, and $\{v_i\}$ denotes the road input velocities. The mathematical derivation of the $\{v_{sc}\}$ and $\{v_{sd}\}$ vectors are presented in equations (2.38) and (2.40). The $\{v_i\}$ vector will be presented in Chapter 4. Once these velocities are determined, the information is sent to the respective suspension sub-model. The suspension sub-model then determines the forces generated by the tires ($\{F_t\}$) and the support force ($\{F_s\}$), which act on the corresponding point of the sprung mass.

## 3.3 Tire Model

Sub-models include not only suspension components, but the tires connected to these components as well. A pneumatic tire, in general, is characterized with nonlinear relationships, but the vertical force displacement relationship can be well captured by a parallel linear spring and damper [8]. The tire spring and damper connect the unsprung mass to the roadway where the input velocity of the road profile is introduced into the system. Forces exerted on the roadway are calculated from these representative tire elements based on the relative displacement of the spring and velocity of the damper.

Common practice is to model a tire with a parallel spring and damper. This means each tire requires two system inputs, a displacement and a velocity. The damper allows the tire to act as a low pass filter [8], eliminating high frequency inputs from the road to the system. The basic tire model is shown in Figure 3.2. This tire model is implemented into the suspension sub-models by calculating the force generated by the relative displacement and velocity across the tire.

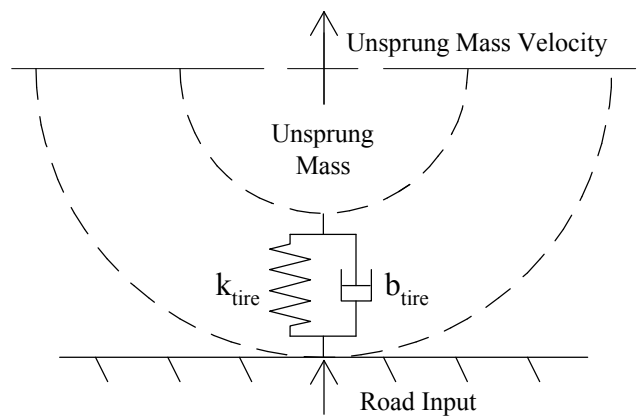


*Figure 3.2 Tire Model Schematic*

The forces generated by this model can be described by

$$F_{b_tire} = b_{tire}\dot{q}_t, \tag{3.3}$$

and

$$F_{k_tire} = k_{tire}q_t. \tag{3.4}$$

The total force the tire exerts on the pavement is the sum of the damping and spring force given in equations (3.3) and (3.4) given as

$$F_t = F_{k_tire} + F_{b_tire}. \tag{3.5}$$

One of the limitations of this model is that if the tires come off the ground, they develop a tension force, pulling the tires back down to the pavement surface. This is unrealistic because the tires cannot physically generate a tensile force in typical applications. In the walking beam and independent leaf spring models this is addressed. The non-linear model used in these two

suspension sub-models enforces the idea that the tire forces must be positive. If a tire force is calculated which is less then zero, the program automatically sets it to zero. Typical values for linear tire damping and stiffness values are given in Table 3.1. These values are presented to give the reader a feel for typical values for linear tire properties. Since the model is a pitch plane model, the tire stiffness is the equivalent stiffness of the tires on the particular axle.

| Tire Stiffness (N/m) | Tire Damping (Ns/m) | Source |
|---|---|---|
| 2.927E6 (Pair) | 4.2E3 | Kirsche report [6] |
| 3.5E6 (Pair) | 4E3 | Cebon [8] |
| 1.225E6 (Single) | 1.05E3 | Karamihas and Gillespie [14] |
| 1.050E6 (Single) | 1.05E3 | Karamihas and Gillespie [14] |

*Table 3.1 Typical Linear Tire Values*

## 3.4 Leaf Spring Suspension

One of the common types of suspension used for an independent axle is a leaf spring. This is characterized physically in Figure 3.3. Usually, this kind of suspension is modeled as a spring and damper attached to a single point on the rigid body it supports directly above the axle. A representation of the modeled characterization used for the mathematical model is illustrated in Figure 3.4. In the mathematical model, the damping value corresponds to the linear viscous damping coefficient. Coulomb damping occurs in this type of suspension due to inter-leaf friction. However in the model developed here, the Coulomb damping is neglected.

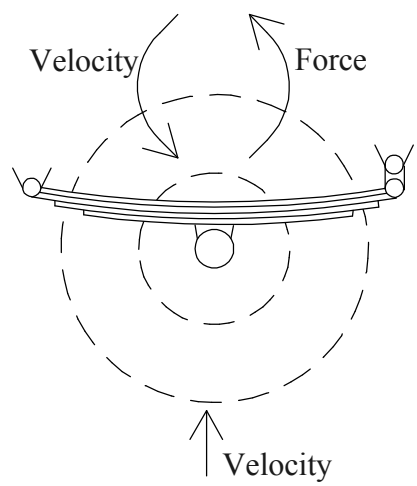


*Figure 3.3 Physical Representation of Leaf Spring Model*

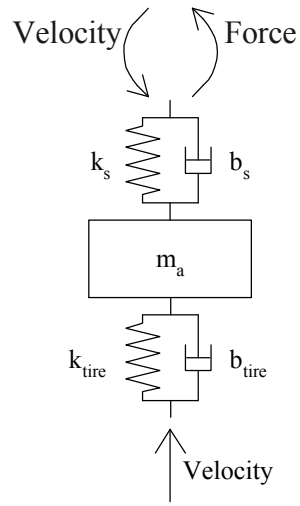


*Figure 3.4 Mathematical Leaf Spring Model Characterization*

The equation of motion contained with in the independent sub-model for the un-sprung mass is given by

$$\ddot{x}_t = \frac{k_{tire} q_t + b_{tire} \dot{q}_t - k_s q_s - b_s \dot{q}_s - m_{us} g}{m_{us}}. \tag{3.6}$$

In addition

$$\dot{q}_s = \dot{x}_t - v_s, \tag{3.7}$$

and

$$\dot{q}_t = \dot{x}_t - v_i, \tag{3.8}$$

must be calculated within the suspension sub-model as additional integration variables, where $v_s$ denotes the suspension velocity, $v_i$ denotes the road input velocity and $\dot{x}_t$ denotes the velocity of the unsprung mass. These equations add three additional variables to the state space vector for the model given as:

$\dot{x}_t$ ≡ Vertical velocity of the un-sprung mass
$q_t$ ≡ Relative displacement across the tire
$q_s$ ≡ Relative displacement across the suspension

In addition to the equations of motion presented above, the model output must be defined. This is the suspension support force and the tire force. The tire force can be defined as

$$F_t = k_{tire} q_t + b_{tire} \dot{q}_t. \tag{3.9}$$

The tire force is an output from the suspension sub-model because this corresponds to the dynamic road load. The other force that is required internally to the model is the suspension support force defined as

$$F_s = k_s q_s + b_s \dot{q}_s, \tag{3.10}$$

which is placed in its proper location in the input vector {u} for equation (2.26). These are the relevant equations used in the independent leaf spring sub-model.

## 3.5 Walking Beam Suspension

Another type of suspension that is implemented in the model is the walking beam suspension. This is a tandem suspension, which means that two sequential axles are connected with some means to share the dynamic load. This is characterized in Figure 3.5. This suspension pivots about the center of the beam underneath the frame of the suspended mass. The benefit of this kind of suspension is that the load is more evenly distributed between the two tires. Studies have shown that an optimum spacing for tandem axles exists which reduces the damage on the pavement by the group. Typically the tandem axles are spaced a distance of approximately 1.5 m (60 in.). This spacing allows the stress field generated by each axle to overlap in a beneficial region [8]. However, there is no significant damping in this type of suspension.

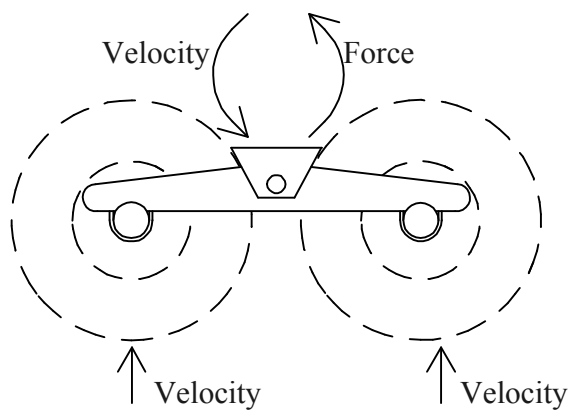


*Figure 3.5 Physical Characterization of Walking Beam Suspension*

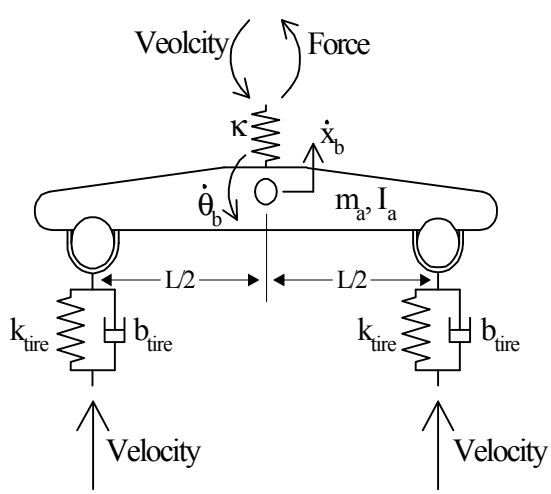


*Figure 3.6 Mathematical Walking Beam Suspension Characterization*

The only damping effect in this suspension model is due to the tires. However, additional damping would physically occur due to friction associated with relative rotation at the pin connection. The mathematical characterization of this suspension is in Figure 3.6. Again, the Karnopp-Margolis [16] method is used to eliminate the algebraic motion constraint generated by the pin. The equations of motion for this system are:

$$\ddot{x}_b = \frac{1}{M_b}\left(-\mathsf{k}q_s + k_{tire}q_{t1} + b_{tire}\dot{q}_{t1} + k_{tire}q_{t2} + b_{tire}\dot{q}_{t2} - M_b g\right), \tag{3.11}$$

and

$$\ddot{\mathsf{q}}_b = \frac{L}{2I_b}\left(\left(k_{tire}q_{t1} + b_{tire}\dot{q}_{t1}\right) - \left(k_{tire}q_{t2} + b_{tire}\dot{q}_{t2}\right)\right). \tag{3.12}$$

In addition,

$$\dot{q}_s = \dot{x}_b - v_s, \tag{3.13}$$

$$\dot{q}_{t1} = v_{i1} - \dot{x}_b + \frac{L}{2}\dot{\mathsf{q}}, \tag{3.14}$$

and

$$\dot{q}_{t2} = v_{i2} - \dot{x}_b - \frac{L}{2}\dot{\mathsf{q}} \tag{3.15}$$

are also determined in the sub-model. This means that there are a total of five integration variables for this sub-model given as:

| | | |
|---|---|---|
| $\dot{x}_b$ | $\equiv$ | Vertical velocity of unsprung mass |
| $\dot{\mathsf{q}}_b$ | $\equiv$ | Angular velocity of sprung mass |
| $q_s$ | $\equiv$ | Displacement across stiff spring |
| $q_{t1}$ | $\equiv$ | Relative displacement across front tire |
| $q_{t2}$ | $\equiv$ | Relative displacement across rear tire |

Now, the information regarding the suspension support forces and the tire forces can be defined by

$$F_s = \mathsf{k}q_s, \tag{3.16}$$

$$F_{t1} = k_{tire}q_{t1} + b_{tire}\dot{q}_{t1}, \tag{3.17}$$

and

$$F_{t2} = k_{tire}q_{t2} + b_{tire}\dot{q}_{t2}. \tag{3.18}$$

These are the relevant equations in the walking beam suspension model, which are implemented into the sub-model for this particular suspension group. Now that the mathematical

representation of the system has been discussed, the initial conditions must be formulated before the equations can be simulated.

## 3.6 Hydro-Pneumatic Suspension Configurations

There are two basic hydro-pneumatic carrier suspension configurations: the conventional axle and the independent suspension. Though these suspensions have notable mechanical differences, they have similar hydraulic systems. The following subsections briefly introduce the conventional axle and independent suspensions, which leads to the development of a single representative model.

### 3.6.1 Conventional Axle Suspension

The conventional axle suspension, depicted in Figure 3.7, utilizes a solid axle housing. A variety of possible suspension link configurations are used to maintain the

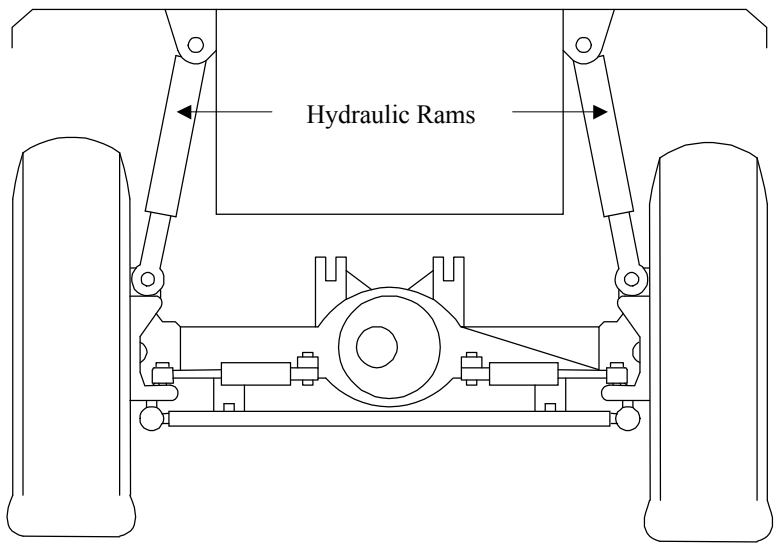


*Figure 3.7 Conventional Axle Suspension*

desired axle location and achieve essentially vertical tire travel. The vertical force of the carrier mass is supported by the hydraulic suspension rams that connect between the axle housing and carrier chassis. Hydraulic lines link the suspension rams to common accumulator. Details of the hydraulic system are discussed in section 3.6.3.

### 3.6.2 Independent Axle Suspension

The independent suspension system is Grove Crane's Megatrak shown in Figure 3.8. The suspension rams are designed for lateral forces and bending moments, therefore completely supporting the carrier. Hydraulically, the Megatrak suspension rams function as standard cylinders and allow only vertical wheel travel [3].

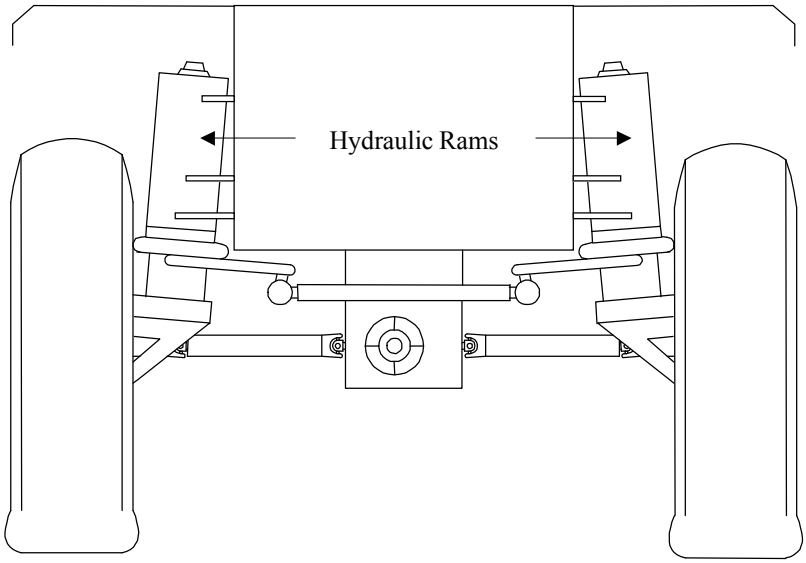


*Figure 3.8 Megatrak Suspension*

The conventional axle or independent suspensions can be greatly simplified when considered as a pitch-plane model. The unsprung mass is allowed vertical motion and connected to the carrier by a hydraulic ram. From a modeling standpoint, the independent suspension has significantly less unsprung mass than the conventional axle.

### 3.6.3 Hydraulic System Configurations

The hydraulic system of a crane traveling down the highway is the same for all suspension configurations. When a hydraulic crane is moved between job sites, the load leveling capabilities of the suspension system are locked out, thereby reducing the system to an accumulator connected to a set of hydraulic rams.

Figure 3.9 shows a representative configuration with three axles connected to single accumulator. This figure does not restrict a carrier with this configuration to have only three axles; this suspension could be found on the left rear portion of a six-axle carrier. Identical systems would be found on the right rear, front left and front right quadrants of the vehicle. There are several hydraulic configuration possibilities and a single accumulator can typically support one to four hydraulic axle rams [30].

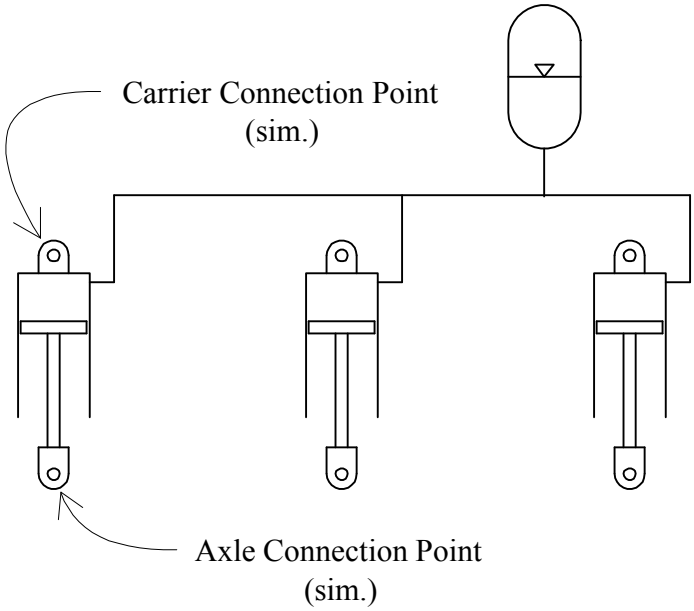


*Figure 3.9 Hydraulic System Schematic*

## 3.7 Hydro-Pneumatic Suspension Sub-model

As discussed in the previous section, hydro-pneumatic suspension systems come in several different hydraulic configurations. Rather than investigate many hydraulic possibilities, a representative model is used to capture the general trends associated with these suspensions. A system of two axle rams joined with a single accumulator system has been investigated.

### 3.7.1 Two Axle Hydro-Pneumatic Configuration

The two axle hydro-pneumatic configuration consists of two rams connected through hydraulic lines to a single accumulator. A hydraulic ram is considered to be an ideal linear transformer with constant piston area, $A_p$. The hydraulic fluid is incompressible and flow in the lines in modeled with linear fluid resistance $R_f$ and inertia $I_f$. The accumulator is nitrogen filled and is assumed to operate at a steady state temperature. Its behavior is governed by the adiabatic gas law

$$PV^{g} = C_H, \tag{3.19}$$

where $C_H$ is the steady state adiabatic gas constant [19].

Each hydraulic ram connects the vehicle frame and the unsprung mass of the axle housing or wheel spindle. The unsprung mass has only a vertical degree of freedom and is represented by constant $m_a$. Tire dynamics are represented by a linear spring and damper connecting the unsprung mass to the road input $v_i(t)$. Figure 3.10 presents a schematic of the two-axle hydro-pneumatic suspension system. It is noted that the suspension sub-model utilizes the common force/velocity interaction discussed in Section 3.2 for connecting the carrier rigid body and suspension sub-models.

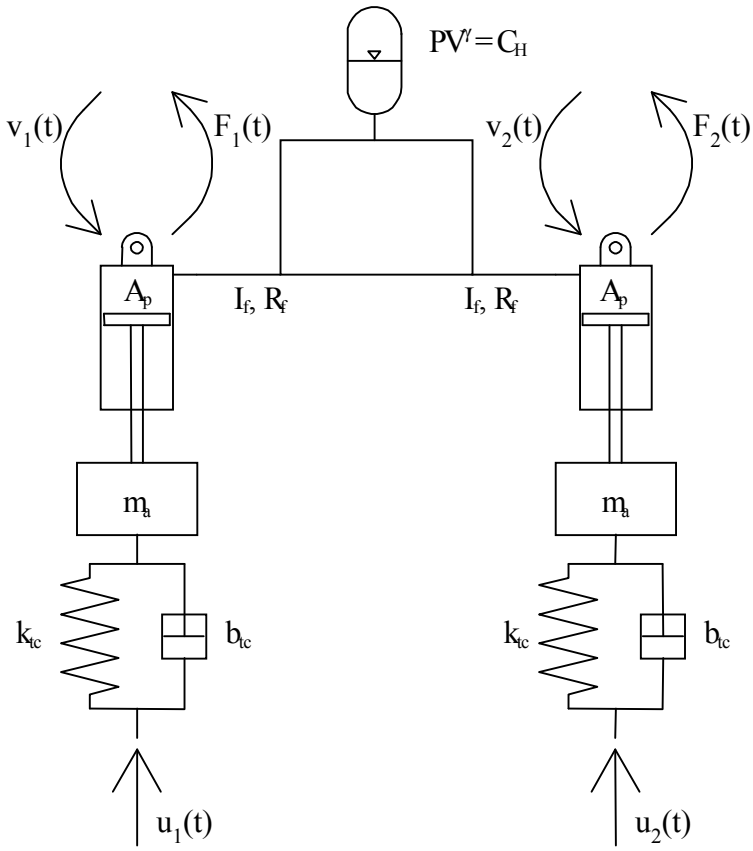


*Figure 3.10 Two Axle Hydro-pneumatic Sub-model*

### 3.7.2 Hydro-Pneumatic State Equations

Equations of motion for the hydro-pneumatic suspension sub-model are derived using the bond graph shown in Figure 3.11. Notice the lower left and lower right portions of the bond graph are identical; each represents the combination of a tire, unsprung mass and hydraulic ram. The upper part of the bond graph represents the fluid properties and the accumulator relationship. Road and rigid body velocities are input through the flow source elements and drive the dynamics of this system.

The model presented in Figure 3.9 would result in a bond graph with two elements in differentiation causality. Formulating algebraic relationships for these elements is not feasible because it requires taking the time derivative of the velocity inputs.

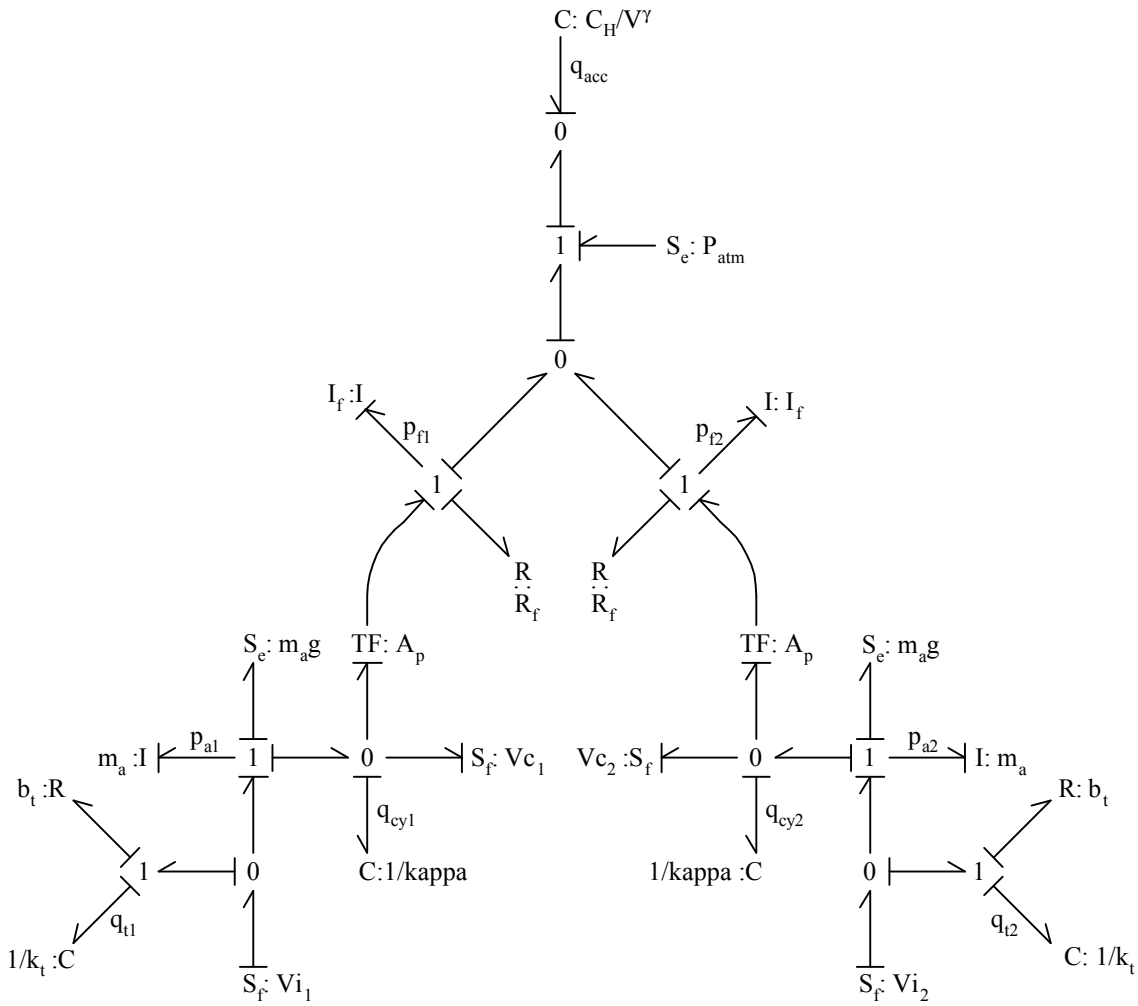


*Figure 3.11 Bond Graph of Two Axle Hydro-pneumatic Sub-model*

A second approach for maintaining integration causality is modeling the hydraulic ram with a stiff spring in the plunger (see Figure 3.12). The bond graph implications of this are included through the '$q_{cy1}$' and '$q_{cy2}$' bonds in Figure 3.11. This approach results in a causal bond graph. Selecting a spring constant with associated frequencies much higher than those of the rest of the system will assure that the stiff springs will not affect the overall dynamics [16].

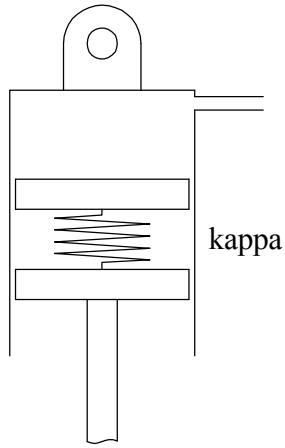


*Figure 3.12 Hydraulic Ram with Stiff Spring in Plunger*

The state variables of the bond graph model in Figure 3.11 are:

| | | |
|---|---|---|
| $q_{t1}$ | ≡ | Displacement across left tire spring |
| $P_{a1}$ | ≡ | Momentum of left unsprung mass |
| $q_{cy1}$ | ≡ | Displacement across left hydraulic ram stiff spring |
| $P_{f1}$ | ≡ | Momentum of fluid in left hydraulic line |
| $q_{t2}$ | ≡ | Displacement across right tire spring |
| $P_{a2}$ | ≡ | Momentum of right unsprung mass |
| $q_{cy2}$ | ≡ | Displacement across right hydraulic ram stiff spring |
| $P_{f2}$ | ≡ | Momentum of fluid in right hydraulic line |
| $q_{acc}$ | ≡ | Displacement of nitrogen in accumulator. |

The state equations are derived directly from the bond graph of Figure 3.11. The final equations are presented in equations (3.20) and a detailed derivation of each state relationship is provided in Appendix B.1. The resulting state equations are:

$$
\begin{aligned}
\dot{q}_{t1} &= v_{i1} - \frac{p_{a1}}{m_a} \\
\dot{p}_{a1} &= k_t q_{t1} + b_t v_{i1} - \frac{b_t}{m_a} p_{a1} - m_a g - \mathsf{k} q_{cy1} \\
\dot{q}_{cy1} &= \frac{p_{a1}}{m_a} - v_{c1} - \frac{p_{f1}}{A_p I_f} \\
\dot{p}_{f1} &= \frac{\mathsf{k}}{A_p} q_{cy1} - \frac{R_f}{I_f} p_{f1} - \frac{C_H}{V^{\mathsf{g}}} + P_{atm} \\
\dot{q}_{t2} &= v_{i2} - \frac{p_{a2}}{m_a} \\
\dot{p}_{a2} &= k_t q_{t2} + b_t v_{i2} - \frac{b_t}{m_a} p_{a2} - m_a g - \mathsf{k} q_{cy2} \\
\dot{q}_{cy2} &= \frac{p_{a2}}{m_a} - v_{c2} - \frac{p_{f2}}{A_p I_f} \\
\dot{p}_{f2} &= \frac{\mathsf{k}}{A_p} q_{cy2} - \frac{R_f}{I_f} p_{f2} - \frac{C_H}{V^{\mathsf{g}}} + P_{atm} \\
\dot{q}_{acc} &= -\frac{p_{f1}}{I_f} - \frac{p_{f2}}{I_f}
\end{aligned}
\tag{3.20}
$$

It is also necessary to derive output equations for both the rigid body connection forces and the tire forces on the roadway. The complete derivation to the equations (3.21) is provided in Appendix B.1. The output equations are:

$$
\begin{aligned}
F_{c1} &= \mathsf{k} q_{cy1} \\
F_{i1} &= k_t q_{t1} + b_t v_{i1} - \frac{b_t}{m_a} p_{a1} \\
F_{c2} &= \mathsf{k} q_{cy2} \\
F_{i2} &= k_t q_{t2} + b_t v_{i2} - \frac{b_t}{m_a} p_{a2}
\end{aligned}
\tag{3.21}
$$

SIMULINK is used to simulate the complete crane model. The suspension equations are assembled in subsystems, which allows them to be combined with the rigid body model. The initial state values are determined by assuming zero initial velocity and solving for initial displacements. A formal derivation of initial conditions and the two-ram hydro-pneumatic SIMULINK subsystem is presented in the final portion of Appendix B.1.

## 3.8 Air Ride Suspension Sub-model

Air ride is a common suspension system found in many heavy haul vehicle applications. Modern crane dollies commonly use air ride suspension to support the boom structure during transport between job sites. This suspension consists of a trailing arm suspension link that suspends the axle from the vehicle chassis with a rear mounted air bag and damper.

### 3.8.1 Air Ride Configuration and Assumptions

In this model formulation, the trailing arm is modeled as a rigid link pin connected to the dolly rigid body. The trailing arm kinematics are expressed in terms of the pin connection velocity $v_{c1}$ and trailing arm angular velocity $\omega$, where the angular velocity is measured relative to the Newtonian reference frame. Rotation of the trailing arm is assumed to be small, therefore the small angle approximation

$$\begin{aligned} \sin\left(\frac{d\mathrm{w}}{dt}\right) &\cong \frac{d\mathrm{w}}{dt} \\ \cos\left(\frac{d\mathrm{w}}{dt}\right) &\cong 1 \end{aligned} \tag{3.22}$$

is used.

Recall from Section 3.2 that the force/velocity relationship used to connect the rigid bodies and sub-models only describe vertical components. As a result, the sub-model only considers vertical velocities in the equation formulation (see Figure 3.13).

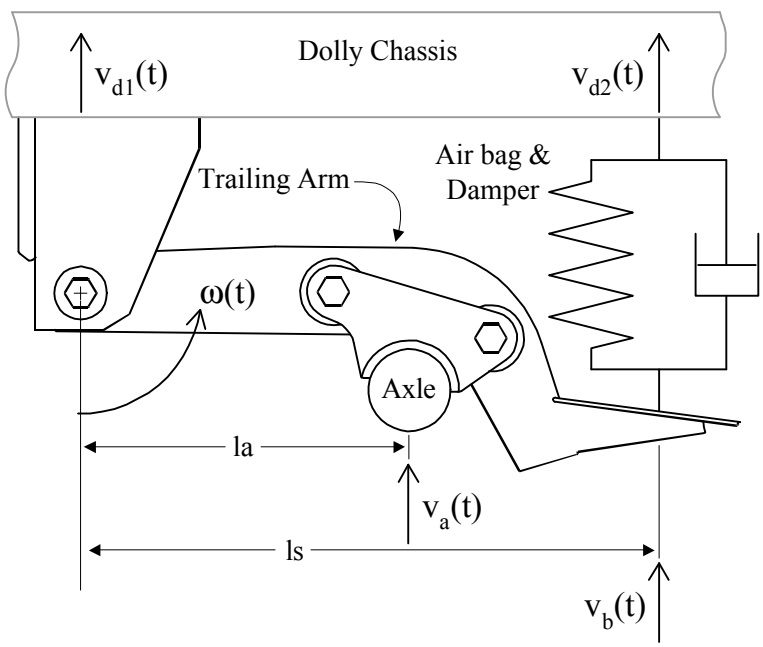


*Figure 3.13 Trailing Arm Velocity Diagram*

Axle velocity $v_a$ is given by

$$v_a(t) = v_{d1}(t) + \omega(t)la \tag{3.23}$$

where $v_{d1}(t)$ is the velocity of the pin connection and la is the horizontal distance from the pin to the axle. The velocity of the air bag and damper connection on the trailing arm is

$$v_b(t) = v_{d1}(t) + \omega(t)ls \tag{3.24}$$

where ls is the horizontal distance between the pin and air bag and damper connection points.

Figure 3.14 presents the air ride sub-model. The axle is located in the center of the swing arm and has mass $m_a$. Rotational inertia affects of the swing arm are considered to be negligible and not included in the model. The tire is connected to the road through the previously discussed linear spring and damper. These tire elements have spring constant $k_t$ and damping constant $b_t$.

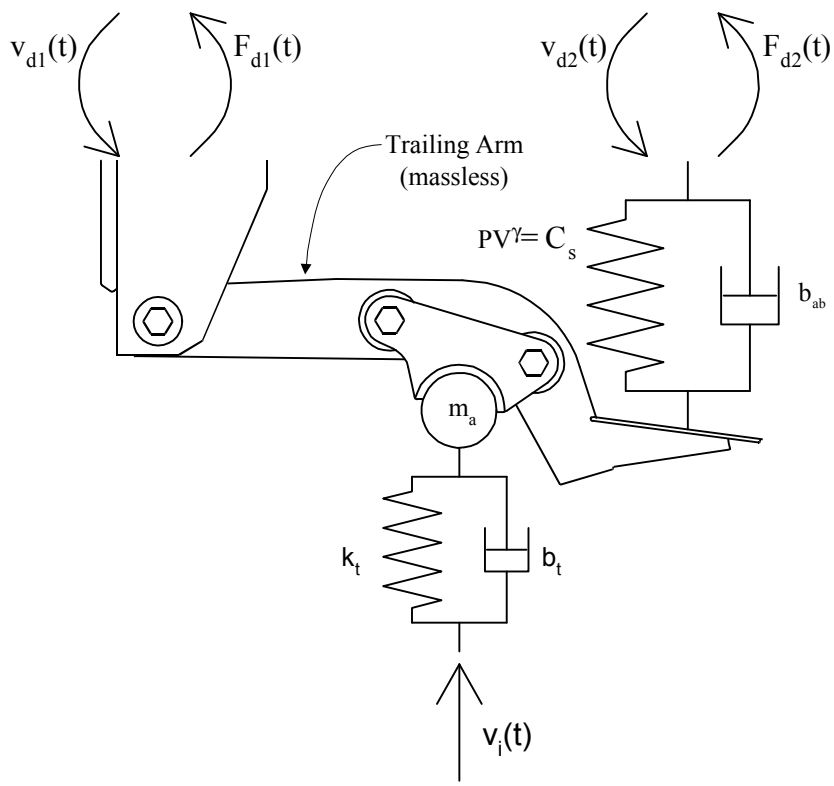


*Figure 3.14 Air Ride Sub-model*

The air bag and damper connect the free end of the trailing arm to the dolly rigid body. The damper is modeled as a linear element with damping constant $b_{ab}$. The air bag is modeled as a piston with constant cross-sectional area, $A_{ab}$. Energy stored due to the expansion of the air bag is considered to be negligible compared to the energy stored due to compressing the air [13]. The air bag is assumed to operate at a steady state temperature and the gas behavior is assumed to be consistent with the adiabatic gas relationship

$$PV^{\gamma} = C_{AR}. \tag{3.25}$$

where $C_{AR}$ is the steady state adiabatic gas constant [19].

Some configurations have an auxiliary air pressure tank connected to the air bag. The line between the bag and tank is typically small. Therefore, the time constant associated with the air flowing through this line will be large. The frequencies that the air bag cycles at relative to the associated time constant of the air line make consideration of the auxiliary tank and air line unnecessary.

### 3.8.2 Air Ride State Equations

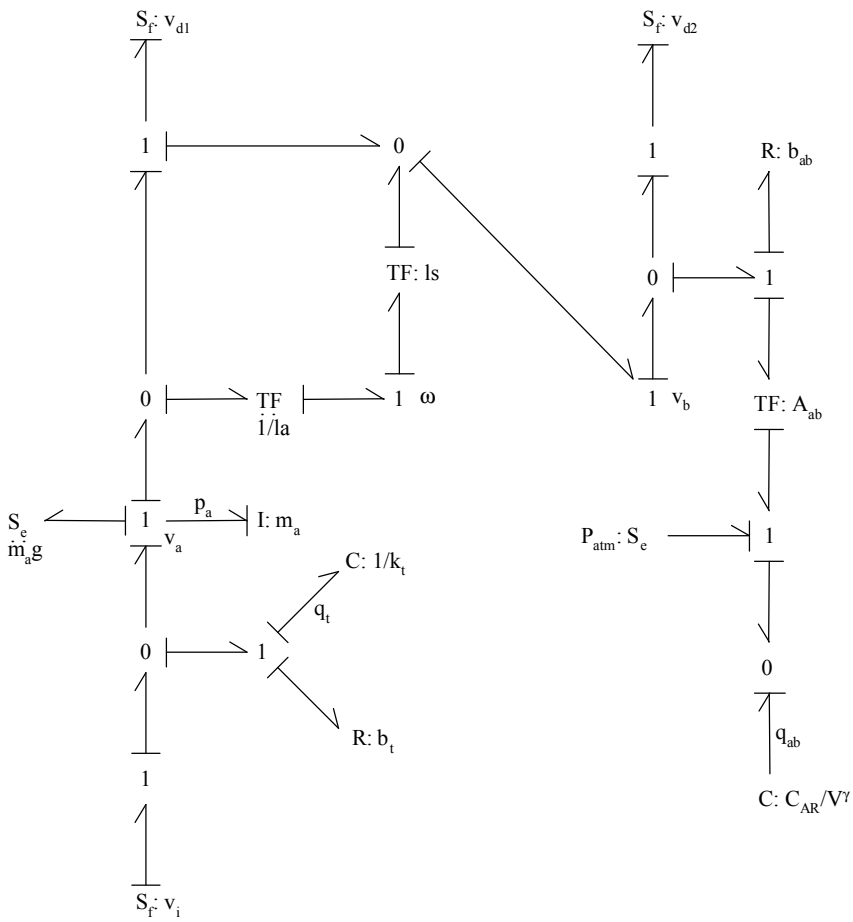


*Figure 3.15 Bond Graph of Air Ride Sub-model*

The equations of motion for the hydro-pneumatic sub-model are derived using the bond graph of Figure 3.15. Notice equations (3.23) and (3.24) are enforced in the upper left portion of the bond graph. The lower left describes axle and tire dynamics and the far right adds air bag and suspension damper affects.

The state variables in the model of Figure 3.11 are:

| | | |
|---|---|---|
| $q_t$ | ≡ | Displacement across tire spring |
| $p_a$ | ≡ | Momentum of unsprung mass |
| $q_{ab}$ | ≡ | Displacement of air in air bag |

State equations are derived directly from the air ride bond graph of Figure 3.15. The final equations are presented here and the complete derivation is reserved for Appendix B.2. The state equations are:

$$\begin{aligned}
\dot{q}_t &= v_i - \frac{p_a}{m_a} \\
\dot{p}_a &= k_{dt} q_t + b_{dt}\left(v_i - \frac{p_a}{m_a}\right) - \frac{ls}{la}\left[b_{ab}\left\{v_{d1}\left(1-\frac{ls}{la}\right) + \frac{ls}{la}\frac{p_a}{m_a} - v_{d2}\right\} + A_{ab}\left(\frac{C_{AR}}{V^{\gamma}} - P_{atm}\right)\right]. \\
\dot{q}_{ab} &= A_{ab}\left\{v_{d2} - v_{d1}\left(1-\frac{ls}{la}\right) - \frac{ls}{la}\frac{p_a}{m_a}\right\}
\end{aligned} \tag{3.26}$$

Output equations for the rigid body connections forces and road forces are:

$$\begin{aligned}
F_{d1} &= \left[b_{ab}\left\{v_{d1}\left(1-\frac{ls}{la}\right) + \frac{ls}{la}\frac{p_a}{m_a} - v_{d2}\right\} + A_{ab}\left(\frac{C_{AR}}{V^{\gamma}} - P_{atm}\right)\right]\left(\frac{ls}{la} - 1\right) \\
F_{d2} &= b_{ab}\left\{v_{d1}\left(1-\frac{ls}{la}\right) + \frac{ls}{la}\frac{p_a}{m_a} - v_{d2}\right\} + A_{ab}\left(\frac{C_{AR}}{V^{\gamma}} - P_{atm}\right) \\
F_i &= k_{dt} q_t + b_{dt}\left(v_i - \frac{p_a}{m_a}\right)
\end{aligned} \tag{3.27}$$

The complete derivation is provided in Appendix B.2.

SIMULINK is used to simulate the complete crane model. The suspension equations are assembled in subsystems allowing them to be added into the main crane model creating the configuration of interest. The initial state values are determined by assuming zero initial velocity and solving for initial displacements. A formal derivation of initial conditions and the air ride SIMULINK subsystem is presented in the final portion of Appendix B.2.

## 3.9 Additional Considerations for Air Ride and Hydro-Pneumatic Suspensions

Both the air ride and the hydro-pneumatic suspension models are developed for one side of the vehicle. Therefore, the model must be slightly modified to compensate for the full pitch plane model that is being developed. This modification is shown pictorially in Figure 3.16.

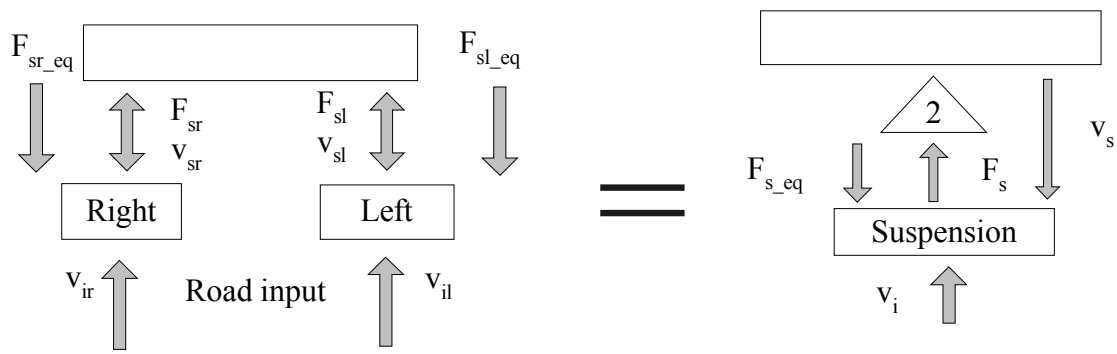


*Figure 3.16 Additional Suspension Considerations*

The equilibrium force on the left and right are considered to be equal in the model, leading to

$$F_{sl_eq} = F_{sr_eq} = F_{s_eq}. \tag{3.28}$$

At equilibrium

$$F_{s_eq} = F_s. \tag{3.29}$$

Accordingly, we have

$$F_{sl_eq} + F_{sr_eq} = 2F_{s_eq}. \tag{3.30}$$

In the model, there is no difference between the velocity of the left and right suspension velocities. In addition, the road input to the left and right tires are also equal due to the nature of the model. This means the relationship stated in equation (3.30) holds up for the dynamic situation, yielding

$$F_{sl} + F_{sr} = 2F_s. \tag{3.31}$$

These are the additional considerations needed to fully implement the air ride and hydro pneumatic suspension sub-models on the crane.

## 3.10 Summary

This chapter discussed the four main suspension models that are implemented in the crane program. Each suspension model was developed based on a single suspension group. These four sub-models are the main building blocks for all of the suspension systems used by the full crane simulation. By connecting these sub-models to the sprung mass models, a complete crane model can be developed. This can easily been done through a SIMULINK file by correctly connecting SIMULINK blocks together. Another very insightful way in which these sub-models can be used is through a quarter-truck model. Looking at the individual suspension groups from this standpoint help develop an understanding of how the suspension performs. This information will be presented in Chapter 6. Chapter 2 provided the equations used to represent the motion of the sprung mass. Chapter 3 provided an explanation of the various suspension sub-models and the equations used to model them. In order to model a complete crane model two more steps must be made before all information needed to simulate the system is developed. An equilibrium point for the system must be established which is covered in Appendix C for the sprung portion and Appendix B for the hydro-pneumatic and air-ride

suspension sub-models. The suspension initial conditions are determined based on the static weight they support. Finally, the road input used to excite the system (covered in Chapter 4) must be determined. Once this is determined, the simulation software development can be explained and a look can be taken at the simulation results.

# CHAPTER 4
# ROAD INPUT GENERATION

## 4.1 Overview

In developing an accurate representation of a vehicle, it is critical to accurately model the vehicle's interactions with the environment. These interactions translate into system inputs. Normally, the most significant system input to a road vehicle model is the road itself. In order to accurately capture the affects of the road, the frequency content must be accurately represented. Generally speaking, the road input should compensate for the vehicles forward velocity. As the forward velocity increases, the value for the time rate of change of road elevation (dy/dt) should increase proportionally to the velocity. The vehicle model uses a parallel spring and damper system to represent each tire. The tire acts like a low pass filter filtering out the high frequency inputs. Therefore, high frequency road inputs can be neglected. Since both the damper and the spring are linear elements, it is necessary to provide both elevation and the time rate of change of elevation to each tire. The road model is tied to the vehicle model both numerically and spatially. This chapter will explain how the road input is tied to the model and present two different road input options available in the program.

## 4.2 Tying the Road Input to the Model

The road model is tied to the system in two ways. The road model is tied to the system numerically, by integrating the time rate of change for road elevation simultaneously with the equations of motion to obtain the road elevation Additionally, the road must be tied to the model spatially by allowing the road input signal to propagate to sequential tires.

The two numerical inputs are required by the model for each tire are the elevation (y) and its time rate of change (dy/dt), which are related as

$$y = \int \frac{dy}{dt} dt \,. \tag{4.1}$$

By taking advantage of this relationship, the state space can be expanded to directly integrate the input velocity giving the input displacement. This means that the only road information needed as an input for each tire is dy/dt.

In order to spatially tie the model to the road, it is important to understand how the road input varies between the tires. In general, the second tire will eventually see the same input signal as the front tire, the only difference is in when it sees the signal. This can be manifested in the notion that the crane is traveling in a straight line. There is a time lag between the front tire and any sequential tires. Since the model assumes that the vehicle is traveling at a constant forward velocity, $v_{forward}$, the time delay for each tire is calculated as

$$t_{delay(i)} = \frac{d_{tire(i)} - d_{tire(ref)}}{v_{forward}} \,. \tag{4.2}$$

A common reference point in time is established by using a common reference distance to determine the time lag. The reference point used in the model is the front axle of the vehicle.

This process ties the road input to the model. The road input is directly integrated by expanding the state vector, tying the input to the system of equations numerically. Through this process, the number of inputs to each tire is now reduced from two inputs to one. A time lag is used to compensate for spatial differences between the tires. Now that the road is tied to the system's equations, it is important to quantify the time rate of change of the roadway's elevation.

### 4.3 Mathematical Road Generation Using a Random White Noise Process

The method used is based on the spectral density of the road profile. Various studies have shown that the slope of the spectral density of the displacement is a straight line [2, 15, and 22]. The equation of this straight line is thus represented as

$$S_{yt}(\omega) = \frac{AV}{2\omega^2} \tag{4.3}$$

where V denotes the forward velocity of the vehicle and A denotes the road roughness parameter. Typical values for A are given in the Table 4.1 [15]. Equation (4.3) represents the spectral density for the displacement. From this equation the power spectral density of the velocity can easily be determined as

$$S_{\dot{y}t}(\omega) = \omega^2 S_{yt}(\omega). \tag{4.4}$$

Now, substituting equation (4.3) into equation (4.4) yields

$$S_{\dot{y}t}(\omega) = \frac{\omega^2 AV}{2\omega^2} = \frac{AV}{2}. \tag{4.5}$$

This shows that the mean spectral density of the slope is constant for all frequencies, and that the road velocity can be modeled as a white noise process.

| Surface | A(m) |
|---|---|
| Poor Highway | 6.40E-5 |
| Average Highway | 1.60E-5 |
| Good Highway | 4.00E-6 |

*Table 4.1 Typical Values for the Road Roughness Parameter*

The spectral density must be converted into the time domain from the frequency domain in order to consider the time response of the system. First, the spectral density must be defined as

$$S_0 = \frac{1}{2\pi} \int_{-\infty}^{\infty} R_{y'}(x)\,dx. \tag{4.6}$$

The above formula shows that the spectral density is a function of the time autocorrelation function ($R_{y'}$). The autocorrelation represents how the values are related from one time to the next. Since the road slope is a random white noise process, there is a small band where the values have some small degree of correlation. Based on this, the autocorrelation

function can be assumed to have the shape shown in Figure 4.1. The area under the autocorrelation curve can be calculated by summing the area of the two triangles yielding

$$\int_{-\Delta t}^{\Delta t} R_{y'}(\xi)\,d\xi = \sigma_{y'}^{2}\Delta t\,. \tag{4.7}$$

This relationship can then be substituted into equation (4.6) and equated to equation (4.5), yielding

$$S_0 = \frac{1}{2\pi}\sigma_{y'}^{2}\Delta t = \frac{AV}{2}\,. \tag{4.8}$$

Accordingly the variance of the slope can be written as a function of A, V, and Δt as

$$\sigma_{y'}^{2} = \frac{AV\pi}{\Delta t} \tag{4.9}$$

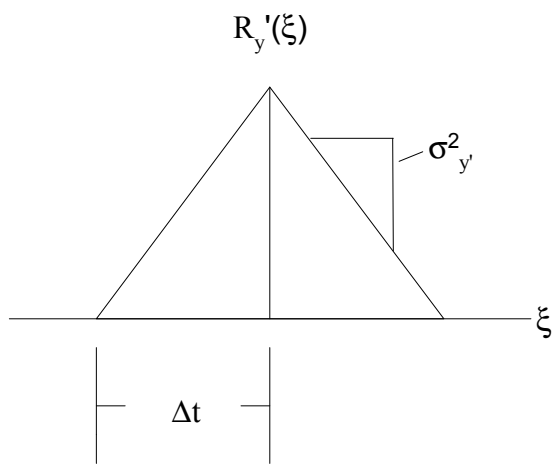


*Figure 4.1 Autocorrelation Function of Road Elevation*

Now there is the matter of determining a valid Δt value. The value of Δt is determined by looking at the highest road frequency of interest. The tires filter most of the high frequency input. This allows a limit to be placed on the highest possible input frequency to the system. The slope is held at a constant value for a period of time ($\Delta t$), the sampling frequency of the road input. In order to accurately capture the dynamics is the system, this sampling frequency needs to be higher then the frequencies of interest in the road input where

$$\Delta t = \frac{1}{f_{\max}}\,. \tag{4.10}$$

From this equation, the variance can finally be calculated.

Once the variance of the system is determined, the process of determining the road profile becomes a statistics problem. The two equations used to calculate the expected value of the slope at some arbitrary time are given below as

$$E(x^2) = \int_{-\infty}^{\infty} x^2 p(x)dx \tag{4.11}$$

and

$$s_x^2 = E(x^2) - (E(x))^2 \tag{4.12}$$

where E(x) denotes the mean, $E(x^2)$ denotes the mean square, and p(x) denotes the probability distribution function.

The final equations used in the simulation are based on a random number generator with a rectangular probability distribution with an average at 0 as in Figure 4.2. N is a random number provided by a random number generator at a particular instant in time. Since the mean is equal to zero, equation (4.12) reduces to

$$s_x^2 = E(x^2). \tag{4.13}$$

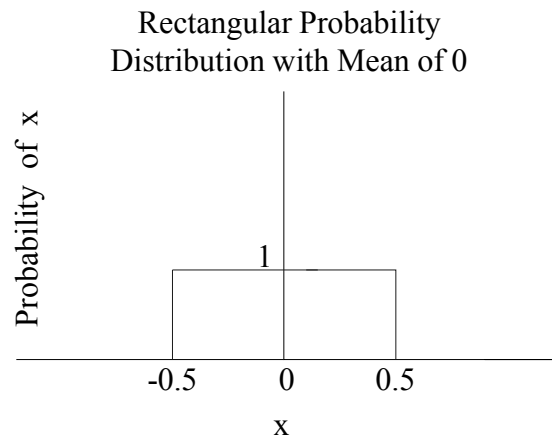


*Figure 4.2 Random Probability Distribution Used for Artificial Road Profile Generation*

In order to get the proper variance that was calculated above, the rectangular distribution must be rescaled so that the area under the probability curve is equal one. Therefore, the probability curve is rescaled as illustrated in Figure 4.3. Since p(x) becomes a constant 1/2B on the interval [-B,B], equation (4.11) can be expressed as

$$E(x^2) = \frac{1}{2B}\int_{-B}^{B} x^2 dx. \tag{4.14}$$

By performing the integration in Equation (4.14)a relationship of the mean square in terms of B can be determined as

$$E(x^2) = \frac{B^2}{3} = \frac{AV\rho}{\Delta t}. \tag{4.15}$$

Solving equation (4.15) for B yields

$$B = \left( \frac{3AV\rho}{\Delta t} \right)^{\frac{1}{2}}. \tag{4.16}$$

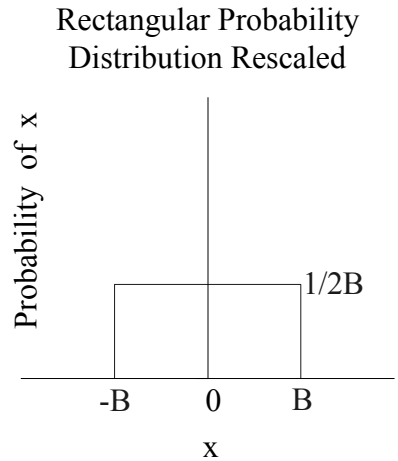


*Figure 4.3 Rescaled Random Number Distribution Used for Input Road Velocity*

Once B is determined, the values for the slope that will correspond to the desired spectral density can be determined as

$$N' = 2BN. \tag{4.17}$$

The value N' is the velocity input to the system. The parameter B scales the random number to yield a realistic magnitude for the road input velocity. One thing that should be noted is that forward velocity is directly proportional to B. This causes the input road velocity to increase as the vehicle is traveling faster. Based on this mathematical formulation, an artificial road profile can be generated and implemented in the model.

Now, the question is, how accurate of a road does this represent? A road profile using a good road roughness parameter is shown in Figure 4.4. Since the process is based on a random number generator, it is difficult to justify the results. However, the profiles generated through this process are very similar in magnitude to the artificial roads generated by Cebon [8]. One of the benefits of using the random generator in MATLAB is that there is a seed number built into the random number generator. If the seed number is not changed between simulations, then the road profile will be identical. This will allow for comparisons to be made between different configurations on the same road profiles.

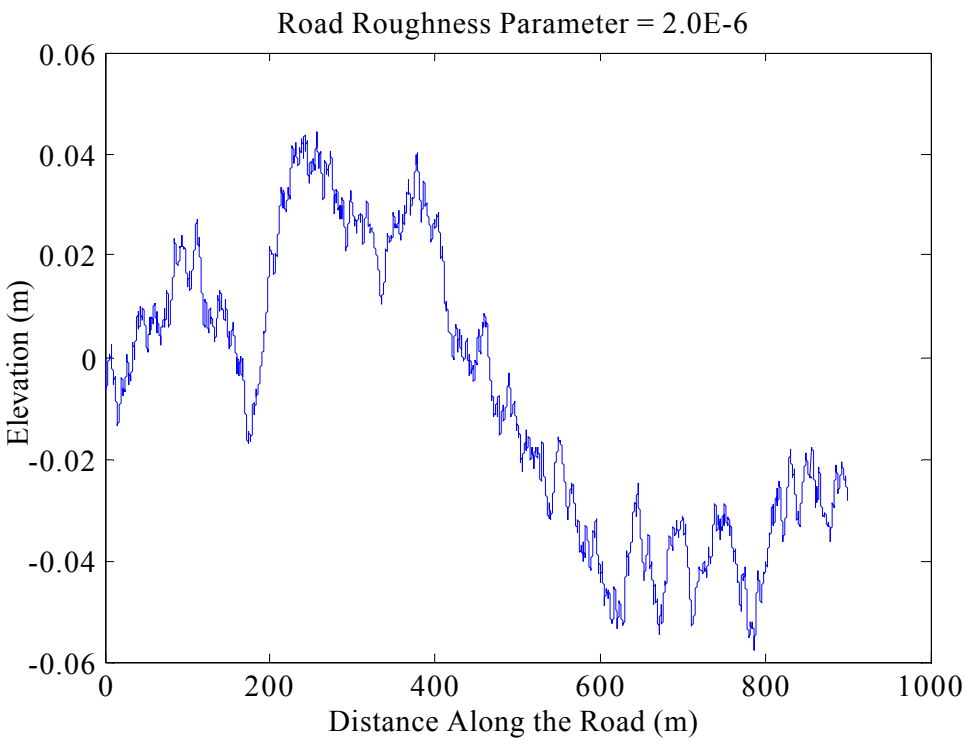


*Figure 4.4 Artificial Road Generated by Using Random Process Sampled at 150Hz.*

The road profile shown in Figure 4.4 is generated using a sampling frequency of 150Hz. This ensures that an input frequency above the system frequencies is contained in the input. By looking a smaller sampling frequency (5Hz), insight can be gained on the road profile generation process. Figure 4.5 shows the road profile for a vehicle traveling at 15 m/s. Since the sampling frequency is 5Hz, the random number generator will change its value for the slope every 3 m as shown in the Figure 4.5. This illustrates how the input velocity is held constant for a specified amount of time.

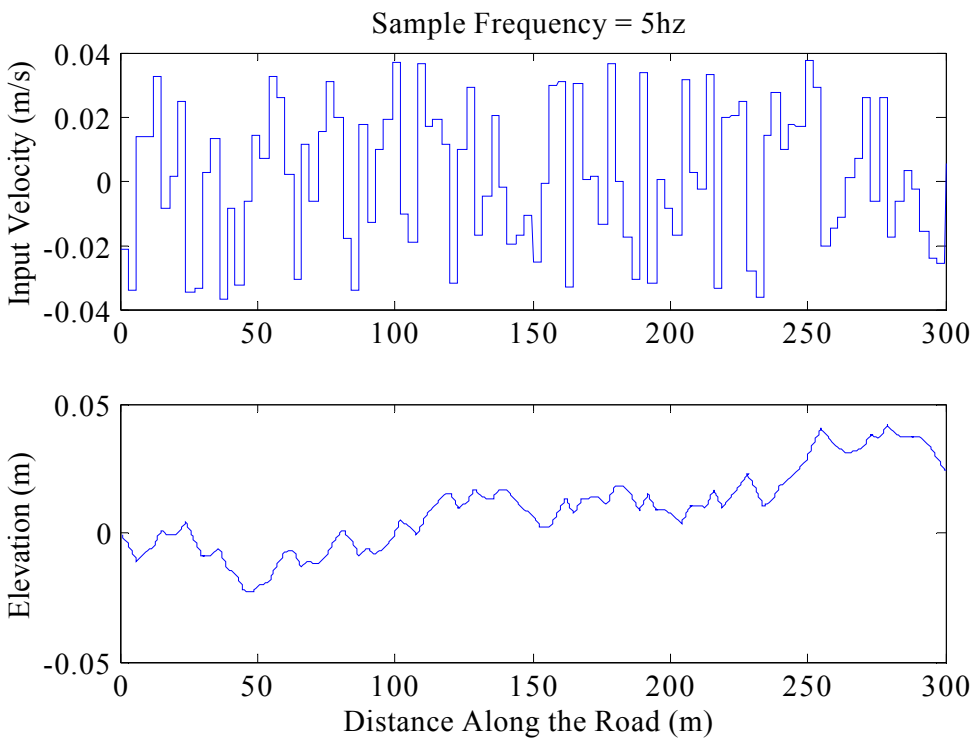


*Figure 4.5 Artificial Road Generated Using Random Process Sampled at 5Hz.*

## 4.4 Road Profile From Data File

Other forms of input can also be interfaced with the model, for example, a physically measured road data file. There are two fundamental issues that arise with this input type. First there needs to be enough resolution to capture the system frequencies. If the road profile does not accurately capture these frequencies, the system response will not be representative of the actual system. The second issue is the fundamental accuracy of the measurements. If the measurements are not sufficiently accurate, the data will not be relevant. The idea of implementing the road profile into the model was analyzed with these questions in mind.

A data file has been provided by Caltrans for this work [28]. This data file's road profile is measured at 6.4 cm (0.21 ft) increments. The spacing of the data is what captures the frequency, however equally important is that the amplitude of the data is accurate. According to Caltrans, the data was measured in two ways. First static measurements are taken at specified increments. Second, the measurements are taken from a vehicle that is traveling down the road. As the vehicle travels, two measurements are taken. One measurement is the acceleration of the vehicle itself. This is measured using an accelerometer and allows the vehicle's acceleration to be defined in a fixed frame. Then, a laser is used to measure the displacement of the road relative to the vehicle. The accelerometer data is integrated twice to establish a reference plane, which can be used to determine the road elevation.

An important aspect is that the frequency content captured by the road is entirely dependent on the vehicle's forward traveling speed in the model. The general relationship is given as:

$$f_{samp} = \frac{v_{forward}}{x_{increment}}, \tag{4.18}$$

where $f_{samp}$ denotes the sampling frequency of the road, $v_{forward}$ denotes the vehicles forward speed, and $x_{increment}$ denotes the measurement spacing. This relationship shows that the road sampling frequency is directly proportional to the forward velocity of the vehicle. Now, that the sampling frequency for the road can be calculated, the next question is what frequency of input signal is represented by that sampling frequency. According to Shannon's sampling theorem, two points are needed to generate a wave. A closer look at this was taken at this by implementing a simple MATLAB program.

According the Shannon's sampling theorem theoretically a sampling rate of twice the highest frequency in the signal is required to capture the frequency content of the signal [21]. However, in practice it is common to use a higher factor. A closer look was taken at the sampling factor required in this model. The analysis compares a regenerated signal to a known signal. For this program, an analytical function generates the known signal and a series of data points. The function is defined to have a continuous first derivative. Since the main question concerns the frequency content, the best type of function to use is a periodic function such as a sine wave. A data set is generated from the analytical function at a consistent sampling frequency ($f_{samp}$). This will allow a comparison to be made between the analytical and regenerated signals. In order to look at how many data points are needed to recreate a given signal, it was decided to make the data set sampling a function of the highest frequency in the analytical function and a sampling factor.

The equation for the data sampling frequency is given as

$$f_{samp} = \frac{f_{signal}}{n}, \tag{4.19}$$

where $f_{samp}$ denotes the data sampling frequency, $f_{signal}$ denotes the lowest frequency of the periodic function, and n denotes the sampling factor determining how many points to look at in each cycle of the periodic function. This data is then sent through a cubic spline curve-fitting algorithm. The curve-fitting algorithm generates a signal that can be compared to the analytical signal. This was done using a sampling frequency that is twice the input signal frequency. The data set only uses the values at the beginning of the wavelength, and the midpoint of the wavelength. For this case, every data point coincides with a nodal point in the analytical signal. When this data is curve-fit, a straight line results, as shown in Figure 4.6.

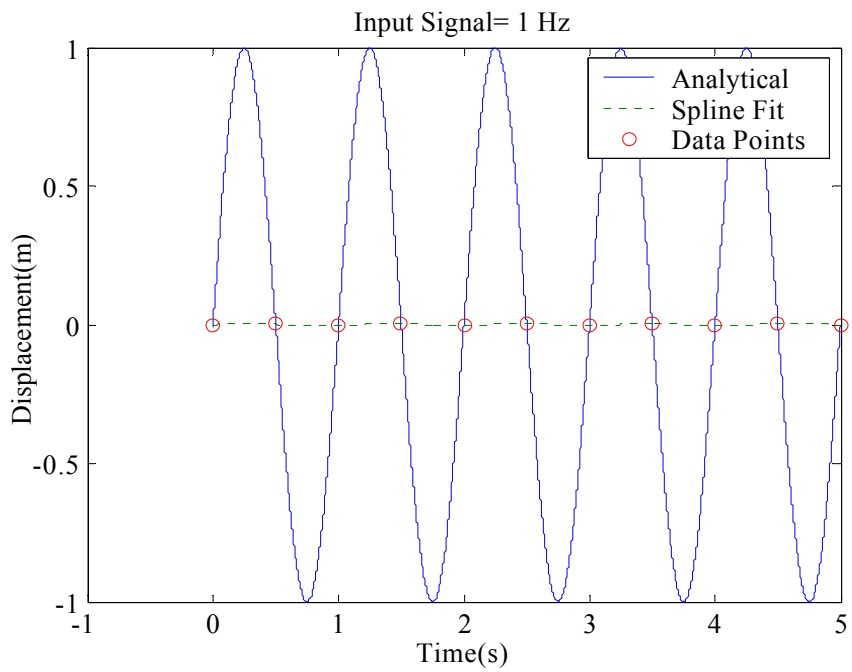


*Figure 4.6 Comparison of Analytical Signal to Spline Fit Using 2 Data Points Per Cycle.*

Now, repeating the process for n equal to three, a better representation of the curve can be regenerated and is given below in Figure 4.7.

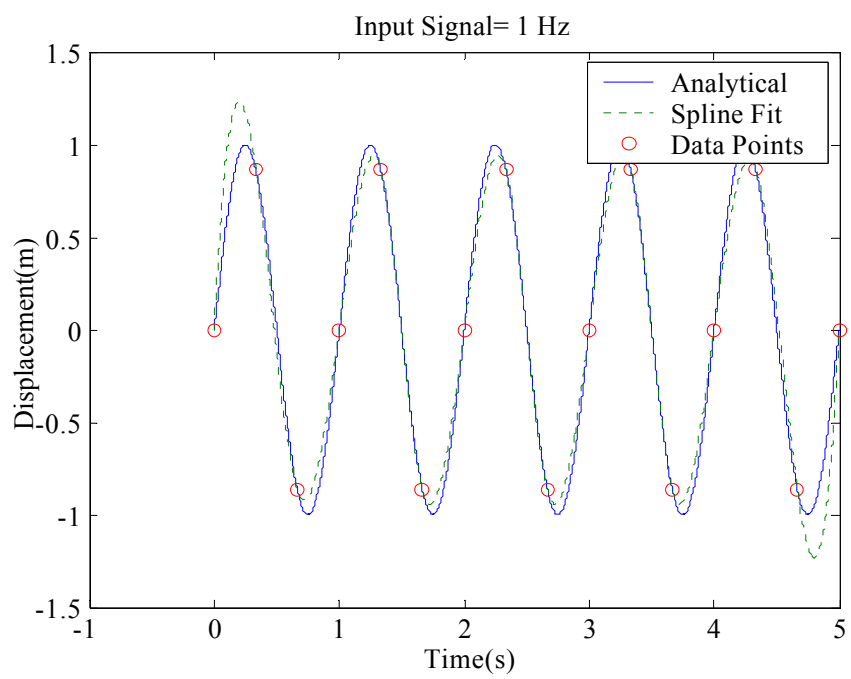


*Figure 4.7 Comparison of Analytical Signal to Spline Fit Using 3 Data Points Per Cycle*

Now, it is clear that the frequency content of the input signal is accurately captured by the regenerated signal by using a sampling frequency three times the highest frequency in the input. The question now becomes what happens if the input signal is a combination of frequencies, which is a more realistic representation of a road input. The same process can be carried out using the function given by

$$y(t) = \sin(\omega t) + \frac{1}{2}\sin\left(\frac{\omega}{3}t\right). \tag{4.20}$$

Here, the value of ω represents the highest frequency in the input signal as shown in Figure 4.8.

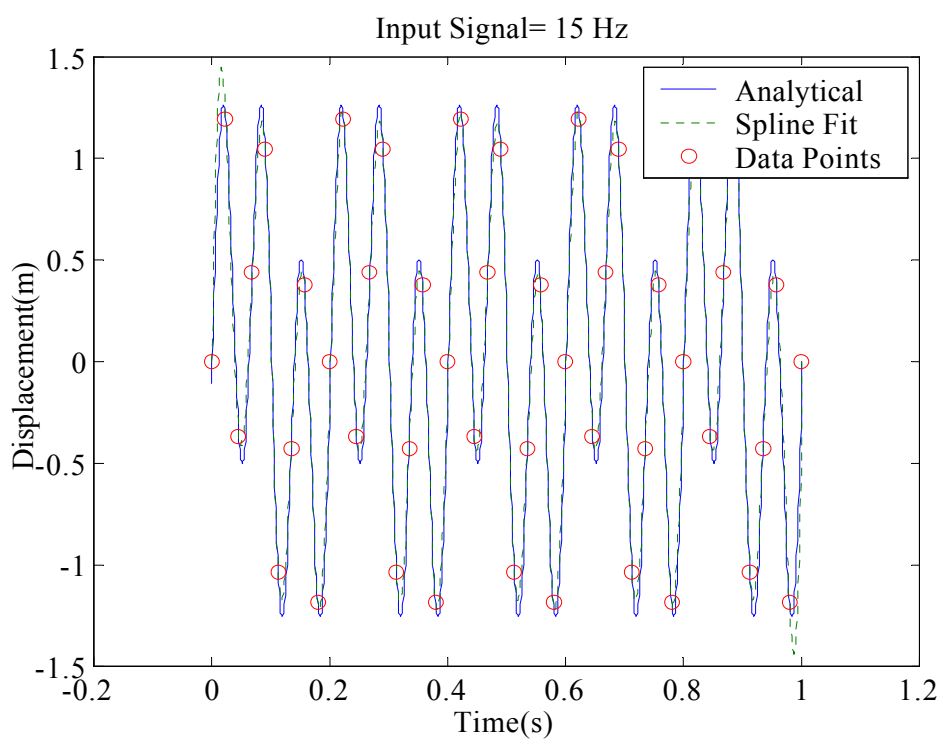


*Figure 4.8 Higher Frequency Regenerated Signal*

The figure shows that the signal can be reproduced accurately using n equal to 3. Based on this idea, a reasonable approximation for the highest frequency in the input signal that can be accurately reproduced is one third of the data sampling frequency.

Now, it is important to understand why the signal used above was defined to have a continuous first derivative. The model is configured so that the input to the system is road velocities. This means that to give the model the proper input, the road displacement signal must be differentiated. This allows the analytical derivative to be compared with the numerical derivative. The function used in MATLAB to curve fit data also has the ability to generate the curve data points at a set resolution. In the program, a resolution of 0.001 seconds is used. This means that the curve-fitting algorithm returns data with a time spacing of 0.001 seconds. The derivative is numerically calculated from the spline fit data by using a forward difference approximation given as

$$\frac{dy}{dt}_i = \frac{y_{i+1} - y_i}{t_{i+1} - t_i} = \frac{y_{i+1} - y_i}{\Delta t}. \tag{4.21}$$

This equation gives accurate results as long as Δt is small. Now, using this formulation a problem in the first derivative is clearly noticeable as shown in Figure 4.9.

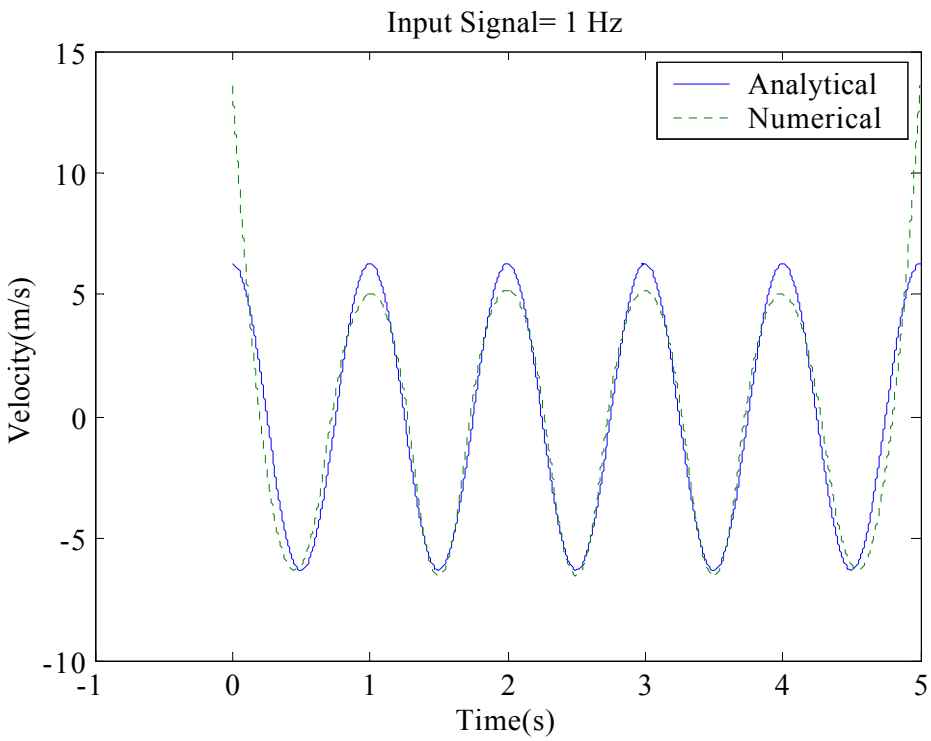


*Figure 4.9 Analytical Derivative vs. Forward Difference*

Figure 4.9 shows a numerically determined derivative based on forward differencing the curve fit data points and the analytical derivative of a sine function. The figure shows that the numerical derivative does a poor job at the endpoints of the time interval. However, in the intermediate regions, it does a good job approximating the derivative. This is because the cubic spline curve has no constraint on the derivative at the endpoints.

In order to correct this problem, two additional data points are added to the data set used for generating the spline data. An additional point is added to the beginning and the end of the data set. These two points are given the same displacement value as the adjoining point in the data set. Figure 4.10 gives the results of this process.

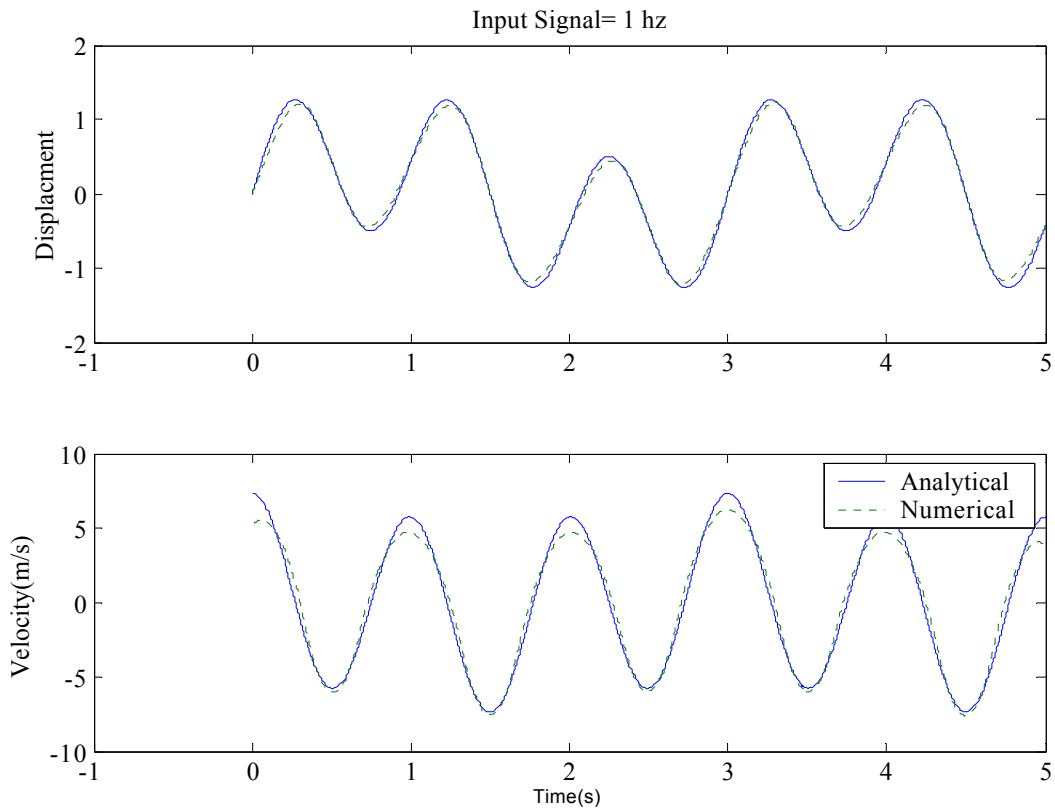


*Figure 4.10 Analytical Derivative vs. Forward Difference Using Correction Terms.*

The first point is justified because the system is in equilibrium. This means that the input relative displacement between two points on the road is zero before the input signal is fed into the model. The last point is reasonable because realistically speaking the data file should contain a longer time span for the road then is needed for a single simulation.

Finally, this entire process would be pointless if the original input signal cannot be created from the numerical derivative since the simulation automatically integrates the signal. A SIMULINK file was written which numerically integrates the velocity, giving the displacement. Figure 4.11 gives the integrated numerical velocity profile as a function of time and the analytical solution. As the figure shows, there is very little information lost through numerically processing the data.

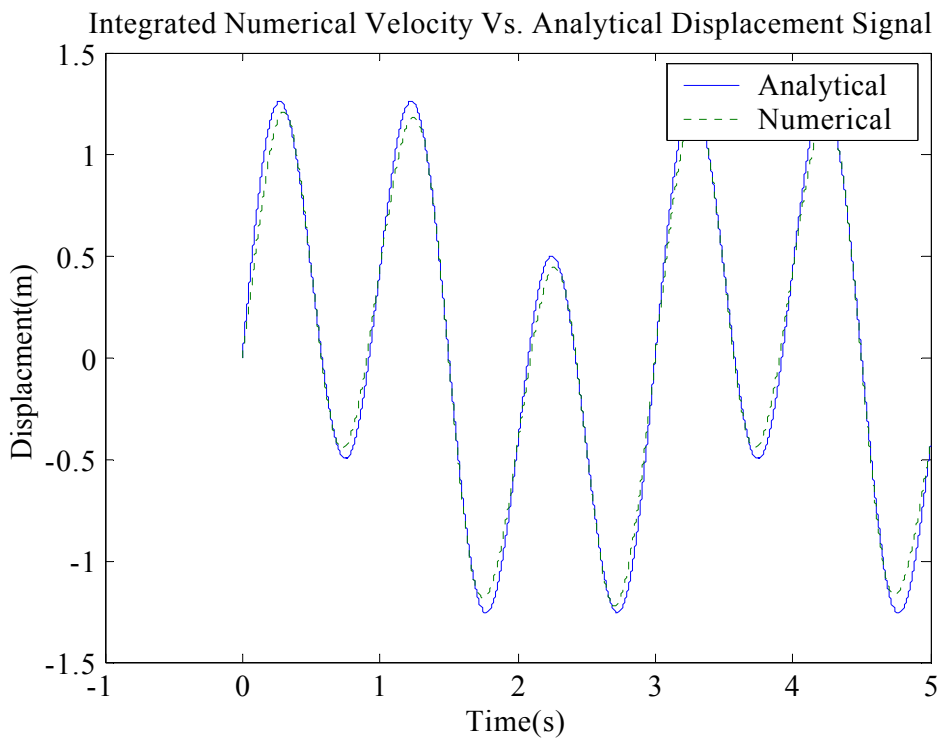


*Figure 4.11 Integrated Forward Difference vs. Initial Analytical Signal*

Now that it has been shown that three data points per cycle are enough to accurately generate an input signal to the system, it is important to reconsider equation (4.18). Since the measurement spacing is 6.4 cm, the validity of this process is completely dependent on how fast the vehicle is traveling. For example, if the vehicle is traveling at 15 m/s (33.5 mph), the road sampling frequency is about 234Hz as given by equation (4.21). This means that an input signal of roughly 78.1Hz can be sufficiently recreated.

$$f_{samp} = \frac{v_{forward}}{\Delta X_{samp}} \tag{4.22}$$

This process was implemented in the program and used on a data file provided by Caltrans. In order to implement this in the program, a text file of displacements listed in a single column must be given. The name of this file must have the '.txt.'extension and the sample spacing must be defined in the input window. Figure 4.12 shows that through the process discussed above there is essentially no difference between the data and the regenerated signal. The original data is shifted down by 0.1 m to allow the two signals to be distinguished. Essentially a road data file is implemented into the program by converting that data into an input velocity profile.

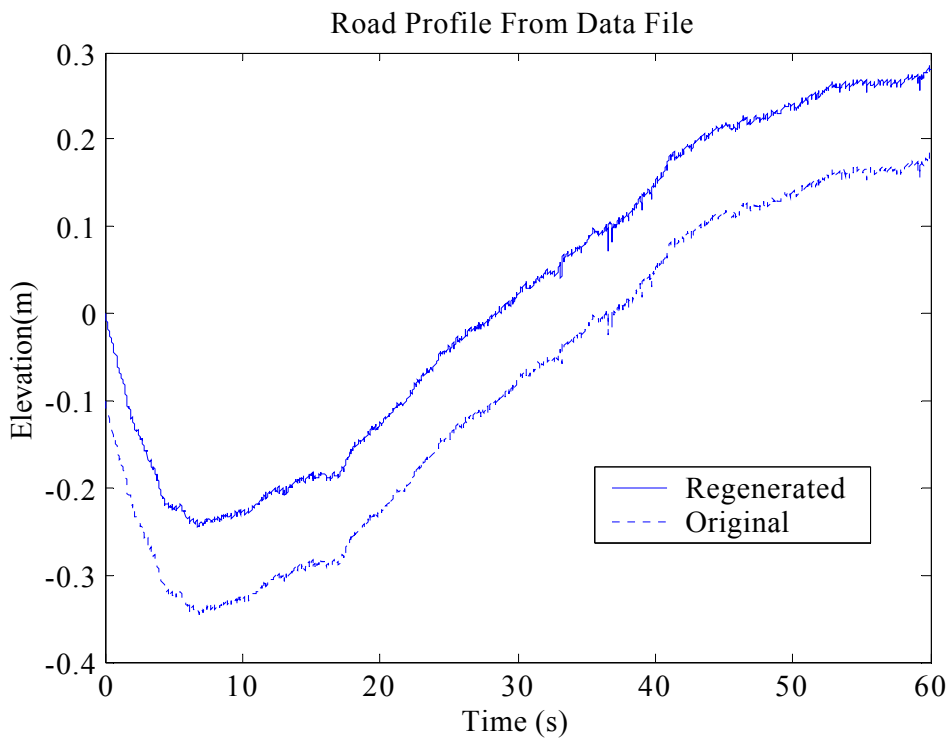


*Figure 4.12 Road Data and Regenerated Input Signal Using the Process Discussed Above*

## 4.5 Summary

This chapter explained the road input to the computer model. In order to model the system's response to the road accurately, the input is tied to the model both numerically and spatially. The road velocity is integrated to determine the elevation. Spatial compensation for the road is incorporated in the idea that the tires see identical input signals, but shifted by a given time delay. A method for generating a random road profile has been developed based on a random white noise process. Also incorporated in the model is the ability to use a road displacement data file. By numerically manipulating the displacement data, an input signal with a frequency of one-third the road data sampling frequency can be confidently regenerated. Using an artificial road generator allows various road profiles to be simulated without the need for collecting actual road data.

# CHAPTER 5
# PROGRAM STRUCTURE

## 5.1 Overview

One of the goals of the project is to develop a tool that provides a way to understand the dynamic road loads generated by mobile cranes. The idea is to structure the program to give the user the ability to look at various configurations and vehicle parameters. The two biggest aspects of the program from the user's standpoint are the input and output methods. The user should be able to change vehicle parameters in a way that is clear and concise. The results must be presented clearly to allow the user to understand the response. This chapter will outline the general flow of the program. The intention here is to provide a general understanding of the program structure without detailing the actual code.

## 5.2 Platform

The first step in developing a user-friendly program is to determine the basic platform. MATLAB and FORTRAN were both considered for the software platform. Both programs have their advantages and disadvantages.

FORTRAN is a basic programming language that is commonly used for numerical computations. Once a FORTRAN program is compiled, a stand-alone application is created. This program can be independently executed without the need for any additional programs. Since FORTRAN involves a pre-compiled code, the program executes faster yielding a shorter simulation runtime. A well-written code tries to minimize run-time without sacrificing numerical accuracy.

Coupled with FORTRAN's advantages, are some disadvantages. The basic library of mathematical operations available in FORTRAN are not much larger then those available on a scientific calculator. In order to develop a complex program in FORTRAN, the required subroutine libraries must be collected for more complex computations. Usually with programs written in FORTRAN, the user input/output takes place in either a data file or a DOS window, which is not very intuitive to the user.

A MATLAB program must be executed through the MATLAB command window. This is different then a program developed in FORTRAN, where the compiled program is self-contained. This is not a big issue due to the fact that MATLAB has become a widely used software package. MATLAB is inherently slow compared to more basic programming platforms. However, through the use of SIMULINK, the overall computational speed of the MATLAB program can be increased. SIMULINK is an added MATLAB toolbox commonly used in signal processing. When a SIMULINK file is executed, the equations embedded in the SIMULINK file are rearranged into the most computationally efficient order before SIMULINK integrates the system [17]. The integration process is the most time consuming part of the program. Therefore the most computationally efficient means to integrate the equations is important.

MATLAB and SIMULINK can be coupled together through MATLAB commands to create a more computationally efficient program. MATLAB has an extensive library of

subroutines readily available which eliminates the need to collect an extensive subroutine library. These subroutines are written in a general format, facilitating their implementation. MATLAB commands are defined that allow the development of graphical user interface programs (GUI), allowing a very intuitive input/output environment to be created. This aids in developing an environment where the user can see many of the vehicle parameters associated with their physical meanings instead of pure text descriptions. The output data can be graphically displayed, which eliminates the need of a data output file that is commonly used by FORTRAN based programs. However, an output file is still available in the simulation.

In conclusion, writing the program in MATLAB is the best option because the benefits of MATLAB far outweigh the disadvantages. MATLAB code is much easier to follow because of all of the basic matrix operations and pre-defined subroutines, which simplify the source code. The GUI interface ability of MATLAB allows for the model to be developed in a user-friendly environment, facilitating the user's ability to look at various vehicle parameters. The features of SIMULINK are taken advantage of in order to speed up the simulation to make up for the increased run-time of a MATLAB simulation in comparison to a theoretical FORTRAN simulation.

The final MATLAB software package that was developed has a few system requirements. Some of the features used by the program require MATLAB 6.1 or newer. SIMULINK is also required, in order to run the program. Finally, the program must be stored on the hard drive in order to execute. Every time the simulation is executed, a temporary file is created, which is then saved. Therefore the program must have the ability to write to the directory where it is stored. This ability is not allowed by current compact disk drives. Sixteen megabytes of free drive space for the program is suggested (Additional space may be required for large output files).

## 5.3 Directory Structure

In the simulation package a directory structure was established. The structure gives the user the option to user either the metric or English version of the program, while reducing the amount of computer memory that is required by the software. The impact of this structure on the end user is minimized by placing data input files and program output files in subdirectories that are separate from the main program files, but are commonly user folders regardless of the selected unit system. This structure facilitates the ability of the user to place the desired input files in the proper location because the same location is used for both metric and English versions of the crane simulation. The memory required by the program is reduced through the implementation of the directory structure by creating a common folder for the graphics used by the program. The general directory structure is presented in Figure 5.1. The Boom_Frequency and Crane_Extras subdirectories are separate from the crane program and will be briefly explained. The crane program is in the English and metric subdirectories. These subdirectories work interactively with the Road_Data_Files, Program_Output, and Pictures subdirectories during the execution of the crane program. The gray boxes indicate main programs that can be run directly from the MATLAB command window.

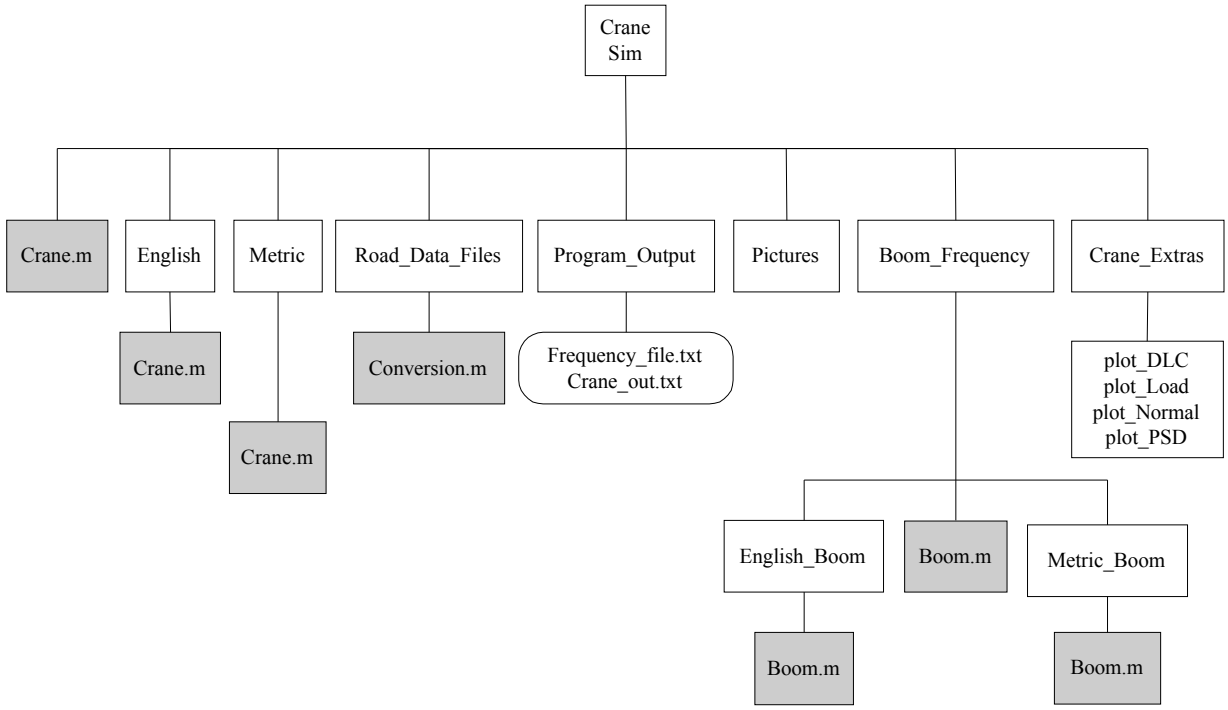


*Figure 5.1 Directory Structure*

There are two available output files that the program can generate. The 'Frequency_file.txt' contains information regarding the mode shapes of the system with the associated frequency. The 'Crane_out.txt' file contains the tire force time histories of a single simulation. Both of the output files are written in a tab-delimited format that facilitates opening the files in EXCEL for additional processing. Both of these files can be found in the Program_Output subdirectory.

The program has only one type of input file. This file is how road profile measurements are implemented in the simulation. The sample spacing of the elevation measurements is given directly to the crane program. The data file must be located in the Road_Data_Files subdirectory because the program automatically looks there for the specified data file. The last consideration for implementing a road data file is that the units of the elevation measurements are consistent with what the program expects. The metric version of the crane program considers the input measurements in terms of meters, while the English version treats the road input in units of inches. Included in the Road_Data_Files subdirectory is a program called 'Conversion.m'. This routine, which works directly through the MATLAB command window, allows the user to convert the data to the proper units and save the converted data under a new file name. Additional help for this program is available through the MATLAB help command. The program can implement a data file that meets these requirements for an input road profile. However, the length of the data file is important to ensure enough data for the desired simulation run time. In an effort to reduce this problem, the program implements a check to ensure the file is long enough for the desired simulation runtime based on vehicle speed and sample spacing. If the data is not long enough for the specified time span, the program changes the time-span to the maximum allowed for the data file and initial time delay.

The Boom_Frequency subdirectory contains a boom analysis program. The program looks at the vibration frequencies of the boom independently of the rest of the system. This tool can help the user to understand the roll that boom vibration plays in the dynamics of the system. This program works interactively with the pictures subdirectory for the graphics as well. The program implements the finite element program used by the crane simulation. Since both the metric and English versions of the crane program are available in the directory structure, the ability to use either unit system is available.

The Crane_Extras subdirectory contains various plotting routines used by the crane program. The copies of these subroutines located in the English and metric subdirectories are used directly by the simulation. The plot_DLC routine plots the dynamic load coefficient of the system. This is defined as the standard deviation of the axle load divided by the mean. The plot_Load routine generates a bar plot of the static axle forces. In addition, to plotting the static forces, this routine plots the first and second standard deviations of the forces are plotted to give an indication of the dynamic loads that are generated by the simulation. The plot_Normal routine generates a Gaussian curve of the data based on its mean and standard deviation. This routine can be used for both the Gaussian curve and the Normalized Gaussian curve. The plot_PSD routine plots the power spectral density of a signal. The signal should have a zero mean because the plot will yield a large amount of power put into the system at a zero frequency, and will not accurately reflect the dynamics of the system. Additional help on these plotting routines is available using the MATLAB help command.

The last part in the directory structure is the English and metric subdirectories. Inside these subdirectories is the MATLAB files required to run the crane simulation. The file crane.m can be called from either the main Crane_Sim directory or the English or metric subdirectories. From the main Crane_Sim folder, the user is then prompted to select the desired units. The program then goes to the appropriate subdirectory. This same idea is used for the boom.m file. At this point it is important to mention that there are duplicate filenames located in different places in the directory structure. These duplicate names are not interchangeable between directories due to the subtle modifications required for the implementation of different units.

This section is presented to provide a general idea of the directory structure used in the final software package. Section 5.4 covers the detailed program architecture of the crane simulation.

## 5.4 Crane Simulation Program Architecture

The program was written with the ability to allow the user to look at different crane configurations. The structure is given in Figure 5.2, which illustrates how the programs interact. The grey arrows are intended to illustrate the aspects of the software that are more related to flow and transfer of information. The black arrows are intended to illustrate portions of the program that are more logic oriented aspects that were created due to the user interface. The program structure seems complex, however, it can be simplified into the three general sections shown in Figure 5.3.

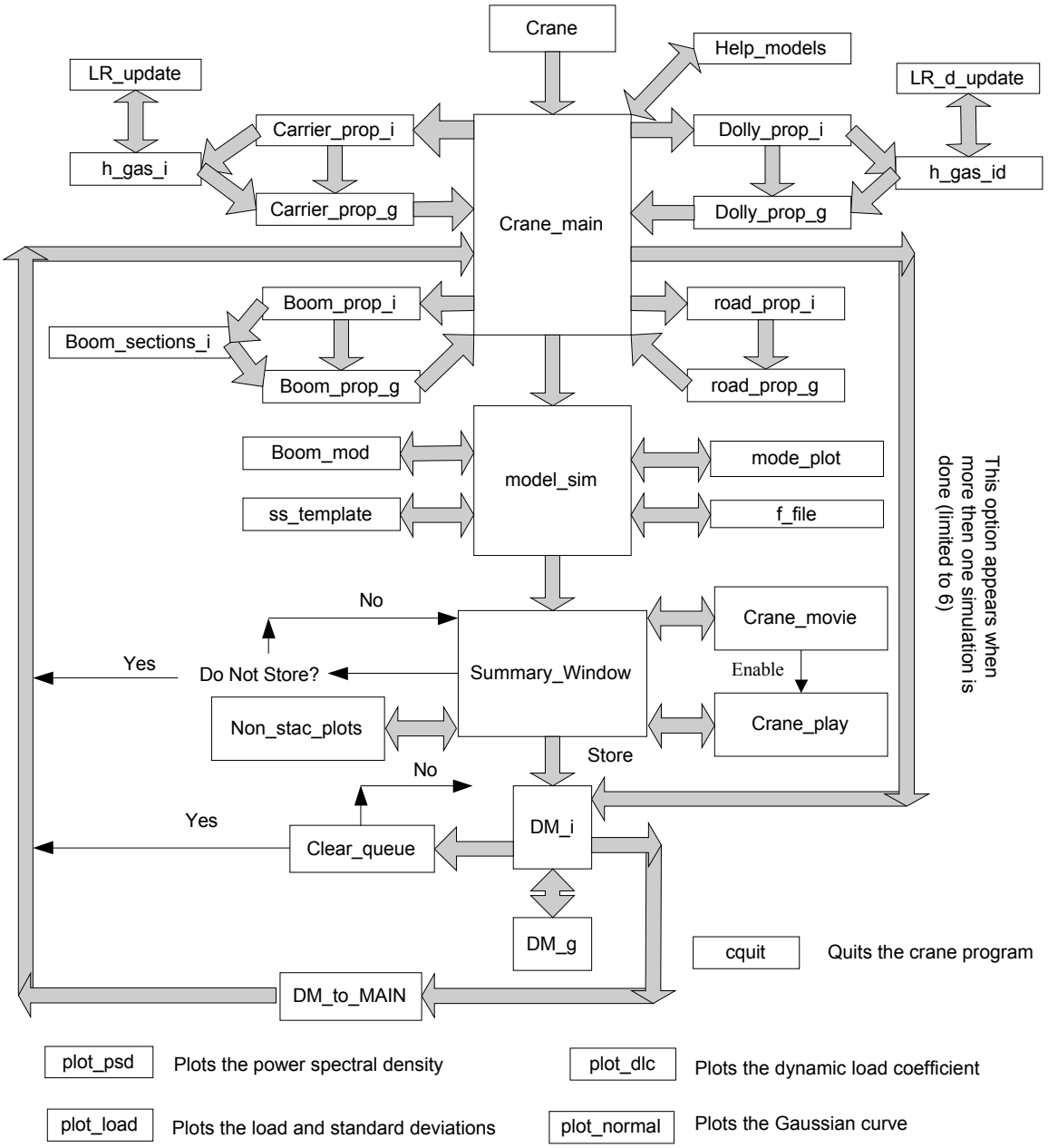


*Figure 5.2 Program Structure*

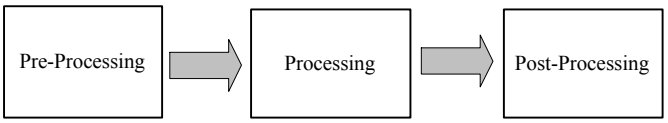


*Figure 5.3 Simplified Program Structure*

The pre-processing part of the program is responsible for collecting the vehicle data and developing some of the independent matrices required for the simulation. The processing section of the program couples the system matrices, determines the initial conditions, edits the

SIMULINK template file, and carries out the numerical integration of the system through SIMULIINK. The post-processing routine takes the results and processes them into a form for the user to see the results. A data file is available to the user for further post process the simulation. The file 'cquit.m' is used to quit the program without completely closing MATLAB. Details of each of the program's elements are to follow.

### 5.4.1 Pre-Processing

The pre-processing part of the program is responsible for collecting all of the vehicle parameters for the various configurations and assembling some of the matrices needed to represent the desired configuration. The general structure of this phase of the program is illustrated in Figure 5.4.

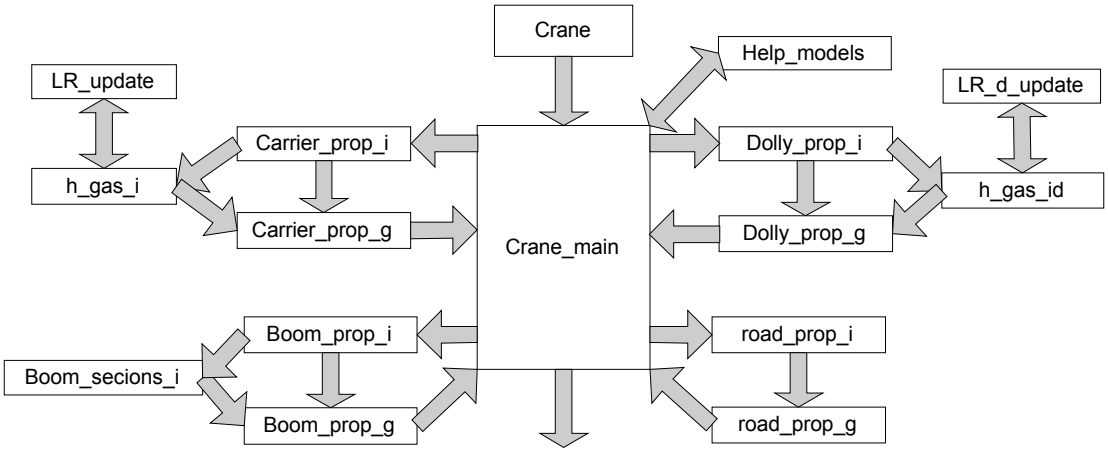


*Figure 5.4 General Program Flow of Pre-processing Section*

The 'Crane.m' file is the initialization file for the program. Here the variable MODEL is set which allows the program to distinguish between the different subsystems in the program. Initially, this is set to an empty model. However, the variable 'MODEL' must be initialized here so that the user can change configurations without having to redefine each subsystem. The variable MODEL is a 1x4 vector, which contains integer values associated with each possible sub-model and allows the program to distinguish between them. At the end of the execution of this file, the 'Crane_main.m' file is automatically executed.

The 'Crane_main.m' file establishes a point where the user can select the various sub-models. The user is allowed to select the various components of the model through the main program via four pull-down menus show in Figure 5.5.

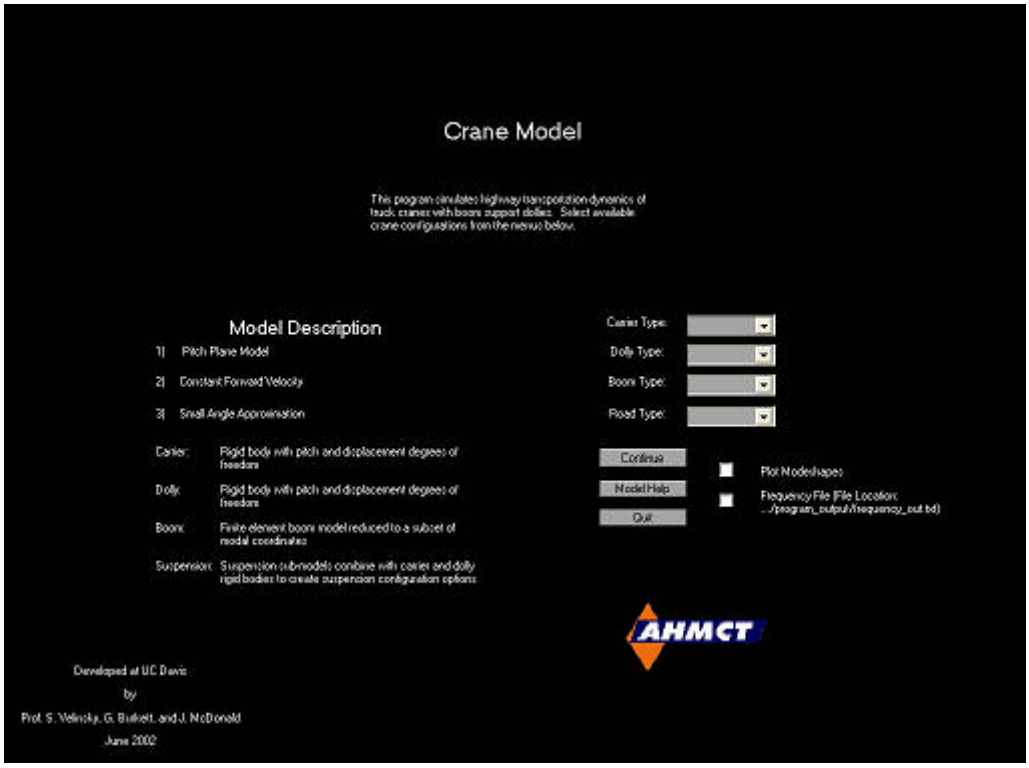


*Figure 5.5 Main Program Screen*

The help model feature, which is accessible through the main screen, provides a more detailed description of the models available in the simulation. Developing a nomenclature for the various models was needed to establish a way to distinguish between different sub-models. Once the user understands the nomenclature, it is very easy to understand. However, this feature was created to provide textual descriptions of the models available in the program and clear up confusion about the nomenclature associated with the sub-model pull down menus.

Each subsystem contains a loop, which allows it to be changed independently of other subsystems. Each pull-down menu is tied to a MATLAB m-file (*_prop_i.m'), which is the first step in each subsystem loop. The loop that is used in the dolly and carrier input routine is illustrated in Figure 5.6.

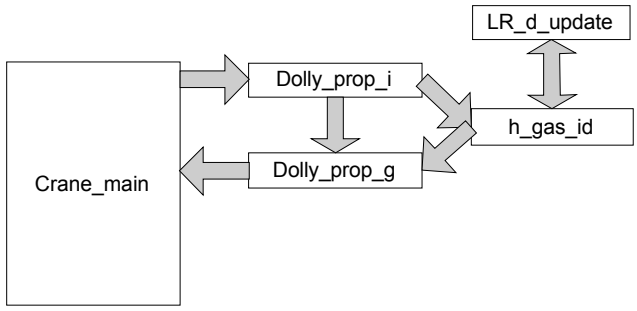


Figure 5.6 Dolly and Carrier Pre-processing Loop

The '*_prop_i.m' file creates an interactive screen that allows the user to specify the parameters associated with that subsystem. The input screen for a three axle dolly with a front walking beam tandem followed by an independent rear axle is illustrated in Figure 5.7. Figure 5.7 is a representative input screen and is common for all subsystems.

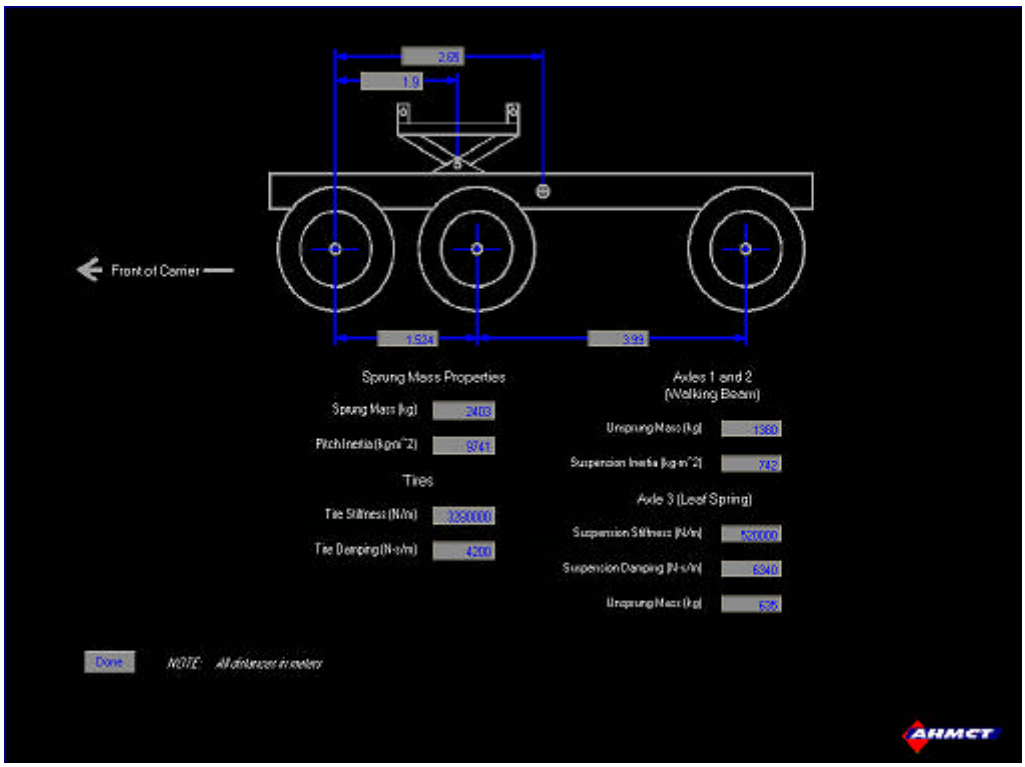


*Figure 5.7 Typical Input Screen*

Both the dolly and carrier submodels include cases where a hydro-pneumatic suspension can be implemented. An additional input screen is required for the hydro-pneumatic carrier and dolly cases, and is built by the 'h_gas_i' or 'h_gas_id' file respectively. In conjunction with these files are the 'RL_update' and 'RL_d_update' files. These two files are responsible for updating the line resistance. The line resistance in the model is a function of line length and

diameter. In the hydro-pneumatic suspension, this is an important factor. Therefore, when either the line diameter or length is changed the line resistance is updated. However, the user still has the ability to adjust the value if more or less line resistance is desired. When a non-hydro-pneumatic carrier is used, these files are bypassed

Once all of the vehicle data for a particular subsystem is defined, a second m-file associated with that sub-system ('*_prop_g.m') is executed by pressing the continue button. Associated with each model are default values to give the user a general idea of vehicle parameters. The defaults are reinitialized when a subsystem model is changed to represent an entirely different subsystem. The primary function of the second file is to collect the relevant vehicle data. This program also creates the part of the state space representation that is associated with these two components of the sprung mass.

The road pre-processing loop is the most simple and only contains two files. This is illustrated in Figure 5.8. This loop implements the two different input routines as discussed in Chapter 4. In order to implement a data file, is must be located in the 'road_data_files' subdirectory. Associated with the data file must be a corresponding sample spacing that the user must specify in the input screen. In addition, a sinusoidal input velocity to the tires can be implemented. This input routine allows the user to specify a stop time, frequency, and amplitude of the sine wave. Included with the input routines is a time delay to compensate for axle spacing. The road input routine is also chosen through the main input screen. The model allows use of three different road input routines. Each road input routine allows the user to specify the simulation run-time, the forward vehicle speed, and the input start time. The road start time allows the user to see that the system is in equilibrium before a non-zero road input signal is given to the tires.

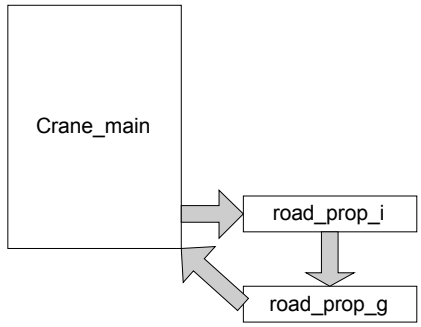


*Figure 5.8 The Road Pre-processing Loop*

In the boom subsystem loop, two different cases can occur as well as with the carrier and dolly loops. The pre-processing loop associated with the boom is given in Figure 5.9. For cases where a lattice boom model is used, the program 'Boom_sections_i.m' is bypassed. This file is used in the telescoping boom case to allow the user to specify the number of inner sections within the boom. The independent boom equations are not determined in the corresponding 'boom_prop_g.m' file because some of the equations that are used to couple the boom to the carrier and dolly subsystems require the distance from the boom connection point to the center of gravity of both the dolly and the carrier. The matrices required to couple the boom to the other subsystems are determined simultaneously with the independent modal representation of the

boom. Therefore, they are defined in the processing section to guarantee that both the carrier and dolly sub-models are defined. This strategy allows the user to change any subsystem component without having to completely redefine any of the other components in the system.

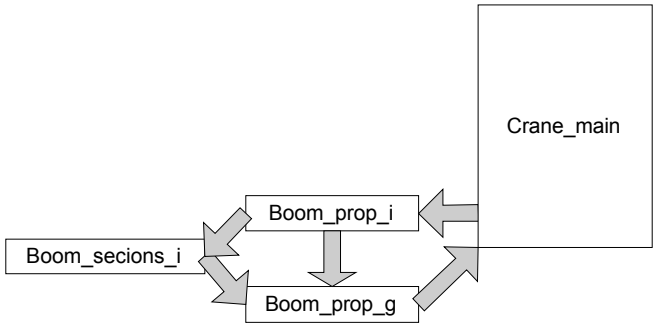


*Figure 5.9 The Boom Pre-processing Loop*

In the boom subsystem loop, two different cases can occur as well as with the carrier and dolly loops. The pre-processing loop associated with the boom is given in Figure 5.9. For cases where a lattice boom model is used, the program 'Boom_sections_i.m' is bypassed. This file is used in the telescoping boom case to allow the user to specify the number of inner sections within the boom. The independent boom equations are not determined in the corresponding 'boom_prop_g.m' file because some of the equations that are used to couple the boom to the carrier and dolly subsystems require the distance from the boom connection point to the center of gravity of both the dolly and the carrier. The matrices required to couple the boom to the other subsystems are determined simultaneously with the independent modal representation of the boom. Therefore, they are defined in the processing section to guarantee that both the carrier and dolly sub-models are defined. This strategy allows the user to change any subsystem component without having to completely redefine any of the other components in the system.

The program utilizes a finite element boom model that reduces the mathematical representation of the boom to within a predetermined frequency range. The program limits the boom vibration to 25Hz, which is reasonable for capturing the frequencies that are significant to the dynamic road loads. However, the user has the ability to treat the boom as a rigid body by limiting the vibration modes to the first two, by checking the box that is provided in the interface. These modes of vibration coincide with the rigid body motion of the boom. This feature aids in understanding the role boom vibration plays in crane dynamics.

Once the user has specified a complete set of system components, the pre-processing portion of the program is done. Embedded in the program are default values. These values are merely representative of the system. By selecting the continue button at this point in the main screen, the system can then be processed which will lead to the simulation results.

### 5.4.2 Processing

The processing section of the program is responsible for coupling the subsystem equations, determining the initial conditions, editing the SIMULINK template file, and integrating the system. The processing section of the program is illustrated in Figure 5.10.

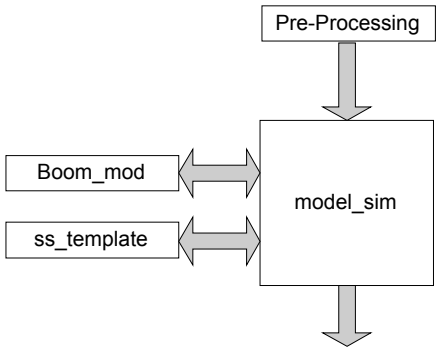


*Figure 5.10 Processing Section*

The processing section starts with the execution of the 'model_sim.m' file. The first step in this section is the execution of the 'Boom_mod' sub-program. The 'Boom_mod' file determines the independent set of equations for the boom in modal coordinates, the matrices required to couple the boom to the other subsystems, and returns the forces that the boom exerts on the connection points at equilibrium. These forces are used to determine the initial conditions of the system.

Once all of the subsystem matrices are determined, the program couples all of the matrices into a single matrix. This routine also sets all the additional parameters needed in the suspension sub-models. Once the system matrix is assembled, the initial conditions of the system, along with the delay between the sequential tires are determined.

Mathematically, the system is now ready to be integrated. However, the SIMULINK file needs to be edited for the configuration that is being modeled. The 'model_sim.m file is not only responsible for preparing the equations for integration, but it also prepares the SIMULINK file for numerical integration of the equations. This is done through the edited SIMULINK template file. The SIMULINK template file contains every configuration in a single file. The benefit of structuring the file in this manner is to allow every configuration available in the program to be available though a single file, thus reducing the total number of files required by the simulation package. The different boom models are taken into account through the formulation of the equations in the MATLAB script files. The SIMULINK template file is shown in Figure 5.11.

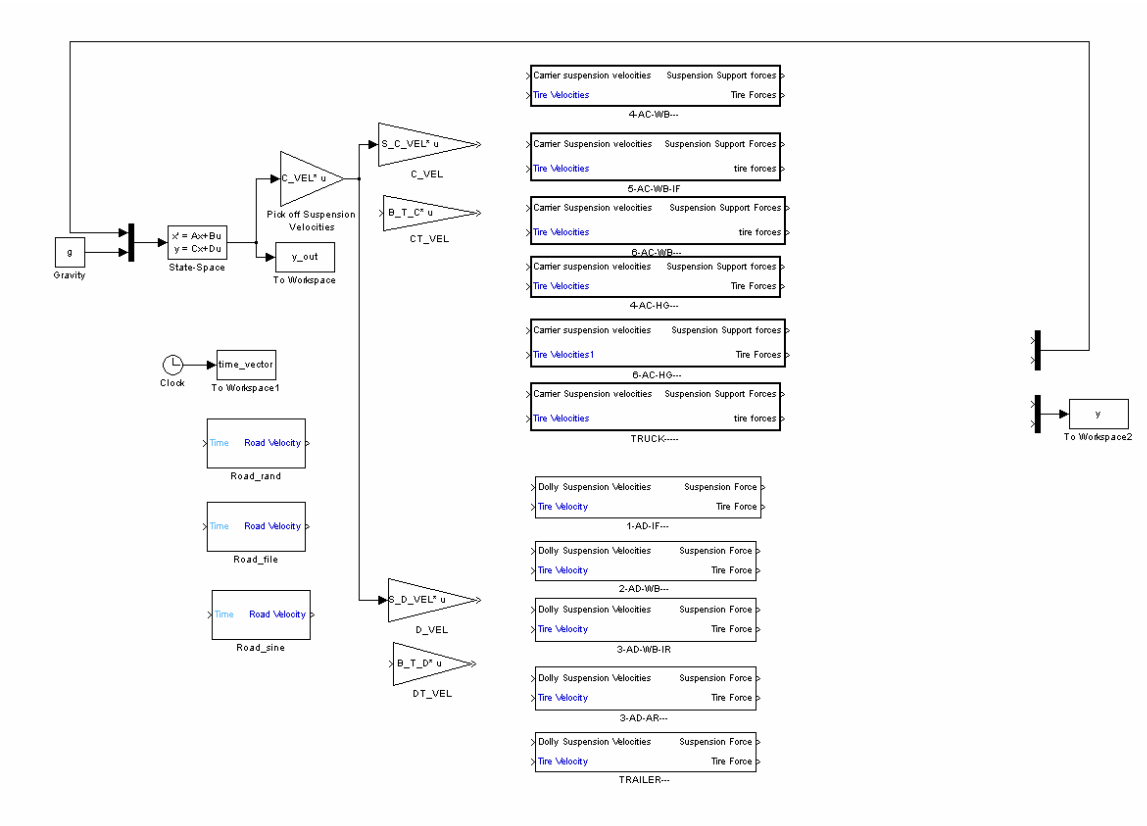


*Figure 5.11 SIMULINK Template File*

The top six subsystem blocks each contain a carrier suspension model. The last five subsystem blocks contain the dolly suspension models. In addition, additional subsystem blocks are used to represent the different road inputs that are available. Contained in the 'model_sim.m' file is a routine that loads the template SIMULINK file (Figure 5.11) and saves it as a temporary file. The temporary file can then be modified without the risk of damaging the original template. The template file is edited in the 'model_sim.m' file to model the selected configuration before the actual integration is performed. A graphical representation of this process is given in Figure 5.12

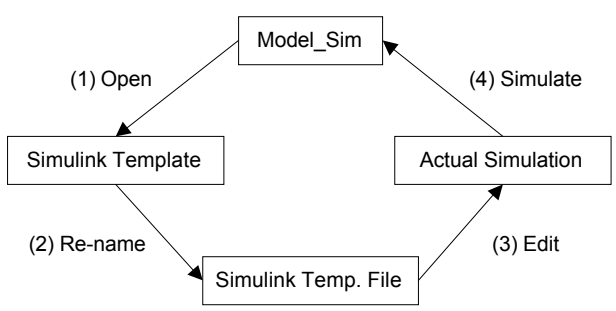


*Figure 5.12 SIMULINK Template File Editing Sequence*

The downfall to this process is that the template is edited during every execution of the program. However, the editing process is not very time consuming in its execution. Figure 5.13 shows the SIMULINK file that integrates the system. This process is done in the background and is not visible to the user. A typical edited SIMULINK file is given in Figure 5.13.

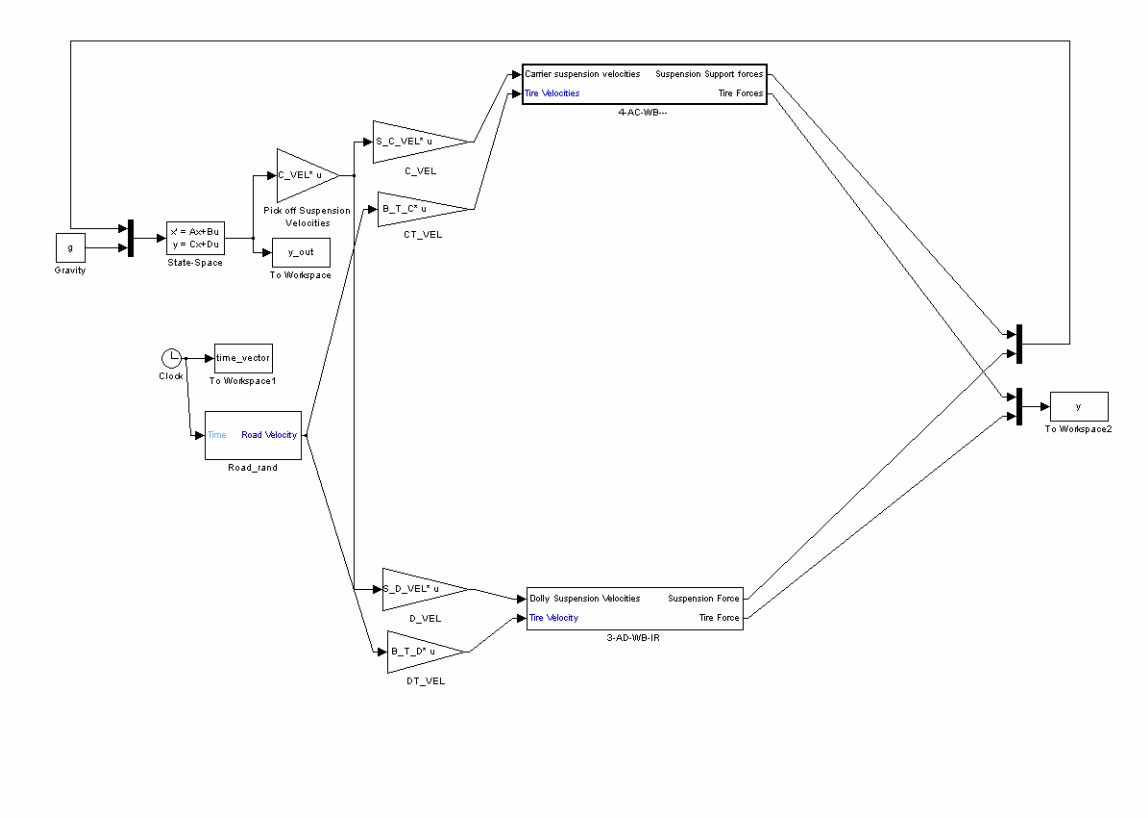


*Figure 5.13 Edited SIMULINK File*

After the file has been properly edited, the system is simulated. The state space block in SIMULINK is used to integrate the matrix representation of the system equations given by equations (2.37) and (2.39). The state space block also requires [C] and [D] matrices to define the output. In the simulation, [C] is the identity matrix, and [D] is a zero matrix. The output of the state space block is then multiplied by the respective matrix presented in equations (2.38) or (2.40) to convert the output to the velocity of the connection points. Once this multiplication is carried out, the velocity vector is then separated into carrier velocities and dolly velocities through a simple matrix multiplication. Similarly the velocity inputs coming in from the input model are separated into dolly tires and carrier tires. The split signals are then sent to their respective subsystems. The output suspension support forces are then assembled to form the input vector to the state space block.

Due to the stiff springs used to represent the pin connections, there are high frequencies in the system. In general, the wheel hop frequencies of a vehicle are on the order of 10-15 Hz and the bounce and heave frequencies are typically less. The stiff springs induce much higher frequencies. Since there is such a wide range of system frequencies, a stiff solver is used to

integrate the system. Once the integration is complete, the program returns to the 'model_sim.m" file and begins post processing the data.

### 5.4.3 Post-Processing

This portion of the program is responsible for presenting the output in a concise manner. The flow of this section of the program is given in Figure 5.14. In Figure 5.14 the 'model_sim' file is shown in grey. This is because this program is primarily part of the processing portion of the simulation. However, two of the available output routines require access to the edited SIMULINK file. The edited SIMULINK file is destroyed at the end of the 'model_sim' file. The frequency file and mode shape output routines are tied to the 'model_sim' file in order to have access to the modified SIMULINK file.

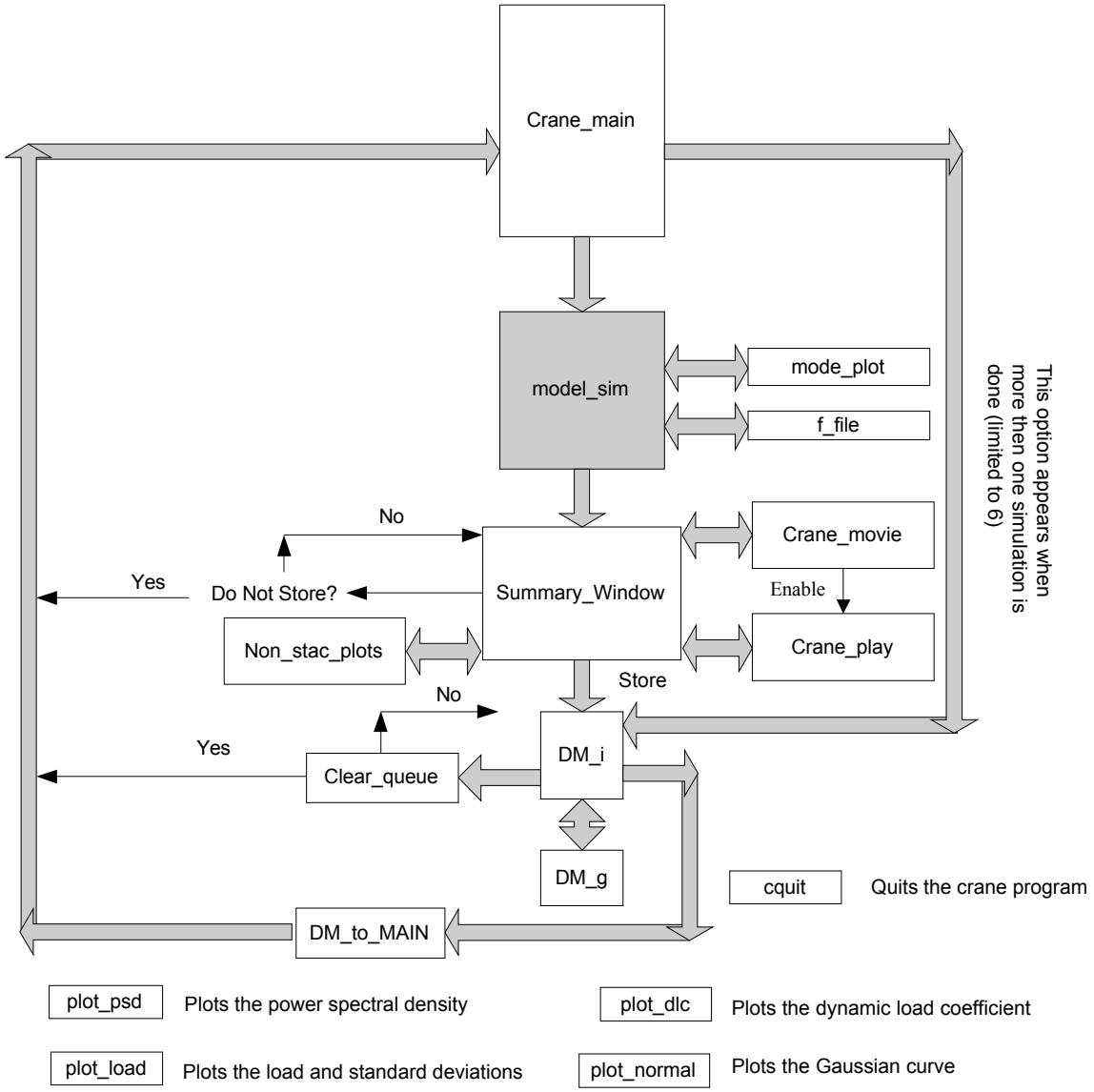


*Figure 5.14 Post-processing*

The two output routines tied directly to the model_sim file are the mode plotting and frequency file routines. Both of these routines provide information regarding the frequency response of the linearized system. The frequency file routine ('f_file.m') creates the file 'frequency_out.txt' and contains the mode shape values listed in column corresponding to the associated system frequencies. The mode plotting routine ('mode_plot.m') plots out the portion of the mode shape associated with the movement of the sprung portion of the system. Since the integration state variables of the boom are modal shape factors, the portion of the eigenvector associated with these must be converted back into displacement coordinates in order to give a more physical presentation of the associated displacement. This routine limits the plots to frequencies under 5Hz, which are sufficient to capture the modes associated with motion of the sprung mass.

The four files listed at the bottom of Figure 5.14 are plotting subroutines that are implemented by the program to generate various output plots. Recall that the routines were briefly dicussed in section 5.3. Additional help for these plotting routines can be obtained by exercising the MATLAB help feature.

Now that some of the basic output options have been mentioned, it is useful to present the basic flow of the program. Two main output windows are used to process the results. The summary window provides a useful environment to develop an understanding of a single simulation run. The data manager allows the user to look at simulation results from a comparative standpoint. The results presented here are based on a mean and standard deviation. Through the development of these two different output screens, an interactive method for presenting simulation results was developed.

A window in the program comes up after the simulation, which allows the user to specify the manner in which to present the data. This window allows the user to look at simulation results for a specific configuration. The summary window is shown in Figure 5.15.

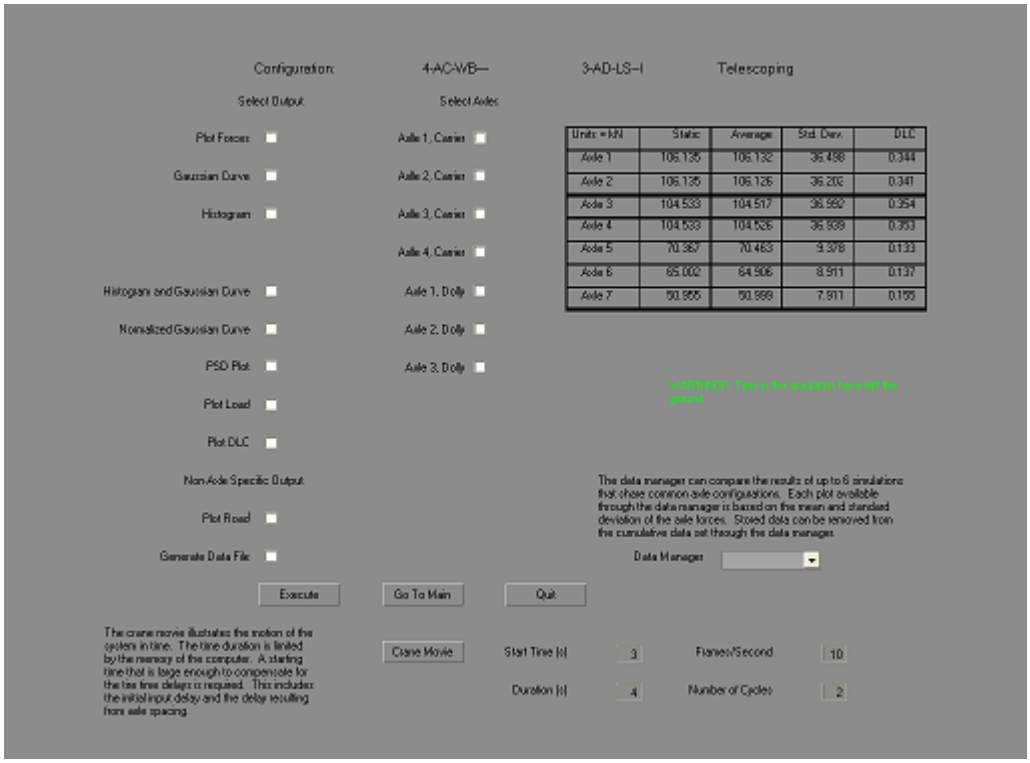


*Figure 5.15 Summary Window*

The window contains basic information about the simulation results, along with providing a place for the user to process the results. The model that was simulated is provided at the top of the window that is consistent with the nomenclature used when selecting the various submodels. A table is provided in the window that presents each axle listed with its static weight, average, standard deviation and dynamic load coefficient. The dynamic load co-efficient is given by

$$dlc_i = \frac{std_i}{mean_i} \; for \; i=1:\#_{tires}. \tag{5.1}$$

Since the dynamic loads should oscillate about the equilibrium value, the average should be reasonably close to the static weight. Each figure is given a generic legend and title, which can be adjusted through the MATLAB command window.

The user can specify the output by selecting the appropriate checkboxes and pressing execute to generate the plots. This window allows the user to look at specific axles for most of the input options that are available. A detailed look at the dynamic system response of a single simulation can be taken.

Through this window, the option to create a movie of the crane motion is available. The movie allows the user to look at the motion of the carrier, dolly, boom, and axles. This gives a very visual representation of the motion of the system. The file 'Crane_movie.m' creates the movie of the crane. The movie is generated by plotting the motion of the system at a specific time capturing the plot as a single frame in the movie. A sequence of figures is created to build a

movie of the system's motion. The predetermined time increment between frames is 0.025 seconds and provides a reasonable amount of smoothness to the movie. The user has the ability to specify the time span in the simulation to look at.

There are three possible problems with this feature. One is that the movie start time must be greater then the total delay to the last axle in the system. This includes the initial input start time and the delay due to axle spacing. The second possible problem is due to limitations on memory available to the program. Since the movie requires a significant amount of memory, the time duration over which the movie can be created is limited. The suggested maximum time span to create a movie is 10 seconds and should be sufficient to give the user a general idea of the vehicle motion. However, the program has the ability to generate a movie spanning any time length provided that computer has sufficient memory resources. The third possible problem with the movie option is if the user tries to generate a movie without having sufficient amount of simulation runtime for the specified movie start time and duration time. For example, the user sets the movie start time to 5 seconds, and the duration to 10 seconds, while only generating 10 seconds of simulation data. In order to minimize these errors, a series of checks are implemented within the program to correct for these problems.

Once the movie is created, the user is given the option to play the movie, which is performed by the file 'Crane_play.m' file. The user has two options for playing the movie. The user may specify the number of times to cycle through the movie continuously. In addition the user can specify the number of frames per second to play in the movie, which controls the speed of the movie. Included with the movie is a subplot of the axle forces at the particular instant in time associated with the frame. This allows the user to see how the suspension generates axle loads. A sample movie frame is provided in Figure 5.16.

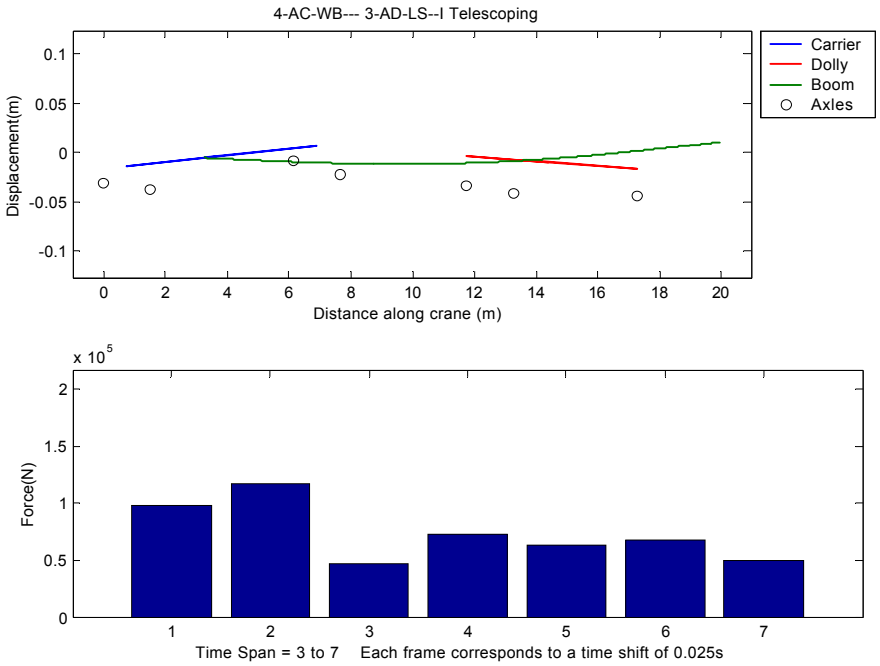


*Figure 5.16 Sample Movie Frame*

In order to compare common axle configurations, an additional output window was developed. In the program, this is referred to as the data manager. The data manager automatically determines if the axle configuration between two sequential runs are compatible for a reasonable comparison. This routine compares the results using the plot_DLC, plot_Load, and plot_Normal subroutines. These subroutines are based on a mean and standard deviation. This allows two single numbers to be used to compare the results between simulations. The justification of using these two numbers to represent the dynamic loads associated with a simulation is provided in Appendix D. The data manager is limited to six different simulations of stored data. One other nice feature of the data manager is that the user has the ability to not only look at specific axles but, only compare particular runs as a subset of the stored data. This allows the user to run various simulations and only compare the simulations of interest. The user is also allows to interactively set legend information and additional information in the plot titles. This allows the user to be more interactive with the program plotting. Another feature of the data manager allows the user to clear out slots in the stored data. This will allow the user to free up some of the available six slots for future additional simulation runs.

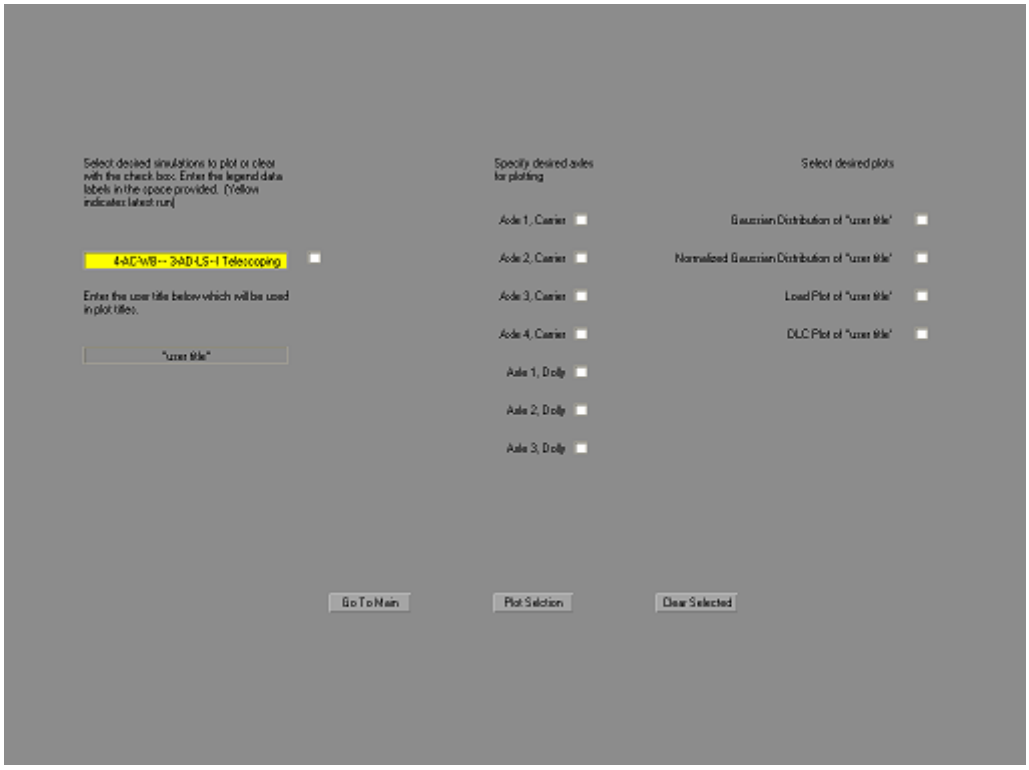


*Figure 5.17 Data Manager*

The development of a more complicated output routine also created a need to develop a more complicated program logic structure. From the summary window, the user has the ability to look at plots associated with a particular simulation. From this window the user can return to the main window by selecting the do not store option from the data manager pull down menu. This will ask the user if they are sure as a safety so that simulation data is not accidentally lost. The data manager can be accessed by selecting store from this menu. This action also places the mean and standard deviation of a single simulation in the storage location used by the data manager. The program then checks for compatibility of the axle configuration. If a mismatch occurs the user is given the option to either return to the summary window or proceed to the data manager and resets it. By resetting the data manager, all previous information regarding prior simulations is lost. From the data manager, the user can go to the main screen without looking at any plots. The user also has the ability to clear out slots in the stored data manager data from here. When the program is prompted to clear out data from the memory, a check is implemented which gives the user a chance to verify that action. In addition, the data manager can be accessed through the main screen once a single slot in the stored data is filled. In the event that all six of the available slots in the data manager are filled, the program automatically eliminates the option of running another simulation until a slot in the stored data is cleared.

The goal of this portion of the report is to give the user an understanding of the flow of the program. By understanding how the program flows together. Table 5.1 provides a list of the various output routines that are available through the two output screens. The 'X' in the table indicates a viable option from the program. The axle specific column indicates the output routines for which the user can look at only specified axles.

| Output Routine | Axle Specific | Summary Window | Data Manager |
|---|---|---|---|
| Crane_out.txt | | X | |
| Frequency_out.txt | NA | X | |
| Mode Shape Plot | NA | X | |
| Plot Road | X –front axle only | X | |
| Plot Forces | X | X | |
| Gaussian Curve | X | X | X |
| Histogram | X | X | |
| Histogram and Gaussian Curve | X | X | |
| Normalized Gaussian Curve | X | X | X |
| PSD Plot | X | X | |
| Plot Load | X | X | X |
| Plot DLC | X | X | X |
| Crane Movie | NA | X | |

*Table 5.1 Output Routines*

## 5.5 Summary

This chapter provided a general understanding of the program structure that was developed. MATLAB was used because of its subroutine library, which facilitates the development of complex programs. SIMULINK is used in conjunction with the MATLAB files to help speed up the simulation because it sorts the equations in a computationally efficient manner before numerically integrating the equations. After selecting the platform for the program, the structure was developed. This structure allows each sub-model to be changed independently without having to redefine each subsystem. Through this process, a user-friendly program was developed to allow the user to easily adjust the various system parameters. Using a single SIMULINK file for all the models greatly reduced the number of files required to model all the configurations available in the program. Table 5.1 provides a list of possible output from the final program. The axle specific indication means that the user has the ability to look at only particular axles in the simulation. The non-stacked feature represents that that plot is available for looking at a single simulation. The stacked feature indicates the plots that are designed to allow comparison between simulations with a common axle configuration. Now that the basic understanding of the simulation program flow has been developed, Chapter 7 will discuss simulation results in detail.

# CHAPTER 6
# QUARTER TRUCK MODEL

## 6.1 Overview

Four different suspension types are commonly found on mobile cranes. The leaf spring and walking beam suspensions are generally used on older cranes. Modern vehicles are commonly equipped with hydro-pneumatic and air ride suspension. It is commonly accepted that the suspensions found on these modern vehicles reduce the dynamic loads. This chapter will present comparison among the suspensions.

The focus of this chapter is to establish the filtering properties of the suspension systems through a quarter truck model. Filtering characteristics of the suspension are established through the frequency response of the dynamic tire force with respect to a road velocity input. Though the frequency response approach is an effective means of qualitative comparison among suspensions, a qualitative analysis of the crane will be preformed in Chapter 7.

## 6.2 Quarter Truck Formulation

This particular model is titled 'quarter truck' because it includes a tandem axle pair instead of a single axle typically found in quarter car models. Since some suspensions are designed for tandem axles, modeling both axles is imperative. The walking beam, for example, is designed around the tandem axle configuration requiring both axles to balance the load.

Including tandem axles introduces a new level of complexity when generating a frequency response. This study focuses on cranes traveling at highway speeds of 20 m/s (45 mph) with a tire spacing of 1.52 m (60 in). Dividing vehicle speed by tire spacing results in a delayed input to the second tire of 0.075 sec. The delayed input to the second tire is modeled with a Pade approximation thus maintaining a single input to the system. This allows the formulation of a transfer function and frequency response data.

Existing suspension sub models will be combined with single degree of freedom blocks to create quarter truck models. Figure 6.1 illustrates the quarter truck model with a general suspension sub-model block. The equation of motion for the general quarter truck block is

$$\ddot{x}_t = \frac{\Sigma F_s}{m_t}. \tag{6.1}$$

Integrating this expression results in the block velocity, the input used in the suspension sub-model.

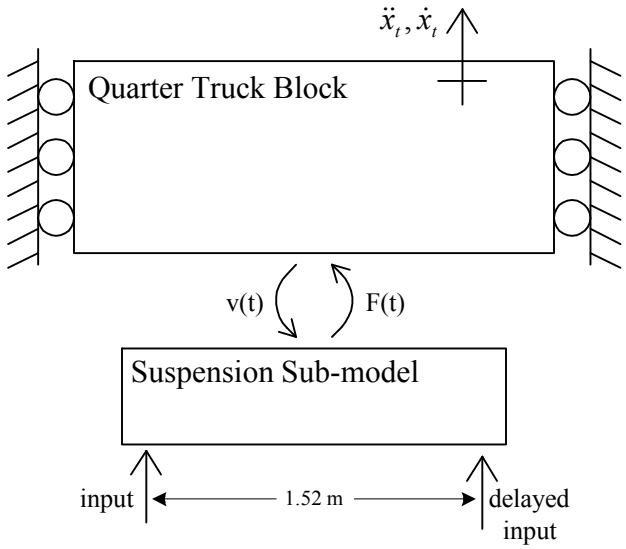


*Figure 6.1 Quarter Truck Connection Diagram*

### 6.2.1 Leaf Spring Quarter Truck

The leaf spring suspension is used on many dollies and the steering axles of some carriers. In brief recap, the leaf spring model accounts for suspension dynamics through a linear spring and damper. A rigid body connecting the suspension elements to the tire's spring and damper represents the unsprung mass. Figure 6.2 shows the quarter truck with leaf spring suspension. Derivation of the leaf spring model is provided in Section 3.4 and modeling parameters are in Appendix E.

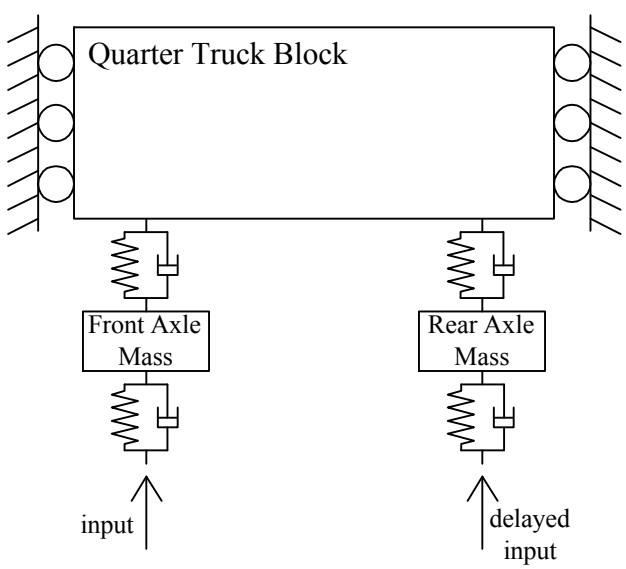


*Figure 6.2 Quarter Truck Leaf Spring Tandem*

### 6.2.2 Walking Beam Quarter Truck

The walking beam is a suspension traditionally found on carriers and some older dollies. In brief recap, a rigid body representing the beam connects the tandem axles and pin connects to the vehicle chassis. For modeling purposes, the walking beam is connected to the carrier through a stiff spring. Lastly, linear springs and dampers represent tires and connect between the walking beam to the road input. Figure 6.3 is the quarter truck model for a walking beam suspension system. Derivation of the walking beam model is provided in Section 3.5 and modeling parameters are in Appendix E.

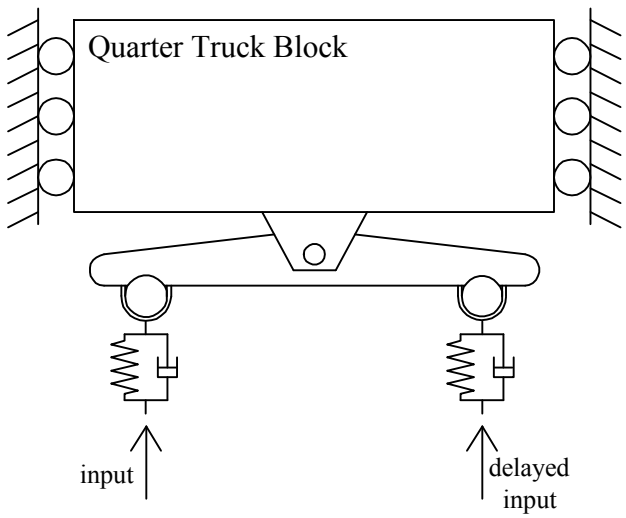


*Figure 6.3Quarter Truck Walking Beam Tandem*

### 6.2.3 Hydro-Pneumatic Quarter Truck

The hydro-pneumatic suspension is used on modern hydraulic. Sections 3.7 presents this sub model in detail. In brief recap, hydraulic cylinders are connected between the unsprung mass and the carrier chassis. Hydraulic lines tie the cylinders to a common accumulator. The tire's spring and damper elements connect the unsprung mass to the road input. Figure 6.4 presents the hydro-pneumatic quarter truck model and model parameters are found in Appendix E.

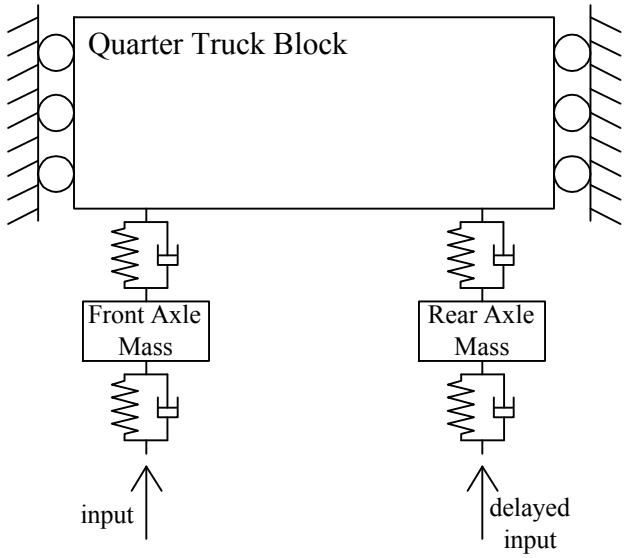


*Figure 6.4 Quarter Truck Hydro-pneumatic Tandem*

### 6.2.4 Air Ride Quarter Truck

Air ride suspension is used on most modern boom dollies. Section 3.8 presents this sub-model in detail. In brief recap, trailing arm suspension links are pin connected to the dolly chassis. The unsprung mass is connected in the middle of the swing arm and the air bag and damper is located at the far end. The air bag provides compliance between the end of the swing arm and the dolly chassis. The tire's spring and damper elements connect the unsprung mass to the road input. Figure 6.5 illustrates the quarter truck model with tandem air ride suspension. Model parameters are found in Appendix E.

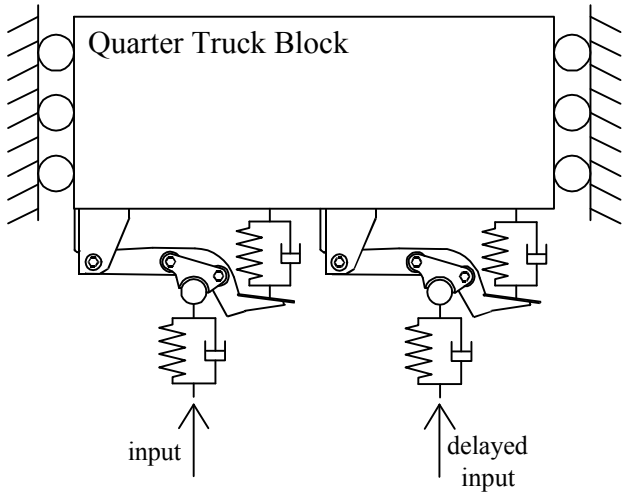


*Figure 6.5 Quarter Truck Air Ride Tandem*

## 6.3 Comparison of Quarter Truck Characteristics

The quarter truck models are used to generate the frequency response plot of the sprung mass with respect to road velocity input. Response plots are used for comparison of different suspensions and parameter variation within a single suspension model.

Several elements of crane suspension are subject to variation. Two types of tires are used: the wide based single and the conventional dual. Wide based singles are wide track heavy-duty tires designed to support substantial weight. The conventional dual is the standard tire found on most semi-trucks.

Both the sprung and unsprung masses are subject to significant variation. In this model sprung mass values are generalized into a heavy mass of 5890 kg (13,000 lbs), a medium mass of 4440 kg (9800 lbs) and a light mass of 2950 kg (6500 lbs). Unsprung masses are categorized by steering axles and drive axles. The drive axles are approximately twice the mass of steering axles. Details of the suspension parameters are presented in Appendix E.

In all quarter truck models, the standard configuration is considered to be a medium weight sprung mass of 4440 kg (9800 lbs), a steering configuration unsprung mass and wide based single tires. In variation cases presented in subsequent sections, the single element of interest in varied while the rest of the vehicle is modeled with the base case parameters.

### 6.3.1 General Quarter Truck Comparison

Quarter truck comparison begins by establishing general trends among the four suspension models. Figure 6.6 introduces the response characteristics of both the front and rear tire force gains on the road with respect to road velocity input. Every model has a characteristic sprung mass heave natural frequency that lies in the 1 to 3 Hz range and wheel hop frequency that ranges from 7 to 11 Hz.

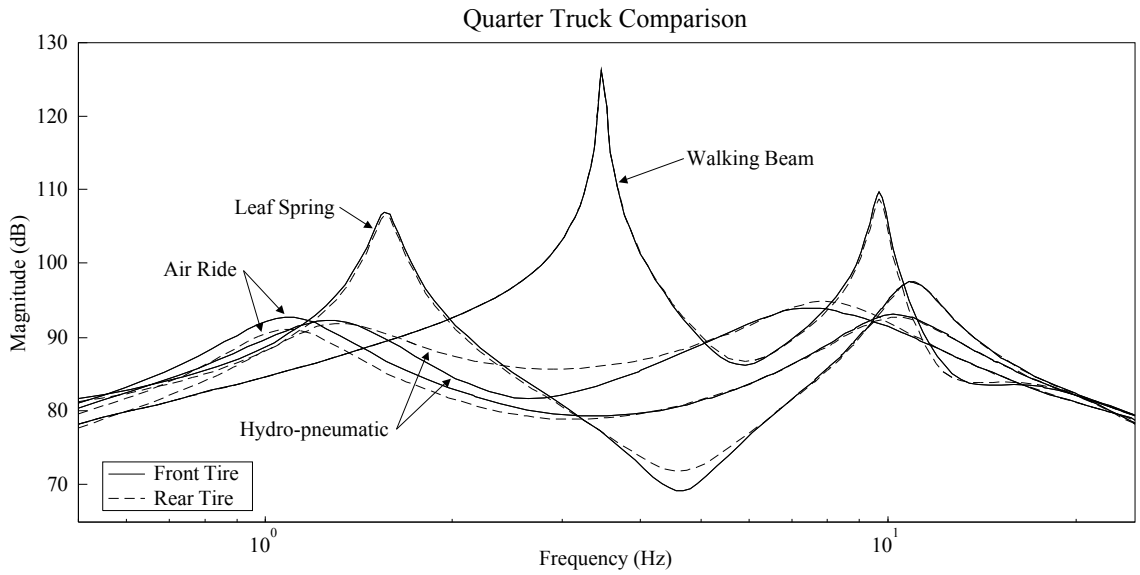


*Figure 6.6 Quarter Truck Comparison*

The walking beam suspension experience the highest dynamic loads. For both axles, bounce natural frequencies occur at 3.5 Hz and wheel hop natural frequencies occur at 9.5 Hz. For this suspension, wheel hop motion is characterized by fore and aft rocking of the walking beam suspension. When comparing this model relative to the others, it is important to remember that the tires are the only compliance elements in the system. As a result, the bounce mode is notably higher in frequency and magnitude than the other suspensions.

The leaf spring suspension dynamic force amplitudes are considerably lower than the walking beam. The bounce frequency occurs at 1.6 Hz and the wheel hop is at 10.7 Hz.

Hydro-pneumatic and air ride suspensions have the lowest dynamic forces. The hydro-pneumatic bounce natural frequency occurs at 1.3 Hz and wheel hop frequency at 7.5 Hz. The air ride suspension is similar with a bounce frequency at 1.1 Hz and wheel hop at 10.2 Hz. Notice the hydro-pneumatic has a slightly lower magnitude bounce frequency than the air ride but a marginally higher amplitude wheel hop. In both these suspensions, the front and rear axle responses have characteristic differences. To capture these differences, front and rear axle responses for these models will be included in subsequent plots.

### 6.3.2 Comparison of Wide Based Single and Conventional Dual Tires

Wide based single tires are used on the steering axles of lattice boom carriers and typically all axles of hydraulic carriers. The conventional dual tire is used on the drive axles of most lattice boom carriers and all dolly axles. The conventional dual is marginally stiffer than the wide based single and has twice the damping constant. Details of the tire parameters are provided in Appendix E.

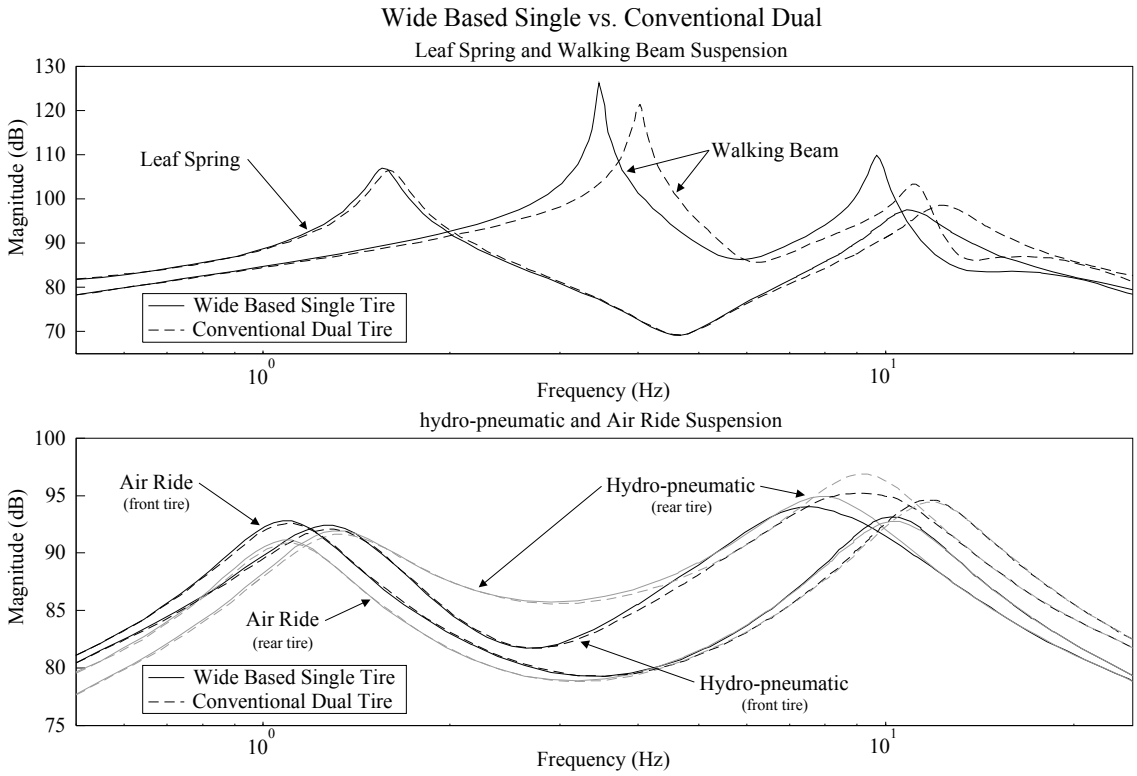


*Figure 6.7 Wide Based Single vs. Conventional Dual Tire*

Figure 6.7 presents the frequency responses of both the wide based single and conventional dual tires on all quarter truck models. From a qualitative point of view, changing from a wide based single tire to a conventional dual increases stiffness in the system and results in higher resonant frequencies which can be seen in the response plots. The walking beam exhibits the largest change in the bounce frequency since the tires provide the only compliance in the system. Both walking beam bounce and wheel hop frequencies exhibit a decrease in force magnitude due to the increased damping in the tires.

The other three suspensions show a slight increase in the bounce frequency when conventional dual tires are introduced. Wheel hop frequencies exhibit a marginal increase in natural frequency and force magnitude.

### 6.3.3 Comparison of Unsprung Masses

Traditional walking beam cranes are commonly equipped with massive drive axles at the rear of the carrier and significantly lighter steering axles in the front. The advent of hydro-pneumatic suspension introduced a variety of axle configurations ranging from all solid drive axles to Grove crane's Megatrak suspension. Megatrak is an independent drive axle suspension with an unsprung mass equivalent to a steering axle. Figure 6.8 establishes the frequency response.

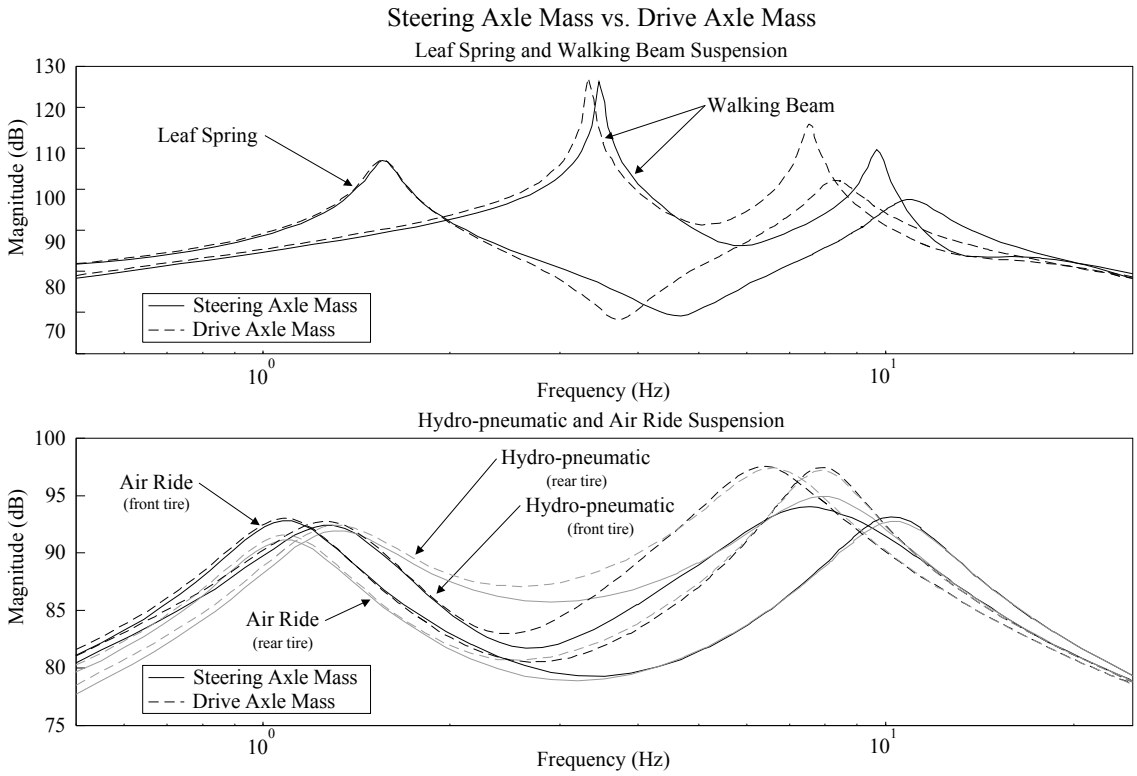


*Figure 6.8 Comparison of Unsprung Mass*

This case is closely related the tire stiffness variation. In this case the mass is approximately doubled causing a decrease in natural frequency. The bounce frequencies show negligible change while the wheel hop frequencies all exhibit a decrease in frequency with increased tire force magnitude. This is a noticeable change on the hydro-pneumatic and air ride suspensions, though it is important to bear in mind that the magnitude ranges are still significantly lower than the other two suspensions.

### 6.3.4 Comparison of Sprung Masses

Many different carrier and dolly configurations exist with widely varying sprung masses. This comparison considers the generalized heavy, medium and light sprung masses. Figure 6.9 presents the sprung mass variation.

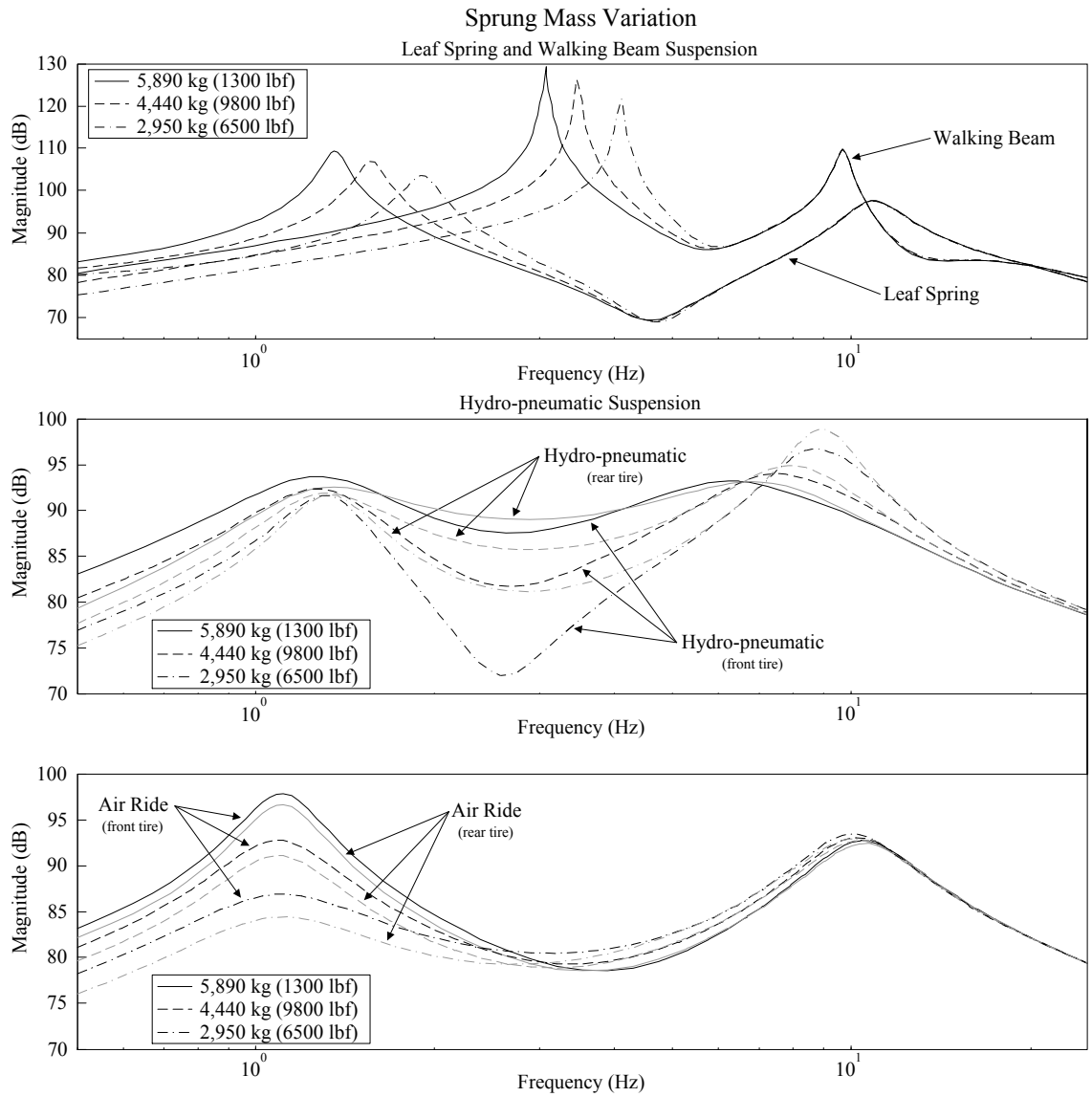


*Figure 6.9 Sprung Mass Variation*

Leaf spring and walking beam suspensions demonstrate a decrease in force magnitude and increase in frequency when the sprung mass is reduced from 5,890 kg (1300 lbf) to 2,950 kg (6500 lbf). The wheel hop frequencies in both cases remain unchanged

In hydro-pneumatic suspension systems, the hydraulic system is designed for a particular operating pressure. The suspension rams are sized to achieve the desired operating pressure. In this model, 10342 kPa (1500 psi) was the desired operating pressure and suspension rams were resized to accommodate varying sprung mass values. In Figure 6.9, hydro-pneumatic suspension exhibits a slight decrease in force amplitude at the bounce frequency with a negligible change in frequency. As a result in the change in piston area, the wheel hop mode increases both frequency and force magnitude when the sprung mass is decreased.

The air ride suspension results show the expected decrease in force magnitude at the bounce frequency when the sprung mass in decreased. A magnitude shift is noticeable up to the wheel hop frequency, but beyond that point, there is no change.

## 6.4 Hydro-pneumatic Suspension Comparison

The hydro-pneumatic suspension is the most modern configuration found on crane carriers. There are three variables that affect the performance of this suspension: hydraulic diameter, hydraulic line length and hydraulic system operating pressure. To better characterize their effects, each will be varied and the frequency response of tire force output related to the tire velocity input will be presented. The standard hydro-pneumatic configuration used in the quarter car models and in the crane simulation utlizes a 0.0127 m (1/2 in) diameter hydraulic line that is 1.22 m (48 in) long. The hydraulic suspension rams are sized for a system operating pressure of 10342 kPa (1500 psi).

### 6.4.1 Variation of Hydraulic Line Diameter

The first consideration is the hydraulic line diameter. Diameter variation ranges from 0.0063 m (1/4 in) to 0.022 m (7/8 in) by increments of 0.0032 m (1/8 in). Figure 6.10 presents the line diameter variation. The curved line indicates the direction of increasing line diameter.

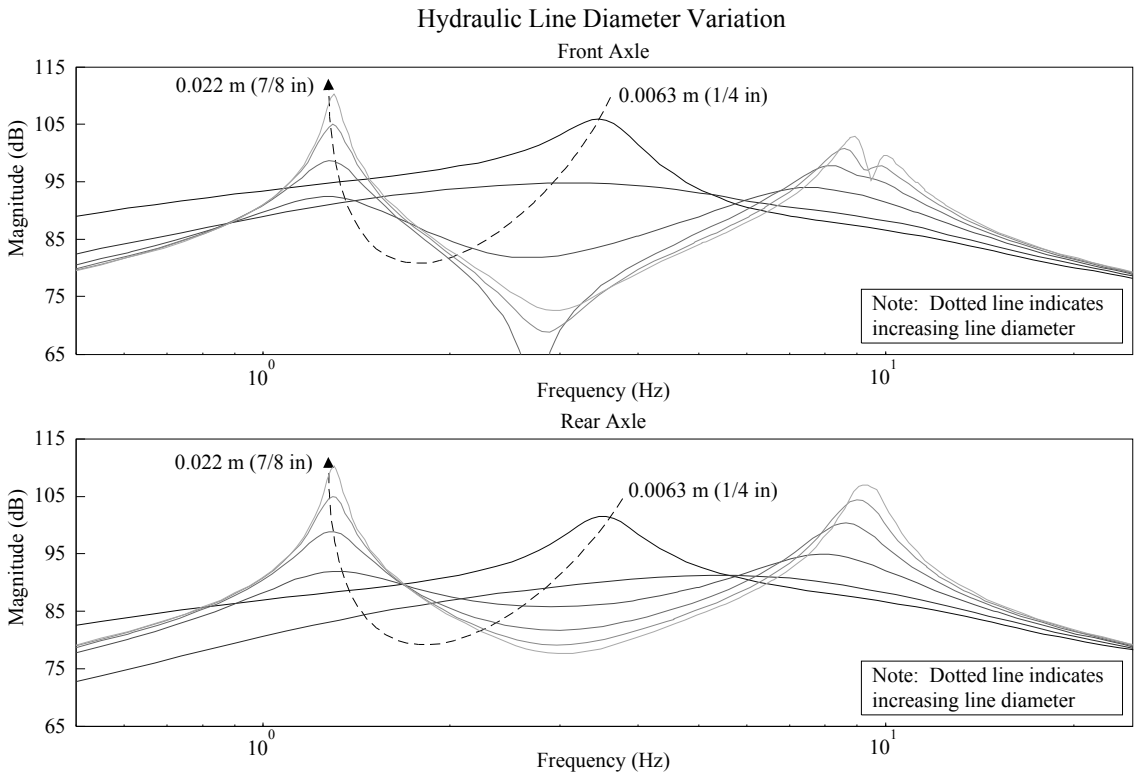


*Figure 6.10 Variation of Hydraulic Line Diameter*

Recall from Section 3.7 that linear fluid resistance in the hydraulic lines is considered. Fluid resistance has a fourth power relationship with hydraulic line diameter. When a change in

line diameter is made it greatly affects the hydraulic line resistance but for identical flow rates, the fluid inertia remains the same.

Line diameter has a significant affect on the hydro-pneumatic suspension system. The 0.0063 m (1/4 in) line creates an over damped system and varying the diameter to 0.022 m (7/8 in) negates the benefit of the hydraulic line resistance. Due to the delayed input to the tires, the front axle experiences significantly more amplitude reduction in the 1 to 3 Hz frequency range.

### 6.4.2 Variation of Hydraulic Line Length

The next consideration is the hydraulic line length. The length variation ranges from 0 m to 5 m (197 in) by 1 m (39 in) increments. Figure 6.11 presents the line diameter variation.

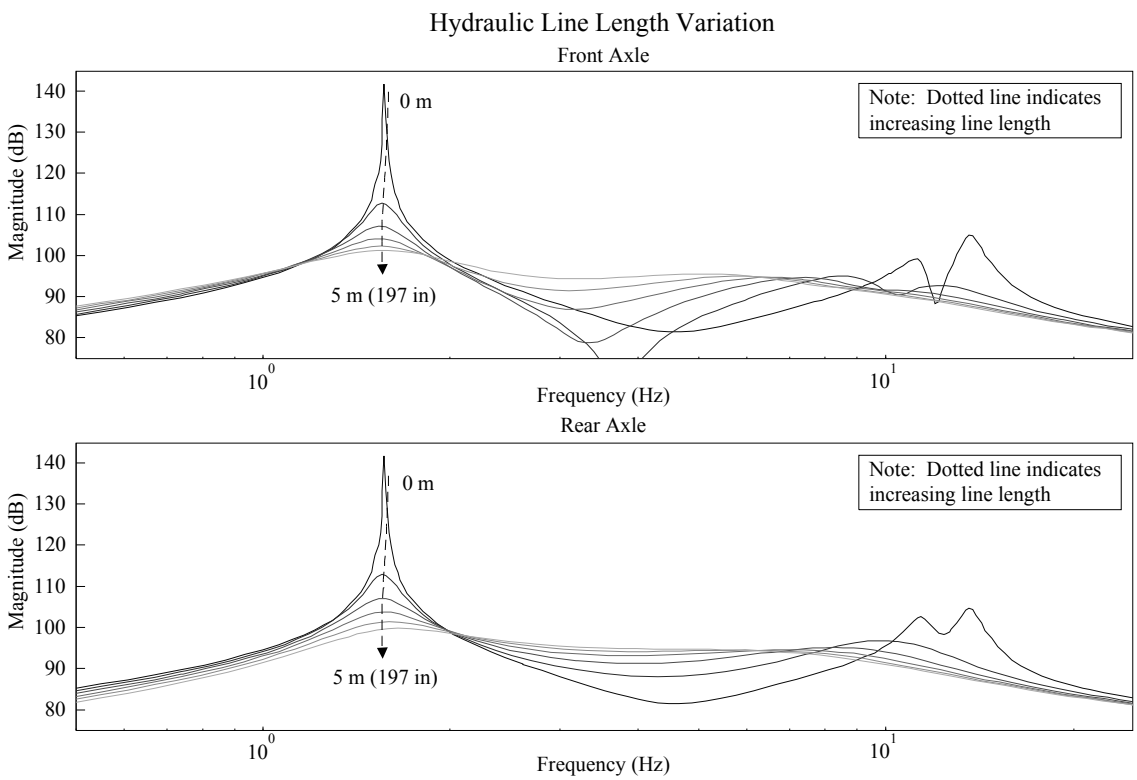


*Figure 6.11 Variation of Hydraulic Line Length*

Hydraulic line length is closely related to line diameter. When length is increased, both the line inertia and resistance are increased. It is important to realize that in this case the change in resistance is linearly related to the line length.

The effect of line length is very significant. If the accumulator is connected directly to the hydraulic ram, all benefits of fluid inertia and resistance are lost and force amplitude at the bounce frequency is similar to the walking beam model. Increasing line length reduces the force amplitude at the bounce frequency and slightly increases the magnitude at the wheel hop. Alternatively, hydraulic lines that are too long introduce excessive inertia and damping moving the system into an over damped state.

### 6.4.3 Variation of Hydraulic System Operating Pressure

The final consideration is the hydraulic system operating pressure. Recall that the operating pressure is determined by the size of hydraulic rams supporting the sprung mass. A larger ram has increased area supporting the sprung mass and consequently a lowered operating pressure. The operating pressure is varied from 1.38 x $10^6$ Pa (2000 psi) to 5.17 x $10^6$ Pa (750 psi) by 1.72 x $10^6$ Pa (250 psi) increments. Figure 6.12 presents the hydraulic operating pressure variation.

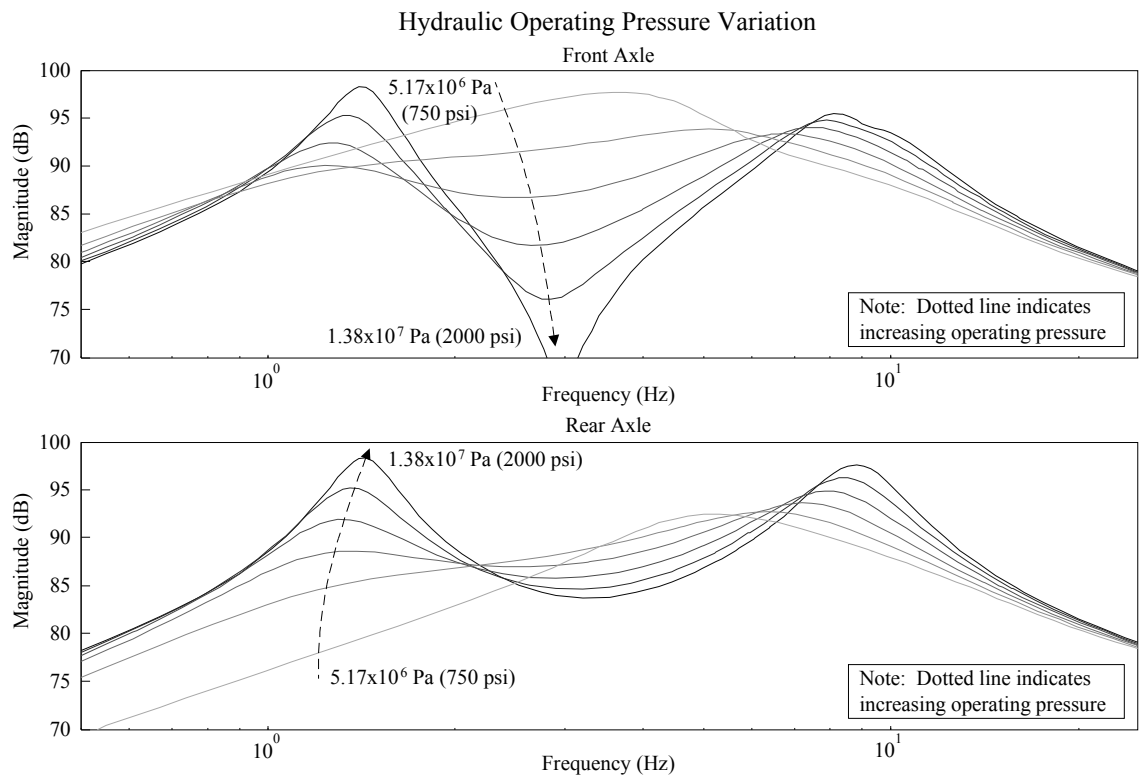


*Figure 6.12 Variation of Hydraulic System Operating Pressure*

The hydraulic system operating pressure has a notable effect on the dynamic tire forces. The highest amplitude is experienced by the 1.38 x $10^6$ Pa (2000 psi) system. Though the relative change in magnitude is not as significant as changing hydraulic line properties, reducing the operating pressure decreases the force magnitude. If the operating pressure is excessively low, a single resonant peak is observed in the 2 to 6 Hz range.

## 6.5 Summary

This chapter investigated the dynamics of the four suspensions commonly found on cranes. A tandem axle quarter truck model was used to simplify the dynamics to focus on the filtering properties of the suspension. From a linearized quarter truck model, frequency response plots of the tire force magnitude on the road were generated.

Walking beam suspension, commonly used on traditional carriers, produce the highest dynamic road loads at bounce and wheel hop frequencies. The high loads are expected when one considers that the tire provide the only source of compliance in the system. As a result, the suspension is fairly sensitive to tire stiffness and the sprung mass.

Leaf spring suspension produces reduced dynamic loads while the hydro-pneumatic and air ride suspensions produced the lowest loads compared to the walking beam model. The leaf spring and air ride are fairly insensitive to tire stiffness and mass variation. While the hydro-pneumatic suspension does have significantly reduced dynamic loads, it is sensitive to hydraulic line properties. The hydraulic line adds fluid inertia and provides the damping that is critical for the optimal performance of the suspension.

(This page is intentionally left blank)

# CHAPTER 7
# SIMULATION OF MOBILE CRANES

## 7.1 Overview

Two types of mobile crane are currently transported on California highways: the lattice boom crane and the telescoping boom crane. These cranes have fundamentally different boom structures and result in notably different dynamic road load characteristics.

The lattice boom is light, fairly flexible and supports a massive load block at the boom tip. Lattice booms are pin connected at the rear of the carrier and the dolly is connected slightly ahead of the boom center of gravity. Due to the dolly connection point and the load block mass at the boom tip, an upward force is generated at the carrier pin connection. The configuration is created intentionally to meet California Transportation Department weight requirements by reducing the static weight on the carrier axles.

The telescoping boom is more massive than a lattice boom. Due to the additional mass, the telescoping boom vibration frequencies are much lower than an equivalent lattice boom. Telescoping booms are pin connected to the carrier near the carrier center of mass. The dolly supports the boom approximately 1/2 to 1/3 of the distance from the boom tip. The dolly supports a majority of the boom weight, but unlike the lattice boom (where weight is commonly lifted off of the carrier), the carrier supports a small portion of the static boom load.

Suspension type is the single largest factor affecting road loads. Lattice boom carriers are typically found with four-axle walking beam suspension. Telescoping boom carriers were traditionally designed with walking beam suspension while modern carriers are commonly equipped with hydro-pneumatic systems. These modern cranes are designed to lift higher capacity loads and as a result the carrier mass and the number of axles needed to support the mass has increased.

Chapter 6 focused on establishing the differences in crane suspensions through quarter truck models. These models were critical for establishing the behavior of the isolated suspension systems. In this chapter, the suspension is incorporated in an entire crane model to reveal the effects of the carrier, boom and dolly.

The system response will be presented here by looking at the system's frequency response and the time response of the dynamic axle loads. The frequency response of the system can be understood by looking at the mode shapes of the linearized system and the power spectral density plots of the time force histories. In order to gain a more physical understanding of the dynamic loads in terms of the magnitude of the forces that are dynamically generated, the time-force history can be represented by a mean and standard deviation (Illustrated in Appendix D). This presentation of the dynamic loads provides a very concise way to see the magnitude of the dynamic loads that are generated.

## 7.2 Dynamics of Traditional Lattice Boom Cranes

The American 8470, illustrated in Figure 7.1, is a crane commonly found on California's highways. This crane will serve as a representative lattice boom crane to establish the behavior of these vehicles.

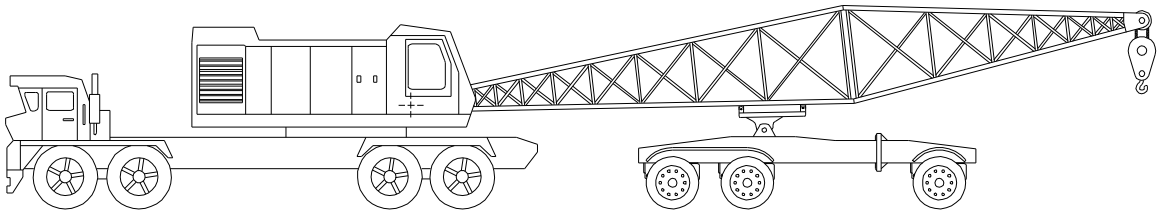

*Figure 7.1 Traditional Lattice Boom Crane (American 8470)*

Lattice boom cranes generally have a massive carrier, and a boom foot that connects near the rear tandem on the carrier. The dolly is intentionally positioned as close to the carrier as California transportation permit policy will allow to lift weight off of the carrier axles. The boom mass is approximately 3,200 kg (220 slugs) and the load block is assumed to weigh 2080 kg (142 slugs). Virtually all lattice boom cranes that travel with a boom support dolly are equipped with a walking beam suspension. Details of the American 8470 crane configuration are provided in E.1.

### 7.2.1 System Mode Shapes and Power Spectral Density

Analysis of the lattice boom crane begins with the presentation of the sprung mass bounce and pitch mode shapes in Figure 7.2. The first mode is predominately bounce motion of the boom and dolly. There is small movement at the circle representing the rear carrier tandem connection, but the front tandem connection experiences no motion. Modes two and three introduce more carrier excitation while maintaining considerable dolly and boom motion. It is important to realize that the compliance in the dolly leaf spring suspension allows for significantly more displacement than the non-compliant walking beam. Therefore, the dolly may appear to undergo considerable motion and introduce minimal force.

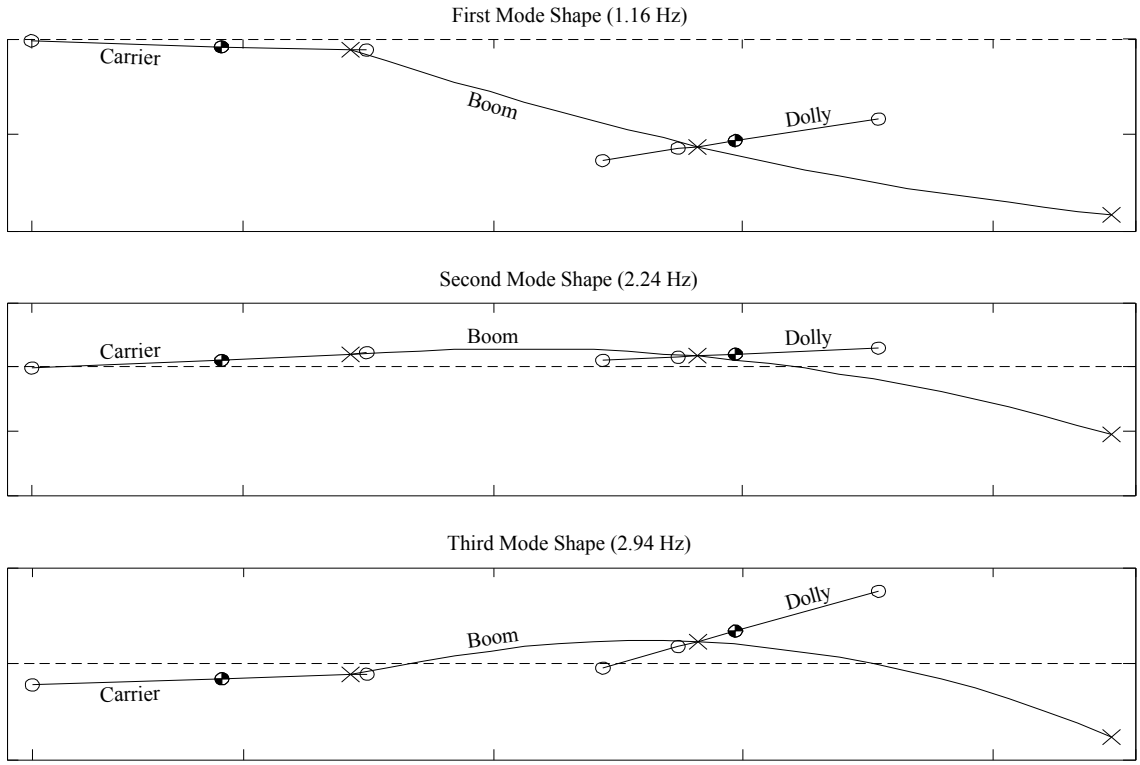


*Figure 7.2 Traditional Lattice Boom Crane ~ Mode Shapes*

With the sprung mass bounce and pitch modes established, Figure 7.3 introduces the power spectral density of each tire force. The three characteristic bounce frequencies can be seen in the low frequency ranges of the PSD plots. The first two subplots present modes 2 and 3 as the major contributors to the carrier tire forces while a small portion of these mode are manifested in the subsequent dolly axle subplots. Conversely, the first mode is predominantly seen in the dolly axles with slight power in the rear carrier tandem and none in the front tandem. This is evidence that the dynamic affect that the carrier and dolly have on each other is small.

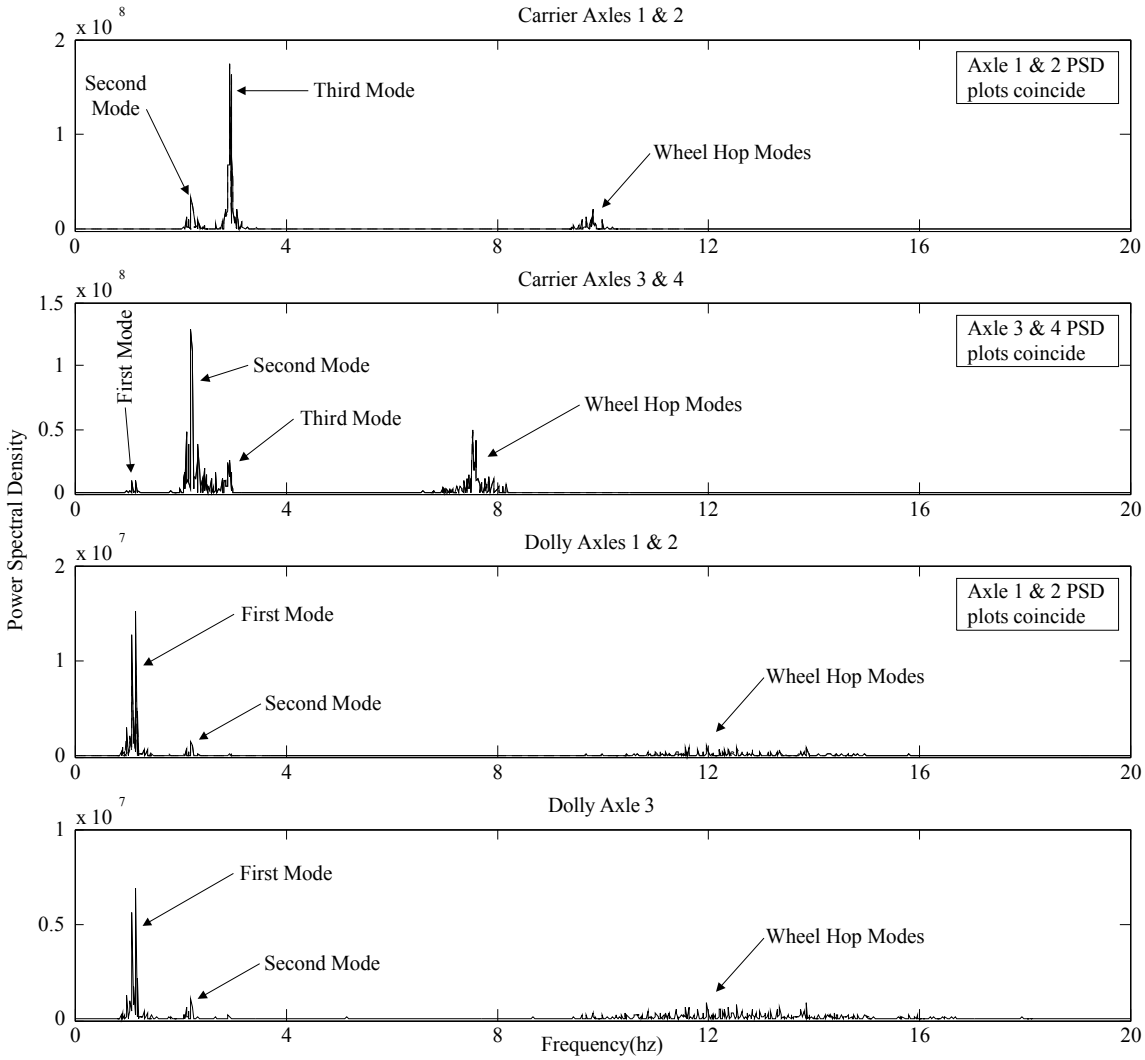


*Figure 7.3 Traditional Lattice Boom Crane ~ PSD*

| Power Percentage for Axle Groups | | | | | | | |
|---|---|---|---|---|---|---|---|
| | Axle 1 | Axle 2 | Axle 3 | Axle 4 | Axle 5 | Axle 6 | Axle 7 |
| Single Axle | 21% | 21% | 26% | 25% | 3% | 2% | 2% |
| Tandem Pairs | 42% | | 51% | | 5% | | |
| Carrier and Dolly | 93% | | | | 7% | | |
| Power Percentage for Each Axle | | | | | | | |
| | Axle 1 | Axle 2 | Axle 3 | Axle 4 | Axle 5 | Axle 6 | Axle 7 |
| 0 to 5 Hz | 79 % | 82% | 63% | 64% | 44% | 41% | 31% |
| Above 5 Hz | 21% | 18% | 37% | 36% | 56% | 59% | 69% |

*Table 7.1 Traditional Lattice Boom Crane ~ Power Percentage*

The area under the power spectral density plots is integrated to determine the percentage of power input at each frequency range. Table 7.1 presents the percentage of power contributed by each axle in the upper section. The lower section of the table introduces, for each axle, the percentage of power input by sprung mass bounce frequencies (0 to 5 Hz) and the percentage of power input by wheel hop frequencies (above 5 Hz).

The single most important result to draw from this table is the carrier contributes 93% of the power to the roadway. The carrier axles do support considerably more mass than the dolly, but as the quarter truck model introduced, the walking beam suspension has much higher dynamic forces than the dolly leaf spring suspension. Breaking down the results further reveals the front tandem introduces 42% of the total power while the back contributes 51%. Looking at the power in terms of the bounce frequency percentage, the front tandem averages approximately 81% of its power in the bounce frequency range while the rear carrier tandem introduces 64% in the bounce range. To further this observation, the quarter truck model of Chapter 6 established that the walking beam suspension has a significantly higher force magnitude gain in the bounce frequency range. The quarter truck also established that an increased unsprung mass reduces the wheel hop frequency. This difference can be seen in the PSD of the front carrier steering tandem and in the massive rear drive axles.

The dolly introduces only 7% of the total power to the roadway, 5% through the tandem and 2% at the rear axle. Dividing the power of each axle into bounce and wheel hop frequency ranges, the dolly tandem averages 43% in the bounce frequency range while the rear dolly axle introduces 31%.

### 7.2.2 Configuration Case Variation

A significant concern with the lattice boom crane is the effect of the boom on the dynamic axle loads. Figure 7.4 introduces the axle loads for a carrier and dolly with no boom, a rigid boom on a leaf spring dolly, a flexible boom on a leaf spring dolly and a flexible boom on a walking beam dolly. Figure 7.5 presents the boom connection forces for the rigid and flexible boom cases.

The first case is a crane and dolly with no boom. It is important to notice that the carrier axles experience the highest dynamic load. In this configuration, the carrier is allowed to move freely. In the second case, a rigid boom has been added to the carrier and the leaf spring dolly. Static loads on the rear carrier axles are reduced because the boom induces an upward static force on the carrier. Dynamic loads are lower because the carrier must now rotate and/or displace the boom mass in addition to its own mass. Recall from the quarter truck that the leaf spring suspension generates considerably lower dynamic forces than the walking beam. Excitation of the boom induced by the carrier is calmed by the smoother riding dolly leaf spring suspension. This reduction in boom motion affects the carrier through the boom connection and reduces the sprung mass motion and dynamic forces.

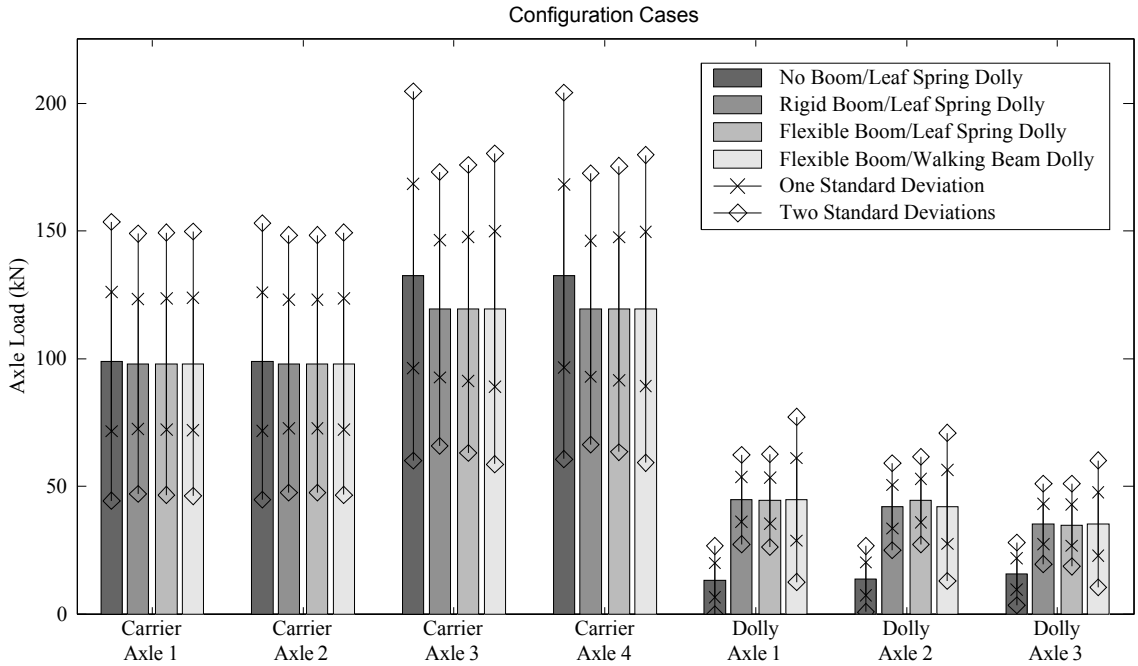


*Figure 7.4 Traditional Lattice Boom Crane ~ Axle Loads*

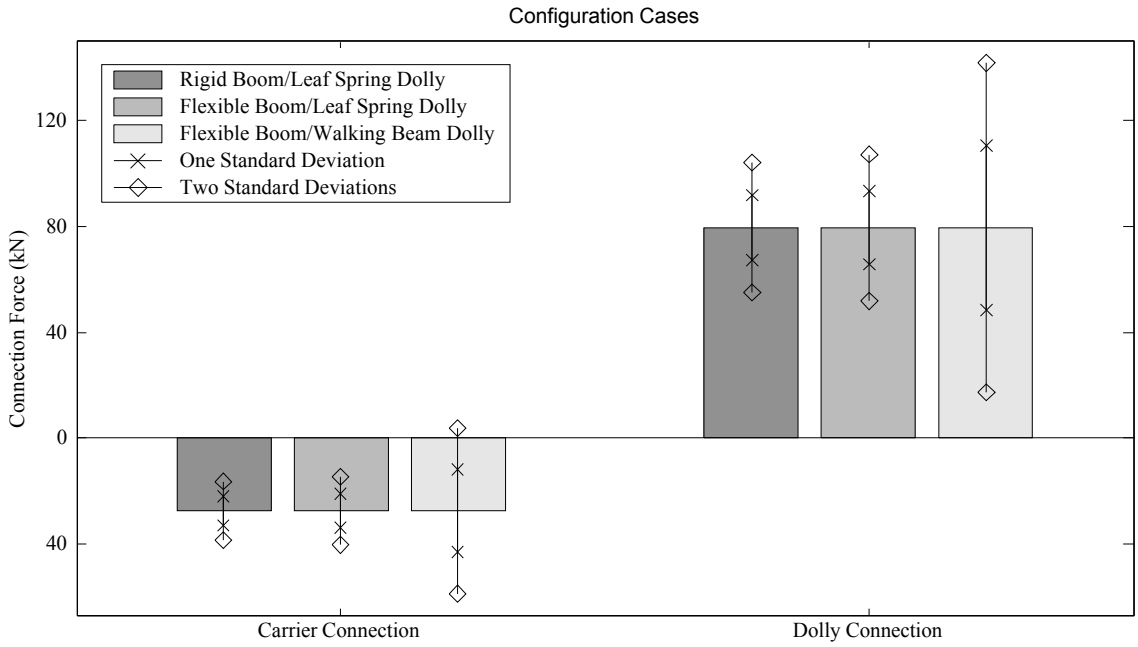


*Figure 7.5 Traditional Lattice Boom Crane ~ Boom Connection Forces*

Adding boom vibration in the third case produces minimal increases in both the boom connection forces and overall dynamic road loads. The boom itself has a free vibration

frequency of 9.8 Hz, a fairly high frequency compared to the sprung mass bounce frequencies. Boom vibration is an important effect and will be more thoroughly addressed in the next section.

In the final case, the dolly suspension is modeled as a walking beam tandem pair with a leaf spring rear. The dolly tandem is now contributing the high dynamic forces introduced in the quarter truck walking beam model. In Figure 7.5, the change is seen in both the carrier and dolly connection forces. The increased dynamic motion manifests itself in increased overall loads on the rear carrier and dolly axles.

7.2.2.1 Boom Stiffness Variation

The crane boom stiffness is a significant contributor in the dynamic behavior of the crane. To capture the affects of boom stiffness, Figure 7.6 characterizes the first standard deviation of the dynamic axle load for the representative lattice boom crane. Scaling the beam element section inertia terms change the free vibration frequency of the lattice boom. Boom inertia was adjusted to vary the fundamental vibration frequency from 4 to 14 Hz where the 4 Hz boom is the softest reasonable boom and above 14 Hz approach the rigid boom case.

The upper plot in Figure 7.6 captures the affects of the boom on the carrier. Front carrier axles are virtually unchanged while the rear axle loads steadily increase as the boom is varied from rigid to soft. The dolly axles, shown in the lower subfigure reveal a region between 6 Hz and 10 Hz where the combined boom and dolly resonate in the boom's fundamental vibration mode.

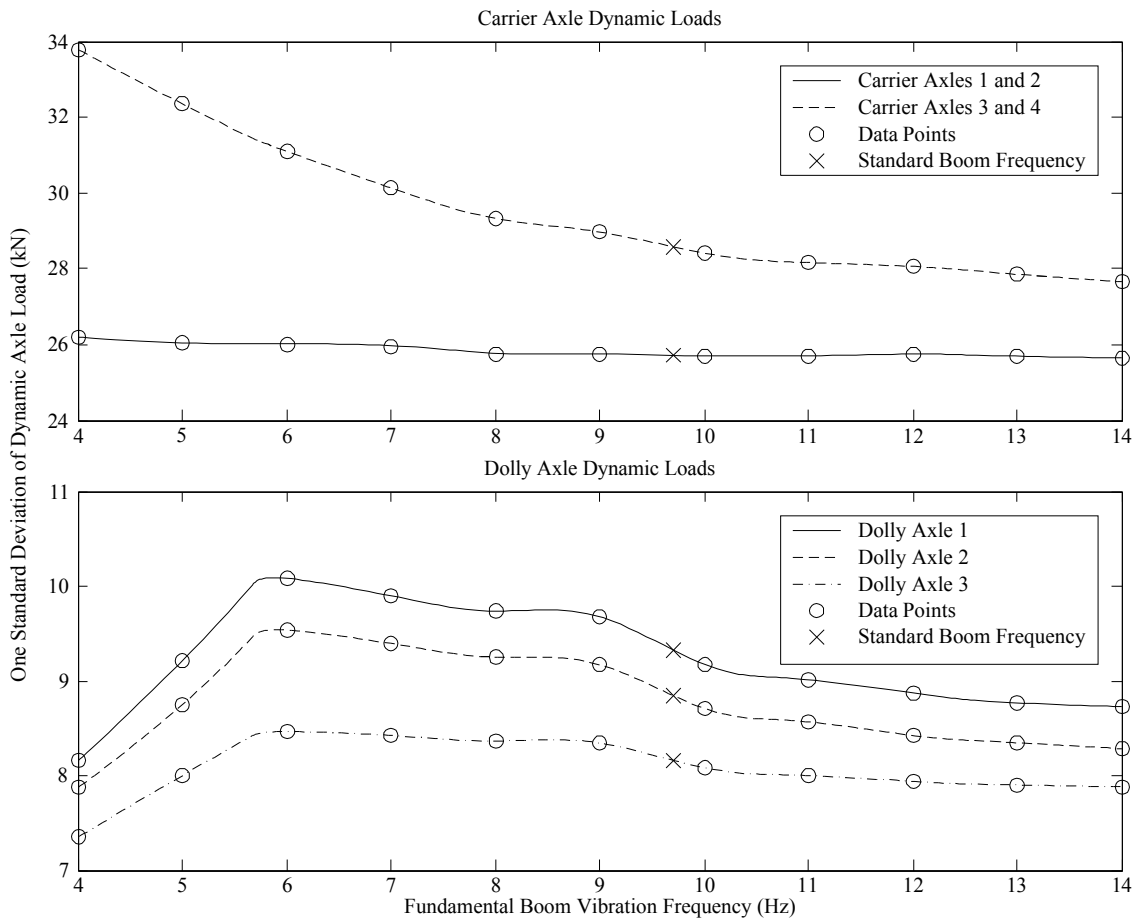


*Figure 7.6 Traditional Lattice Boom Crane ~ Boom Vibration Variation*

### 7.2.3 Load Block Mass Variation

Lattice booms are commonly transported with massive load blocks supported at the boom tip. This is done to lift weight off of the overloaded carrier axles. The dynamic affect of this added weight is an ongoing concern. Figure 7.7 establishes the affects of the load block on the road loads. To characterize the dynamics, the load block is varied from zero mass to 5200 kg (356 slugs).

The rear carrier axles with no load block experience the highest dynamic load. Conversely, this configuration presents the lowest load on the dolly axles because they only have the boom mass to support. As the load block mass is increased, the overall load on the rear carrier axles decreases while an increase can be seen on the dolly axles. A slight increase in rear carrier axle dynamic load can be seen, but the reduction in static load significantly outweighs the dynamic effect. As a result, a heavy load block does not significantly increase the dynamic load but can significantly reduce the static load of the carrier axles.

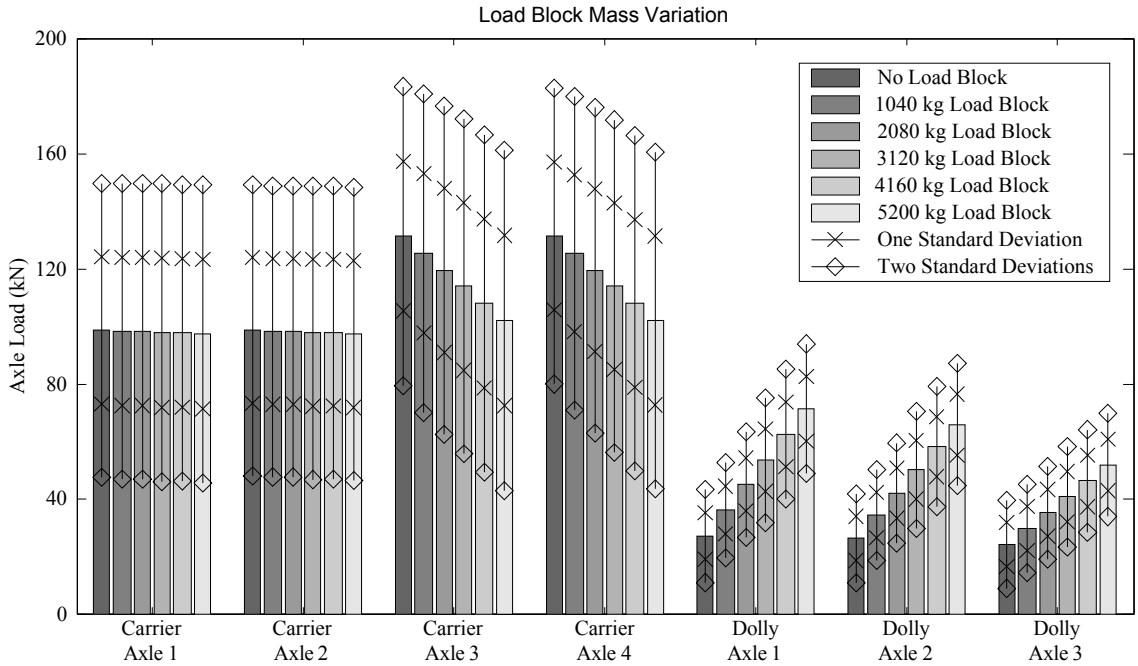


*Figure 7.7 Traditional Lattice Boom Crane ~ Load Block Variation*

### 7.2.4 Dolly Connection Variation

The dolly on a lattice boom crane is typically positioned as close to the carrier as California transportation permit policy will allow. This is done to lift weight off of the overloaded carrier axles. Much like the load block, the concern is exciting excessive dynamic motion with the cantilevered boom mass. Figure 7.8 establishes the affects of the dolly and boom connection location. To characterize the dynamics, the dolly connection location is varied from just behind the carrier at 1/4 of the boom span to the end of the boom in a simply supported configuration.

When the dolly is connected at 1/4 of the boom span, the overall load on the carrier is at a minimum and the load in the dolly is maximized. As the dolly connection is moved back, the carrier axle load is increased while overall dolly load decreases. The crane does not exhibit excessive dynamic load when the dolly is moved close to the carrier. The reduction in static weight is the key factor that makes this a desirable configuration.

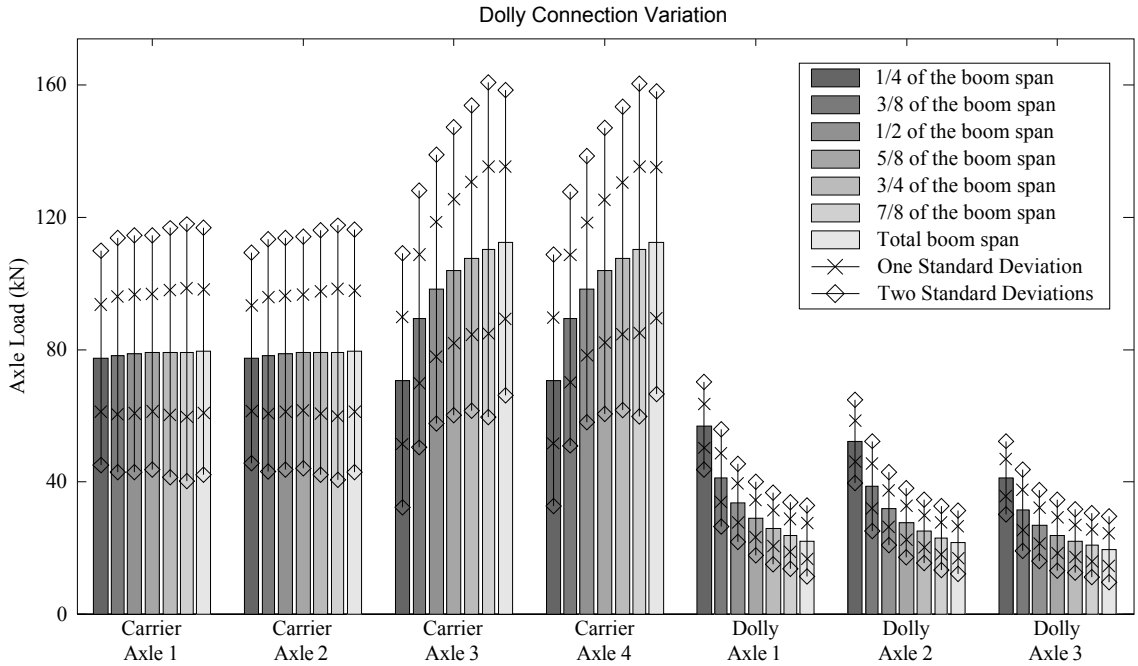


*Figure 7.8 Traditional Lattice Boom Crane ~ Dolly Connection Variation*

## 7.3 Dynamics of Traditional Telescoping Boom Cranes

The Grove TM9120, illustrated in Figure 7.9, is an older model telescoping boom crane still commonly found on California's highways. This crane has walking beam suspension on the carrier. A dolly with leaf spring suspension will be used as a representative case to establish the vehicles motion.

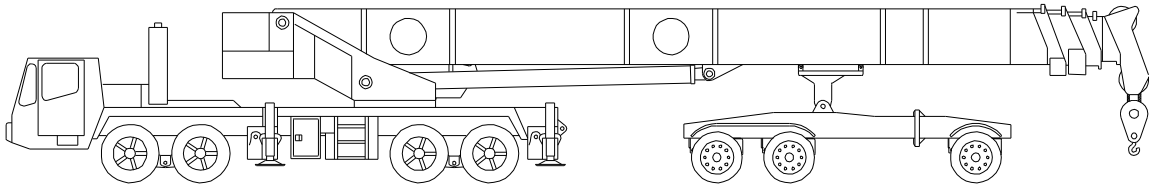

*Figure 7.9 Traditional Telescoping Boom Crane (Grove TM9120)*

Telescoping boom cranes generally support a massive boom. The boom foot typically connects near the carrier's center of gravity. The dolly supports the massive boom just behind the boom's center of gravity. For the Grove TM9120, the boom is estimated to weigh 13,000 kg (891 slugs) supporting a 2080 kg (143 slugs) load block. Configuration details of the representative telescoping boom crane are provided in E.1.

### 7.3.1 System Mode Shapes and Power Spectral Density

Analysis of the telescoping boom crane begins with the presentation of the sprung mass bounce and pitch mode shapes in Figure 7.10. The first mode is predominately bounce motion of

the boom and dolly. Modes two and three introduce more carrier excitation while maintaining considerable dolly and boom motion. As in the lattice boom crane, it is important to realize that the compliance in the dolly leaf spring suspension allows for significantly more displacement than the non-compliant walking beam. The dolly may appear to undergo considerable motion and introduce minimal force.

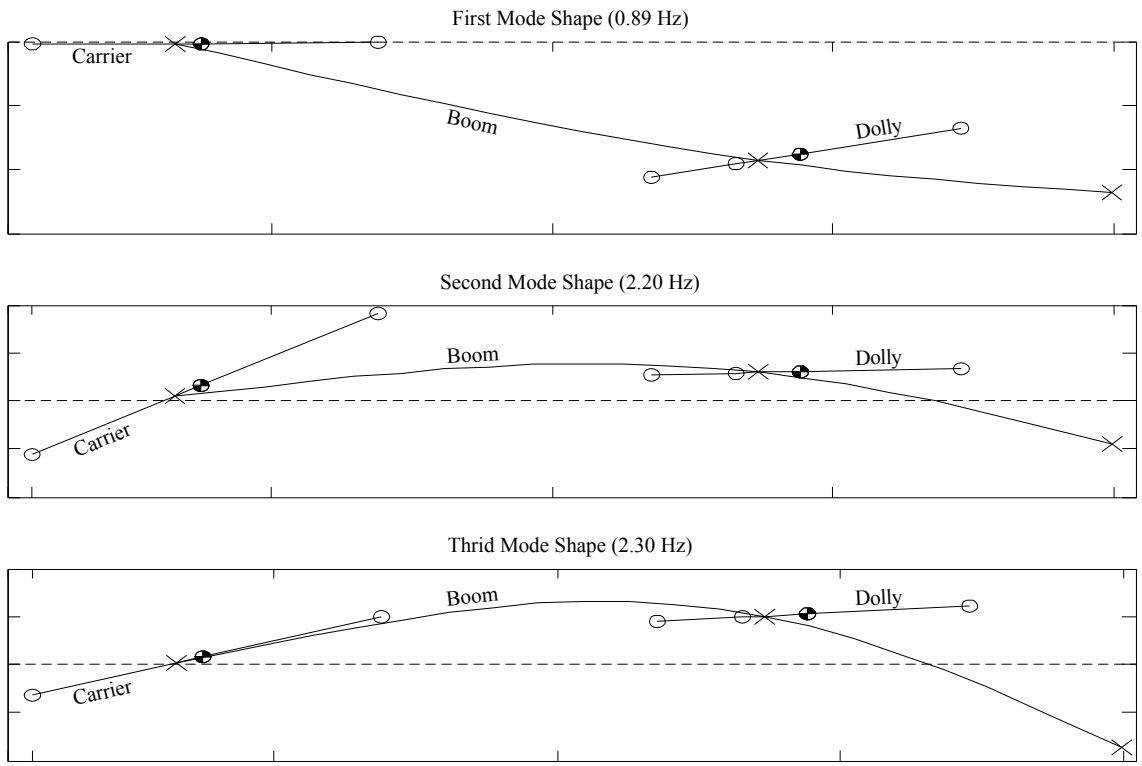


*Figure 7.10 Traditional Telescoping Boom Crane ~ Mode Shapes*

With the sprung mass bounce and pitch modes established, Figure 7.11 introduces the power spectral density of each tire force. Three characteristic bounce frequencies can be seen in the low frequency ranges of these PSD plots. The first two subplots characterize the carrier axles and establish modes 2 and 3 as the major contributors to the carrier tire forces. The first mode is only seen in the dolly axle subplots.

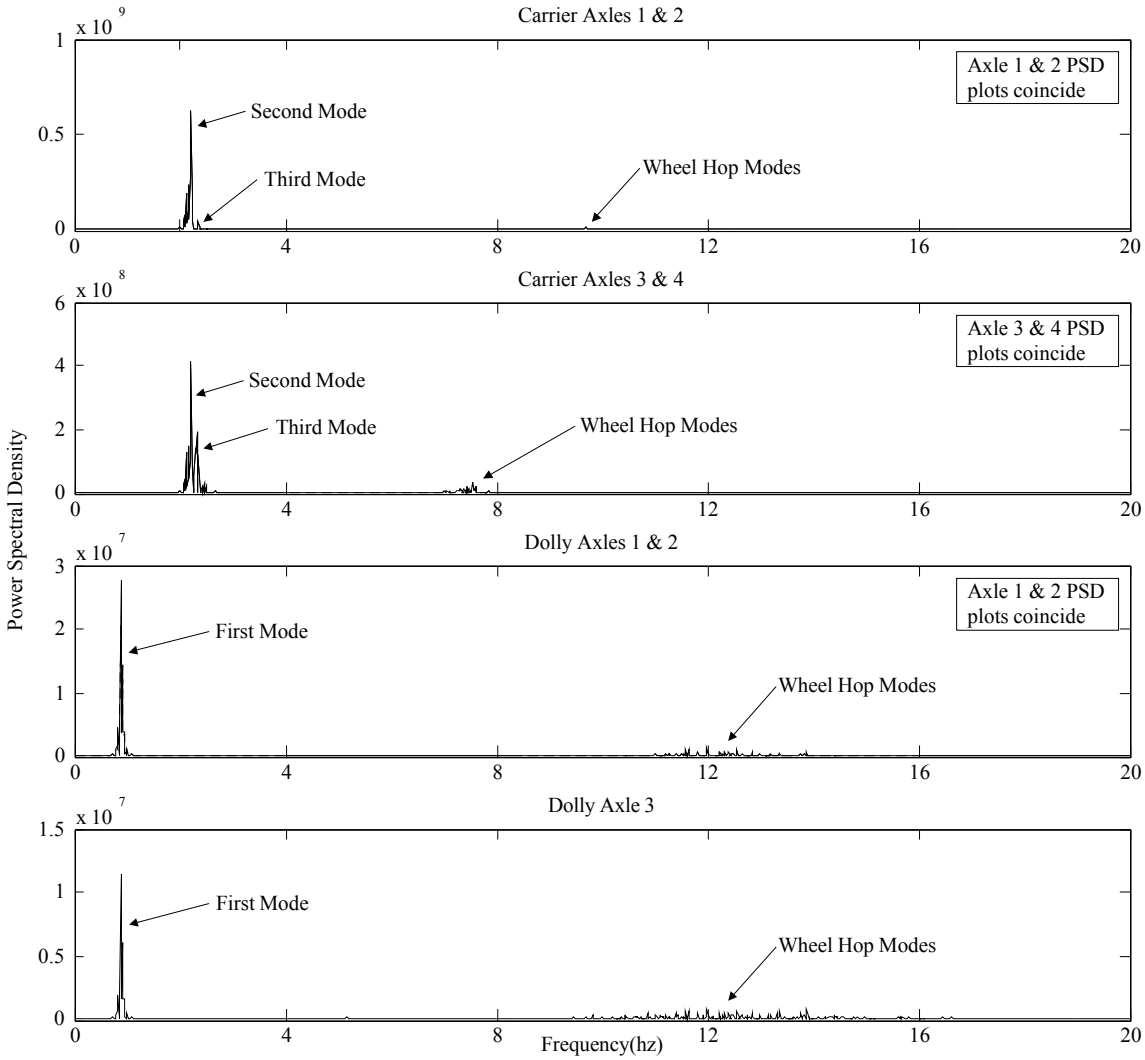


*Figure 7.11 Traditional Telescoping Boom Crane ~ PSD*

| Power Percentage for Axle Groups | | | | | | | |
|---|---|---|---|---|---|---|---|
| | Axle 1 | Axle 2 | Axle 3 | Axle 4 | Axle 5 | Axle 6 | Axle 7 |
| Single Axle | 24% | 23% | 24% | 24% | 2% | 1% | 1% |
| Tandem Pairs | 47% | | 49% | | 3% | | |
| Carrier and Dolly | 96% | | | | 4% | | |
| Power Percentage for Each Axle | | | | | | | |
| | Axle 1 | Axle 2 | Axle 3 | Axle 4 | Axle 5 | Axle 6 | Axle 7 |
| 0 to 5 Hz | 88% | 90% | 80% | 81% | 45% | 41% | 30% |
| Above 5 Hz | 12% | 10% | 20% | 19% | 55% | 59% | 70% |

*Table 7.2 Traditional Telescoping Boom Crane ~ Power Percentage*

The area under the power spectral density plots is integrated to determine the percentage of power input at each frequency range. Table 7.2 estab lishes the percentage of power contributed by each axle in the upper section. The lower section of the table introduces the percentage of power input by sprung mass bounce frequencies (0 to 5 Hz) and the percentage of power input by wheel hop frequencies (above 5 Hz).

The single most important result to draw from this table is that the carrier contributes 96% of the power to the roadway. The carrier axles do support more mass than the dolly, but as the quarter truck model introduced, the walking beam suspension has much higher dynamic forces than the dolly leaf spring suspension. Breaking down the results further reveals that the front and rear carrier tandems introduce similar total power percentages at 47% and 49%, respectively. Looking at the power in terms of the bounce frequency, the front tandem averages 89% of its power in the bounce frequency range while the rear carrier tandem introduces approximately 81% in this same range. The quarter truck model of Chapter 6 established that the walking beam suspension has a significantly higher force magnitude gain in the bounce frequency range. The quarter truck also established that an increased unsprung mass reduces the wheel hop frequency. This difference can be seen in the PSD of the front carrier steering tandem and in the massive rear drive axles.

The dolly introduces only 4% of the total power to the roadway. Dividing this power into frequency ranges, the front dolly tandem and rear dolly axle respectively introduce approximately 43% and 30% of their power in the wheel hop range.

### 7.3.2 Configuration Case Variation

A significant concern with the telescoping boom crane is the effect of the boom on the dynamic system. Figure 7.12 introduces the axle loads for the carrier and dolly with no boom, a rigid boom on a leaf spring dolly, a flexible boom on a leaf spring dolly and a flexible boom on a walking beam dolly. Figure 7.13 presents the boom connection forces for the rigid and flexible boom cases.

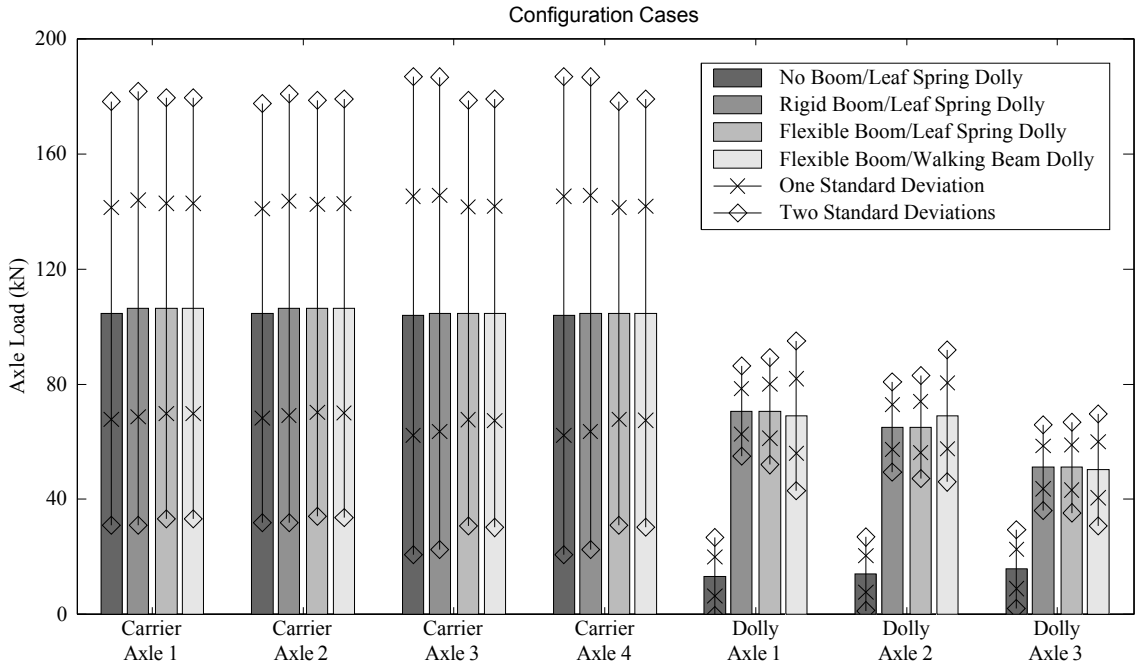


*Figure 7.12 Traditional Telescoping Boom Crane ~ Axle Loads*

The first case introduces a crane and dolly with no boom and the second case is the same carrier and dolly with a rigid boom. Figure 7.13 establishes that the addition of a rigid boom adds a small amount of static and dynamic load at the boom/carrier connection. This slightly increases the carrier axle loads in Figure 7.12. The dolly experiences a significant increase in static load and a minimal increase in dynamic load when the rigid boom is added.

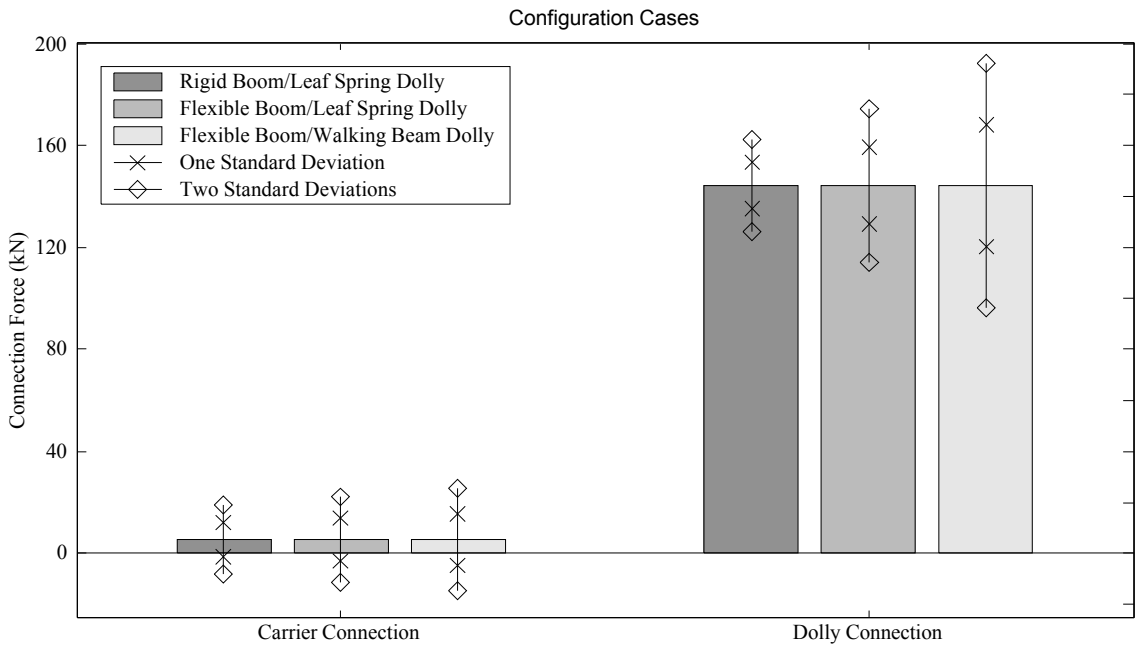


*Figure 7.13 Traditional Telescoping Boom Crane ~ Boom Connection Forces*

Adding boom vibration in the third case produces minimal increases in both the boom connection forces and the dolly dynamic road loads. Carrier dynamic loads decrease due to the added boom vibration. The boom has a free vibration frequency of 2.7 Hz, similar to the bounce frequency of the walking beam suspension established in the quarter truck model. Boom vibration is an important effect and will be more thoroughly addressed in the next section.

In the final case, the dolly suspension is modeled as a walking beam tandem pair with a leaf spring rear. The dolly tandem is now contributing the high dynamic forces introduced in the quarter truck walking beam model. In Figure 7.13, the change is seen in both the carrier and dolly connection forces. The increased dynamics manifests itself in increased overall loads on the rear carrier and dolly axles.

7.3.2.1 Boom Stiffness Variation

The crane boom stiffness is a significant contribution to the behavior of the overall system. To capture the affects of the boom with different stiffness, Figure 7.14 characterizes the first standard deviation of the dynamic axle load for the representative telescoping boom crane. Scaling the beam element section inertia terms changes the free vibration frequency of the telescoping boom. Boom inertia was adjusted to vary the boom fundamental free vibration frequency from 1 to 10 Hz where the 1 Hz boom is the softest reasonable boom and above 10 Hz approach the rigid boom case.

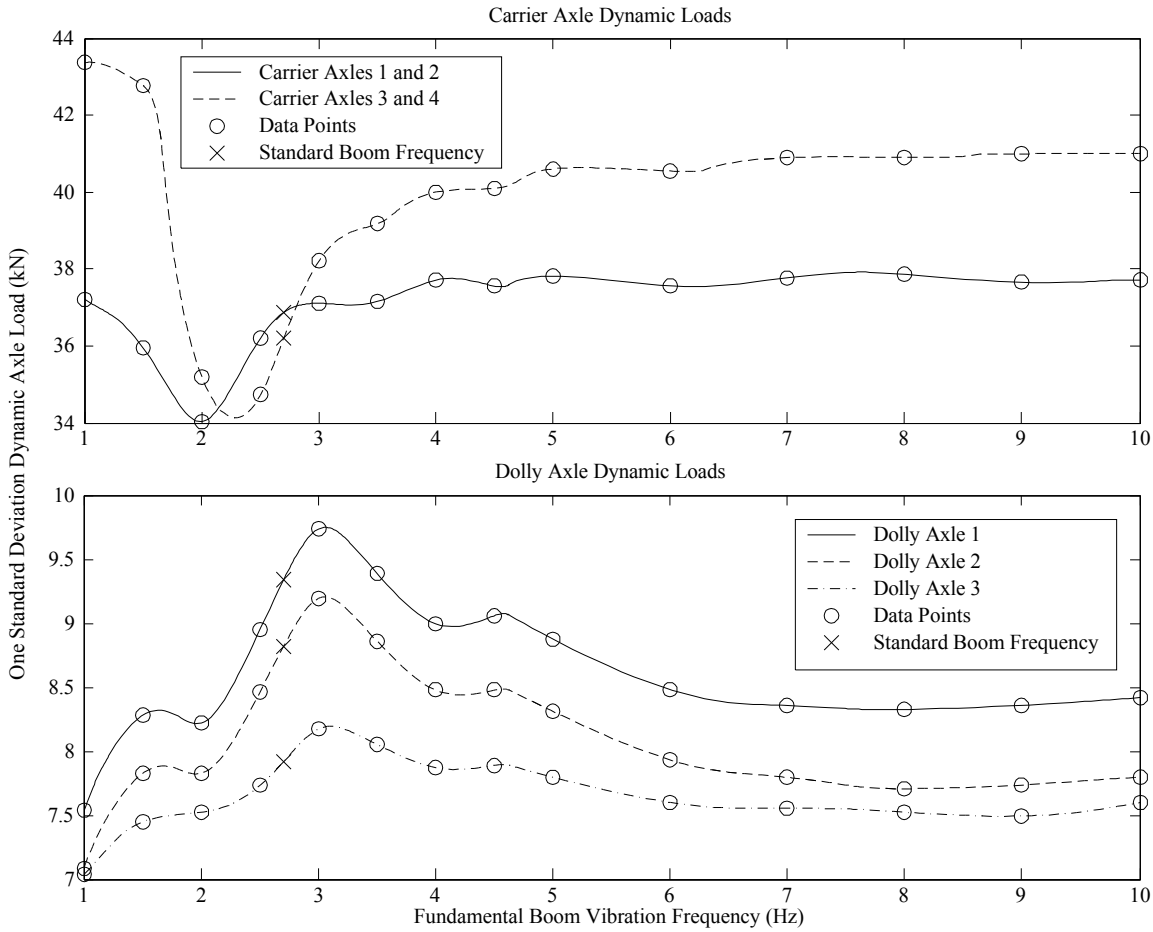


*Figure 7.14 Traditional Telescoping Boom Crane ~ Boom Vibration Variation*

The upper plot in Figure 7.14 captures the affects of the boom on the carrier. Between 2 Hz and 3.5 Hz, the carrier experiences a reduction in dynamic force. The boom free vibration frequencies are in the range of the carrier rigid body frequencies and produce anti-resonance. Dolly axles experience marginal increases in dynamic loads between 2 Hz and 4 Hz. While the combination of the boom and dolly does experience a resonant bounce frequency due to boom compliance, it is important to notice that the scale of the lower subfigure only ranges from 7 to 10 Hz.

### 7.3.3 Load Block Mass Variation

Telescoping boom cranes are commonly transported with the load block suspended at the end of the boom. This boom is a massive structure and the load block only adds a marginal amount of weight. Figure 7.15 establishes the affects of the load block on road loads. To characterize the dynamics, the load block is varied from zero mass to 5200 kg (356 slugs).

With no load block, the carrier axles experience the highest dynamic load. Conversely, this configuration presents the lowest load on the dolly axles because they only have the boom

mass to support. As the load block mass is increased, both the static and dynamic load on the carrier axles decreases. The dolly axle static loads increase with negligible change to the dynamic load. As a result, a heavy load block does not significantly increase the dynamic load but can significantly reduce the static load of the carrier axles.

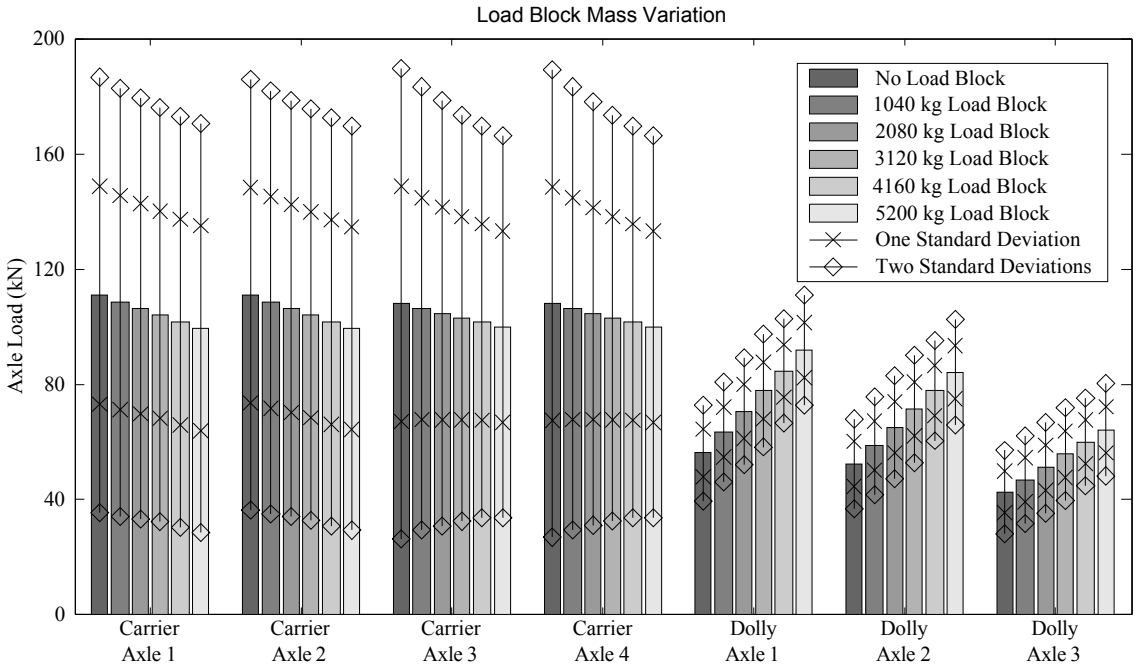


*Figure 7.15 Traditional Telescoping Boom Crane ~ Load Block Variation*

### 7.3.4 Dolly Connection Variation

The dolly on the representative telescoping boom crane is positioned slightly behind the boom's center of gravity. Much like the load block, the concern is cantilevered boom mass resulting in excessive dynamic axle loads. Figure 7.16 establishes the affects of the dolly and boom connection location. To characterize the dynamics, the dolly location is varied from just behind the carrier at 1/2 of the base boom sleeve span to the end of the base boom sleeve.

When the dolly is connected at 1/2 of the base boom sleeve span, the overall load on the carrier is at a minimum and the load in the dolly is maximized. As the dolly connection is moved back, the carrier axle load is increased while the overall dolly load decreases. The crane does not exhibit excessive dynamic load when the dolly is at 1/2 span. The reduction in static weight is the key factor that makes this a desirable configuration.

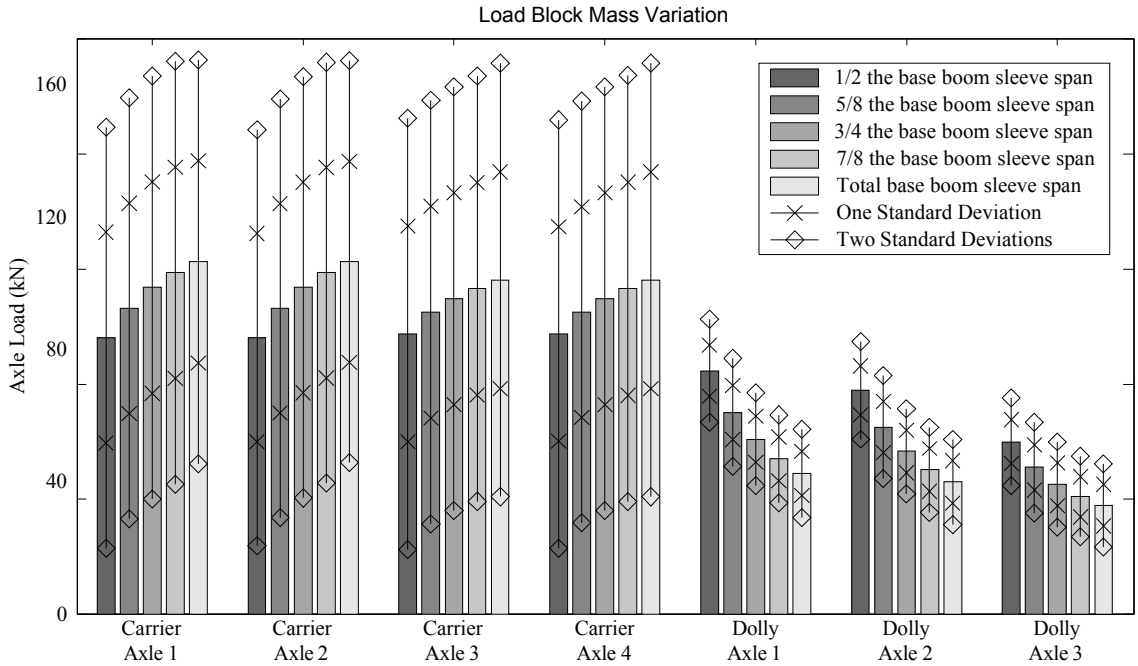


*Figure 7.16 Traditional Telescoping Boom Crane ~ Connection Variation*

## 7.4 Dynamics of Telescoping Boom Cranes with Hydro-pneumatic Carriers

Modern telescoping boom cranes are commonly equipped with hydro-pneumatic carrier suspension. The quarter truck model of Chapter 6 introduced the hydro-pneumatic suspension and established that it produces significantly lower dynamic road loads than its walking beam predecessor. This section presents a four and six axle carrier equipped with this suspension.

### 7.4.1 Four Axle Hydro-pneumatic Carrier

The dynamic behavior of the traditional four axle telescoping boom crane with walking beam suspension has been established in Section 7.3. To determine the affects of hydro-pneumatic suspension, the same Grove TM9120 crane will be modeled with the hydro-pneumatic subsystem of Section 3.7. All other aspects of the crane will remain unchanged and configuration details of the representative telescoping boom crane are provided in E.1.

#### 7.4.1.1 System Mode Shapes and Power Spectral Density

Analysis of the telescoping boom crane begins with the presentation of the sprung mass bounce and pitch mode shapes in Figure 7.17. As found in the walking beam version, the first mode is predominately bounce motion of the boom and dolly. Modes two and three introduce more carrier excitation while maintaining noticeable dolly and boom motion.

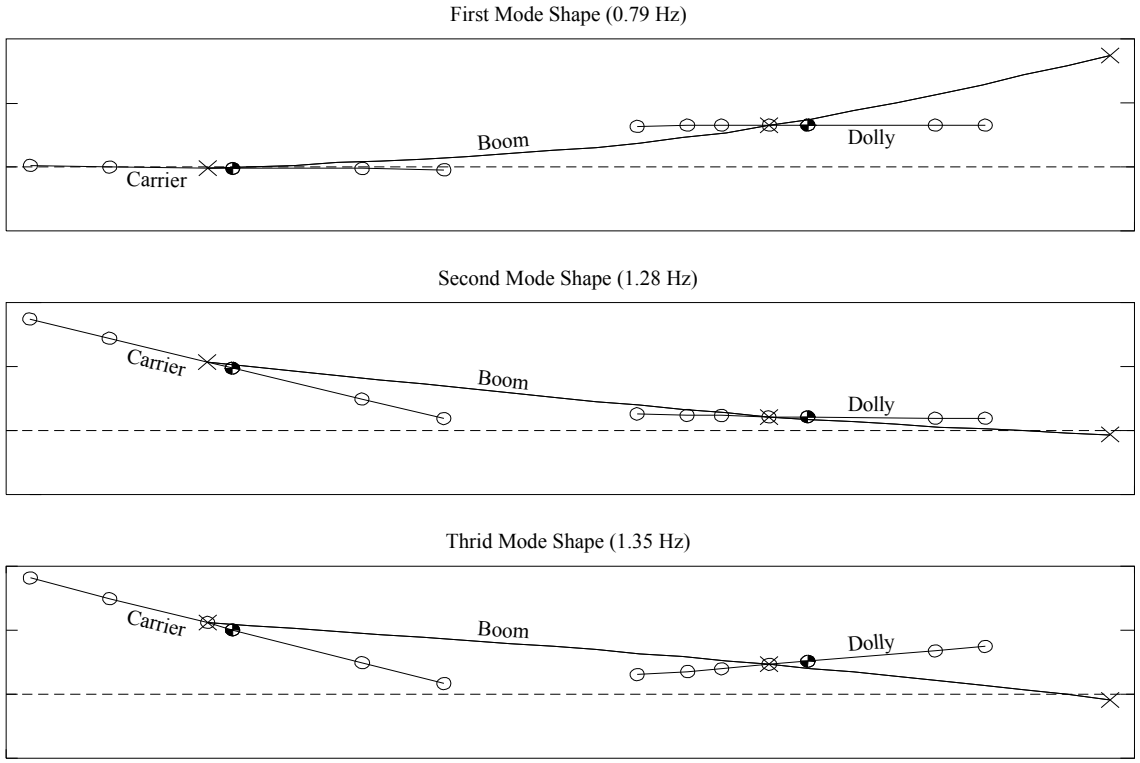


Figure 7.17 Four Axle Hydro-pneumatic Carrier ~ Mode Shapes

With the sprung mass bounce and pitch modes established, Figure 7.18 introduces the power spectral density of each tire force. Three characteristic bounce frequencies are present in the low frequency ranges of these PSD plots. The first two subplots characterize the carrier axles and establish modes 2 and 3 as the major contributors to the carrier tire forces with minimal contribution from the first mode. The dolly axles in the remaining two subplots predominately contain the first mode.

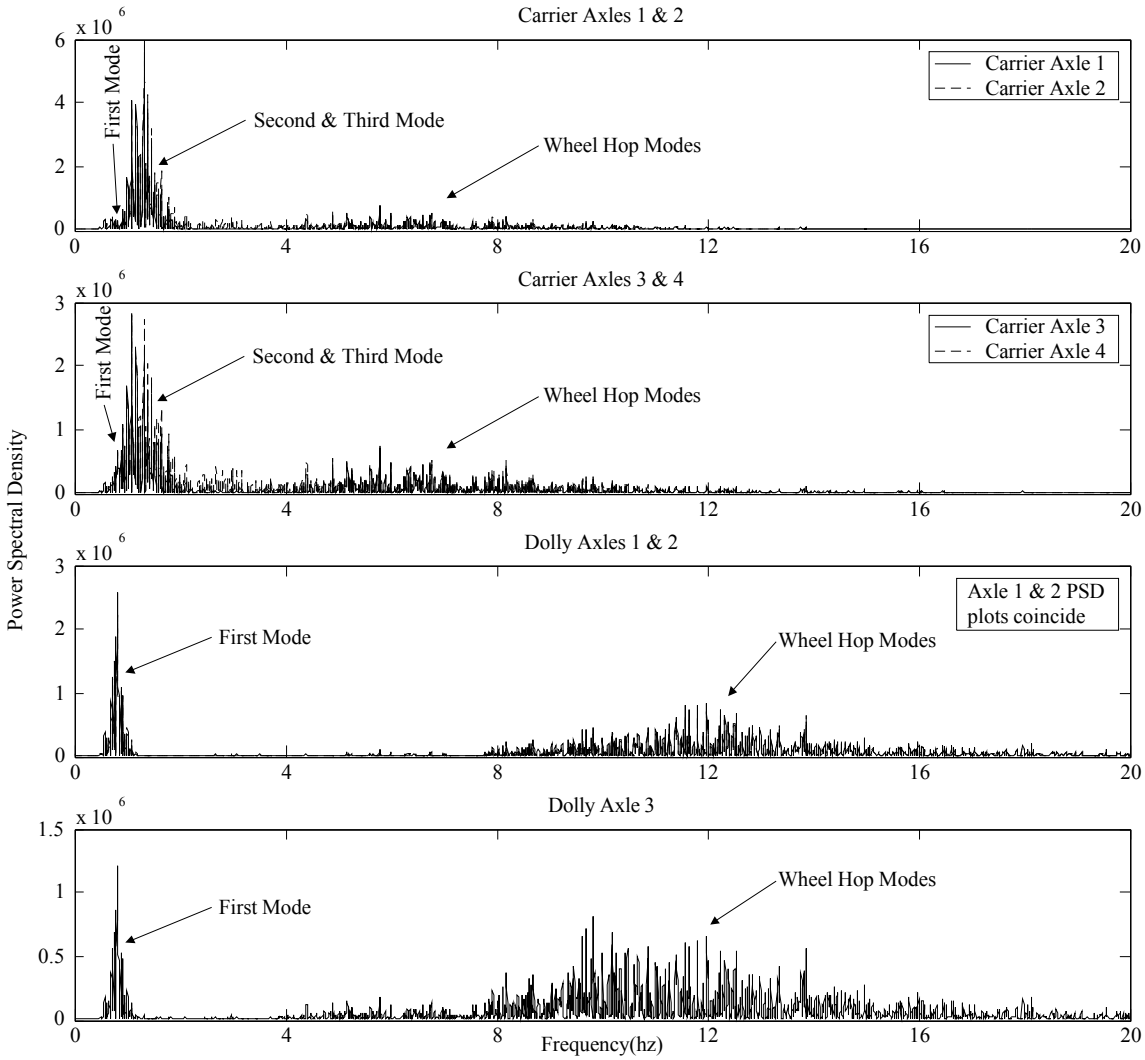


*Figure 7.18 Four Axle Hydro-pneumatic Carrier ~ PSD*

| Power Percentage for Axle Groups | | | | | | | |
|---|---|---|---|---|---|---|---|
| | Axle 1 | Axle 2 | Axle 3 | Axle 4 | Axle 5 | Axle 6 | Axle 7 |
| Single Axle | 15% | 18% | 12% | 15% | 14% | 13% | 14% |
| Tandem Pairs | 33% | | 27% | | 27% | | |
| Carrier and Dolly | 60% | | | | 40% | | |
| Power Percentage for Each Axle | | | | | | | |
| | Axle 1 | Axle 2 | Axle 3 | Axle 4 | Axle 5 | Axle 6 | Axle 7 |
| 0 to 5 Hz | 56% | 61% | 47% | 53% | 18% | 16% | 10% |
| Above 5 Hz | 44% | 39% | 53% | 47% | 82% | 84% | 90% |

*Table 7.3 Four Axle Hydro-pneumatic Carrier ~ Power Percentage*

The area under the power spectral density plots is integrated to determine the percentage of power input at each frequency range. Table 7.3 presents the percentage of power contributed by each axle in the upper section. The lower section of the table introduces, for each axle, the percentage of power input by sprung mass bounce frequencies (0 to 5 Hz) and the percentage of power input by wheel hop frequencies (above 5 Hz).

The hydro-pneumatic carrier suspension greatly reduces the power input through the carrier axles. The traditional telescoping boom crane with walking beam carrier input 96% of the total power to the road and while changing to hydro-pneumatic suspension reduced total power from the carrier to 60%. Breaking down the results further reveals the front and rear carrier tandems introduce similar total power percentages at 33% and 27% respectively. Looking at the power in terms of the bounce frequency, the front tandem contribute approximately 58% of their power in the bounce frequency range while the rear carrier tandem introduces 50% in this same range. These results are consistent with the quarter truck. Hydro-pneumatic suspension quarter truck models demonstrated a significant reduction in force compared to the walking beam.

The quarter truck established that the hydro-pneumatic and air ride suspension have similar response characteristics. To support this, the air ride dolly introduces 40% of the total power to the roadway when used with this hydro-pneumatic carrier. Dividing this power into bounce and wheel hop frequency ranges, the front dolly tandem and rear dolly axle respectively introduce approximately 17% and 10% of their power in the bounce frequency range.

7.4.1.2 Configuration Case Variation

The telescoping boom dynamic affect is greatly reduced when hydro-pneumatic suspension is introduced. Figure 7.12 presents the axle loads for a carrier and dolly with no boom, a rigid boom on an air ride dolly, a flexible boom on a leaf spring dolly and a flexible boom on an air ride dolly. For comparison, the final two results capture a walking beam carrier with a flexible boom on a walking beam dolly and the same carrier and boom on an air ride dolly. Figure 7.13 presents the boom connection forces for the rigid and flexible boom cases.

The first case is a crane and dolly with no boom and the second case is the same carrier and dolly with a rigid boom. Figure 7.20 establishes that the rigid boom adds a small amount of static load and slightly increases dynamic load. In turn, Figure 7.19 exhibits the expected static load increase with negligible dynamic change.

Adding boom vibration and a leaf spring dolly in the third case produces minimal increases in both the boom connection forces and the dynamic road loads. Carrier changes are not noticeable while dolly increases are small. The fourth case introduces air ride suspension to the dolly. Connection forces are reduced because of the smoother riding suspension. Noticeable dynamic load reductions occur on the dolly while the carrier is virtually unaffected.

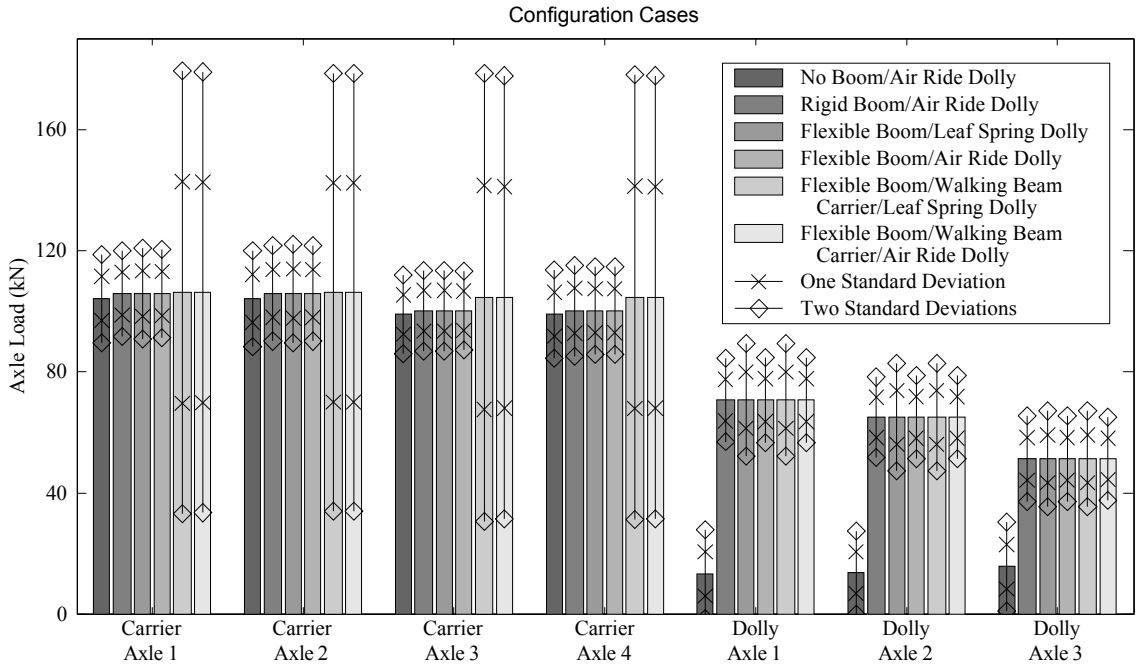


*Figure 7.19 Four Axle Hydro-pneumatic Carrier ~ Axle Loads*

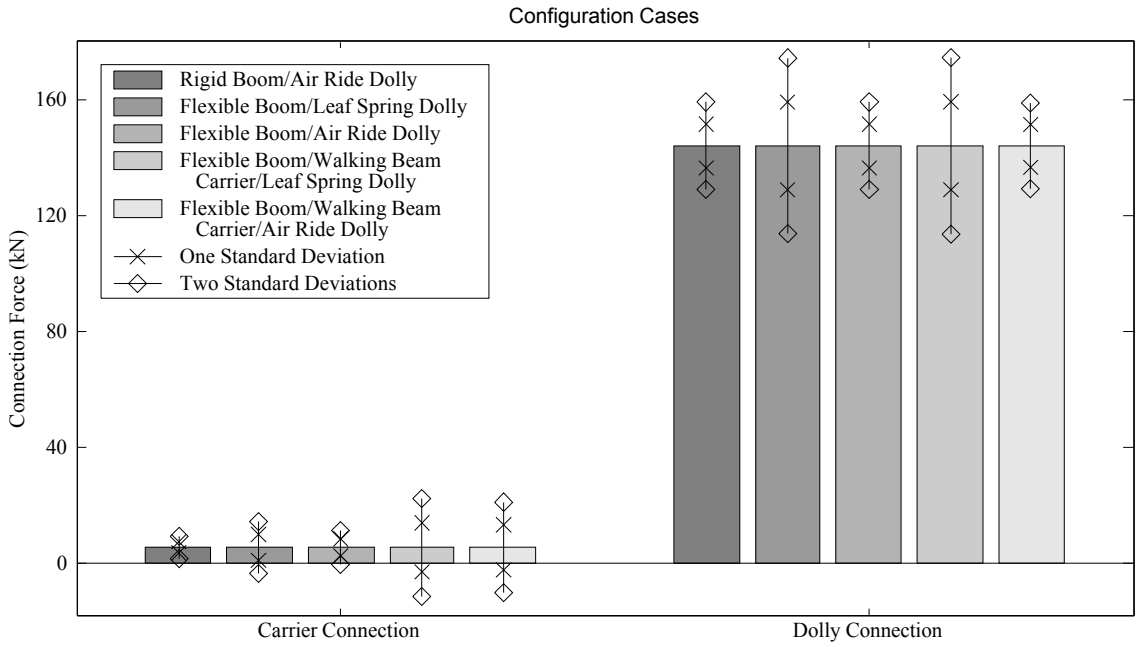


*Figure 7.20 Four Axle Hydro-pneumatic Carrier ~ Boom Connection Forces*

Cases five and six investigate a leaf spring and air ride dollies with the traditional walking beam carrier. Notice in Figure 7.20 the dolly connection forces remain unchanged from the hydro-pneumatic case while a marginal increase in connection force is seen at the carrier. In

Figure 7.19, the carrier axle dynamic loads demonstrate a huge dynamic load increase while the dolly axles have negligible change.

### 7.4.2 Six Axle Hydro-pneumatic Carrier

The Grove GMK6250, illustrated in Figure 7.21, is a modern telescoping boom crane with hydro-pneumatic carrier suspension. For this model, the boom will be supported on an air ride dolly.

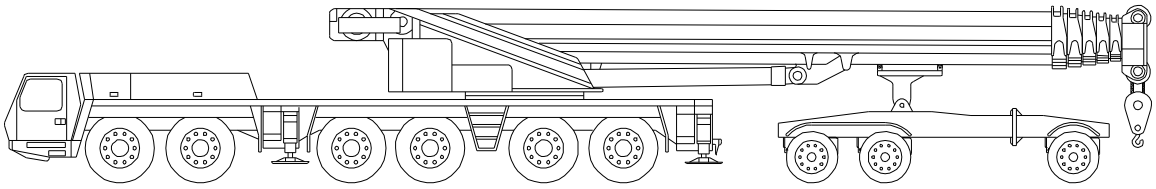

*Figure 7.21 Six Axle Hydro-pneumatic Carrier (Grove GMK6250)*

Much like the four axle telescoping boom crane, the boom foot typically connects near the carrier's center of gravity. The dolly supports the massive boom approximately 1/3 of the distance form the boom tip. For the Grove GMK6250, the boom is estimated to weigh 22,000 kg (1507 slugs) supporting a 2080 kg (143 slugs) load block. Configuration details of the representative telescoping boom crane are provided in E.1.

#### 7.4.2.1 Power Spectral Density and Mode Shapes

Analysis of the six-axle telescoping boom crane begins with the presentation of the sprung mass bounce and pitch mode shapes in Figure 7.22. As found in the other cranes, the first mode is predominately bounce motion of the boom and dolly. Modes two and three introduce more carrier excitation while maintaining noticeable dolly and boom motion.

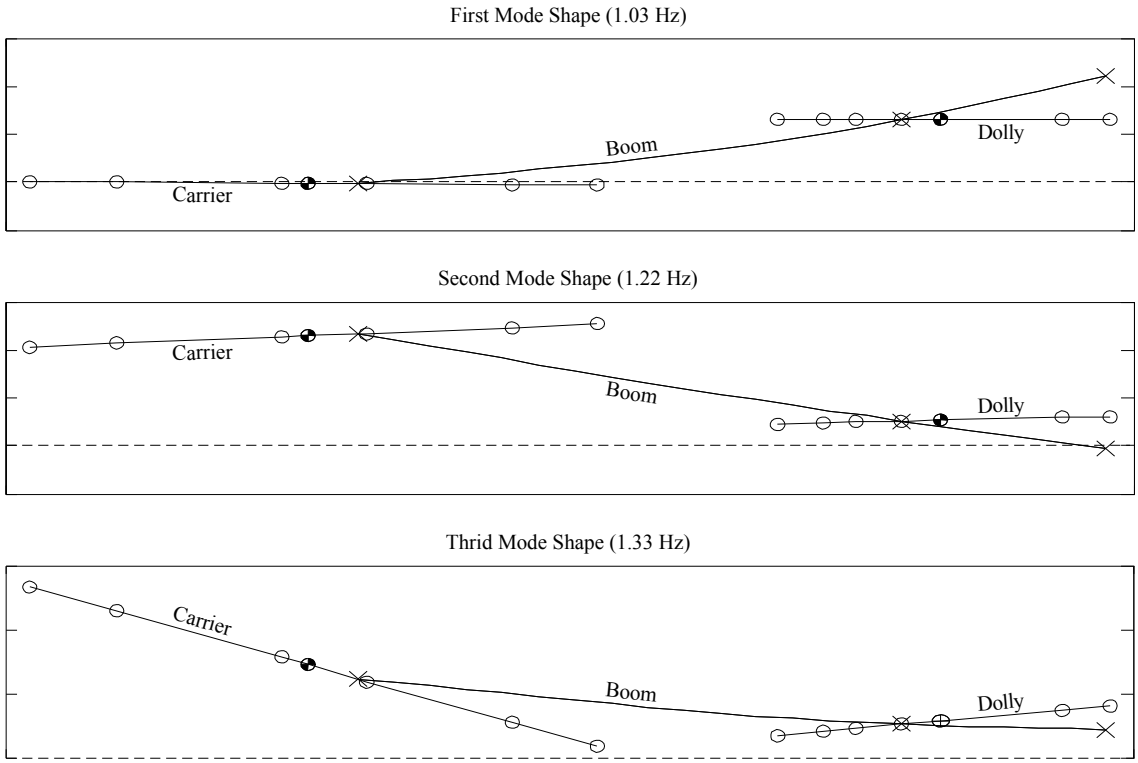


Figure 7.22 Four Axle Hydro-pneumatic Carrier ~ Mode Shapes

With the sprung mass bounce and pitch modes established, Figure 7.23 introduces the power spectral density of each tire force. The first three subplots present the PSD of the carrier tandems. Due to the much more massive boom, the carrier axles contain the significant contribution from the first mode. The final two subplots are dolly axle results and contain only the first mode.

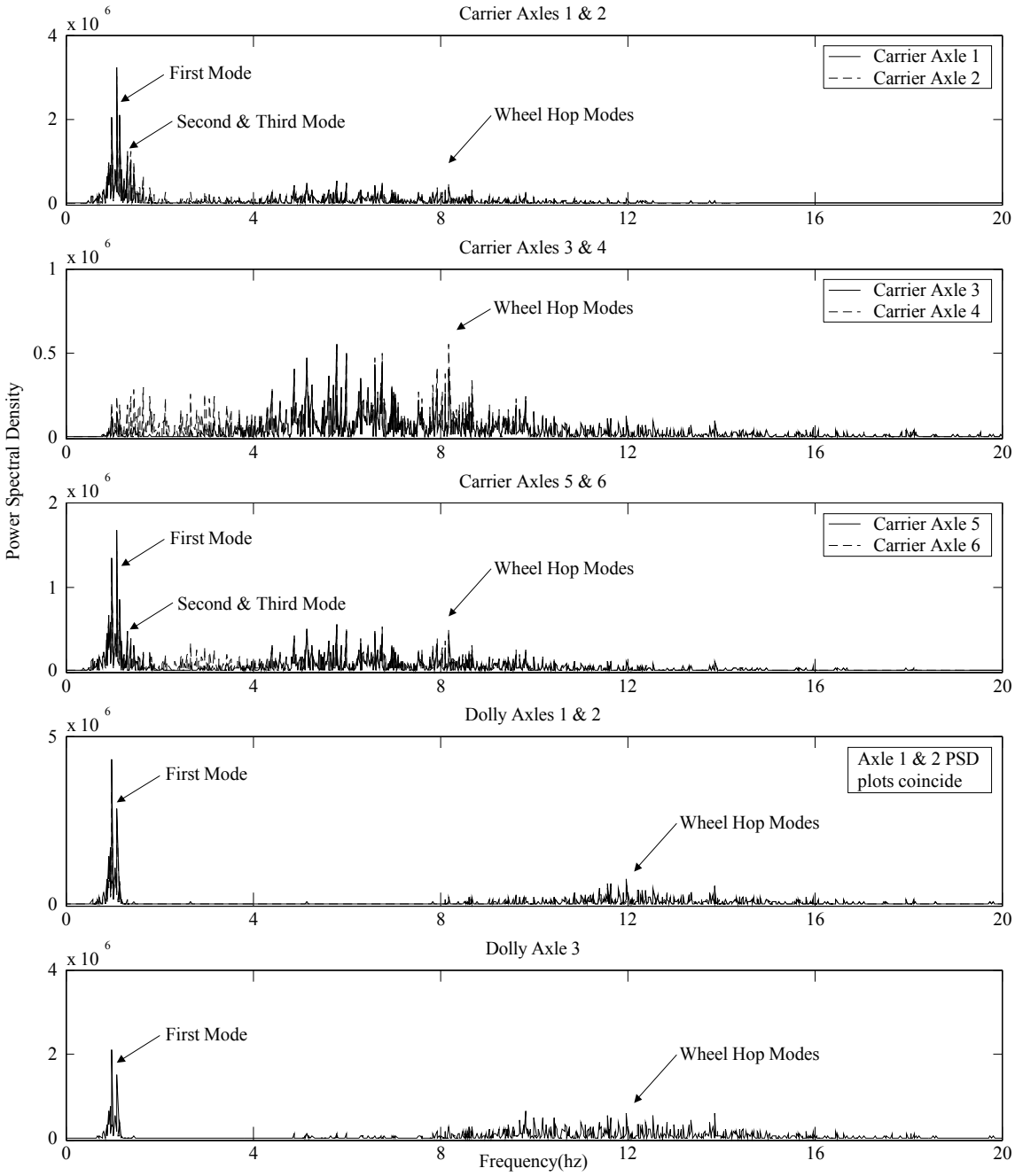


*Figure 7.23 Four Axle Hydro-pneumatic Carrier ~ PSD*

| Power Percentage for Axle Groups | | | | | | | | | |
|---|---|---|---|---|---|---|---|---|---|
| | Axle 1 | Axle 2 | Axle 3 | Axle 4 | Axle 5 | Axle 6 | Axle 7 | Axle 8 | Axle 9 |
| Single Axle | 11% | 13% | 8% | 9% | 9% | 11% | 13% | 12% | 14% |
| Tandem Pairs | 24% | | 17% | | 20% | | 25% | | |
| Carrier and Dolly | 61% | | | | | | 39% | | |
| Power Percentage for Each Axle | | | | | | | | | |
| | Axle 1 | Axle 2 | Axle 3 | Axle 4 | Axle 5 | Axle 6 | Axle 7 | Axle 8 | Axle 9 |
| 0 to 5 Hz | 44% | 46% | 16% | 26% | 32% | 36% | 24% | 21% | 13% |
| Above 5 Hz | 56% | 54% | 84% | 73% | 67% | 64% | 76% | 79% | 87% |

*Table 7.4 Four Axle Hydro-pneumatic Crane ~ Power Percentage*

The area under the power spectral density plots is integrated to determine the percentage of power input at each frequency range. Table 7.4 presents the percentage of power contributed by each axle in the upper section. The lower section of the table introduces, for each axle, the percentage of power input by sprung mass bounce frequencies (0 to 5 Hz) and the percentage of power input by wheel hop frequencies (above 5 Hz).

In terms of total power, 61% is input through the carrier axles and 39% through the dolly. Reducing the results further reveals the front, middle and rear carrier tandems introduce similar total power percentages at 24%, 17% and 20%, respectively. The dolly contributes 25% of its power at the tandem and 14% at the rear axle.

Looking at the power in terms of the bounce frequency, the front carrier tandem contribute approximately 45% of the power in the bounce frequency range, the middle contributes an average of 21%, and the rear averages 29%. The dolly tandem averages 23% in the bounce frequency range and the rear axle contributes 13% of its power in the bounce range.

7.4.2.2 Configuration Case Variation

The following configuration cases are introduced to establish the behavior of a six-axle hydraulic crane. Figure 7.24 introduces the axle loads for a carrier and dolly with no boom, a rigid boom on an air ride dolly, a flexible boom on a leaf spring dolly and a flexible boom on an air ride dolly. Figure 7.25 presents the boom connection forces for the rigid and flexible boom cases.

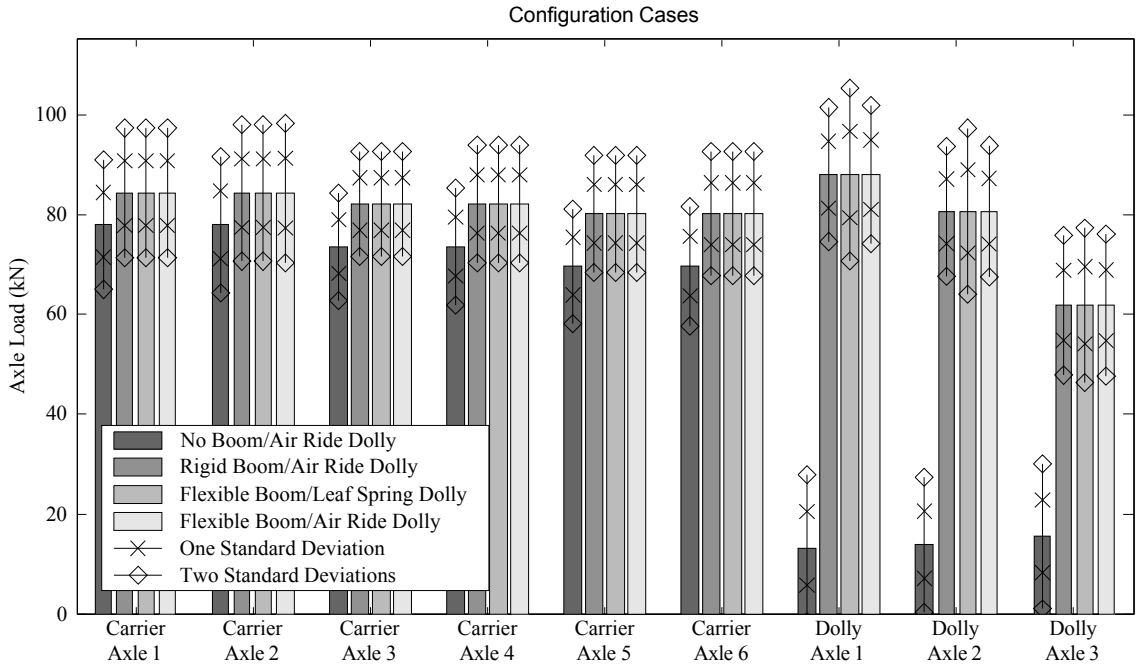


*Figure 7.24 Four Axle Hydro-pneumatic Crane ~ Axle Loads*

The first case is a crane and dolly with no boom and the second case is the same carrier and dolly with a rigid boom. Figure 7.25 establishes that the addition of a rigid boom adds considerable static load. A slight amount of dynamic load is present at the

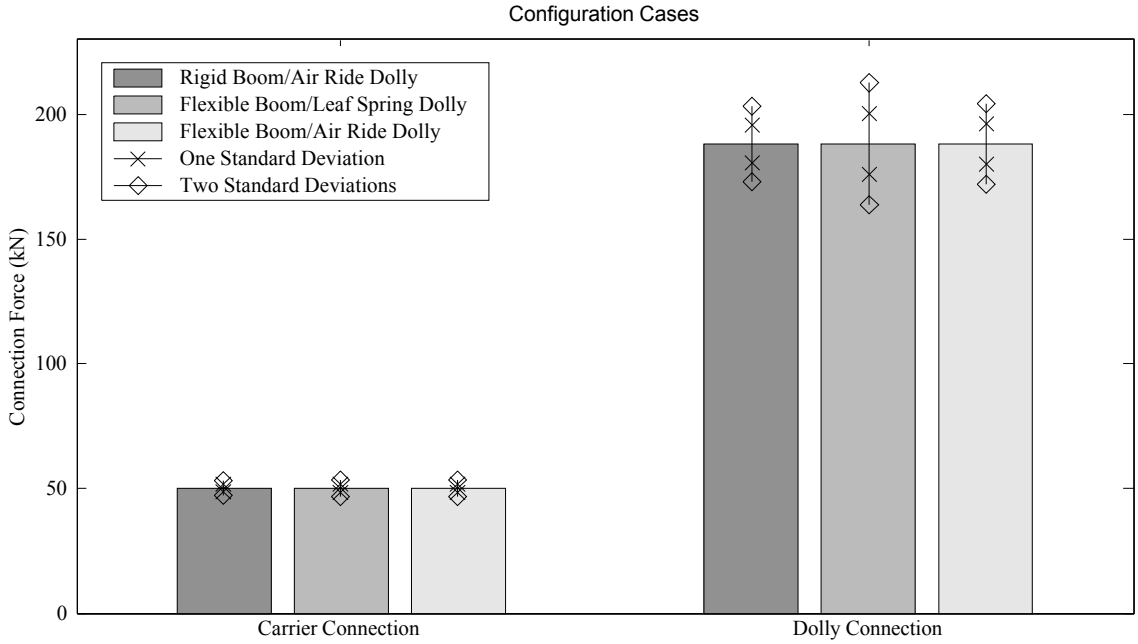


*Figure 7.25 Four Axle Hydro-pneumatic Crane ~ Boom Connection Forces*

carrier and a marginal amount at the dolly. In Figure 7.24, the addition of a boom increases the static load without noticeable change to the dynamic load.

The final two cases present a flexible boom with a leaf spring dolly or an air ride dolly. Changing from a rigid to a flexible boom with an air ride dolly resulted in no noticeable dynamic load change but switching to a leaf spring dolly results in higher dynamic axle loads on the dolly only.

## 7.5 Truck and Semi-trailer Model

A truck and semi-trailer model was developed to provide some insight to how it compares to a mobile crane. The model used for comparison is a five axle truck and semi-trailer combination. The truck has an independent front axle. The tandem suspension used on both the rear of the truck and the semi-trailer is a spring mounted walking beam. This suspension is implemented by replacing the $\kappa$ spring of the original walking beam suspension model with a parallel spring and damper. The kingpin is centered over the truck tandem. The truck and semi-trailer model used in the simulation is illustrated in Figure 7.26.

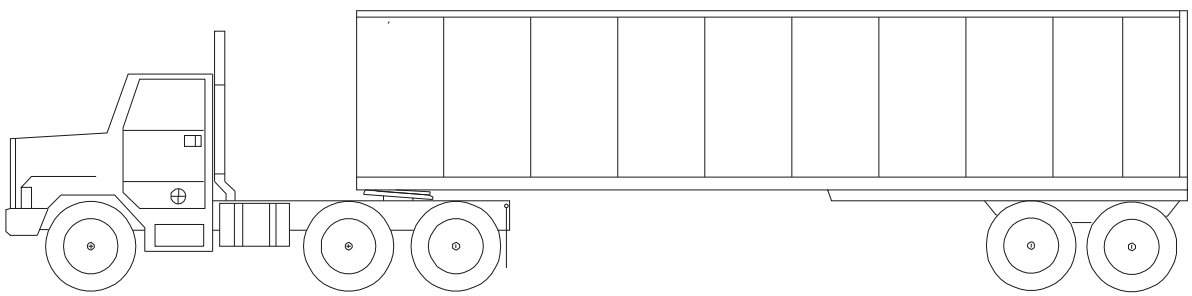

*Figure 7.26 Five Axle Truck and Semi-trailer Configuration*

The truck and semi-trailer model is implemented in the complete model by dividing it into subsystems equivalent to the crane. The truck is implemented as a three axle carrier. The semi-trailer is a combination of the finite element boom and dolly models. The sprung portion of the semi-trailer is represented through the finite element boom model and is limited to only the rigid body modes. The suspension is captured through a massless two axle dolly. Breaking the truck and semi-trailer up in this manner allows a mathematical representation of this system to be implemented in the same manner as the crane.

### 7.5.1 System Mode Shapes and Power Spectral Density

Analysis of the truck and semi-trailer begins with the presentation of the sprung mass bounce and pitch mode shapes in Figure 7.27. The first mode shape shows a large pitching motion of the truck pivoting about the kingpin. The second mode is primarily semi-trailer bounce with noticeable truck motion present due to the kingpin connection. The third mode is primarily a combination of truck and semi-trailer pitching modes.

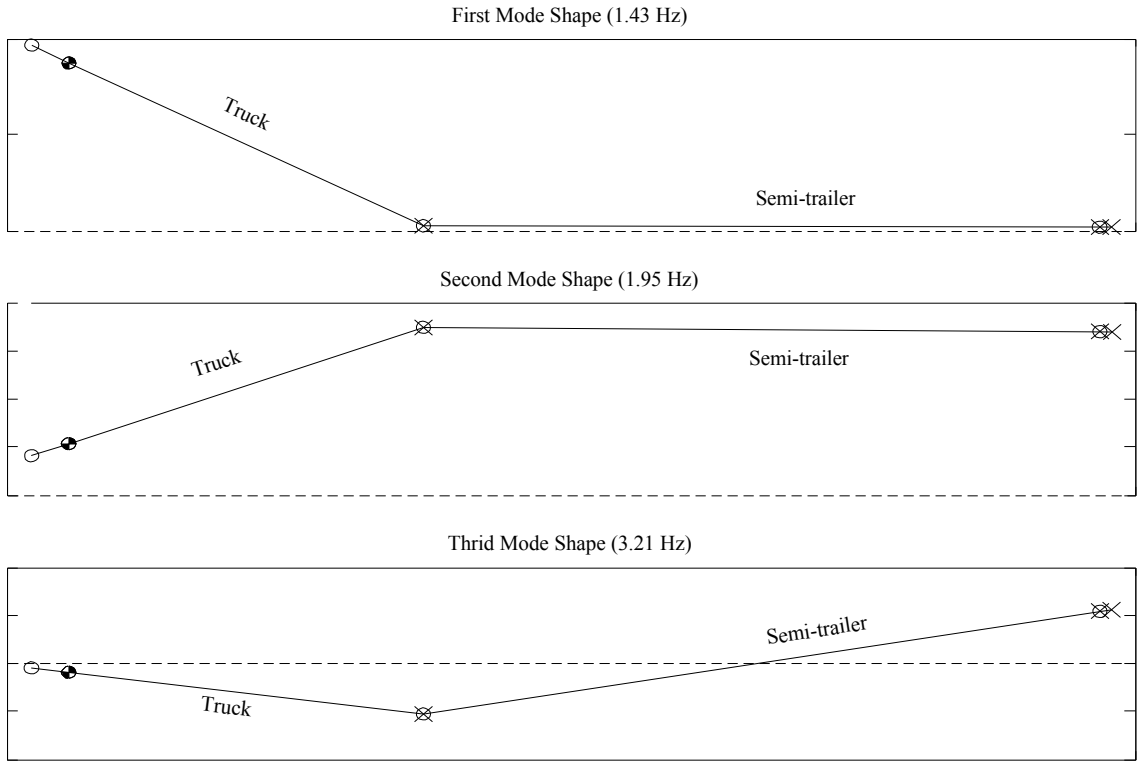


*Figure 7.27 Five Axle Truck and Semi-trailer ~ Mode Shapes*

With the sprung mass bounce and pitch modes established, Figure 7.28 introduces the power spectral density of each tire force. The first two subfigures contain truck axle results while the last subfigure contains semi-trailer axles. The system resonant frequencies relating the mode shapes have been labeled in each subfigure.

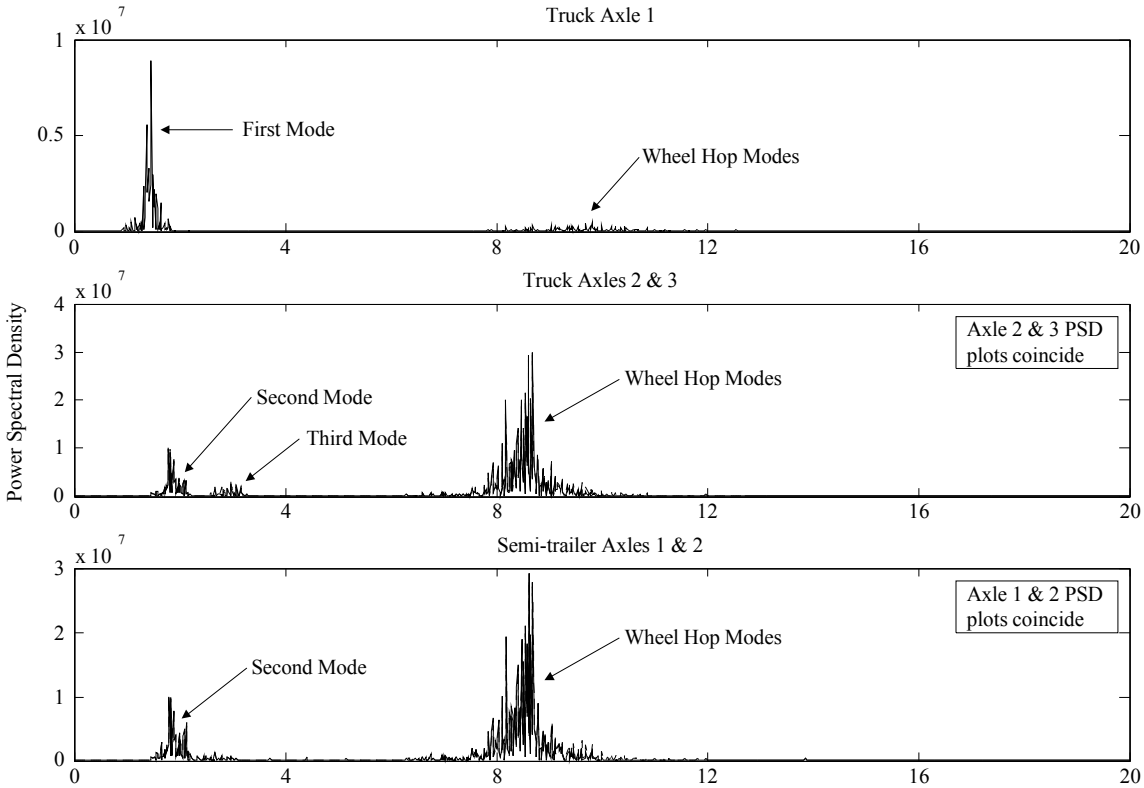


*Figure 7.28 Five Axle Truck and Semi-trailer ~ PSD*

The area under the power spectral density plots is integrated to determine the percentage of power input at each frequency range. Table 7.5 presents the percentage of power contributed by each axle in the upper table. The lower portion of the table introduces the percentage of power input by sprung mass heave and pitch frequencies (0 to 5 Hz) and the percentage of power input by wheel hop frequencies (above 5 Hz).

| Power Percentage for Axle Groups | | | | | |
|---|---|---|---|---|---|
| | Axle 1 | Axle 2 | Axle 3 | Axle 4 | Axle 5 |
| Single Axle | 3% | 24% | 25% | 24% | 24% |
| Tandem Pairs | | 49% | | 48% | |
| Truck and Semi-trailer | 52% | | | 48% | |
| Power Percentage for Each Axle | | | | | |
| | Axle 1 | Axle 2 | Axle 3 | Axle 4 | Axle 5 |
| 0 to 5 Hz | 64% | 17% | 19% | 17% | 18% |
| Above 5 Hz | 36% | 83% | 81% | 83% | 82% |

*Table 7.5 Five Axle Truck and Semi-trailer Configuration ~ Power Percentage*

In terms of total power, 52% is input through the truck axles and 48% through the semi-trailer. Reducing the results further reveals the front and rear tandems introduce similar total

power percentages at 49%, and 48%, respectively. The independent front axle of the truck introduces only 3% of the total power.

Looking at the power in terms of the bounce frequency, the front truck axle contributes approximately 64% in the bounce range and the rear truck tandem contributes an average of 18%. The semi-trailer tandem averages 17.5% in the bounce frequency range. Notice the high power percentages in the wheel hop frequency range experienced by the spring mounted walking beam axles. It is important to realize that this suspension only has vertical damping and no rotational damping of the walking beam. With the beam freely rotating, wheel hop becomes the dominant frequency.

Figure 7.29 looks at the loads generated by a five axle truck and semi-trailer model implementing two different suspension systems. A significant reduction in dynamic load in the spring mounted waking beam compared to the standard walking beam is shown in Figure 7.29.

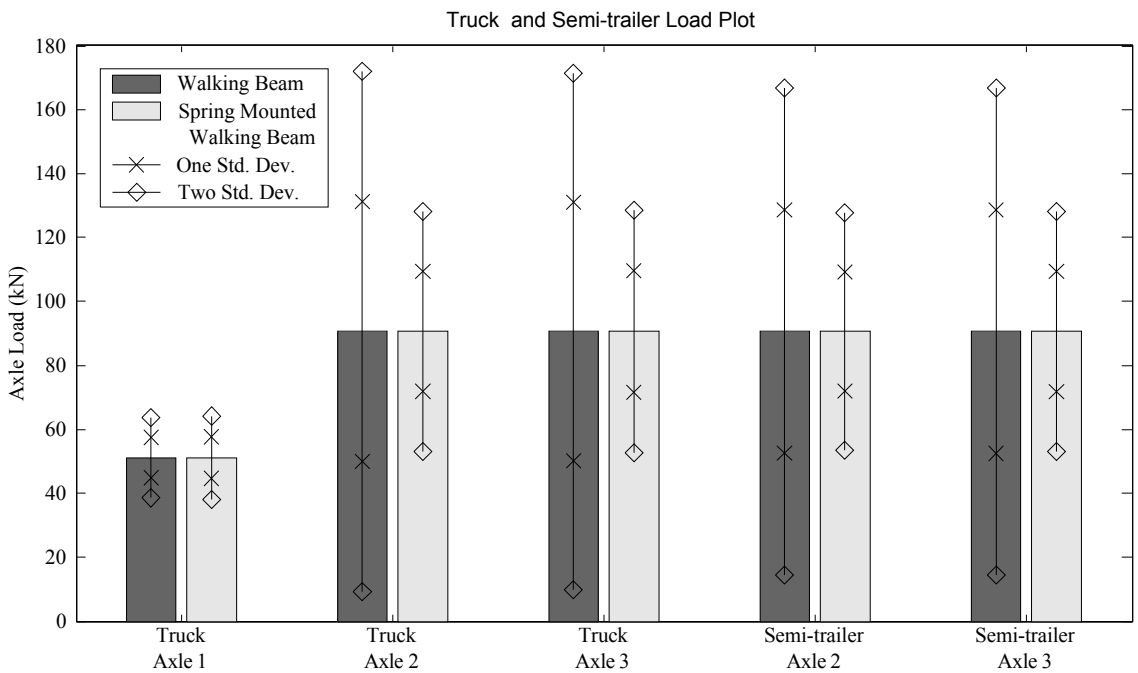


*Figure 7.29 Truck and Semi-trailer Load Plot*

## 7.6 Truck and Semi-Trailer Comparison

The purpose of developing a truck and semi-trailer model is to determine how it dynamically compares to a crane. In the discussion provided above, four different cranes were presented and will be summarized in Table 7.6 (Cases 1-4). In this section, two different truck and semi-trailer configurations are presented (Cases 5 and 6). Each truck model has a leaf spring steering axle in the front. Both of these models are set to a medium load of 180 kN (40,500 lbf) per tandem. The difference lies in the tandem suspension system utilized on the rear of the truck and on the semi-trailer.

| Case | Description |
|---|---|
| 1 | Four axle walking beam carrier with a leaf spring dolly and a lattice boom |
| 2 | Four axle walking beam carrier with a leaf spring dolly and a telescoping boom |
| 3 | Four axle hydro-pneumatic carrier with a air ride dolly and a telescoping boom |
| 4 | Six axle hydro-pneumatic carrier with a air ride dolly and a telescoping boom |
| 5 | Truck and semi-trailer with a walking beam suspension |
| 6 | Truck and semi-trailer with a spring mounted walking beam suspension |

*Table 7.6 Summary of Models*

Selecting a common axle location is important to properly compare the response of models that do not have a common axle configuration. The last axle on the carrier (or truck) will be looked at for comparison. Table 7.6 presents configuration details and the configuration case number used to correlate the subsequent plot.

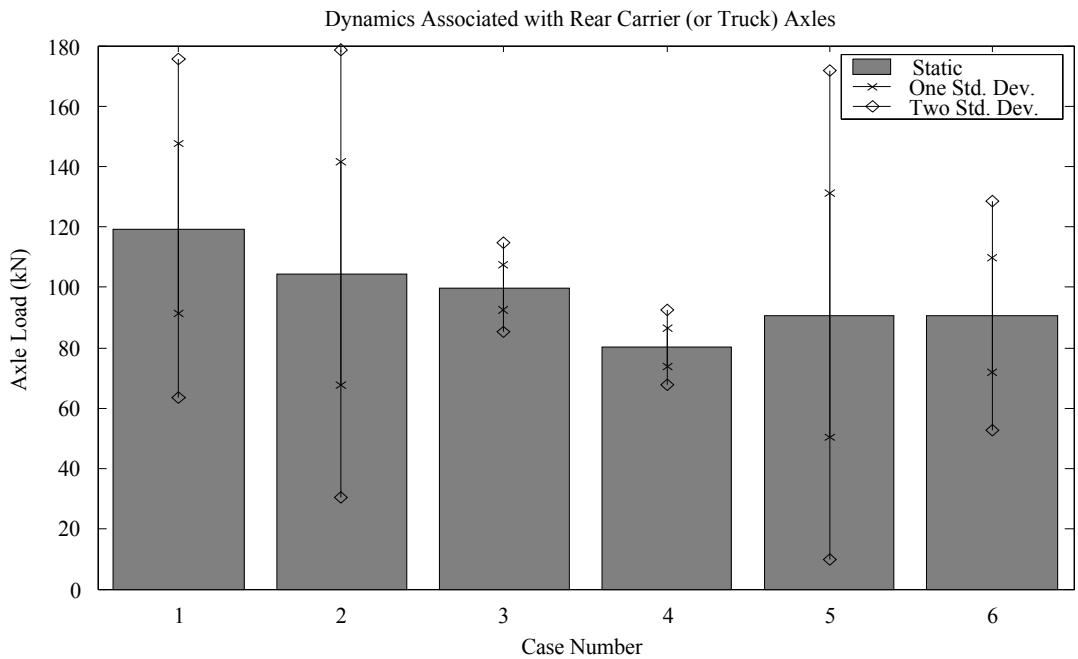


*Figure 7.30 Dynamics Associated with Rear Carrier Axles*

Figure 7.30 indicates that the static weights of the various models are similar in magnitude. The dynamic load generated by the spring mounted walking beam truck and semi-trailer (Case 6) lie between the two different carrier suspensions. Both the walking beam suspension carrier models (Cases 1 and 2) generate a significantly higher load than the two hydro-pneumatic carrier models (Cases 3 and 4). Recall that the truck and semi-trailer model from case six has a spring mounted walking beam that provides uspension compliance and damping while the walking beam suspension model implemented on the carrier provides none. A truck and semi-trailer (Case 5) implementing the same suspension as a walking beam carrier creates a similar peak dynamic load.

## 7.7 Summary

This chapter presents simulation results from the crane model. The goal of this chapter is to determine the dynamic road loads trends associated with each type of crane. Mode shape and power spectral density plots focused on the establishing the motion of the crane while axle load plots present the forces subjected to the roadway.

Suspension type is the single most important factor affecting crane dynamic road loads. Hydro-pneumatic suspension found on modern hydraulic crane carriers is far superior to the traditional walking beam. The harsh ride of the non-compliant walking beam excites significant motion of the carrier sprung mass and boom while the hydro-pneumatic isolates the sprung mass from the road motion below. The air ride found on the modern dollies is a marginal improvement over its leaf spring predecessor. Though the dynamic improvement seen in air ride is marginal, it is an important consideration on a dolly accompanying a hydro-pneumatic carrier.

Boom vibration has a marginal affect on dynamic road loads. Lattice booms have low mass and average a fairly high section inertia resulting in a high boom free vibration frequencies. Reduced free vibration frequencies moves the boom and dolly into a resonant bounce range and increase the whipping affect on the rear carrier tandem. The telescoping boom has much higher mass resulting in reduced boom free vibration frequencies. Again, low lattice boom frequencies enter the boom and dolly into a resonant bounce range. The flexible boom reduces the affect the carrier and dolly dynamic loads have on each other.

Load block and dolly connection are two concerns surrounding crane transportation dynamics. On the lattice boom crane, increasing the load block and moving the dolly as far forward as permit policy will allow is beneficial. This reduces the overall load on the rear carrier axles without significant dynamic increases. The boom structure is so light the dolly axle loads remain low compared to the carrier. The telescoping boom crane experiences similar trends. The boom cantilever does not adversely affect the rest of the system and increasing the load block is beneficial for reducing carrier axle loads provided the dolly axle loads are low.

Comparing the crane response to the response of a five axle truck and semi-trailer model was performed. These results showed that the dynamic forces generated by a truck and semi-trailer lie between the loads generated by the two very different carrier suspension systems. Additionally, the results indicate that a truck utilizing an identical suspension as a crane generates similar peak dynamic loads. This indicates, that the permit weights should take into consideration the suspension system the vehicle is implementing.

( This page is intentionally left blank. )

# CHAPTER 8
# CONCLUSION

## 8.1 Summary

A mathematical model of crane with boom support dolly was generated. The finite element method was used to generate boom equations of motion. From these equations a reduced set of modal equations was generated for simulation. The boom was coupled with the rigid body carrier and dolly. Four suspension sub-models were generated. Suspensions were combined with the carrier and dolly through a common force displacement relationship.

System dynamics were determined using two-part approach. First, quarter truck models of each suspension were generated. Since suspension type is a key factor in crane transportation dynamics, the quarter trucks were used to establish the behavior of each suspension. Tire force frequency response plots were used to compare suspensions and establish the factors affect their performance.

After the quarter truck, simulation results of the entire crane model were used to determine the dynamic road loads trends associated with each type of crane. Mode shape and power spectral density plots focused on establishing the motion of the crane while axle load plots present the forces subjected to the roadway.

## 8.2 General Simulation Results

Suspension type is the single most important factor affecting crane dynamic road loads. The walking beam suspension was traditionally used on crane carriers while modern hydraulic cranes commonly use hydro-pneumatic suspension. Quarter truck results established that the hydro-pneumatic suspension produces a huge reduction in dynamic load compared to the traditional walking beam. The crane simulation supported the quarter truck results. Power spectral density plots revealed significant power reduction at the sprung mass bounce frequencies and significant reductions were seen in the carrier dynamic load. The air ride found on the modern dollies is a marginal improvement over its leaf spring predecessor. Though the dynamic improvement seen in air ride is marginal, it is an important consideration on a dolly accompanying a hydro-pneumatic carrier. The simulation results support the idea of establishing weight permits that take into consideration the suspension implemented on the vehicle.

A truck model was developed to compare the dynamic loads of the a five axle truck to a crane. The simulation results showed that cranes implementing a walking beam suspension generated higher dynamic loads, while hydro-pneumatic cranes generated lower dynamic loads. This would indicate that the loads generated by a truck are not significantly different then the loads associated with a crane.

Boom vibration has a marginal affect on dynamic road loads. Lattice booms have low mass and average a fairly high section inertia resulting in a high boom free vibration frequencies. Reduced free vibration frequencies moves the boom and dolly into a resonant bounce range and increase the whipping effect on the rear carrier tandem. The telescoping boom has much higher mass resulting in reduced boom free vibration frequencies. Again, low lattice boom frequencies enter the boom and dolly into a resonant bounce range. The flexible boom reduces the effect that the carrier and dolly dynamic loads have on each other.

Load block and dolly connection are two concerns surrounding crane transportation dynamics. On the lattice boom crane, increasing the load block and moving the dolly as far

forward as permit policy will allow is beneficial. This reduces the overall load on the rear carrier axles without significant dynamic increases. The boom structure is so light that the dolly axle loads remain low compared to the carrier. The telescoping boom crane experiences similar trends. The boom cantilever does not adversely affect the rest of the system and increasing the load block is beneficial for reducing carrier axle loads provided that the dolly axle loads are low.

### 8.3 Recommendations for Future Work

This research encompassed the mathematical derivation and simulation of crane transportation dynamics. The general trends of the quarter truck and crane simulation are consistent with other road vehicle research. Furthermore, the modeling methods of this work have been applied to a tractor semi-trailer in a parallel study as part of this same project. The results of the tractor semi-trailer simulation are in strong agreement with published experimental results and thus, the crane simulation results appear valid [8]. Still, to ensure accuracy of the crane simulation it is recommended that this simulation is experimental verified through tests on an actual crane.

The model parameters used in this study were generated for representative comparison only. Suspension properties were gained from credible vehicle dynamics research. To accurately characterize the dynamics of a specific crane, detailed information on carrier and dolly inertia and boom properties are needed.

# APPENDIX A
# DERIVATION OF FINITE ELEMENT MATRICES

## A.1 Mass Matrix

The mass matrix is calculated from

$$[M] = \int \rho A \{N\}^T \{N\} du \, .$$

An arbitrary element of the mass matrix will take the form

$$M_{ij} = \int_0^L \rho \left( A_1 + \frac{x}{L} A_2 \right) N_i(x) N_j(x) dx$$

where the indicies i and j both range from 1 to 4. For example $M_{11}$ is

$$M_{11} = \int_0^L \rho \left( A_1 + \frac{x}{L} A_2 \right) N_1(x) N_1(x) dx = \rho L \left( \frac{3A_2 + 13A_1}{35} \right).$$

The resulting mass matrix is

$$[M] = \rho L \begin{bmatrix} \frac{3}{35}A_2 + \frac{13}{35}A_1 & \left(\frac{1}{60}A_2 + \frac{11}{210}A_1\right)L & \frac{9}{140}A_2 + \frac{9}{70}A_1 & \left(\frac{-1}{70}A_2 + \frac{-13}{420}A_1\right)L \\ \left(\frac{1}{60}A_2 + \frac{11}{210}A_1\right)L & \left(\frac{1}{280}A_2 + \frac{1}{105}A_1\right)L^2 & \left(\frac{1}{60}A_2 + \frac{13}{420}A_1\right)L & \left(\frac{-1}{280}A_2 + \frac{-1}{140}A_1\right)L^2 \\ \frac{9}{140}A_2 + \frac{9}{70}A_1 & \left(\frac{1}{60}A_2 + \frac{13}{420}A_1\right)L & \frac{2}{7}A_2 + \frac{13}{35}A_1 & \left(\frac{-1}{28}A_2 + \frac{-11}{210}A_1\right)L \\ \left(\frac{-1}{70}A_2 + \frac{-13}{420}A_1\right)L & \left(\frac{-1}{280}A_2 + \frac{-1}{140}A_1\right)L^2 & \left(\frac{-1}{28}A_2 + \frac{-11}{210}A_1\right)L & \left(\frac{1}{168}A_2 + \frac{1}{105}A_1\right)L^2 \end{bmatrix}.$$

## A.2 Bending Stiffness Matrix

The linear stiffness matrix is calculated from

$$[K] = \int A \{B\}^T [D] \{B\} du \, .$$

Recall from the text that $\{B\}$ is defined as

$$\{B\} = -y \frac{d^2\{N\}}{dx^2} \, .$$

An arbitrary element of the stiffness matrix will take the form

$$K_{ij} = \int_0^L \left( A_1 + \frac{x}{L} A_2 \right) \left( -y \frac{d^2}{dx^2} \left( N_i(x) \right) \right) E \left( -y \frac{d^2}{dx^2} \left( N_j(x) \right) \right)$$

where the indices i and j both range from 1 to 4. For example, $K_{11}$ is

$$K_{11} = \int_0^L \left( A_1 + \frac{x}{L} A_2 \right) \left( -y \frac{d^2}{dx^2} \left( N_1(x) \right) \right) E \left( -y \frac{d^2}{dx^2} \left( N_1(x) \right) \right) = \frac{E}{L} \left( 3A_2 + 4A_1 \right) y^2 .$$

The resulting stiffness matrix is

$$[K] = \frac{E}{L^3} \begin{bmatrix} 6(A_2 + 2A_1)y^2 & 2L(A_2 + 3A_1)y^2 & -6(A_2 + 2A_1)y^2 & 2L(2A_2 + 3A_1)y^2 \\ 2L(A_2 + 3A_1)y^2 & L^2(A_2 + 4A_1)y^2 & -2L(A_2 + 3A_1)y^2 & L^2(A_2 + 2A_1)y^2 \\ -6(A_2 + 2A_1)y^2 & -2L(A_2 + 3A_1)y^2 & 6(A_2 + 2A_1)y^2 & -2L(2A_2 + 3A_1)y^2 \\ 2L(2A_2 + 3A_1)y^2 & L^2(A_2 + 2A_1)y^2 & -2L(2A_2 + 3A_1)y^2 & L^2(3A_2 + 4A_1)y^2 \end{bmatrix}.$$

Recognizing that

$$I = \int y^2 dA$$

then the matrix can be reduced to

$$[K] = \frac{E}{L^3} \begin{bmatrix} 6(I_2 + 2I_1) & 2L(I_2 + 3I_1) & -6(I_2 + 2I_1) & 2L(2I_2 + 3I_1) \\ 2L(I_2 + 3I_1) & L^2(I_2 + 4I_1) & -2L(I_2 + 3I_1) & L^2(I_2 + 2I_1) \\ -6(I_2 + 2I_1) & -2L(I_2 + 3I_1) & 6(I_2 + 2I_1) & -2L(2I_2 + 3I_1) \\ 2L(2I_2 + 3I_1) & L^2(I_2 + 2I_1) & -2L(2I_2 + 3I_1) & L^2(3I_2 + 4I_1) \end{bmatrix}.$$

## A.3 Gravitational Force Matrix

The gravitational force matrix is calculated from

$$\{F_g\} = \int \mathsf{r} A \{N\}^T du .$$

An arbitrary element of the gravitational force matrix will take the form

$$F_{gi} = \int_0^L \mathsf{r} \left( A_1 + \frac{x}{L} A_2 \right) N_i(x) dx$$

where the indices i and j both range from 1 to 4. For example, $F_{g1}$ is

$$F_{g1} = \int_0^L \mathsf{r}\left( A_1 + \frac{x}{L} A_2 \right) N_1(x) dx = \mathsf{r} L^2 \left( \frac{-1}{20} A_2 - \frac{1}{12} A_1 \right).$$

The resulting gravitational force matrix is

$$\{F_g\} = \mathsf{r} L \begin{Bmatrix} \frac{3}{20} A_2 + \frac{1}{2} A_1 \\ \left( \frac{1}{30} A_2 + \frac{1}{12} A_1 \right) L \\ \frac{7}{20} A_2 + \frac{1}{2} A_1 \\ \left( \frac{-1}{20} A_2 - \frac{1}{12} A_1 \right) L \end{Bmatrix}.$$

( This page is intentionally left blank. )

# APPENDIX B
# DERIVATION OF SUSPENSION SUB-MODELS

The bond graph modeling technique is used to formulate state and output equations for the suspension sub-models. In the derivations, the following relationships are used.

| Inertia | Capacitor | Transformer | Flow Junction | Effort Junction |
|---|---|---|---|---|
| $p = If$ | $q = Ce$ | $e1 = m \cdot e2$ | $e1 + e2 + e3 = 0$ | $f1 + f2 + f3 = 0$ |
| Resistor | | $f1 \cdot m = f2$ | $f1 = f2 = f3$ | $e1 = e2 = e3$ |
| $e = Rf$ | | | | |

## B.1 Hydro-pneumatic Suspension Derivation

The bond graph representation of the two ram hydro-pneumatic sub-model is shown below.

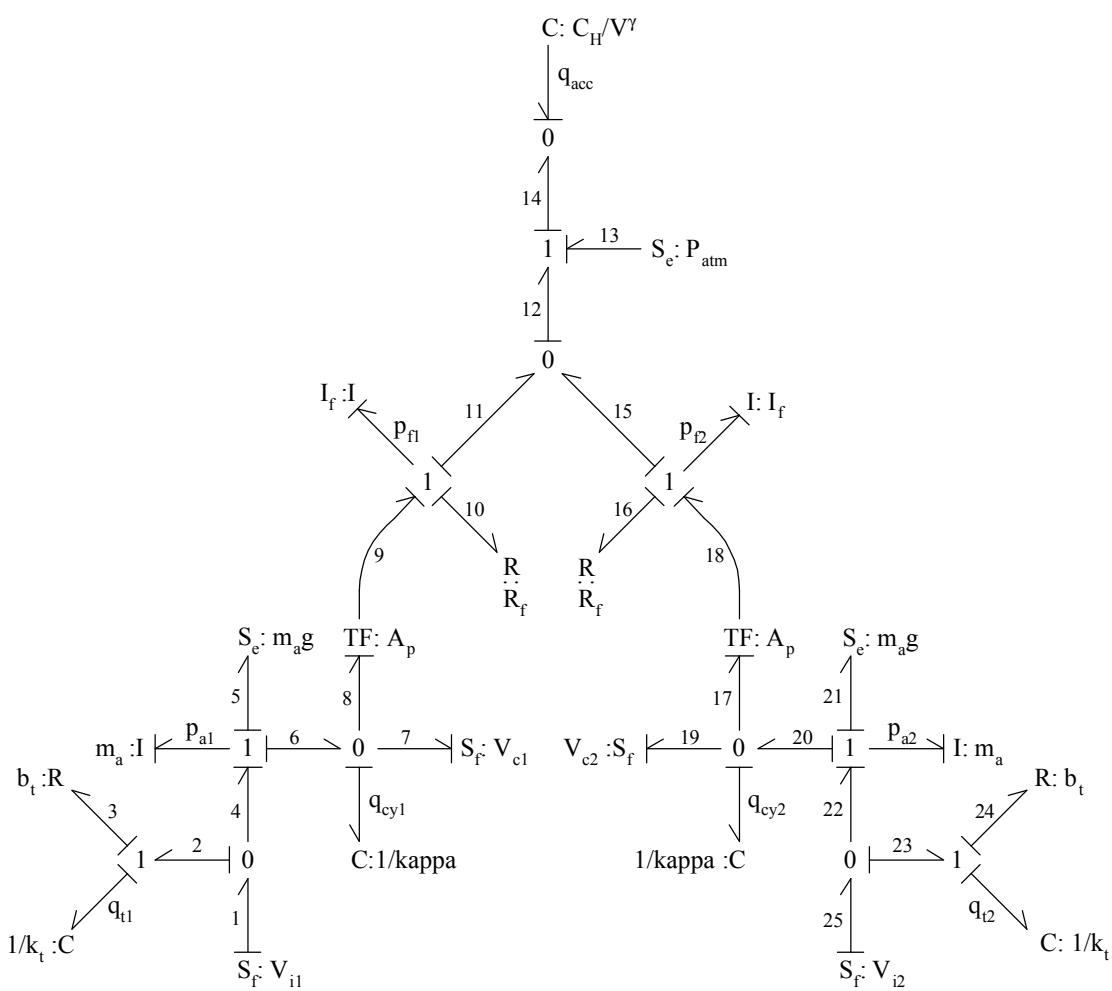

### B.1.1 Derivation of State Equations From the Bond Graph

The flow on the tire dampers is determined by:

$$f3 = f2 = f1 - f4 = v_{i1} - \frac{p_{a1}}{m_a}$$
$$f24 = f23 = f25 - f22 = v_{i2} - \frac{p_{a2}}{m_a}.$$

<u>Left Half of the Suspension</u>

The displacement across the left tire spring is

$$\dot{q}_{t1} = f2 = f1 - f4 = v_{i1} - \frac{p_{a1}}{m_a}.$$

The momentum of the left axle mass is

$$\dot{p}_{a1} = e4 - e5 - e6 = e2 - m_a g - \mathsf{k} q_{cy1} = k_t q_t + b_t f3 - m_a g - \mathsf{k} q_{cy1}$$

and substituting the left tire damper flow relation yields

$$\dot{p}_{a1} = k_t q_{t1} + b_t \left( v_{i1} - \frac{p_{a1}}{m_a} \right) - m_a g - \mathsf{k} q_{cy1}.$$

The displacement on the left hydraulic ram stiff spring is

$$\dot{q}_{cy1} = f6 - f7 - f8 = \frac{p_{a1}}{m_a} - v_{c1} - \frac{1}{A_p} \frac{p_{f1}}{I_f}.$$

The momentum of the hydraulic fluid in the left line is

$$\dot{p}_{f1} = e9 - e10 - e11 = \frac{1}{A_p} e8 - R_f f10 - e12 = \frac{\mathsf{k}}{A_p} q_{cy1} - R_f \frac{p_{f1}}{I_f} - e14 + e13$$

$$= \frac{\mathsf{k}}{A_p} q_{cy1} - R_f \frac{p_{f1}}{I_f} - \frac{C_H}{V^{\mathsf{g}}} + P_{atm}.$$

<u>Right Half of the Suspension</u>

The displacement across the right tire is

$$\dot{q}_{t2} = f23 = f25 - f22 = v_{i2} - \frac{p_{a2}}{m_a}.$$

The momentum of the right axle mass is

$$\dot{p}_{a2} = e22 - e21 - e20 = e23 - m_a g - \mathsf{k} q_{cy2} = k_t q_{t2} + b_t f24 - m_a g - \mathsf{k} q_{cy1}$$

and substituting the right tire damper flow relation yields

$$\dot{p}_{a2} = k_t q_{t2} + b_t \left( v_{i2} - \frac{p_{a2}}{m_a} \right) - m_a g - \mathsf{k} q_{cy2}.$$

The displacement on the right stiff hydraulic ram spring is

$$\dot{q}_{cy2} = f20 - f19 - f17 = \frac{p_{a2}}{m_a} - v_{c2} - \frac{1}{A_p} \frac{p_{f2}}{I_f}.$$

The momentum of the hydraulic fluid in the right line is

$$\dot{p}_{f2} = e18 - e16 - e15 = \frac{1}{A_p} e17 - R_f f16 - e12 = \frac{\mathsf{k}}{A_p} q_{cy2} - R_f \frac{p_{f2}}{I_f} - e14 + e13$$

$$= \frac{\mathsf{k}}{A_p} q_{cy2} - R_f \frac{p_{f2}}{I_f} - \frac{C_H}{V^{\mathsf{g}}} + P_{atm}.$$

<u>Accumulator Equation</u>

The displacement of the nitrogen in the accumulator is

$$\dot{q}_{acc} = -f14 = -f12 = -f11 - f15 = -\frac{p_{f1}}{I_f} - \frac{p_{f2}}{I_f}.$$

<u>Final State Equations</u>

The final state equations are:

$$\dot{q}_{t1} = v_{i1} - \frac{p_{a1}}{m_a}$$

$$\dot{p}_{a1} = k_t q_{t1} + b_t v_{i1} - \frac{b_t}{m_a} p_{a1} - m_a g - \mathsf{k} q_{cy1}$$

$$\dot{q}_{cy1} = \frac{p_{a1}}{m_a} - v_{c1} - \frac{p_{f1}}{A_p I_f}$$

$$\dot{p}_{f1} = \frac{\mathsf{k}}{A_p} q_{cy1} - \frac{R_f}{I_f} p_{f1} - \frac{C_H}{V^{\mathsf{g}}} + P_{atm}$$

$$\dot{q}_{t2} = v_{i2} - \frac{p_{a2}}{m_a}$$

$$\dot{p}_{a2} = k_t q_{t2} + b_t v_{i2} - \frac{b_t}{m_a} p_{a2} - m_a g - \mathsf{k} q_{cy2}$$

$$\dot{q}_{cy2} = \frac{p_{a2}}{m_a} - v_{c2} - \frac{p_{f2}}{A_p I_f}$$

$$\dot{p}_{f2} = \frac{\mathsf{k}}{A_p} q_{cy2} - \frac{R_f}{I_f} p_{f2} - \frac{C_H}{V^{\mathsf{g}}} + P_{atm}$$

$$\dot{q}_{acc} = -\frac{p_{f1}}{I_f} - \frac{p_{f2}}{I_f}$$

B.1.2 Derivation of the Force Equations From the Bond Graph

Left Side Force Equations

The left tire force is

$$F_{i1} = e1 = e2 = k_t q_{t1} + b_t f3$$

and substituting the left tire damper flow relation yields

$$F_{i1} = k_t q_{t1} + b_t \left( v_{i1} - \frac{p_{a1}}{m_a} \right).$$

The left suspension connection point force is

$$F_{c1} = e7 = \mathsf{k} q_{cy1}.$$

Right Side Force Equations

The right tire force is

$$F_{i2} = e25 = e23 = k_t q_{t2} + b_t f24$$

and substituting the left tire damper flow relation yields

$$F_{i2} = k_t q_{t2} + b_t \left( v_{i2} - \frac{p_{a2}}{m_a} \right).$$

The right suspension connection point force is

$$F_{c2} = e19 = \mathsf{k} q_{cy2}.$$

<u>Final Force Equations</u>

The final output equations are

$$\begin{aligned} F_{c1} &= \mathsf{k} q_{cy1} \\ F_{i1} &= k_t q_{t1} + b_t v_{i1} - \frac{b_t}{m_a} p_{a1} \\ F_{c2} &= \mathsf{k} q_{cy2} \\ F_{i2} &= k_t q_{t2} + b_t v_{i2} - \frac{b_t}{m_a} p_{a2} \end{aligned}.$$

### B.1.3 Determining Initial Conditions

Assume the derivatives of all the states are initially zero:

$$\dot{q}_{t1} = \dot{p}_{a1} = \dot{q}_{cy1} = \dot{p}_{f1} = \dot{q}_{t2} = \dot{p}_{a2} = \dot{q}_{cy2} = \dot{p}_{f2} = \dot{q}_{acc} = 0.$$

Assume there is no initial momentum:

$$\dot{p}_{a1} = \dot{p}_{f1} = \dot{p}_{a2} = \dot{p}_{f2} = 0.$$

The initial condition force on the hydraulic rams at the rigid body connection point is $F_{IC}$.

<u>Initial Conditions From the Force Equations</u>

The left connection force equation is

$$F_{c1} = F_{IC} = \mathsf{k} q_{cy1}$$

or

$$q_{cy1} = \frac{F_{IC}}{\mathsf{k}}.$$

Similarly, the right connection point force equation is

$$q_{cy2} = \frac{F_{IC}}{\mathsf{k}}.$$

<u>Initial Conditions From the State Equations</u>

The displacement of the left tire spring is

$$\dot{p}_{a1} = 0 = k_t q_{t1} + b_t 0 - \frac{b_t}{m_a} 0 - m_a g - \frac{\mathsf{k}}{\mathsf{k}} F_{IC}$$

or

$$q_{t1} = \frac{m_a}{k_t} g + \frac{1}{k_t} F_{IC} = \frac{F_{IC} + m_a g}{k_t}.$$

Similarly, the displacement of the right tire spring is

$$q_{t2} = \frac{F_{IC} + m_a g}{k_t}.$$

The displacement of the nitrogen in the accumulator is

$$\dot{p}_{f1} = 0 = \frac{\mathsf{k}}{A} \frac{F_{IC}}{\mathsf{k}} - \frac{R_f}{I_f} 0 - \frac{C_H \cdot}{V^{\mathsf{g}}} + P_{atm}$$

or

$$V = \left( \frac{C_H}{\frac{F_{IC}}{A} + P_{atm}} \right)^{1/\mathsf{g}}.$$

<u>Final State Initial Condition Equations</u>

The final state initial conditions are:

$$q_{t1} = \frac{F_{IC} + m_a g}{k_t}$$

$$p_{a1} = 0$$

$$q_{cy1} = \frac{F_{IC}}{\mathrm{k}}$$

$$p_{f1} = 0$$

$$q_{t2} = \frac{F_{IC} + m_a g}{k_t}$$

$$p_{a2} = 0$$

$$q_{cy2} = \frac{F_{IC}}{\mathrm{k}}$$

$$p_{f2} = 0$$

$$q_{acc} = \left( \frac{C_H}{\frac{F_{IC}}{A} + P_{atm}} \right)^{1/\mathrm{g}} .$$

B.2 Air Ride Suspension Derivation

The bond graph representation of the air ride sub-model is shown below.

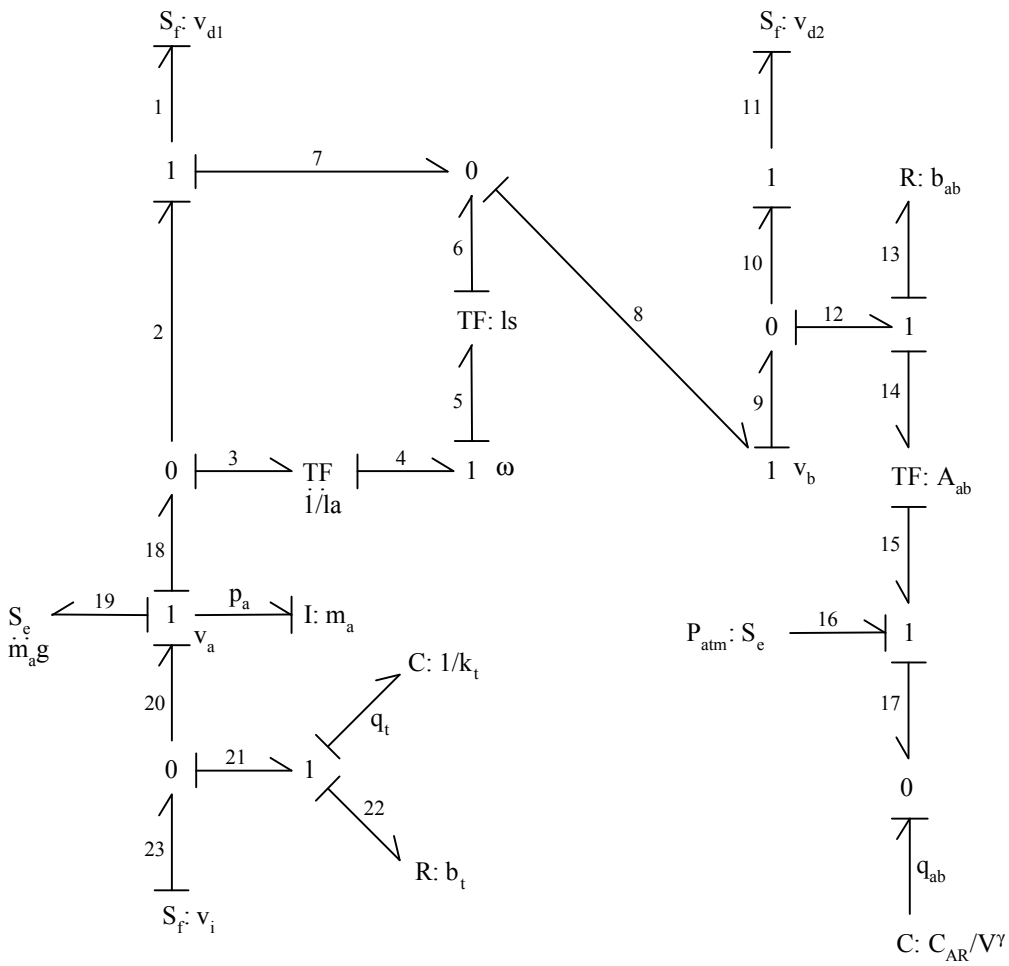


B.2.1 Derivation of State Equations From the Bond Graph

The flow on the tire and suspension dampers is determined by:

$$f22 = f21 = f23 - f20 = v_i - \frac{p_a}{m_a}$$

$$f13 = f12 = f9 - f10 = f9 - f11 = f8 - v_{d2} = f7 + f6 - v_{d2} = f1 + lsf5 - v_{d2}$$

$$= f1 + lsf4 - v_{d2} = f1 - \frac{ls}{la} f3 - v_{d2} = f1 - \frac{ls}{la}\left(f18 - f2\right) - v_{d2}$$

$$= f1 - \frac{ls}{la}\left(\frac{p_a}{m_a} - f1\right) - v_{d2} = v_{d1}\left(1 - \frac{ls}{la}\right) + \frac{ls}{la}\frac{p_a}{m_a} - v_{d2}$$

<u>Tire and Axle Equations</u>

The displacement across the tire spring is

$$\dot{q}_t = f21 = f23 - f20 = v_i - \frac{p_a}{m_a}.$$

The momentum of the axle mass is

$$\dot{p}_a = e20 - e18 - e19 = e21 - e3 - m_a g = k_t q_t + b_t f22 - e3 - m_a g$$

$$\begin{aligned}
&= k_t q_t + b_t f22 - \frac{1}{la} e4 - m_a g = k_t q_t + b_t f22 - \frac{1}{la} e5 - m_a g \\
&= k_t q_t + b_t f22 - \frac{ls}{la} e6 - m_a g = k_t q_t + b_t f22 - \frac{ls}{la} e8 - m_a g \\
&= k_t q_t + b_t f22 - \frac{ls}{la} e9 - m_a g = k_t q_t + b_t f22 - \frac{ls}{la} e12 - m_a g \\
&= k_t q_t + b_t f22 - \frac{ls}{la}(e13 + e14) - m_a g \\
&= k_t q_t + b_t f22 - \frac{ls}{la}(b_{ab} f13 + A_{ab} e15) - m_a g \\
&= k_t q_t + b_t f22 - \frac{ls}{la}(b_{ab} f13 + A_{ab}(e17 - e16)) - m_a g \\
&= k_t q_t + b_t f22 - \frac{ls}{la}\left\{ b_{ab} f13 + A_{ab}\left( \frac{C_{AR}}{V^{g}} - P_{atm} \right) \right\} - m_a g
\end{aligned}.$$

Substituting the tire damper flow relation yields

$$\dot{p}_{a1} = k_t q_t + b_t\left( v_i - \frac{p_a}{m_a} \right) - \frac{ls}{la}\left[ b_{ab}\left\{ v_{d1}\left( 1 - \frac{ls}{la} \right) + \frac{ls}{la}\frac{p_a}{m_a} - v_{d2} \right\} \right] - \frac{ls}{la} A_{ab}\left( \frac{C_{AR}}{V^{g}} - P_{atm} \right) - m_a g.$$

<u>Air Bag State Equation</u>

The displacement of the air in the air bag is

$$\dot{q}_{ab} = -f17 = -f15 = -A_{ab} f14 = -A_{ab} f12 = -A_{ab}(f9 - f10) = -A_{ab}(f8 - f11)$$

$$
\begin{aligned}
&= -A_{ab}\left(f7 + f6 - v_{d2}\right) = -A_{ab}\left(f1 + lsf5 - v_{d2}\right) = -A_{ab}\left(f1 + lsf4 - v_{d2}\right) \\
&= -A_{ab}\left(f1 + \frac{ls}{la} f3 - v_{d2}\right) = -A_{ab}\left(f1 + \frac{ls}{la}\left(f18 - f2\right) - v_{d2}\right) \\
&= -A_{ab}\left\{f1 + \frac{ls}{la}\left(\frac{p_a}{m_a} - f1\right) - v_{d2}\right\} = -A_{ab}\left\{v_{d1} + \frac{ls}{la}\left(\frac{p_a}{m_a} - v_{d1}\right) - v_{d2}\right\} \\
&= A_{ab}\left\{v_{d2} - v_{d1}\left(1 - \frac{ls}{la}\right) - \frac{ls}{la}\frac{p_a}{m_a}\right\}
\end{aligned}
.
$$

<u>Final State Equations</u>

The final state equations are:

$$
\begin{aligned}
\dot{q}_t &= v_i - \frac{p_a}{m_a} \\
\dot{p}_{a1} &= k_t q_t + b_t\left(v_i - \frac{p_a}{m_a}\right) - \frac{ls}{la}\left[b_{ab}\left\{v_{d1}\left(1 - \frac{ls}{la}\right) + \frac{ls}{la}\frac{p_a}{m_a} - v_{d2}\right\}\right] - \frac{ls}{la} A_{ab}\left(\frac{C_{AR}}{V^{\mathrm{g}}} - P_{atm}\right) - m_a g \\
\dot{q}_{ab} &= A_{ab}\left\{v_{d2} - v_{d1}\left(1 - \frac{ls}{la}\right) - \frac{ls}{la}\frac{p_a}{m_a}\right\}
\end{aligned}
.
$$

## B.2.2 Derivation of the Force Equations From the Bond Graph

<u>Road Force Equation</u>

The tire force is

$$F_i = e24 = e23 = e21 = k_t q_t + e22 = k_t q_t + b_t f22$$

and substituting tire damper flow relation yields

$$F_{i1} = k_t q_t + b_t\left(v_i - \frac{p_a}{m_a}\right).$$

<u>Connection Force Equations</u>

The pin connection force is

$$F_{d1} = e1 = e2 + e7 = e3 + e8 = \frac{1}{la} e4 + e8 = \frac{1}{la} e5 + e8 = \frac{ls}{la} e6 + e8 = \frac{ls}{la} e8 + e8$$

$$= e8\left(1+\frac{ls}{la}\right) = e9\left(1+\frac{ls}{la}\right) = e12\left(1+\frac{ls}{la}\right) = \left(e13+e14\right)\left(1+\frac{ls}{la}\right)$$

$$= \left(b_t f13 + A_{ab} e15\right)\left(1+\frac{ls}{la}\right) = \left(b_t f13 + A_{ab}\left(e17-e16\right)\right)\left(1+\frac{ls}{la}\right).$$

$$= \left\{b_t f13 + A_{ab}\left(\frac{C_{AR}}{V^{\gamma}} - P_{atm}\right)\right\}\left(1+\frac{ls}{la}\right)$$

Substituting the suspension damper flow relations yields

$$F_{d1} = \left[b_{ab}\left\{v_{d1}\left(1-\frac{ls}{la}\right)+\frac{ls}{la}\frac{p_a}{m_a} - v_{d2}\right\} + A_{ab}\left(\frac{C_{AR}}{V^{\gamma}} - P_{atm}\right)\right]\left(1+\frac{ls}{la}\right)$$

The air bag damper connection force is

$$F_{d2} = e11 = e10 = e12 = e13 + e14 = b_t f13 + A_{ab} e15 = b_t f13 + A_{ab}\left(e17-e16\right)$$

$$= b_t f13 + A_{ab}\left(\frac{C_{AR}}{V^{\gamma}} - P_{atm}\right).$$

Substituting the suspension damper flow relation yields

$$F_{d2} = b_{ab}\left\{v_{d1}\left(1-\frac{ls}{la}\right)+\frac{ls}{la}\frac{p_a}{m_a} - v_{d2}\right\} + A_{ab}\left(\frac{C_{AR}}{V^{\gamma}} - P_{atm}\right).$$

<u>Final Force Equations</u>

The final force equations are:

$$F_{i1} = k_t q_t + b_t\left(v_i - \frac{p_a}{m_a}\right)$$

$$F_{d1} = \left[b_{ab}\left\{v_{d1}\left(1-\frac{ls}{la}\right)+\frac{ls}{la}\frac{p_a}{m_a} - v_{d2}\right\} + A_{ab}\left(\frac{C_{AR}}{V^{\gamma}} - P_{atm}\right)\right]\left(1+\frac{ls}{la}\right).$$

$$F_{d2} = b_{ab}\left\{v_{d1}\left(1-\frac{ls}{la}\right)+\frac{ls}{la}\frac{p_a}{m_a} - v_{d2}\right\} + A_{ab}\left(\frac{C_{AR}}{V^{\gamma}} - P_{atm}\right)$$

### B.2.3 Determining Initial Conditions

Assume the derivatives of all the states are initially zero:

$$\dot{q}_t = \dot{p}_a = \dot{q}_{ab} = 0 .$$

Assume there is no initial momentum or initial input velocity

$$p_a = v_i = v_{d1} = v_{d2} = 0 .$$

The initial condition force, $F_{IC}$, will be considered at a point in the rigid body that is directly above the axle. Initial condition forces are not specified at the two connection points because the mass of the trailing arm is lumped into the axle.

<u>Initial Conditions From the Force Equations</u>

The resulting force on the tire is

$$F_{IC} + m_a g = k_t q_t .$$

Therefore, the tire displacement is

$$q_t = \frac{F_{IC} + m_a g}{k_t} .$$

<u>Initial Conditions From the State Equations</u>

The momentum of the axle is

$$\dot{p}_{a1} = 0 = k_t q_t + b_t\left(0 - \frac{0}{m_a}\right) - \frac{ls}{la}\left[b_{ab}\left\{0\left(1 - \frac{ls}{la}\right) + \frac{ls}{la}\frac{0}{m_a} - 0\right\}\right] - \frac{ls}{la} A_{ab}\left(\frac{C_{AR}}{q_{ab}^{\gamma}} - P_{atm}\right) - m_a g$$

or

$$k_t q_t + \frac{ls}{la} A_{ab}\left(\frac{C_{AR}}{q_{ab}^{\gamma}} - P_{atm}\right) - m_a g = 0 .$$

Substituting in the tire displacement initial condition yields

$$k_t\left(\frac{F_{IC}+m_a g}{k_t}\right)+\frac{ls}{la}A_{ab}\left(\frac{C_{AR}}{q_{ab}^{\gamma}}-P_{atm}\right)-m_a g=0$$

and simplifying this equation results in

$$\frac{ls}{la}\frac{C_{AR}}{q_{ab}^{\gamma}}=\frac{F_{IC}}{A_{ab}}+\frac{ls}{la}P_{atm}\,.$$

Expressing in terms of air bag displacement yields

$$q_{ab}=\left(\frac{ls}{la}\frac{C_{AR}}{\frac{F_{IC}}{A_{ab}}+\frac{ls}{la}P_{atm}}\right)^{1/\gamma}.$$

<u>Final State Initial Condition Equations</u>

The final state initial conditions are:

$$\begin{aligned} q_{t1} &= \frac{F_{IC}+m_a g}{k_t} \\ p_a &= 0 \\ q_{ab} &= \left(\frac{ls}{la}\frac{C_{AR}}{\frac{F_{IC}}{A_{ab}}+\frac{ls}{la}P_{atm}}\right)^{1/\gamma} \end{aligned}.$$

( This page is intentionally left blank. )

# APPENDIX C
# DERIVATION OF INITIAL SUSPENSION FORCES

The initial conditions are determined to allow the system to be in static equilibrium. The basic methodology of solving the initial conditions is to solve for the forces and then set the relevant displacements. One way to determine the initial conditions is by running the system and allowing it to settle to the equilibrium point. However, this requires time for the system to settle and is an inefficient use of computing time. Therefore, an equilibrium point is determined analytically to make the program more computationally efficient.

The finite element boom model can be configured to determine the support forces at the connection points as mentioned in Section 2.2. This force is used to determine an equilibrium point for the other system components. In the model, the primary idea behind the initial conditions is to solve for the initial suspension displacements and rotations, and set the sprung mass displacements and rotations to zero. Treating boom gravity in this manner means that initially there is no bend in the boom, allowing these initial conditions to be set to zero. Since the boom model is a linear system, the initial operating point does not affect the dynamics of the system. Physically, this means that the suspension is brought up to keep the sprung mass at the zero displacement position.

For the four-axle carrier with a walking beam suspension case, the suspension support forces can be determined from statics. The same $L_{FCi}$ variables defined in Appendix A are used in this analysis. The basic equations of equilibrium can be applied in order to determine $F_{sc1}$ and $F_{sc2}$ given as

$$F_{sc1} = \frac{M_C g L_{FC2} + F_c (L_{FC2} - l_c)}{L_{FC2} - L_{FC1}}, \tag{C.1}$$

and

$$F_{sc2} = M_C g + F_c - F_{sc1}. \tag{C.2}$$

$F_{sc1}$ and $F_{sc2}$ represent the suspension support forces for the carrier. Next, the information of the forces must be propagated even further into the suspension sub-models.

The suspension sub-models used for the front and the back of the four-axle walking beam carrier are identical as illustrated in Figure 3.6. Both tires associated with a simple pair are given the same stiffness and damping coefficients and are called $k_{tirec}$ and $b_{tirec.}$ In order to determine the initial conditions, the force $F_s$ and the gravity force caused by the mass are assumed to act at the center of the beam. This means that the initial value of $\theta$ for the beam is zero. The values of interest here are the displacements in each spring. Both the front and rear tires of a single pair see the same displacement because the load is equally shared between the two tires. In essence, the walking beam groups in a particular model can be replaced by a mathematical equivalent shown in Figure C.1.

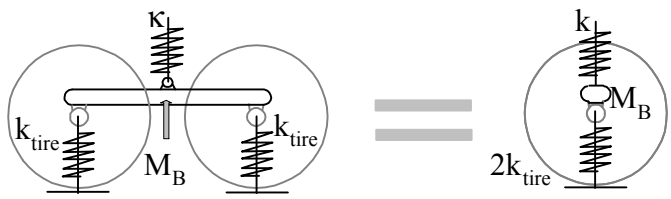


*Figure C.1 Equivalent Walking Beam Model Used to Determine Equilibrium*

This allows the equivalent tire deflection to be determined by

$$\delta_{t,i} = \frac{F_{s,i} + M_{B,i} g}{2k_{tire}}. \tag{C.3}$$

The displacements in the stiff spring ($\delta_{k,i}$) can be determined by

$$\delta_{k,i} = \frac{F_{s,i}}{k}. \tag{C.4}$$

Here the subscript 'i' denotes the front and rear group. Ideally, $\delta_{\kappa i}$ should be zero. However due to the stiff spring approximation, a small amount of deflection does occur and must be quantified in the initial conditions. The four values determined in equations (C.3) and (C.4) are the complete set of initial conditions required for this carrier model.

The derivation of the initial conditions for this particular carrier is trivial because the system is statically determinant. However, for a five and six axle carrier, there are three unknown suspension forces, making the system indeterminate because there are only two equilibrium equations. In order to determine the initial conditions for these carriers, variational calculus is used along with the principle of stationary potential energy [9]. The variational indicator is determined by summing up all of the potential energy stored in the system along with any external work terms. The variational indicator is used to determine the equations of motion using Lagrange's equations [9]. Here, the focus is on the equilibrium point of the system. Therefore, the kinetic energy terms are left out.

Mathematically, the variational indicator is given by

$$V.I. = \sum PE_i - \sum WG_j - WB, \tag{C.5}$$

where $PE_i$ denotes the potential energy stored in the suspension springs, $WG_j$ denotes the work done by gravity on the system masses, and WB denotes the work done by the boom on the system. Using the mathematical equivalent shown in Figure C.1, the five-axle walking beam carrier turns into the system shown in Figure C.2 for equilibrium.

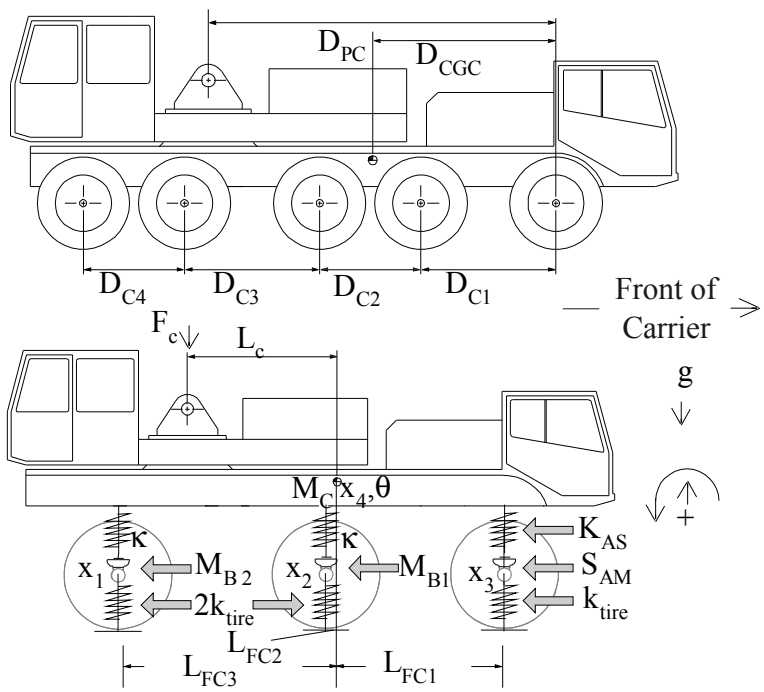


*Figure C.2 Model Simplification of a Five Axle Carrier for Equilibrium*

The potential energy stored in each spring is given by

$$PE = \frac{1}{2}(K)(x)^2, \tag{C.6}$$

where x is the displacement from the springs free length. Applying this to the five-axle carrier yields

$$\begin{aligned}\sum PE = \frac{1}{2}\Big(&2k_{tire}x_1^2 + 2k_{tire}x_2^2 + 2k_{tire}x_3^2 + K_{AS}(x_4 + L_{FC1}\theta - x_3)^2 \\ &+ k(x_4 + L_{FC2} - x_2)^2 + k(x_4 + L_{FC3}\theta - x_1)^2\Big).\end{aligned} \tag{C.7}$$

Next, all of the work done must be defined. The general equations for this is given by

$$WG_j = \int\left(F_j \bullet ds_j\right), \tag{C.8}$$

where '$F_j$' denotes the particular gravity force associated with a given mass and '$ds_j$' denotes the distance through which that force is applied. In this case, the force, $F_j$, is the constant force that acts opposite the displacement coordinate, $ds_j$. Due to the small angle approximation, the $ds_j$ term simply becomes the displacement coordinate associated with a particular mass element. These two facts reduces (C.8) to

$$WG_j = -F_j x_j. \tag{C.9}$$

The total work done by gravity is given by

$$\sum WG = -S_{AM} g x_3 - M_{B1} g x_1 - M_{B2} g x_2 - M_C g x_4 . \tag{C.10}$$

Additionally, the force the boom exerts on the carrier does work on the system and is given by

$$WB = -F_C \left( x_4 + L_c \mathsf{q} \right). \tag{C.11}$$

Once all of these equations are defined, the variational indicator can be determined

In this case, the variational indicator has 5 generalized coordinates. The principle of stationary potential energy states

$$\frac{\partial V.I.}{\partial x_i} = 0 , \tag{C.12}$$

where $x_i$ represents the generalized coordinates of the system.

Explicitly written in matrix form, this becomes

$$[0] = \begin{bmatrix} 2k_{tire} + \mathsf{k} & 0 & 0 & -\mathsf{k} & -\mathsf{k} L_{FC3} \\ 0 & 2k_{tire} + \mathsf{k} & 0 & -\mathsf{k} & -\mathsf{k} L_{FC2} \\ 0 & k_{tire} + K_{AS} & k_{tire} + K_{AS} & -K_{AS} & -K_{AS} L_{FC1} \\ -\mathsf{k} & -\mathsf{k} & -K_{AS} & 2\mathsf{k} + K_{AS} & \mathsf{k}\left(L_{FC3} + L_{FC2}\right) + K_{AS} L_{FC1} \\ -\mathsf{k} L_{FC3} & -\mathsf{k} L_{FC2} & -K_{AS} L_{FC1} & \mathsf{k}\left(L_{FC3} + L_{FC2}\right) + S_{AK} L_{FC1} & \mathsf{k}\left(L_{FC2}^2 + L_{FC3}^2\right) + K_{AS} L_{FC1}^2 \end{bmatrix} \begin{bmatrix} x_1 \\ x_2 \\ x_3 \\ x_4 \\ \mathsf{q} \end{bmatrix} + \begin{bmatrix} M_{B2} g \\ M_{B1} g \\ S_{AM} g \\ M_C g + F_c \\ F_C L_c \end{bmatrix} . \tag{C.13}$$

This set of equations is solved for the unknown displacements and rotations. These displacements correspond to the initial conditions of the system, but must be converted through a linear transform to the relative displacements across the suspension springs. This transformation can be given by

$$\begin{bmatrix} x_{s1} \\ x_{ss} \\ x_{s3} \\ x_{s4} \\ x_{s5} \\ x_{s6} \end{bmatrix} = \begin{bmatrix} 0 & 0 & -1 & 0 & 0 \\ 0 & 0 & 1 & -1 & -L_{FC1} \\ 0 & -1 & 0 & 0 & 0 \\ 0 & 1 & 0 & -1 & -L_{FC2} \\ -1 & 0 & 0 & 0 & 0 \\ 1 & 0 & 0 & -1 & -L_{FC3} \end{bmatrix} \begin{bmatrix} x_1 \\ x_2 \\ x_3 \\ x_4 \\ \mathsf{q} \end{bmatrix} . \tag{C.14}$$

where the physical meaning of $x_{si}$ is given in Table C.1.

*Table C.1 Physical Description of the Suspension Initial Conditions*

| Variable | Meaning |
|---|---|
| $x_{s1}$ | Displacement in independent suspension spring |
| $x_{s2}$ | Displacement in independent tire |
| $x_{s3}$ | Displacement in first stiff spring assumption |
| $x_{s4}$ | Displacement in first walking beam pair tires |
| $x_{s5}$ | Displacement in second stiff spring assumption |
| $x_{s6}$ | Displacement in second walking beam pair tires |

The same principles of variational calculus can be carried out for a six-axle carrier, yielding

$$[0] = \begin{bmatrix} 2k_{tire}+\mathrm{k} & 0 & 0 & -\mathrm{k} & -\mathrm{k}L_{FC3} \\ 0 & 2k_{tire}+\mathrm{k} & 0 & -\mathrm{k} & -kL_{FC2} \\ 0 & 0 & 2k_{tire}+\mathrm{k} & -\mathrm{k} & -\mathrm{k}L_{FC1} \\ -\mathrm{k} & -\mathrm{k} & -\mathrm{k} & 3\mathrm{k} & \mathrm{k}\left(L_{FC3}+L_{FC2}+L_{FC1}\right) \\ -\mathrm{k}L_{FC3} & -\mathrm{k}L_{FC2} & -\mathrm{k}L_{FC1} & \mathrm{k}\left(L_{FC3}+L_{FC2}+L_{FC1}\right) & \mathrm{k}\left(L_{FC2}^2+L_{FC3}^2+L_{FC1}^2\right) \end{bmatrix} \begin{bmatrix} x_1 \\ x_2 \\ x_3 \\ x_4 \\ \mathrm{q} \end{bmatrix} + \begin{bmatrix} M_{B3}g \\ M_{B2}g \\ M_{B1}g \\ M_C g + F_C \\ F_C L_C \end{bmatrix}. \tag{C.15}$$

The values for $L_{FC1}$, $L_{FC2}$, and $L_{FC3}$ are different for this case but correspond to the same physical quantities, which are the center of rotation for each respective walking beam pair as defined in Appendix A. Again, this set of equations can easily be solved to find the initial values of the generalized coordinates. The same linear transformation described in equation (C.14) can be used. However, the variables $x_{s1}$ and $x_{s2}$ now correspond to the displacement for the stiff spring assumption and the tire displacement for the walking beam group that replaced the independent group for the five axle case.

The derivation of the initial conditions for the four-axle hydro-pneumatic carrier's initial conditions are similar to a four axle-walking beam. The sub-model initial conditions are derived based on an equivalent force that sits about the center of the axle pair. In the case of the four-axle hydro-gas carrier, the equations used to determine $[F_s]$ in the four-axle walking beam case can be used to determine the initial conditions for the suspension, because the equivalent suspension forces act at the same point as a walking beam attachment point in terms of the variables used.

The six-axle hydro-pneumatic carrier's initial conditions are determined by calculating the weight of the carrier supported by each suspension group similarly to the six-axle walking beam case. This is done by applying variational calculus to a beam that is supported by three springs, which are located at the equivalent center of the hydro pneumatic pair. The can be done

because the load is equally shared between the two axles associated with a single hydro-pneumatic group. This force is then used to determine the initial displacements in the suspension by setting the velocity and acceleration terms in the state equations presented by equation (3.20) to zero and solving for the initial displacements.

All of the dolly models are statically determinant, except for the case of the air ride dolly. Variational calculus can be used for the three-axle air ride dolly case, by supporting the dolly by points directly over the axles. The initial conditions for an air ride suspension can then be derived by solving the state equations presented by (3.26) for the static conditions using the force derived from variational calculus.

The key benefit of this initial condition routine is that the equations used to determine the equilibrium point are derived independently of the equations used in the simulation. This provides a check for the set of equations used. If there is an inconsistency in the equations, it would be visible in the simulation because the initial conditions derived here would not keep the system at equilibrium. In addition to this check, the results here coincide with the results provided through the execution of the MATLAB 'TRIM' command which can also be used to determine the initial conditions of a SIMULINK model.

# APPENDIX D
# LOAD CHARACTERIZATION

A method must be selected to best express the results of the simulations in a concise and meaningful manner. Figure D.1 shows the time response of the last carrier axle for a 4 axle carrier over a 60 second time span. The first second of the response shows that the system is in equilibrium, which indicates that the initial conditions are properly set.

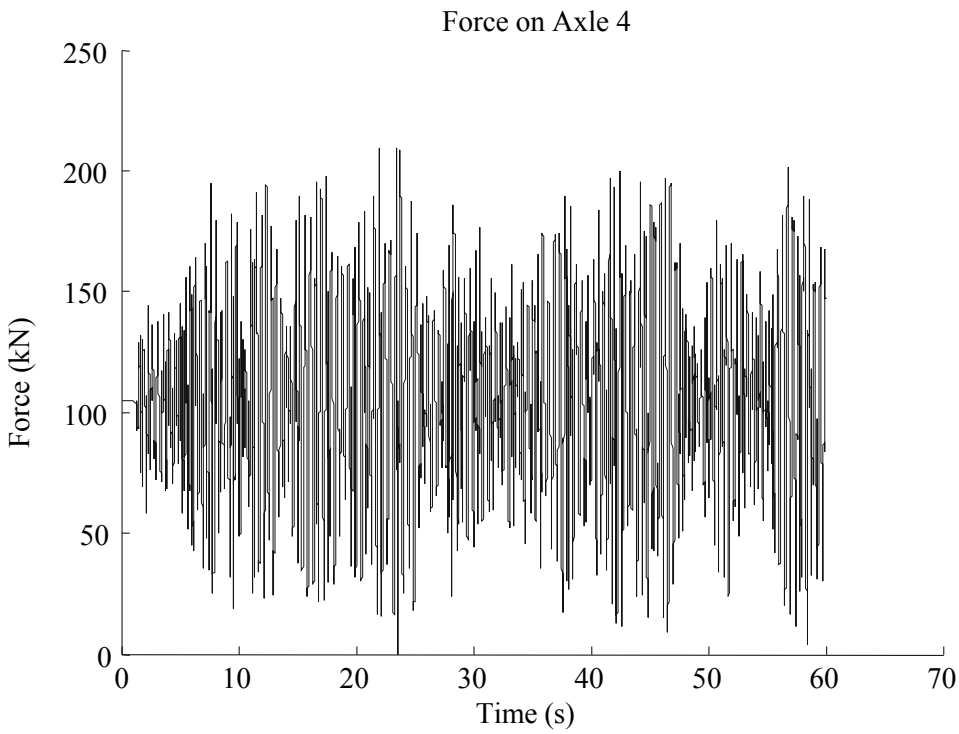


*Figure D.1 Representative Dynamic Tire Load on Axle 4*

Figure D.1 shows that the peak load is approximately 1.5 times the static load. However, it is difficult to interpret more information from the graph, and a means of looking at the data in a more concise manner is important.

A histogram counts the number of occurrences of a given data set that lie within a certain interval, and is an intrinsic plotting routine in MATLAB. Using the time response data from Figure D.1, the histogram of Figure D.2 is generated.

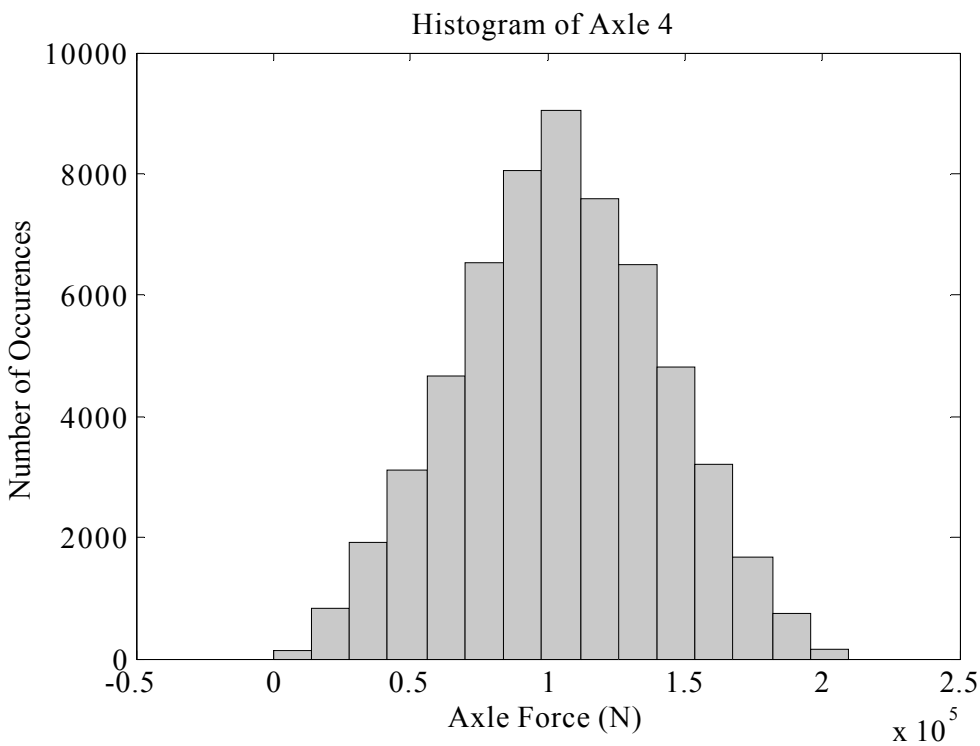


*Figure D.2 Histogram of Dynamic Loading for Axle 4*

The MATLAB function has the ability to generate numerical data regarding the number of occurrences and the mean load within a given interval. The subroutine allows the user to define the number of intervals, therefore the width of each interval is easily calculated by

$$\Delta = \frac{F_{\max} - F_{\min}}{n_{\text{int}}}. \tag{D.1}$$

From the equation, the total area under the curve is easily determined by

$$A_{total} = \Delta \sum_{i=1}^{n_{\text{int}\,erval}} Occurences_i . \tag{D.2}$$

The quantity $A_{total}$ can then be used as a scaling factor to reduce the total area under the plot to be equal to one. Scaling the total area to this value is helpful because it is a property of probability distribution functions. However, through this process, the first second of data must be truncated to eliminate the data showing that the crane is in equilibrium because it skews the distribution curve. By increasing the number of intervals, the general shape of the distribution becomes more apparent, which is shown Figure D.3. The data has been derived from the simulation of a 4 axle walking beam carrier with a three axle leaf spring dolly.

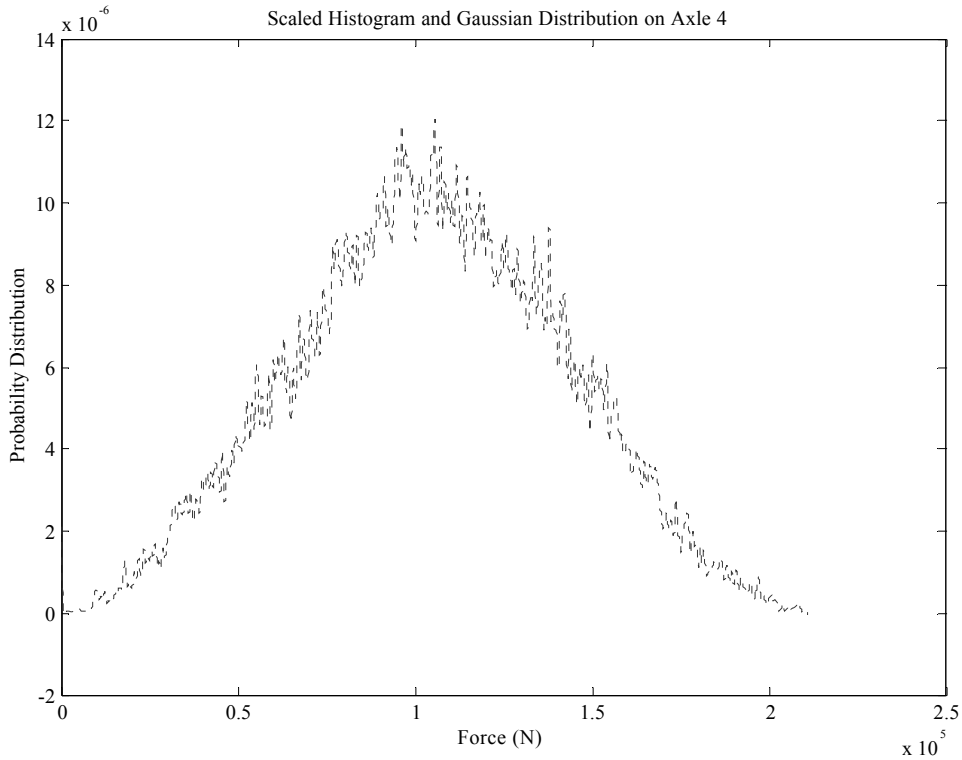


*Figure D.3 Rescaled Histogram of Dynamic Tire Load with Reduced Interval Spacing*

After looking at this plot, a Gaussian curve defined by

$$f(x) = \frac{1}{\sigma\sqrt{2\pi}} e^{\left[-\frac{(x-\mu)^2}{2\sigma^2}\right]}, \tag{D.3}$$

is superimposed on the scaled histogram data. After applying equation (D.3) to the time response data, a similarity between the two is shown in Figure D.4.

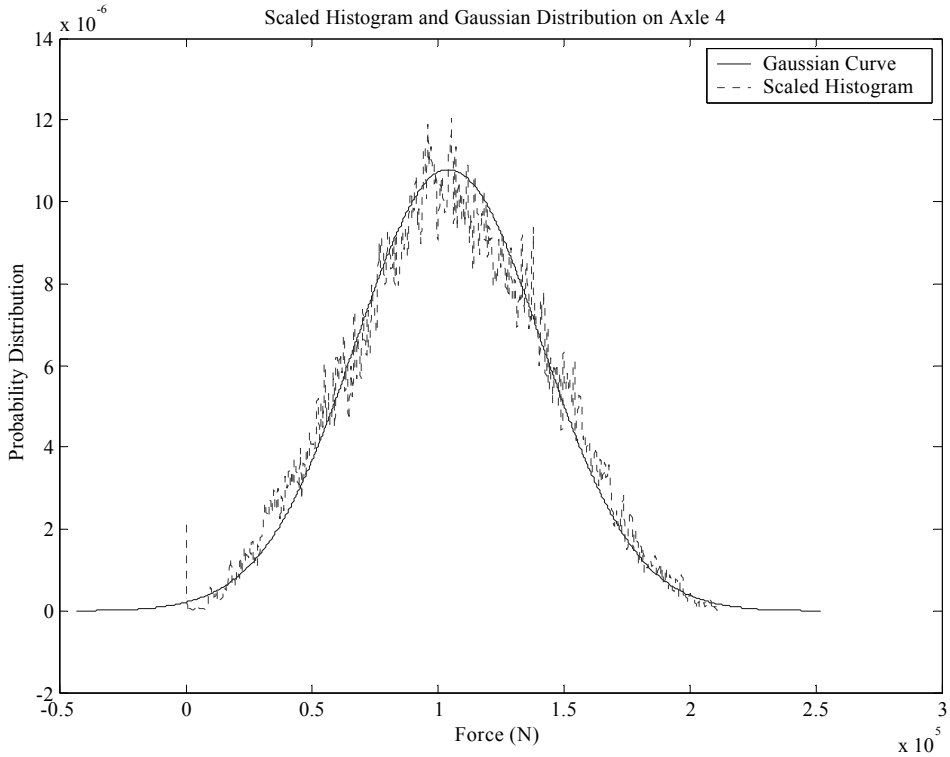


*Figure D.4 Gaussian Distribution vs. Rescaled Histogram*

In Figure D.4, a peak in the probability distribution is shown at the zero value. The non-linear tire model generates this feature in the data that is presented. The key interest is on the dynamic loads above the static weights. Although the non-linear tire model slightly distorts the distribution in the low tire force region, the effect is negligible in the upper force region of the distribution.

If the same process is used for a simulation using a larger time span, the data converges to the Gaussian curve as shown in Figure D.5 with a simulation run time of 140 seconds.Figure D.5 shows that the dynamic load converges to the Gaussian curve for the loading above the static weight. If the same plot is developed using the dolly axle which does not leave the ground in the simulation, the convergence is much more apparent as shown in Figure D.6. Now, from this result, the dynamic load of the crane can be characterized as a mean and a standard deviation. The probability distribution curves present the data in a form, which is clearer to see in comparison to the time response data. This aids in a broader understanding of the system response. The percentage of loads that lie in a certain interval can be determined by taking the area under the curve between the two endpoints of the particular interval.

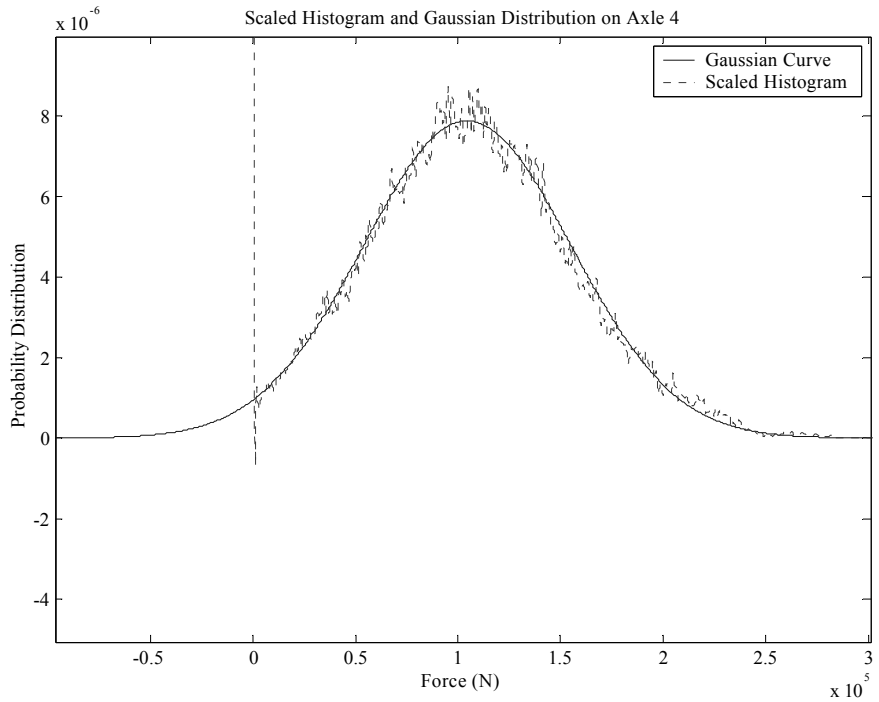


*Figure D.5 Gaussian Distribution vs. Rescaled Histogram*

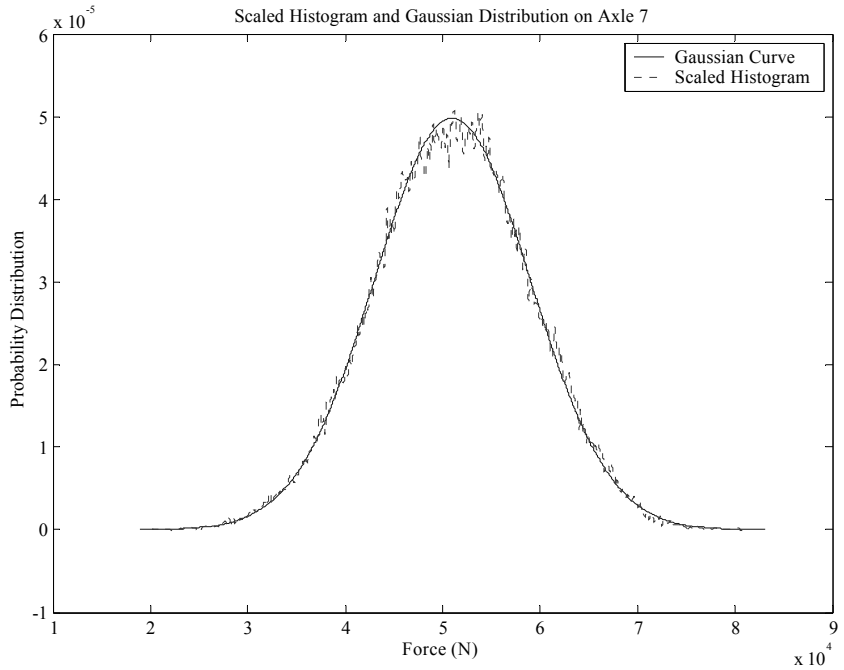


*Figure D.6 Gaussian Distribution vs. Rescaled Histogram on Seventh Axle*

The dynamic load is commonly characterized by the dynamic load coefficient defined as [8]

$$DLC = \frac{s}{F_{mean}}. \tag{D.4}$$

This measure is useful for comparing results with a common static value. However, when the static values between the cases being compared are not equal, the dynamic load coefficient does not contain enough information to represent the dynamic tire forces because it provides no indication of the actual magnitude of the force generated.

The information presented above illustrates that characterizing the dynamic loads generated by the simulation can be done by a mean and standard deviation. Using these two numbers to represent the loads generated by a system drastically simplifies the presentation of the results in a clear and concise manner.

# APPENDIX E
# QUARTER TRUCK PROPERTIES

## E.1 General Tire and Axle Properties

| Tire Properties[1] | | |
|---|---|---|
| *Wide Based Single (one tire)* | | |
| Tire spring constant ($k_t$) | $1.225 \times 10^6$ | N/m |
| Tire damping constant ($b_t$) | $1.05 \times 10^3$ | N-s/m |
| *Conventional Dual (one dual pair)* | | |
| Tire spring constant ($k_t$) | $1.64 \times 10^6$ | N/m |
| Tire damping constant ($b_t$) | $2.10 \times 10^3$ | N-s/m |
| Axle Properties | | |
| *Unsprung Axle Mass (one axle)* | | |
| Steering axle mass ($m_a$) | 635 | kg |
| Drive axle mass ($m_a$) | 1,089 | kg |

[1]Karamihas, S.M. and Gillespie, T.D., 'Characterizing trucks for dynamic load prediction,' Heavy Vehicle Systems, Special Series, Int. J. of Vehicle Design,, Vol.1, No. 1 (1993), pp. 3-19.

## E.2 Independent Suspension Properties

| Independent Suspension Properties[1] | | |
|---|---|---|
| Suspension spring constant ($k_s$) | $5.2 \times 10^5$ | N/m |
| Suspension damping constant ($b_s$) | $6.34 \times 10^3$ | N-s/m |

[1]Karamihas, S.M. and Gillespie, T.D., 'Characterizing trucks for dynamic load prediction,' Heavy Vehicle Systems, Special Series, Int. J. of Vehicle Design,, Vol.1, No. 1 (1993), pp. 3-19.

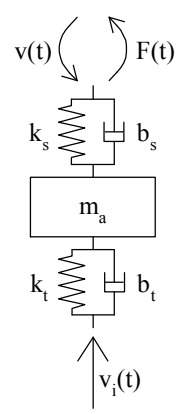

## E.3 Walking Beam Suspension Properties

| Walking Beam Suspension Properties[1] | | |
|---|---|---|
| *Unsprung Axle Mass (two axles and beam)* | | |
| Steering axle mass ($m_a$) | 1,380 | kg |
| Steering axle inertia ($I_a$) | 742 | kg |
| Drive axle mass ($m_a$) | 2,222 | kg |
| Drive axle inertia ($I_a$) | 1,266 | kg |
| *Additional Properties* | | |
| Stiff connection spring ($\kappa$) | $1 \times 10^{10}$ | N/m |
| Beam Span (L) | 1.52 | m |

[1]Karamihas, S.M. and Gillespie, T.D., 'Characterizing trucks for dynamic load prediction,' Heavy Vehicle Systems, Special Series, Int. J. of Vehicle Design,, Vol.1, No. 1 (1993), pp. 3-19.

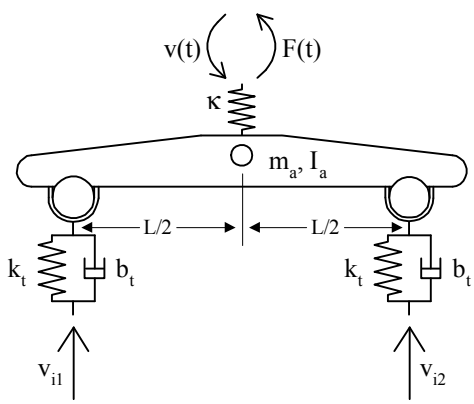


## E.4 Hydro-pneumatic Suspension Properties

| Hydro-pneumatic Suspension Properties[1] | | |
|---|---|---|
| *Hydraulic Accumulator Properties* | | |
| Static accumulator pressure | $1.034 \times 10^{4}$ | kPa |
| Static accumulator volume | $1.23 \times 10^{-3}$ | $m^3$ |
| Gas constant ($\gamma$) | 1.4 | |
| *Hydraulic Line and Piston Properties* | | |
| Hydraulic line length (L) | 0.76 | m |
| Hydraulic line diameter | 0.0063 | $m^2$ |
| Hydraulic fluid density | 900 | $kg/m^3$ |
| Hydraulic fluid viscosity | 0.29 | kg/m-s |
| Hydraulic piston area (Ap) | $6.55 \times 10^{-3}$ | $m^2$ |
| *Additional Properties* | | |
| Stiff connection spring ($\kappa$) | $1 \times 10^{10}$ | N/m |

[1] McGhie, J., *Hydraulic Schematic*, Transworld Crane Mechanical Drawing, June 2000.

White, F.M., *Fluid Mechanics*, 3rd ed. Boston: McGraw-Hill, 1999.

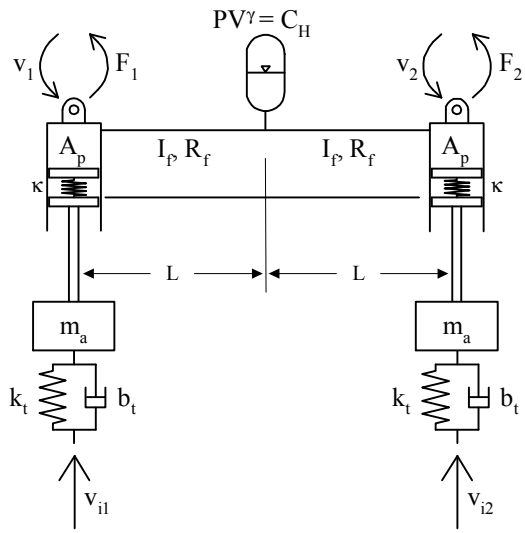


E.5 Air Ride Suspension Properties

| Air Ride Suspension Properties[1] | | |
|---|---|---|
| *Air Bag Properties* | | |
| Static air bag pressure | $6.90 \times 10^{2}$ | kPa |
| Static air bag volume | $2.08 \times 10^{-2}$ | $m^3$ |
| Gas constant ($\gamma$) | 1.4 | |
| Equivalent air bag area | 0.05 | $m^2$ |
| *Swing Arm Properties* | | |
| Swing arm length ($l_s$) | 0.9 | m |
| Distance from pin to axle ($l_a$) | 0.51 | m |
| *Additional Properties* | | |
| Suspension damping constant ($b_s$) | $2.47 \times 10^{3}$ | N-s/m |

[1] Galizin, G., *Data Tables for the RL-250 Suspension*, Holland (Air Ride) Data Tables, April 2002.

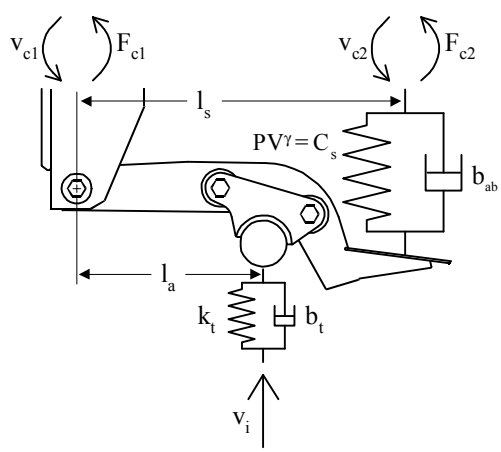

(This page is intentionally left blank)

# APPENDIX F CRANE PARAMETERS

In order to get reasonable results, a representative set of data had to be developed for the cases that are looked at. The data set that is used is pieced together from numerous sources. Many parameters associated with unsprung masses were estimated using values for similar quantities found in literature [8 and 14]. A majority of the information regarding the various distances that are used were determined from drawings [10 and 32] and Caltrans [6]. Additional information on system dimensions were obtained through personnel contacts [29, 30, and 31]. The information collected through these sources provided a majority of the parameters used in the simulation. However, additional parameters such as the sprung masses and pitch moments of inertia had to be estimated. Based on the system geometry and static weights of the system [6, 29, 30, and 31], the data could be supplemented through the application of basic engineering principles. The numbers used here are purely representative, and further research is required to obtain more accurate parameters for the system.

F.1 Representative Four Axle Carrier with Leaf Spring Dolly and Lattice Boom

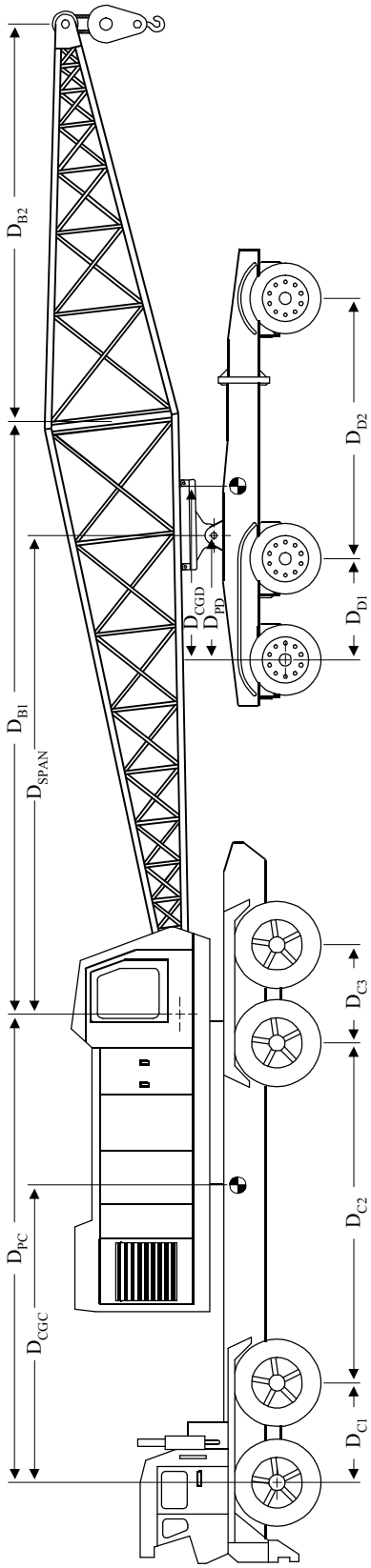

| Variable | Value | Units | Description |
|---|---|---|---|
| **Carrier** | | | 4 axle walking beam |
| *Distances* | | | |
| $D_{C1}$ | 1.52 | m | Distance between axles 1 and 2 |
| $D_{C2}$ | 5.181 | m | Distance between axles 2 and 3 |
| $D_{C3}$ | 1.524 | m | Distance between axles 3 and 4 |
| $D_{CGC}$ | 4.35 | m | Distance between axle 1 and carrier CG |
| $D_{PC}$ | 7.16 | m | Distance between axle 1 and boom pin |
| *Mass and inertia (Carrier)* | | | |
| $M_C$ | 4.35E+04 | kg | Sprung mass of the carrier |
| $I_C$ | 2.99E+05 | $kgm^2$ | Carrier Inertia |
| *Suspension* | | | *walking beam* |
| $K_{TIREC}$ | 2.45E+06 | N/m | Carrier tire stiffness |
| $B_{TIREC}$ | 2.10E+03 | Ns/m | Carrier tire damping |
| $M_{us1}$ | 1380 | kg | Axles 1 and 2 unsprung mass |
| $I_{us1}$ | 724 | $kgm^2$ | Axles 1 and 2 inertia |
| $M_{us2}$ | 2222 | kg | Axles 3 and 4 unsprung mass |
| $I_{us2}$ | 1256 | $kgm^2$ | Axles 3 and 4 inertia |
| **Dolly** | | | 3 axle independent leaf spring |
| (axles are numbered 5, 6 and 7) | | | |
| *Distances* | | | |
| $D_{D1}$ | 1.52 | m | Distance between axles 5 and 6 |
| $D_{D2}$ | 3.99 | m | Distance between axles 6 and 7 |
| $D_{CGD}$ | 2.65 | m | Distance between axle 5 and dolly CG |
| $D_{PD}$ | 1.9 | m | Distance between axle 5 and dolly pin |
| *Mass and inertia (Dolly)* | | | |
| $M_D$ | 2.40E+03 | kg | Dolly sprung mass |
| $I_D$ | 9.74E+03 | kg | Dolly inertia |
| *Suspension* | | | *Axles 5 and 6 - walking beam, Axle 7 - independent* |
| $K_{TIRED}$ | 3.28E+06 | N/m | Dolly tire stiffness |
| $B_{TIRED}$ | 4.20E+03 | Ns/m | Dolly tire damping |
| SAK | 5.20E+05 | N/m | Suspension stiffness (same for 5, 6 and 7) |
| SAB | 8.76E+03 | Ns/m | Suspension damping (same for 5, 6 and 7) |
| $M_{us3,4,5}$ | 635 | kg | Unsprung axle mass (same for 5, 6 and 7 |

| **Boom** | | | Lattice |
|---|---|---|---|
| *Distances* | | | |
| $D_{B1}$ | 6.1 | m | Length of front taper |
| $D_{B2}$ | 9.1 | m | Length of rear taper |
| $D_{span}$ | 6.93 | m | Distance between carrier pin and dolly pin |
| *Other* | | | |
| LBM | 2.08E+03 | kg | Load block mass |

| Section | Area | Units | Inertia | Units |
|---|---|---|---|---|
| 1 | 0.0273 | $m^2$ | 3.28E-04 | $m^4$ |
| 2 | 0.0273 | $m^2$ | 0.0109 | $m^4$ |
| 3 | 0.0273 | $m^2$ | 3.28E-04 | $m^4$ |

F.2 Four Axle Carrier With Three Axle Dolly Using a Telescoping Boom

The next to sets of parameters are four two different crane configurations. The first case is a walking beam carrier implementing a walking beam suspension. The dolly associated with configuration uses leaf spring suspension. The second case is a four axle hydro-pneumatic suspension carrier. The dolly associated with this configuration uses the air ride suspension. The parameters for these two models are presented together, because the nomenclature for the distances are identical between the two cases.

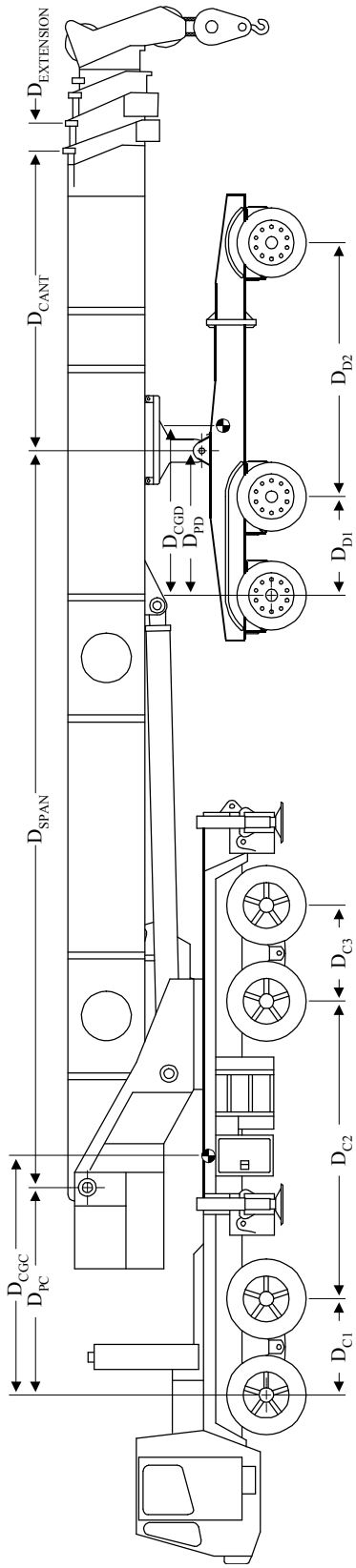
D_EXTENSION
D_CANT
D_SPAN
D_CGC
D_PC
D_CGD
D_PD
D_D2
D_D1
D_C3
D_C2
D_C1

| | |
|---|---|
| Carrier | **4 axle walking beam** |
| Dolly | **3 axle independent leaf spring** |
| Boom | **Telescoping** |

| Variable | Value | Units | Description |
|---|---|---|---|
| **Carrier** | | | 4 axle walking beam |
| *Distances* | | | |
| $D_{C1}$ | 1.5 | m | Distance between axles 1 and 2 |
| $D_{C2}$ | 4.65 | m | Distance between axles 2 and 3 |
| $D_{C3}$ | 1.5 | m | Distance between axles 3 and 4 |
| $D_{CGC}$ | 3.74 | m | Distance between axle 1 and carrier CG |
| $D_{PC}$ | 3.28 | m | Distance between axle 1 and boom pin |
| *Mass and Inertia (Carrier)* | | | |
| $M_C$ | 3.88E+04 | kg | Carrier sprung mass |
| $I_C$ | 4.46E+05 | $kgm^2$ | Carrier inertia |
| *Suspension* | | | *walking beam* |
| $K_{TIREC}$ | 2.45E+06 | N/m | Carrier tire stiffness |
| $B_{TIREC}$ | 2.10E+03 | Ns/m | Carrier tire damping |
| $M_{us1}$ | 1.38E+03 | kg | Axles 1 and 2 unsprung mass |
| $I_{us1}$ | 742 | $kgm^2$ | Axles 1 and 2 inertia |
| $M_{us2}$ | 2.22E+03 | kg | Axles 3 and 4 unsprung mass |
| $I_{us2}$ | 1266 | $kgm^2$ | Axles 3 and 4 inertia |
| **Dolly** | | | 3 axle independent leaf spring |
| (axles are numbered 5, 6 and 7) | | | |
| *Distances* | | | |
| $D_{D1}$ | 1.52 | m | Distance between axles 5 and 6 |
| $D_{D2}$ | 3.99 | m | Distance between axles 6 and 7 |
| $D_{CGD}$ | 2.65 | m | Distance between axle 5 and dolly CG |
| $D_{PD}$ | 1.9 | m | Distance between axle 5 and dolly pin |
| *Mass and Inertia (Dolly)* | | | |
| $M_D$ | 2.40E+03 | kg | Dolly sprung mass |
| $I_D$ | 9.74E+03 | kg | Dolly inertia |

| *Suspension* | *Axles 5, 6 and 7 - leaf spring* | | |
|---|---|---|---|
| $K_{TIRED}$ | 3.28E+06 | N/m | Dolly tire stiffness |
| $B_{TIRED}$ | 4.20E+03 | Ns/m | Dolly tire damping |
| SAK | 5.20E+05 | N/m | Suspension stiffness (same for 5, 6 and 7) |
| SAB | 8.76E+03 | Ns/m | Suspension damping (same for 5, 6 and 7) |
| $M_{us3,4,5}$ | 635 | kg | Unsprung axle mass (same for 5, 6 and 7 |

| **Boom** | telescoping | | |
|---|---|---|---|
| *Distances* | | | |
| $D_{span}$ | 10.38 | m | Distance between carrier pin and dolly pin |
| $D_{cant}$ | 6.32 | m | Boom cantilever length |
| D_extension | 0.5 | m | Length of section extending out of previous |
| *Other* | | | |
| LBM | 2.08E+03 | kg | Load block mass |
| N_sections | 4 | | Total number of boom sections |

| Section | Area | Units | Inertia | Units |
|---|---|---|---|---|
| 1 | 0.0264 | $m^2$ | 0.0041 | $m^4$ |
| 2 | 0.0249 | $m^2$ | 0.0035 | $m^4$ |
| 3 | 0.0235 | $m^2$ | 0.0029 | $m^4$ |
| 4 | 0.022 | $m^2$ | 0.0024 | $m^4$ |

| | |
|---|---|
| Carrier | **4 axle hydro-pneumatic** |
| Dolly | **3 axle air-ride** |
| Boom | **Telescoping** |

| Variable | Value | Units | Description |
|---|---|---|---|
| **Carrier** | 4 axle hydro-pneumatic | | |
| *Distances* | | | |
| $D_{C1}$ | 1.5 | m | Distance between axles 1 and 2 |
| $D_{C2}$ | 4.65 | m | Distance between axles 2 and 3 |
| $D_{C3}$ | 1.5 | m | Distance between axles 3 and 4 |
| $D_{CGC}$ | 3.74 | m | Distance between axle 1 and carrier CG |
| $D_{PC}$ | 3.28 | m | Distance between axle 1 and boom pin |
| *Mass and Inertia (Carrier)* | | | |
| $M_C$ | 3.88E+04 | kg | Carrier sprung mass |
| $I_C$ | 4.46E+05 | $kgm^2$ | Carrier inertia |

| | | | |
|---|---|---|---|
| *Suspension* | | | *hydro-pneumatic* |
| $K_{TIREC}$* | 1.22E+06 | N/m | Carrier tire stiffness |
| $B_{TIREC}$* | 1.05E+03 | Ns/m | Carrier tire damping |
| ma1* | 317.5 | kg | Axles 1 and 2 unsprung mass |
| Rf1* | 5.54E+07 | $kg/sm^4$ | Axles 1 and 2 line resistance |
| L1* | 1.22 | m | Axles 1 and 2 hydraulic line length |
| D1* | 0.0127 | m | Axles 1 and 2 hydraulic line diameter |
| ma2* | 317.5 | kg | Axles 3 and 4 unsprung mass |
| Rf2* | 5.54E+07 | $kg/sm^4$ | Axles 3 and 4 line resistance |
| L2* | 1.22 | m | Axles 3 and 4 hydraulic line length |
| D2* | 0.0127 | m | Axles 3 and 4 hydraulic line diameter |
| Vac* | 1.23E-03 | $m^3$ | Accumulator volume |
| Pac* | 1.04E+07 | $N/m^2$ | Accumulator precharge |
| AP* | 6.55E-03 | $m^2$ | Piston Area |
| *Parameters are for one side only | | | |
| **Dolly** | | 3 axle air ride | |
| **Dolly axles are numbered 5, 6 and 7 | | | |
| *Distances* | | | |
| $D_{D1}$ | 1.52 | m | Distance between axles 1 and 2 |
| $D_{D2}$ | 3.99 | m | Distance between axles 2 and 3 |
| $D_{CGD}$ | 2.65 | m | Distance between axle 1 and dolly CG |
| $D_{PD}$ | 1.9 | m | Distance between axle 1 and dolly pin |
| *Mass and Inertia (Dolly)* | | | |
| $M_D$ | 2.40E+03 | kg | Dolly sprung mass |
| $I_D$ | 9.74E+03 | kg | Dolly inertia |
| *Suspension* | | | *air ride* |
| Air-ride suspension parameters are the same for each axle | | | |
| *Parameters are for one side only | | | |
| $K_{TIRED}$* | 1.64E+06 | N/m | Dolly tire stiffness |
| $B_{TIRED}$* | 2.10E+03 | Ns/m | Dolly tire damping |
| $l_a$ | 0.51 | m | Distance between swing arm connection point and axle |
| $l_s$ | 0.9 | m | Length of swing arm |
| P_AR* | 6.90E+05 | $N/m^2$ | Air-ride precharge pressure |
| b_AR* | 2470 | Ns/m | Shock damping |
| A_AR* | 5.00E-02 | $m^2$ | Eq. Air bag area |
| V_AR* | 2.08E-02 | $m^3$ | Air bag volume |
| m* | 317.5 | kg | Un-sprung mass |

| **Boom** | | | telescoping |
|---|---|---|---|
| *Distances* | | | |
| $D_{span}$ | 10.38 | m | Length between carrier pin and dolly connection |
| $D_{cant}$ | 6.32 | m | Boom cantilever length |
| D_extensi | 0.5 | m | Boom sleeve overhang |
| *Other* | | | |
| LBM | 2080 | kg | Load block mass |
| N_section | 4 | | Total number of boom sections |

| Section | Area | Units | Inertia | Units |
|---|---|---|---|---|
| 1 | 0.0264 | $m^2$ | 0.0041 | $m^4$ |
| 2 | 0.0249 | $m^2$ | 0.0035 | $m^4$ |
| 3 | 0.0235 | $m^2$ | 0.0029 | $m^4$ |
| 4 | 0.022 | $m^2$ | 0.0024 | $m^4$ |

## F.3 Six Axle Hydro-pneumatic Carrier with Three Axle Air Ride Dolly and Six Sleeve Telescoping Boom

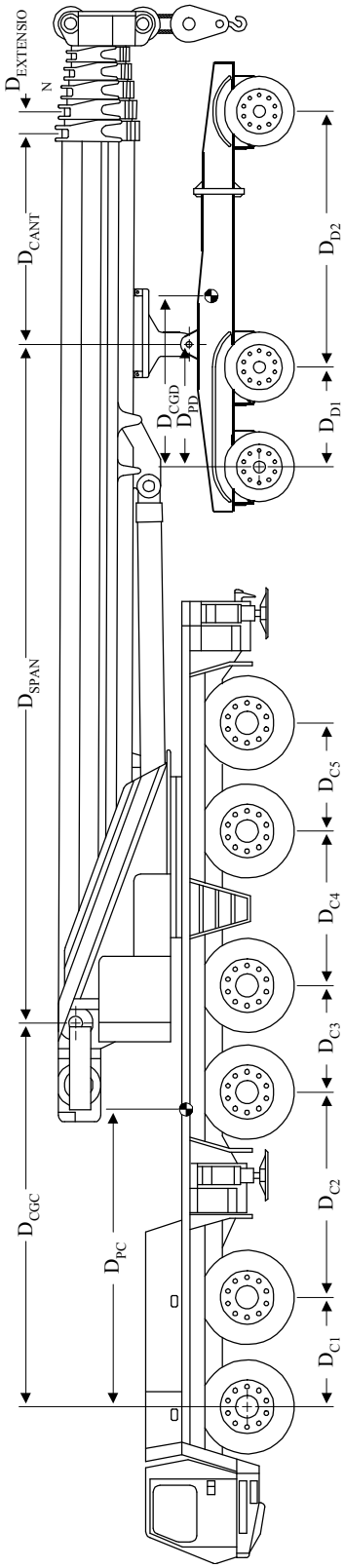

| **Carrier** | | | 6 axle hydro-pneumatic |
|---|---|---|---|
| *Distances* | | | |
| $D_{C1}$ | 1.7 | m | Distance between axles 1 and 2 |
| $D_{C2}$ | 3.2 | m | Distance between axles 2 and 3 |
| $D_{C3}$ | 1.65 | m | Distance between axles 3 and 4 |
| $D_{C4}$ | 2.8 | m | Distance between axles 4 and 5 |
| $D_{C5}$ | 1.65 | m | Distance between axles 5 and 6 |
| $D_{CGC}$ | 5.39 | m | Distance between axle 1 and carrier CG |
| $D_{PC}$ | 6.35 | m | Distance between axle 1 and boom pin |
| *Mass and Inertia (Carrier)* | | | |
| $M_C$ | 4.13E+04 | kg | Carrier spurng mass |
| $I_C$ | 8.28E+05 | $kgm^2$ | Carrier inertia |
| *Suspension* | | | hydro-pneumatic |
| $K_{TIREC}$* | 1.22E+06 | N/m | Carrier tire stiffness |
| $B_{TIREC}$* | 1050.8 | Ns/m | Carrier tire damping |
| ma1* | 317.5 | kg | Axles 1 and 2 unsprung mass |
| Rf1* | 5.54E+07 | $kg/sm^4$ | Axles 1 and 2 line resistance |
| L1* | 1.22 | m | Axles 1 and 2 hydraulic line length |
| D1* | 0.0127 | m | Axles 1 and 2 hydraulic line diameter |
| ma2* | 555.5 | kg | Axles 3 and 4 unsprung mass |
| Rf2* | 5.54E+07 | $kg/sm^4$ | Axles 3 and 4 line resistance |
| L2* | 1.22 | m | Axles 3 and 4 hydraulic line length |
| D2* | 0.0127 | m | Axles 3 and 4 hydraulic line diameter |
| ma3* | 317.5 | kg | Axles 5 and 6 unsprung mass |
| Rf3* | 5.54E+07 | $kg/sm^4$ | Axles 5 and 6 line resistance |
| L3* | 1.22 | m | Axles 5 and 6 hydraulic line length |
| D3* | 0.00127 | m | Axles 5 and 6 hydraulic line diameter |
| Vac* | 1.23E-03 | $m^3$ | Accumulator volume |
| Pac* | 1.03E+07 | $N/m^2$ | Accumulator precharge |
| A_P* | 6.55E-03 | $m^2$ | Piston area |
| *Parameters are for one side only | | | |

| **Dolly** | | | 3 axle air ride |
|---|---|---|---|
| (axles are numbered 7, 8 and 9) | | | |
| *Distances* | | | |
| $D_{D1}$ | 1.52 | m | Distance between axles 7 and 8 |
| $D_{D2}$ | 3.99 | m | Distance between axles 8 and 9 |
| $D_{CGD}$ | 2 | m | Distance between axle 7 and dolly CG |
| $D_{PD}$ | 1.98 | m | Distance between 7 and boom pin |
| *Mass and Inertia (Dolly)* | | | |
| $M_D$ | 4.20E+03 | kg | Dolly sprung mass |
| $I_D$ | 6.23E+03 | $kgm^2$ | Dolly inertia |
| *Suspension* | | | air ride |
| Air ride suspension parameters are the same for each axle | | | |
| $K_{TIRED}$* | 1.64E+06 | N/m | Dolly tire stiffness |
| $B_{TIRED}$* | 2.10E+03 | Ns/m | Dolly tire damping |
| $l_a$ | 0.51 | m | Distance between swing arm connection point and axle |
| $l_s$ | 0.9 | m | Length of swing arm |
| P_AR* | 6.90E+05 | $N/m^2$ | Air-ride precharge pressure |
| b_AR* | 2470 | Ns/m | Shock damping |
| A_AR* | 5.00E-02 | $m^2$ | Eq. Air bag area |
| V_AR* | 2.08E-02 | $m^3$ | Air bag volume |
| m* | 317.5 | kg | Un-sprung mass |
| *Parameters are for one side only | | | |
| **Boom** | | | telescoping |
| *Distances* | | | |
| $D_{span}$ | 10.52 | m | Length between carrier pin and dolly connection |
| $D_{cant}$ | 3.93 | m | Boom cantilever length |
| D_extension | 0.3 | m | Boom sleeve overhang |
| *Other* | | | |
| LBM | 2.08E+03 | kg | Load block mass |
| N_sections | 6 | | Total number of boom sections |

| Section | Area | Units | Inertia | Units |
|---|---|---|---|---|
| 1 | 0.0354 | $m^2$ | 0.008 | $m^4$ |
| 2 | 0.0338 | $m^2$ | 0.007 | $m^4$ |
| 3 | 0.0321 | $m^2$ | 0.0061 | $m^4$ |
| 4 | 0.0305 | $m^2$ | 0.0052 | $m^4$ |
| 5 | 0.0289 | $m^2$ | 0.0045 | $m^4$ |
| 6 | 0.0273 | $m^2$ | 0.0038 | $m^4$ |

## F.4 Truck Parameters

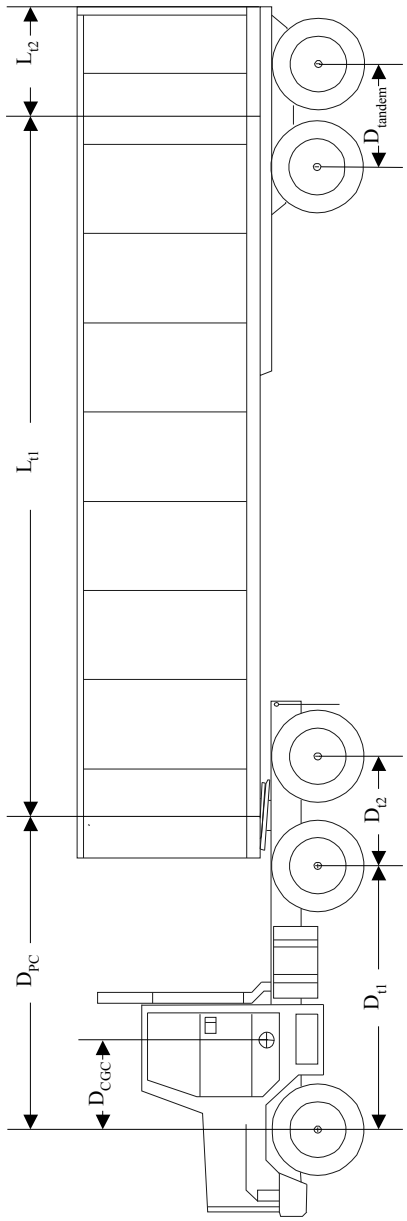

| Variable | Value | Units | Description |
|---|---|---|---|
| **Truck** | | | 3 axle: independent front with walking beam rear |
| *Distances* | | | |
| $D_{t1}$ | 5.981 | m | Distance between axles 1 and 2 |
| $D_{t2}$ | 1.5 | m | Distance between axles 2 and 3 |
| $D_{PC}$ | 6.731 | m | Distance between axle 1 and hitch pinot |
| $D_{CG}$ | 0.661 | m | Distance between axle 1 and truck CG |
| *Mass and Inertia (Truck)* | | | |
| $M_{truck}$ | 5.07E+03 | kg | Sprung mass of the truck |
| $I_{truck}$ | 3.55E+04 | $kgm^2$ | Truck Inertia |
| *Suspension* | | | *axle 1 - leaf spring, axle 2 and 3 walking beam* |
| $K_{TIREC}$ | 3.28E+06 | N/m | Rear tire stiffness-4 accross |
| $B_{TIREC}$ | 4.20E+03 | Ns/m | Rear tire damping-4 across |
| $K_{TIRECF}$ | 1.64E+06 | N/m | Front tire stiffnes |
| $B_{TIRECF}$ | 2.10E+03 | Ns/m | Rear tire stiffness |
| $M_{us1}$ | 6.35E+02 | kg | Un-sprung mass of axle one |
| AK | 5.20E+02 | N/m | Suspension stiffness of axle 1 |
| AB | 6.34E+03 | Ns/m | Suspension damping of axle 1 |
| $M_{us2}$ | 2.22E+03 | kg | Axles 2 and 3 unsprung mass |
| $I_{us2}$ | 1266 | $kgm^2$ | Axles 2 and 3 inertia |
| **Trailer** | | | 2 axle walking beam |
| (axles are numbered 4 and 5) | | | |
| *Distances* | | | |
| $D_{tandem}$ | 1.5 | m | Distance between axles 4 and 5 |
| $L_{t1}$ | 11.62 | m | Distance between hitch and rear suspension center |
| $L_{t2}$ | 0.18 | m | Distance past suspension center to end of trailer |
| *Mass (Trailer)* | | | |
| $M_{trailer}$ | 3.20E+04 | kg | Sprung weight of trailer |
| *Suspension* | | | *Axles 4 and 5 walking beam* |
| $K_{TIRED}$ | 3.28E+06 | N/m | Trailer tire stiffness |
| $B_{TIRED}$ | 4.20E+03 | Ns/m | Trailer tire damping |
| $M_{us3}$ | 2.22E+03 | kg | Axles 4 and 5 unsprung mass |
| $I_{us3}$ | 1266 | $kgm^2$ | Axles 4 and 5 inertia |
| $K_{BD}$ | 4.00E+06 | N/m | Susp. Stiff. for sprung mount walking beam |
| $B_{BD}$ | 8.00E+04 | N/m | Susp.Damp. for sprung mount walking beam |

## REFERENCES

[1] Beckwith, Lienhard, and Marangoni. *Mechanical Measurements*. Reading, Mass. Addison-Wesley Publishing Co. 1993, 5th. Ed.

[2] Bender, Erich K., Karnopp, Dean C. and Paul, Igor L., 'On the Optimization of Vehicle Suspensions Using Random Process Theory',(67-TRAN-12). Copy obtained directly from Dean Karnopp.

[3] Bishop, Phil. "Hanging Tough", Cranes Today. April, 2001

[4] Burkett, George. Thesis 2002

[5] California State Budget Summary, 2001-02 http://www.dof.ca.gov/HTML/Budgt01-02/FinalSpiral01.pdf, 5/23/02 pg. 67

[6] Caltrans internal report: Ken Kirsche 1994/95 Draft report.

[7] Campbell, Colin, and Redfern, Darrner, *The MATLAB 5 Handbook*, Springer-Verlag New York, Inc. 1998.

[8] Cebon, David. *Handbook of Vehicle-Road Interaction: Vehicle Dynamics, Suspension Design, and Road Damage*, Netherlands, Swets & Zeitlinger Publishers. 1999

[9] Crandall, Stephen H., Karnopp, Dean C., Kurtz, Edward F. Jr., and Pridmore-Brown, *Dynamics of Mechanical and electromechanical systems*, New York, McGraw-Hill, 1968

[10] CTA Crane Discussion, Indian Wells Calif. June 14,2000

[11] De Pont, John. 'The influence of vehicle dynamics on pavement life', John De Pont, Bryan Pidwerbesky, Bruce Steven. Heavy vehicle systems. Vol. 6 no. 1-4 (1999)

[12] Félez, J. and C. Vera., Bond graph assisted models for hydro-pneumatic suspensions in crane vehicles, Vehicle system dynamics. Vol. 16, no. 5-6 (1987) p. [313]-332 : ill. ; 24 cm.

[13] Galizin, Greg, *Data Tables for the RL-250 Suspension*, Holland (Air Ride) Data Tables, April 2002.

[14] Karamihas, S.M. and Gillespie, T.D. (1993) 'Characterization of trucks for dynamic load prediction' Heavy Vehicle Systems, Special Series, Int. J. of Vehicle Design. Vol. 1. No. 1 pp. 3-19.

[15] Karnopp, Dean, Notes from MAE 220 Spring 2001, UCDavis

[16] Karnopp, Dean C., Margolis, Donald L., Rosenberg, Ronald C. *System Dynamics: Modeling and Simulation of Mechtronic Systems*, New York, John Wiley & Sons, Inc. 3rd ed. 2000.

[17] *Learning SIMULINK*, The Mathworks inc. 1999

[18] Logan, D. L.. A First Course in the Finite Element Method, Boston Mass. PWS Kent Publishing Company 1986

[19] Martin, H., *The Design of Hydraulic Components and Systems*, New York: Ellis Horwood, 1995.

[20] McDonald, John, Thesis 2002

[21] Marks, Rober J. II, *Advanced topics in Shannon Sampling and Interpolation Theory*. NewYork, Springer-Verlag 1993

[22] Mitschke, M., Dynamik det Kraftfahrzeuge, Band B:Schwingungen, Springer-Varlag,1984

[23] 'Road Simulator Study of Heavy-Vehicle Wheel Forces', U.S. Department of Transportation, Sept. 1998

[24] Rouillard, Vincent, Ben Bruscella, and Michale Sek, 'Classification of Road Surface Profiles',Journal of Transportation Engineering, January/February 2000

[25] Thompson,W. T., *Theory of Vibration with Applications*,4th ed.,New Jersey, Prentice Hall, 1993

[26] Tielking, J.T.(1995) 'Wide base radial truck tyres: properties and performance.' Heavy Vehicle Systems, Special Series. Int. J. of Vehicle Design. Vol. 2. Nos ¾, pp. 187-207

[27] White, F.M., *Fluid Mechanics*, 3rd ed. Boston: McGraw-Hill, 1999.

Personal Contacts

[28] Lee, James
Caltrans
Phone: (916) 227-7139
Email: James_N_lee@dot.ca.gov

[29] Martin, Bob
Caltrans
Phone: (916) 653-5732
Email: bmartin@dot.ca.gov

[30] McGhie, Jim
Transworld Crane
Phone: (702) 798-8920
Email: NA

[31] Olsen, Stephon
Freightliner
Phone: (425) 828-5148
Email: NA

Manufactures

[32] Terex – American 800 Series Truck Crane General Specification
American Crane Corporation
202 Raleigh Street
Wilmington, North Carolina 28403